Synthesis and Application of Oxidised Cellulose

Jin, Yun

Award date:
2016

Awarding institution:
University of Bath

Synthesis and Application of Oxidised Cellulose

Yun Jin

A thesis submitted for the degree of Doctor of Philosophy

University of Bath

Department of Chemistry

Nov 2015

Table of Contents

Acknowledgements

I am extremely thankful to my supervisors Karen Edler and Janet Scott for the assistance, guidance and support throughout my PhD study, which enabled me to develop critical thinking and work independently in my research area. I also thank Professor Frank Marken for the help of the electrochemistry experiments, which inspired me a lot at the beginning of my PhD study.

I acknowledge Professor Len Barbour for accommodating me as part of his group during the research visit at Stellenbosch University. I would also like to thank a number of colleagues at University of Bath who I was fortunate to work with and helped a lot in my experiments; namely Dr John Lowe, Dr John Mitchels, Mr Fernando Acosta and Mrs Ursula Potter. I am grateful to all the members in the Edler and Scott Research groups for making my time an enjoyable and rewarding experience.

I would like to thank my family for all their continuous support during my undergraduate, master and PhD, both financially and emotionally, which has allowed me to pursue my aspirations. I am immensely grateful, thank you.

Finally, I acknowledge University of Bath for the graduate school scholarship, which funded my PhD study, and Unilever for the financial support towards my research project.

Abstract

Oxidised cellulose nanofibrils (OCNF) prepared from renewable sources of cellulose, one of the largest biopolymers, have applications in various fields. In this thesis research towards developing a sustainable electro-chemical method for the selective oxidation of cellulose to increase the dispersibility of the corresponding OCNF in aqueous solutions is reported, and some potential applications of OCNF explored.

Initial work involved developing a facile method for rapid voltammetric screening of mediators, pH and buffer solutions in order to optimise the reaction conditions for electro-oxidation of cellulose. The electro-oxidation of cellulose was optimised based on the voltammetric screening results (using a TEMPO mediator in carbonate buffer at pH 10), and the reaction was accomplished in a comparable amount of time (2-3 h) to that used in the chemical oxidation. The electro-oxidised cellulose particles possessed a similar fibril-like morphology to chemically oxidised cellulose, although higher aldehyde contents were observed (a post-polishing step was required to convert aldehydes into carboxylates).

OCNF were shown to stabilise the hexadecane-water interface without the addition of other emulsifiers, producing Pickering emulsions with oil droplets of *ca* 2 μm in diameter in the aqueous phase, which remained stable for a period of weeks. The behaviour of OCNF at the oil-water interface under various salt concentrations was explored *in situ* by small angle scattering, demonstrating that salt addition thickened OCNF shell in the Pickering emulsion, which allowed the release of oil-soluble drug from the emulsion to be controlled. The study showed the potential of OCNF to be developed into an ingredient in cosmetic products and to reduce the use of some irritating surfactants (e.g. sodium lauryl sulfate) in formulations.

Two metal organic frameworks/OCNF (or bacterial cellulose) composites were prepared at ambient temperature via facile synthesis methods, forming self-standing membranes upon drying. $[Cu_3(\textit{benzene-1,3,5-tricarboxylate})_2]_n$ was investigated for the CO_2/N_2 sorption property, and $(Ni(NCS)_2(\textit{para-phenylpyridine})_4$ was explored for the separation of xylene isomer vapours. The cellulose based composites allow incorporation of selected particles for various applications (e.g. catalysts, purification), while enabling the metals used to be recycled easily after the use of the composites.

Chapter 1 Introduction

Cellulose, the most abundant natural resources of wood bio-mass at present,[1] has long been utilized by humans for more than million years.[2] Humans use cellulose containing materials for textiles,[3] papers,[4] construction[5] and wound dressings,[6] after mechanical and/or chemical treatment.[7]

The chemical structure of cellulose is a homogenous linear polymer of D-glucose (Chart 1.1), containing an average degree of polymerization (DP) varying from 200 (e.g. regenerated cellulose) to 10,000 (e.g. native cellulose) anhydroglucose (1→4)-β-glycoside bond linked units, contingent on the type of cellulose.[8]

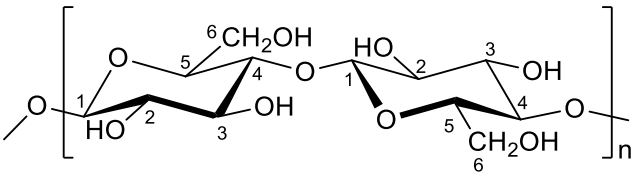

Chart 1.1 Structure of cellulose

In nature, the cellulose polymer chains are assembled to form crystalline microfibrils by hydrogen bonding and van der Waals Interactions,[9] which are further bundled into macrofibrils and fibres in a hierarchical structure (Figure 1.1). The cellulose microfibrils are semi-crystalline and there are also some amorphous regions and some irregularities such as twists of the microfibrils.[10] This results in the partial hydration of cellulose fibres by water.[11]

There are four types of cellulose structure,[12] which vary according to the relative orientation of the cellulose chains: Cellulose I (a mixture of two polymorphs I_α and I_β), also known as native cellulose, is the form existing in nature. Cellulose produced by primitive organisms (e.g. *Acetobacter xylinum*) is enriched in I_α (triclinic structure) while cellulose I_β (monoclinic structure) is predominant in higher plants. Cellulose II, can be obtained irreversibly from cellulose I by either regeneration, which is the process of solubilisation of cellulose I in a solvent (e.g. ionic liquid, LiCl/DMSO) followed by re-precipitation using an anti-solvent (e.g. water, methanol),[13] or mercerization (the process of swelling cellulose in concentrated sodium hydroxide to yield cellulose II). Cellulose I has a parallel chain alignment, while cellulose II has anti-parallel chain alignment in a two-molecule unit cell.[14] This refers to the chain

direction with regards to the position of the reducing and non-reducing ends of the polymer (Chart 1.1). Cellulose III_I and III_{II} can be obtained in a reversible process by the treatment of cellulose I and II correspondingly, using liquid ammonia. Cellulose IV (IV_I and IV_{II}) is formed by heating cellulose III (III_I and III_{II}) to 206 °C in glycerol.

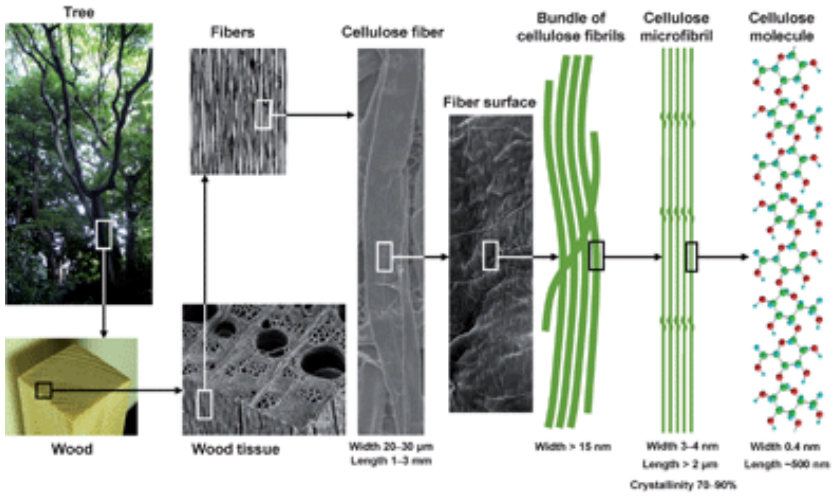

Figure 1.1 Hierarchical structure of wood biomass and the characteristics of cellulose microfibrils.[15] Reproduced from Ref. 15 with permission from The Royal Society of Chemistry.

Nanocellulose (including nanofibrillated cellulose, NFC) are fibres with at least one nano-dimension (1-100 nm). In the past 20 years, there has been a growing interest in the use of nanocellulose from both academics and industry, with the increasing demand for products produced from renewable, non-toxic, abundant and non-petroleum based resources.[1,16] Mechanical, or chemical-assisted nanofibrillation is required to prepare NFC by breaking the strong hydrogen bonding between the microfibrils.[16] High energy consumption is inevitable when preparing NFC by mechanical nanofibrillation. Therefore, chemical-assisted methods (acid hydrolysis,[17] enzymatic pretreatment[18] and chemical oxidation[19]) are often used to assist the nanofibrillation process and reduce the overall energy consumption of NFC production, as only mild mechanical treatments are required to disintegrate the chemically modified cellulose.

The acid hydrolysis and enzymatic hydrolysis processes result in needle shaped cellulose nanocrystals, as the amorphous regions are removed faster than the crystalline regions.[20] The hydrolysis reaction is dependent on the reaction time,

temperature and concentration of the acid used, which control the yield and the physical properties of the nanocrystals.[21] The resulting hydrolysed suspension is then diluted with excess water to stop the reaction followed by repeated washing with centrifugation.[22] The obtained suspension is then dialysed against distilled water to remove any free acid. These cellulose derived nanomaterials, known as cellulose nanowiskers (CNW) or cellulose nanocrystals (CNC), have been used for various applications including composite materials,[23,24] chiral nematic films for sensors,[25] and electrodes for chemical detection.[26]

Further modification of CNC could deliver new surface properties to the nanocrystals and a range of modifications has been reviewed by Eyley and Thielemans.[27] Surface modifications can render cellulose compatible with many polymers, for example, esterification or amidation may be used to allow 'grafting to' or 'grafting from' cellulose surfaces.[28]

In contrast to CNC, oxidised cellulose nanofibrils contain amorphous cellulose materials as well as the crystalline portions and can be produced from cellulose by the action of a wide range of oxidising agents, such as chlorine,[29] hydrogen peroxide,[29] nitrogen dioxide,[30] permanganate,[31] hypochlorous acid[32] and metal oxide (e.g. CuO).[33] Oxidised cellulose may contain carboxylate, aldehyde, and/or ketone groups, in addition to the original hydroxyl groups, depending on the nature of the oxidant and reaction conditions.[34-36] The oxidised cellulose materials produced are mainly used as surgical hemostats,[37] but in many cases, the oxidising chemicals used are rather toxic, and the reactions are accompanied by substantial degradation of the cellulose and non-selective oxidation, which limits the application of the oxidised cellulose.[38]

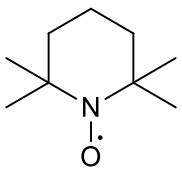

Chart 1.2 Molecular structure of TEMPO

A promising selective oxidation of primary alcohols was first reported by Semmelhack *et al*., using 2,2,6,6-tetramethyl-1-piperidinyloxy radical (TEMPO, Chart

1.2) as mediator, which is oxidised *in situ* and regenerated by a primary oxidant.[39] In the following report, the cellulose that is selectively oxidised at the C6 hydroxyl group (Chart 1.3) by TEMPO mediated oxidation is referred to as 'oxidised cellulose' or 'oxidised cellulose nanofibrils'.

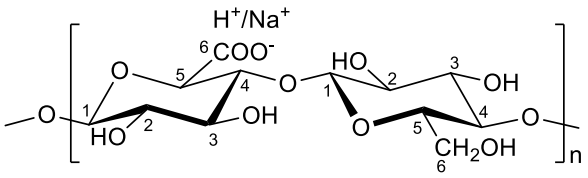

Chart 1.3 Molecular structure of C6 oxidised cellulose

The selectively oxidised cellulose, once mechanically dispersed, is in the form of nano-fibres (one diameter < 100 nm) which are 3-4 nm in width and a few microns in length.[40] Due to electrostatic repulsion between anionically charged cellulose microfibrils, the zeta potentials of which are approximately -80 mV in water,[41] completely individualized oxidised cellulose nanofibrils may be obtained.[42]

Oxidised cellulose nanofibrils (OCNF) have larger surface area, higher aspect ratio and flexible fibrils, which are different from the bulk cellulose and CNC. The properties of oxidised cellulose nanofibrils impart distinctive rheology behaviour[43] and better mechanical performance in composites,[44] compared to CNC, making OCNF more desirable in certain applications. In this study, we investigate the greener and more sustainable production of oxidised cellulose and its use in various applications.

1.1 TEMPO Mediated Oxidation of Cellulose

The partial C6 oxidation of cellulose mediated by TEMPO with NaClO as the primary oxidant was first introduced by Isogai in 1998.[45] The aqueous TEMPO mediated system selectively oxidised primary hydroxyl groups over secondary hydroxyl groups in the oxidation. This system is not only applicable to carbohydrate substrates like cellulose,[46] starch,[47] hyaluronan,[48] paramylon and curdlan,[49] but also can be applied to many hydroxyl group containing compounds. Such derivatives yield

polyelectrolytes and valuable intermediates (e.g. production of DHA from glycerol).[50-52]

Cellulose (Chart 1.1), as the most abundant natural biopolymer, has been extensively investigated by many researchers for various purposes due to its relative cheapness, abundance, recyclability and diversity of sources.[53] In addition, use of cellulose as a feedstock does not, in general, compete with food production and thus cellulose is more attractive to academia and industry than other carbohydrates like starch.[54]

The aqueous NaClO/NaBr/TEMPO system to selectively oxidise cellulose at the C6 hydroxyl groups and has been widely used as a method for selective cellulose oxidation in a basic medium since it was first introduced (the reaction is proposed as a two-step oxidation: aldehyde groups are formed from hydroxyl groups in the first stage and transformed into carboxylate groups in the second stage).[45,55,56] In the oxidation system, NaClO serves as the primary oxidant, while NaBr is a cocatalyst, and TEMPO is a mediator (Scheme 1.1).

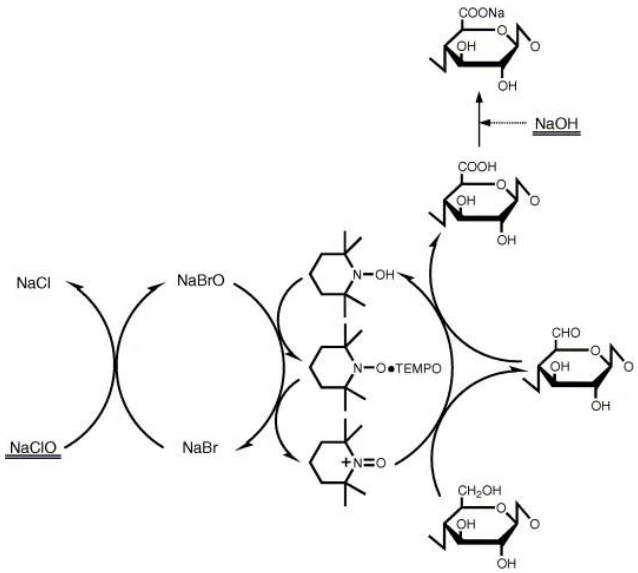

Scheme 1.1 Scheme of TEMPO-mediated oxidation of cellulose[57]. Reproduced from Ref. 57 with permission from Elsevier (© Elsevier 2006).

In the TEMPO mediated system, only catalytic amounts of TEMPO are required for the reaction, as the mediator is constantly regenerated by the primary oxidant and the NaBr co-catalyst; TEMPO:NaBr ratio is 1:10.[40] The content of carboxylate groups

formed on the fibrils surface is dependent on the amount of NaClO per gram of cellulose (ratio of NaClO/anhydroglucose unit), and typically 1.3-5.0 mmol NaClO per gram of cellulose is used in the oxidation. The maximum amount of the carboxylate groups available on the OCNF surface (which varies from 0.5 to 1.7 $mmol \cdot g^{-1}$) is dependent on the crystal size of cellulose, where higher carboxylate contents are achieved in the oxidised cellulose with smaller crystal size, as proportionally more C6 hydroxyl groups are exposed on the fibril surface for oxidation in the smaller crystals.[42]

Several variables affect the reaction: pH, mediator type (TEMPO analogue), temperature, cellulose type and reaction time.

Amongst these variables, pH seems to be the most important factor affecting reaction rate: The reaction has been demonstrated to be fast under basic conditions, and much slower in a neutral or acidic environment.[58] However, side reactions did occur under more alkaline conditions (pH >10), resulting in the degradation of the cellulose chain caused by hydroxyl radicals formed from NaBrO and TEMPOH in NaClO/NaBr/TEMPO system (Scheme 1.2).[59]

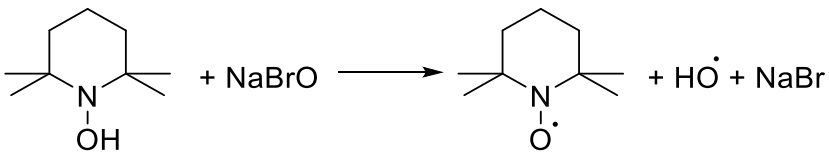

Scheme 1.2 Hydroxyl radicals ($HO^{\cdot}$) formed in NaClO/NaBr/TEMPO system

The possible mechanisms of TEMPO oxidation of alcohols at different pHs have been investigated both by studying intermediates and considering the hydrogen isotope effect (measure the change in the reaction rate when hydrogen atoms in the reactants are substituted with deuterium).[60,61] The difference in reaction rate under alkali and acidic conditions could be explained by the mechanism proposed by de Nooy shown in Scheme 1.3:[62] In the catalytic cycle, TEMPO or TEMPOH is first oxidised to $TEMPO^{+}$ by primary oxidant (NaClO, enzyme, or electro-oxidation). At higher pH (> pH 8), the reaction is hypothesized to proceed via the intramolecular cyclic elimination and the formation of the oxoammonium/alkoxide complex is the rate determining step, which is directed by the steric effect (primary alcohols react

faster than secondary alcohols).[15,38] Under acidic or neutral conditions, intermolecular hydrogen transfer is the rate limiting step for the oxidation, where the rate of abstraction of the α-proton of the alcohol substrate by the anion determines the rate of the oxidation.[63,64] The hydroxyl groups are first oxidised to aldehyde groups by $TEMPO^+$, and the hydrated aldehydes are further oxidised to carboxylates (the reaction can be halted at the aldehyde stage in non-aqueous media, which can be used to form useful intermediates by proper choice of the reaction media).[63]

A hydride transfer mechanism has been postulated under very acidic conditions (pH <4),[65] supported by the result that the oxidation of isopropyl alcohol was faster than the oxidation of methanol.[66] The hydride mechanism was demonstrated to occur when the reaction was carried out in different solvents (e.g. CH_2Cl_2).[67]

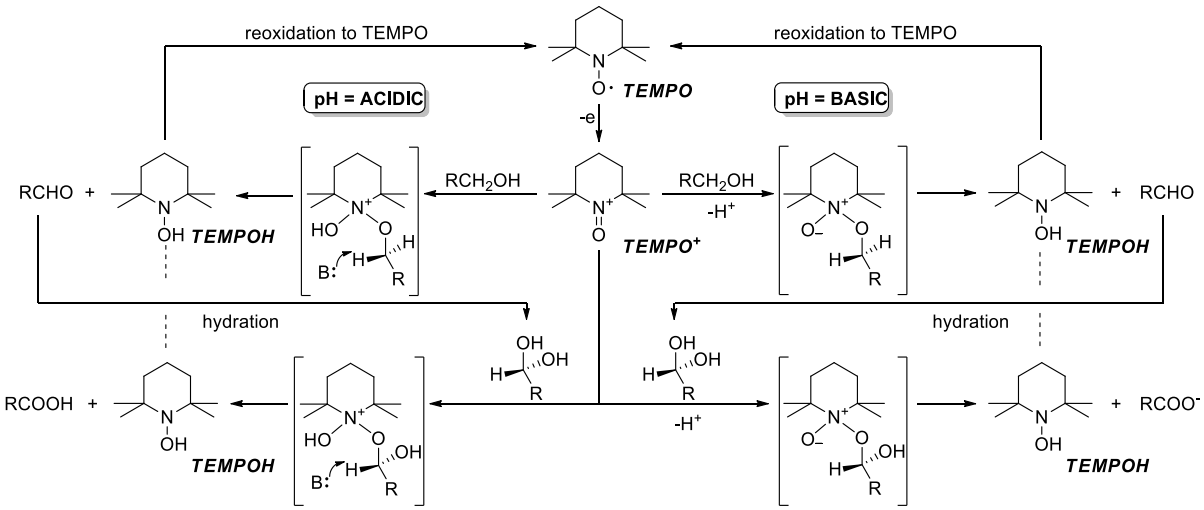

Scheme 1.3 TEMPO catalysed oxidation of primary alcohols under different pH regimes

Many TEMPO nitroxide analogues show similar catalytic effects to TEMPO in alcohol oxidation.[68-71] In a study comparing cellulose oxidation using a range of TEMPO analogues under alkali conditions, TEMPO itself was shown to be the most active mediator providing the shortest oxidation time and yielding product with the highest carboxylate content and yield.[69] It was proposed that the reaction rate depended on the rate of formation of the nitrosonium ion from TEMPO (the actual oxidising species in NaClO/NaBr/TEMPO system), which was predicted to be dependent on redox potential (e.g. the redox potential vs. MSE, Hg/Hg_2SO_4, was 0.108 V for TEMPO and 0.211 V for 4-acetamido-TEMPO), explaining the better performance of TEMPO under basic conditions.[69] Under neutral or acidic conditions, the

NaClO/NaBr/TEMPO system was no longer viable since NaClO decomposes under low pH. Therefore, the $NaClO_2$/NaClO/TEMPO system was found to be effective for cellulose oxidation (the aldehydes were converted to carboxylates by $NaClO_2$, resulting in NaClO, and the reduced TEMPO was again oxidized to the *N*-oxoammonium ions by NaClO), and 4-acetamido-TEMPO was found to oxidise cellulose more effectively than TEMPO under both neutral and acidic conditions.[72] It should also be noted that only TEMPO and some derivatives bearing substituents at the 4 position (Chart 1.4) are commercially available at affordable prices for industrial production of oxidised cellulose. This restricts the choice of mediator for cellulose oxidation at scale.

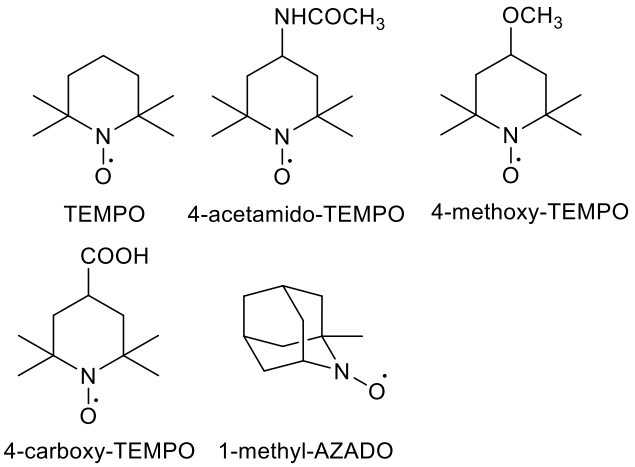

Chart 1.4 TEMPO and its analogues

Some TEMPO analogues were shown to be stable under the conditions of the oxidation reaction and were considered to be recyclable,[64] although no recyclability test was carried out to determine the reusability and efficiency of the recycled mediator. Patel studied the stability of 4-acetamido-TEMPO during the oxidation, showing that degradation proceeded under both alkali and acidic conditions.[73] This result suggested that the recyclability of 4-acetamido-TEMPO was rather limited, indicating that quantities of the mediator would need to be increased, or mediator added periodically when scaling the oxidation reaction for continuous production. Therefore, a stable mediator with a high efficiency over several reaction cycles is desirable for a green oxidation (the synthesis of mediator involves much energy and the synthesis procedures were not always environmentally friendly).[74] However, no

systematic work has been carried out to increase the life time of the mediator. Last but not least, some naturally derived *N*-oxyl radicals may serve as catalysts, e.g. from nortropane,[75] but have not been tested in cellulose oxidation systems.

The degree of polymerisation (DP) of oxidised cellulose nanoparticles was found to be strongly correlated to the reaction temperature and the DP value affects the mechanical properties of the bulk materials.[76,77] Higher temperatures shortened the oxidation time, but resulted in a low degree of polymerisation due to β-elimination, or oxidation, by hydroxyl radicals formed *in situ* (Scheme 1.2), of aldehyde-containing oxidised cellulose (formed in the first step of the oxidation, Scheme 1.1).[78] Using low temperature avoided such side reactions during the oxidation reaction, but a longer reaction time was necessary.[45] The possible depolymerisation mechanism is illustrated in Figure 1.2.

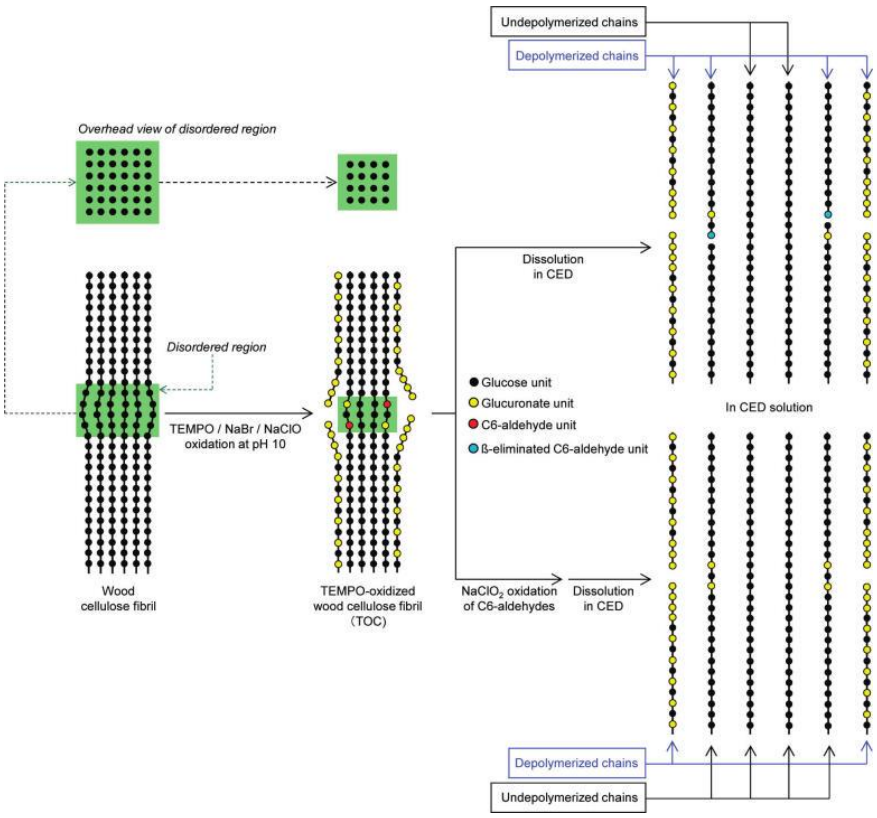

Figure 1.2 Schematic model of disordered regions of wood cellulose fibrils, and depolymerization pathways of oxidised cellulose or depolymerization-avoidable mechanism of oxidised cellulse−$NaClO_2$ in alkaline copper ethylenediamine (CED) solution.[79] Reprinted with permission from Ref. 79 with permission from American Chemical Society (© American Chemical Society 2011).

The kinetics of oxidation of cellulose from different sources was studied[50] and it was found that cellulose I was the most difficult to oxidise due to the inaccessibility of the polymer chains (cellulose I has a highly ordered crystal structure with few hydroxyl groups exposed for reaction). It was easier for TEMPO to penetrate into the fibres with the more accessible surface area, resulting in a higher carboxylate content and shorter oxidation time.

Apart from chlorine containing oxidants like NaClO and $NaClO_2$, which are suspected carcinogens for humans,[80] many other primary oxidants were also investigated in the TEMPO mediated system for cellulose oxidation.[71,81] After review of a range of possibilities, the use of enzymes such as laccases[82] or electro-chemistry[83] were considered to be sustainable and promising approaches to green primary oxidants in the TEMPO mediated oxidation system.

The main issue associated with using laccases as co-oxidants (reduction of oxygen from air) is the stability. It was shown that laccase (EC 1.10.3.2) deactivated during TEMPO mediated oxidations, particularly at high TEMPO concentration and this was ascribed to the oxidation of the enzyme itself.[84] Therefore, maintaining a low TEMPO concentration with respect to laccase and rapidly removing the oxoammonium ion from the enzyme catalyst would be desirable. A laccase-membrane reactor (a laccase “tea bag”[85]) may be a suitable technology to oxidise TEMPO continuously particularly if redesigned as a flow reactor, although various parameters of the reactor are yet to be determined and optimised.

Compared with the lacccase/TEMPO system, electrochemistry seems to be an attractive option, obviating issues of enzyme stability and high costs, while providing a “clean” oxidation method (electro-oxidation could be considered a green method contingent on the energy source being sustainable e.g.—wind energy, solar energy, etc.). Previously described electrochemical methods for cellulose oxidation require relatively large amounts of TEMPO (or other mediator) and take considerable periods of time (more than 24 hours) for the completion of reaction,[86] which is not efficient or desirable for industrial applications. In addition to the factors affecting the reaction of oxidised TEMPO with cellulose mentioned above, the surface area of the working electrode is also an essential variable in cellulose oxidation. However, to the

best our knowledge, influence of electrode surface area has not been investigated in the work published so far.[83,86,87]

It has been reported that the major difference in the cellulose products prepared using the laccase system, electro-oxidation or the NaClO/NaBr/TEMPO system is a higher content of aldehyde groups formed on the surface of the resultant cellulose fibrils for laccase and electro-oxidation.[86,88,89] Therefore, a further step may be necessary if low aldehyde content is essential in the final product. This could be achieved by using non-chlorine based oxidants, H_2O_2 for a further oxidation "polishing" step,[90] or by the action of NaOH.[89] The latter was reported to induce formation of carboxylate groups by the Cannizzaro reaction (base-induced disproportionation of aldehydes, forming corresponding alcohols and carboxylates).[89] While this reaction normally requires absence of an α-hydrogen atom (the presence of which would allow formation of the enolate), Patel *et al* argued that α-alkoxy aldehydes can undergo disproportionation and the conversion of aldehyde to carboxylate in the presence of 1 *M* NaOH without added oxidants suggested that this may occur.[91]

1.2 Applications of Oxidised Cellulose

Oxidised cellulose can be dispersed into nanofibrils 3–4 nm (Figure 1.3) in width after various mild mechanical and/or chemical treatment of cellulose fibres from a range of sources.[15] The nanofibrillation process can be achieved by mechanical disintegration of oxidised cellulose aqueous slurries using a household blender for 10 days,[40] a blender-type homogenizer for 2 min,[92] or an ultrasonic homogenizer for 3 min.[93] The prepared oxidised cellulose nanofibril dispersion is transparent (Figure 1.3) if the carboxylate content of the oxidised cellulose is above 1.5 mmol·g^{-1}.[40]

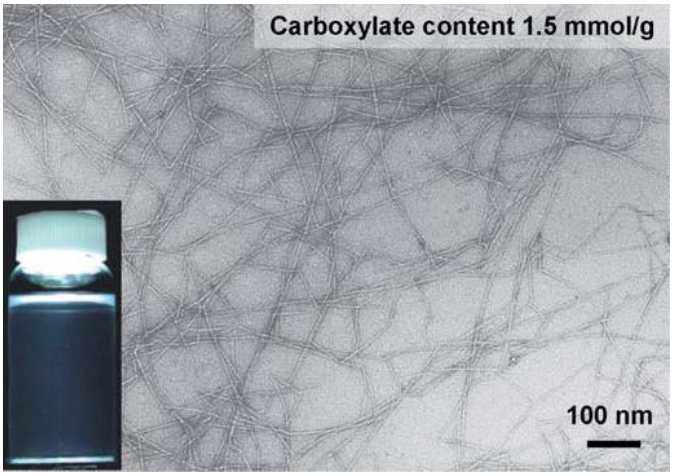

Figure 1.3 TEM images of dried dispersions of TEMPO-oxidized celluloses with carboxylate contents of 1.5 mmol·g^{-1}, the inset shows the corresponding aqueous dispersions.[40] Reproduction of images from Ref. 40 with permission from American Chemical Society (©American Chemical Society 2007).

Various applications of oxidised cellulose exploit the properties of its nanofibril structure and the negative surface charge in the form of carboxylate groups. Ion-exchange behavior of the carboxylate groups formed on oxidised cellulose fibres has been studied to explore the possibility of using this abundant and renewable biopolymer to remove and recover toxic metal ions from wastewater.[94] Oxidised cellulose was also used to improve the wet strength of paper,[95,96] and as a reinforcing filler for composites.[7] Shear thinning gels formed by oxidised cellulose in the presence of salts or surfactants were investigated to provide a novel method for thickening aqueous formulations, using a much lower concentration of the oxidised cellulose compared to the surfactant required to achieve the same result,[97] and has been patented by Unilever.[98] In addition, highly dispersed, oxidised cellulose nanofibrils were found to stabilise oil in water emulsions along with other surfactants and claimed as ingredients in novel “greener” personal care products to reduce the use of petro-derived chemicals.[99] However, the role of oxidised cellulose nanofibrils in the emulsion was not clear. Other particles (e.g. enzymes, nanoparticles) could be incorporated into oxidised cellulose matrices for various applications, including green catalysts and composites used in loudspeakers.[100-103] In this study, an attempt was made to immobilise metal organic frameworks onto oxidised cellulose to form self-standing membranes. It should be also pointed out that non-oxidised bacterial

cellulose (*ca*. 100 nm in width) can also be used to immobilise various particles with high loadings,[104,105] indicating that hydrogen bonding or metal-oxygen coordination is viable to bind particles effectively onto to the high surface area fibre surfaces (for cellulose obtained from wood, it is necessary to oxidised the surface of the fibres to provide high surface areas).

In order to illustrate the possible applications of the oxidised cellulose nanofibrils, dispersed oxidised cellulose nanofibrils suspension were exploited in stabilising Pickering emulsions (it was pointed to by the Unilever patent, but not elaborated on[106]), and metal organic frameworks on the cellulose self-standing supporting membranes were synthesised that could be used for molecular recognition/sensor/capture.

1.2.1 Metal-Organic-Frameworks

Metal-organic frameworks (MOFs) are crystalline compounds (dependant on the coordination of metal ions with linkers to form 1-3D structures,[107] Figure 1.4) with large pore size and high surface areas, consisting of transition metal ions and organic linkers.[108] The highest specific surface area of MOFs obtained experimentally was *ca* 7000 $m^2 \cdot g^{-1}$ determined by the Brunauer–Emmett–Teller method, and the proposed maximum surface area was calculated to be *ca* 14600 $m^2 \cdot g^{-1}$ computationally.[109]

Some of the main driving forces for research on MOFs are the potential applications in interdisciplinary research areas, including gas storage,[110] chemical sensors (based on, for example, solvatochromic behaviour, Figure 1.5),[111] catalysts for chemical reactions,[112] and separation (based on selectivity),[73,74] due to the tunable surface area and pore size of MOFs, which allow certain guest molecules to diffuse into the MOFs and adsorb onto the surface or interact with the metal ions in the framework.

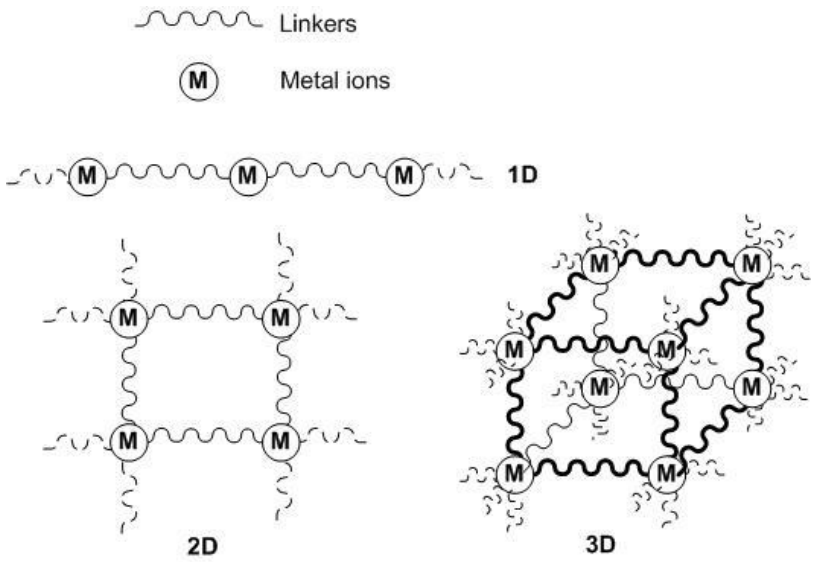

Figure 1.4 Representation of one- (1D), two- (2D) and three (3D) dimensional MOFs.

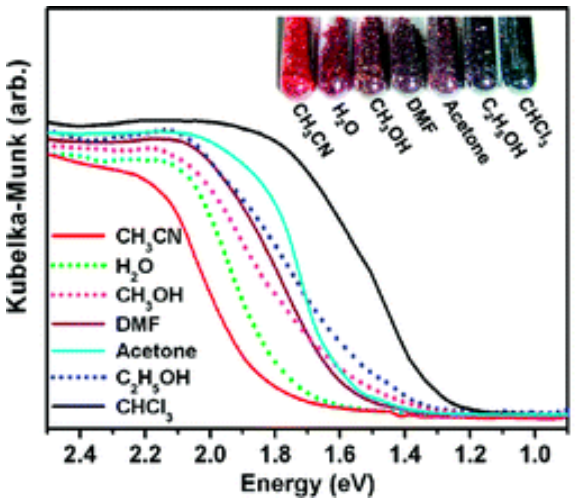

Figure 1.5 The UV-vis spectra and photograph of the synthesised MOF, $(WS_4Cu_4)I_2$[3,6-di-(pyridin-4-yl)-1,2,4,5-tetrazine)]$_3$, with solvents.[111] Reprinted with permission from Ref. 111 with permission from American Chemical Society (© American Chemical Society 2011).

Versatile synthetic methods have been developed to achieve MOFs with high yield, and a short summary is given here. MOFs are conventionally and most frequently synthesized in large quantities (gram scale) by solvothermal synthesis at elevated temperature due to the ease of the set-up in the laboratories, although other assisted methods (e.g. microwave, ultrasonic, electrochemical and mechanical approaches) have also been investigated (Figure 1.6).[113] Meanwhile, some MOFs synthesized by these approaches often require special apparatus or set-up and the precursors may

be unstable and break down under the synthesis conditions, which is not desirable for manufacture on industrial scale.[114,115] Therefore, room temperature synthesis in green solvents (e.g. aqueous solution) are sustainable and industrially preferred synthesis conditions.[115]

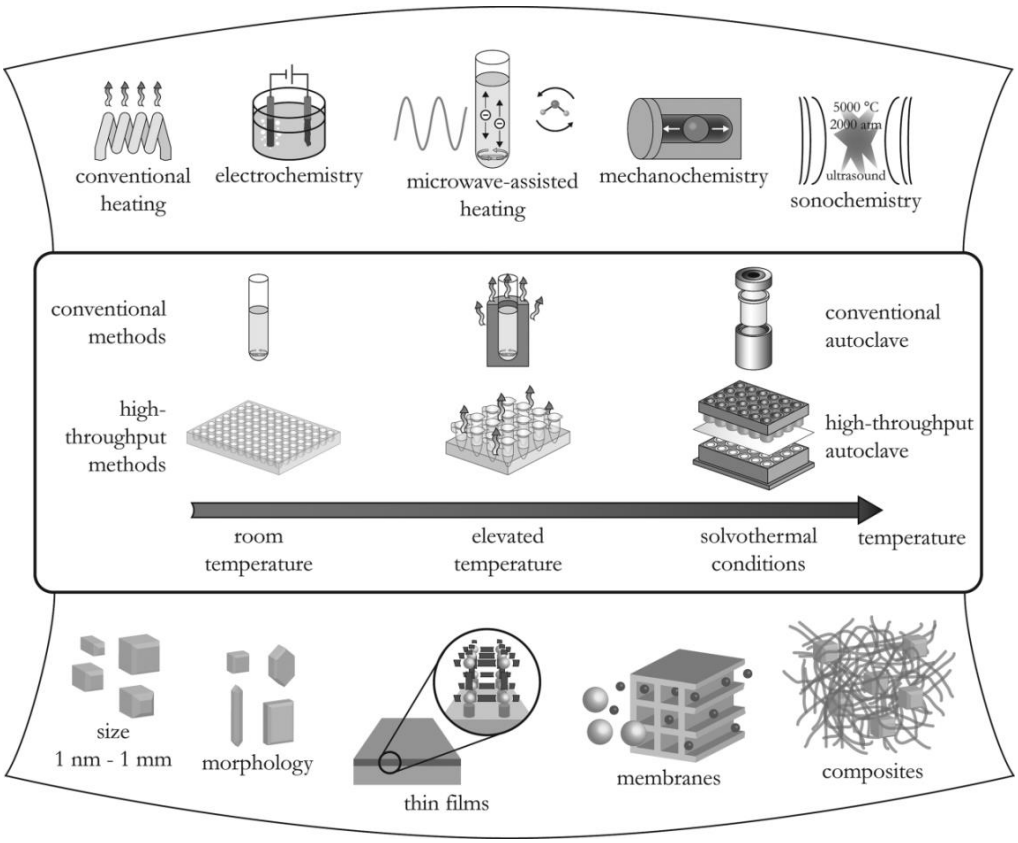

Figure 1.6 Overview of synthesis methods, possible reaction temperatures, and final reaction products in MOF synthesis.[113] Reprinted with permission from Ref. 113 with permission from American Chemical Society (© American Chemical Society 2015).

MOFs are crystalline powders, making them very difficult to handle in practice (fine powders tend to form dust released in the air and cause health and safety problems). Immobilisation is normally required, and MOFs may be coated onto a substrate to make various devices via (i) direct growth of MOFs thin films, (ii) assembly of controlled-size nanocrystals, or (iii) layer-by-layer growth of films.[116] The MOF-based devices can achieve some specific functions (e.g. gas storage, separation and catalysis) based on the functional properties, which could be used in different applications (e.g. water purification, CO_2 capture).[117,118]

However, these immobilisation processes can be quite time consuming and labour intensive. In addition, substrates used to support MOFs are frequently not renewable materials (e.g. silicon, gold).[119] It was therefore postulated here that renewable materials derived from nature with high surface area (e.g. bacterial cellulose, which also exhibited excellent tensile strength[120]), could be used to prepare self-standing MOFs rearing membranes.

Among many MOFs available, one MOF was of particular interest in this study due to the ease of synthesis, robust structure and widely investigated properties. MOF-199, also known as HKUST-1 or Cu-BTC, is a copper based nano-porous material first reported by the Williams group in 1999.[121] MOF-199 can be obtained under solvothermal conditions at elevated temperature or in mixed solvents (DMF/ethanol/water) at room temperature and the surface area and porosity of the synthesised MOFs are dependent on the reaction conditions.[122]

MOF-199 shows a wide range of applications in various areas. The solvatochromic behaviour of MOF-199 in the presence of certain molecules (e.g. benzaldehyde, Figure 1.7) indicates the coordination of molecules with the metal ions (although the difference of change in colour is small).[123] To make a readily distinguishable change in colour, ligands with strong π-acceptor properties and labile electronic structure responsive to solvent polarity are essential in the solvatochromic response.[111] Apart from the colour change with different molecules, the change in resistance response in the presence of distinctive molecules can also be used as an indicator mechanism relying on molecular recognition.[124] MOF-199 with a hollow capsule structure was synthesised by micro-emulsion template and shown to possess selective permeability for molecules with different size.[125] The nanostructured materials obtained from the pyrolysis of MOF-199 were demonstrated to be a good anode candidate for rechargeable Li-ion batteries.[126]

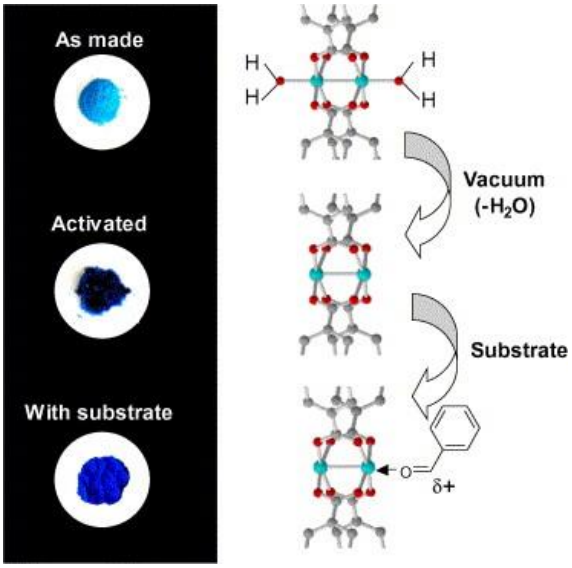

Figure 1.7 Colour changes during the dehydration (activation) of $Cu_3(BTC)_2(H_2O)_3 \cdot xH_2O$ to give $Cu_3(BTC)_2$, and subsequent re-adsorption of the aldehyde to give $Cu_3(BTC)_2(C_6H_5CHO)_x$.[123] Reproduction of images from Ref. 123 with permission from Elsevier (© Elsevier 2004).

1.2.2 Pickering Emulsions

Emulsions are part of a general classification of condensed matters known as colloids, found in various daily products (e.g. cosmetics, agricultural products, food and medicine).[127] Understanding the physical principles which determine the stability of emulsions is essential for industry, allowing adoption of suitable compounds to stabilise or destabilise emulsions depending on their use and leading to develop greener products.

An emulsion consists of two pure, incompletely miscible liquids mixed into each other by agitation induced by mechanical forces (shaking, stirring, homogenization, or exposure to ultra-sonication).[128] An emulsifier is usually added to stabilise an emulsion against flocculation, creaming or sedimentation, Ostwald ripening and coalescence (Figure 1.8).[129,130] Flocculation is the process where emulsion droplets aggregate together and form flocs. Creaming is the migration of emulsion droplets towards the top of an emulsion, while sedimentation is the migration of emulsion droplets towards the bottom of an emulsion. Coalescence is the process where several emulsion droplets move closer and merge to form a bigger droplet. Ostwald

ripening is the process where smaller droplets deposit on larger particles and result in a more thermodynamically stable state (larger droplets have lower surface energy with the lower surface to volume ratio, compared to smaller droplets).[131]

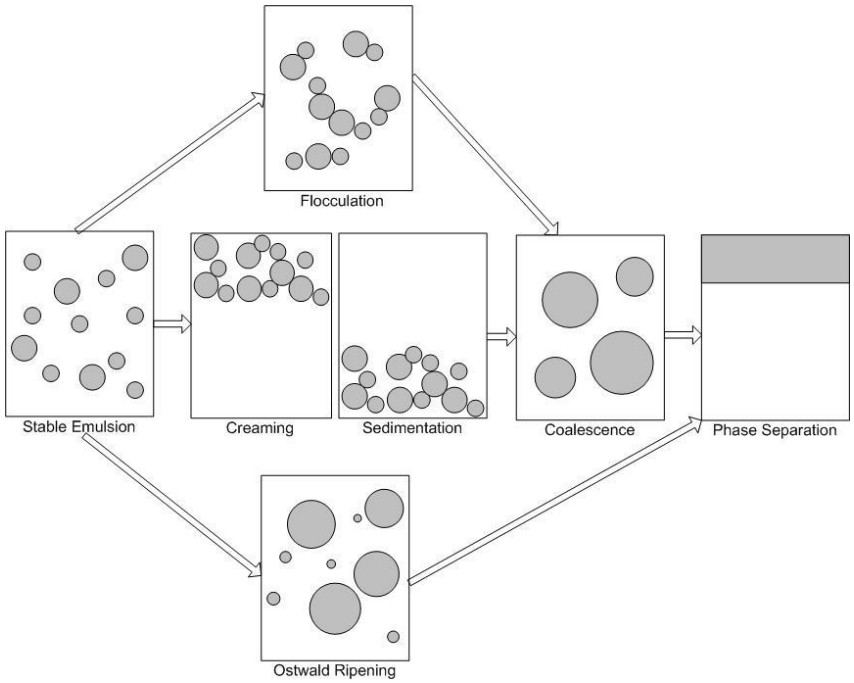

Figure 1.8 Mechanisms of emulsion instability process

The stability of an emulsion can be explained by: (i) interfacial tension theory: emulsions can form spontaneously ($\Delta G_{formation} \leq 0$) upon lowering the surface tension (σ_{OW}) at the oil/water interface (Equation 1.1). Because the break-up energy $\Delta G_{break} = -\Delta G_{formation}$, low surface tension at the interface stabilises the droplets against coalescence; (ii) repulsion theory: stable emulsions can be created by forming a barrier between the droplets and the continuous phase (charge stabilization or steric stabilization); and (iii) viscosity modification theory: emulsions are more stable in viscous media which slows creaming.[132-134]

$$\Delta G_{formation} = \Delta\sigma_{OW} \cdot \Delta A - T \cdot \Delta S \qquad \textbf{(1.1)}$$

Where $\Delta G_{formation}$ and ΔS are the change in Gibbs free energy and entropy before and after the emulsification, σ_{OW} is the change in surface tension at the oil/water

interface, ΔA is the change in interfacial surface area and T is the temperature in Kelvin.

The macroscopic behaviours of emulsions are indicators of the emulsion stability and can be characterised by various techniques. For instance, the formation of emulsions could be easily identified optically, as the turbidity of the emulsion would increase when the formed emulsion was stable.[135] The change of the volume fraction of emulsions was used to evaluate the stability of the emulsion over time.[136] Rheological measurements were conducted at constant shear rate to evaluate the effect of temperature on emulsion stability, based on the change of the viscosity.[137]

A Pickering emulsion relies on solid particles as the emulsifier (rather than surfactants or polymers used to stabilise normal emulsions), arrayed at the interface between phases, to stabilise the emulsion.[138] The solid particles assemble on the surface of the droplets and form barriers between droplets, preventing the coalescence of the droplets (Figure 1.9).[139,140]

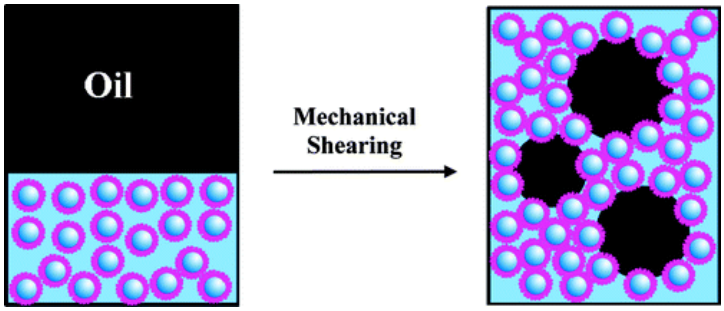

Figure 1.9 Schematic showing the spontaneous formation of a gel emulsion stabilized by core−shell particles.[141] Reprinted with permission from Ref. 141 with permission from American Chemical Society (© American Chemical Society 2010).

Pickering emulsions occur widely: milk is a representative example of Pickering emulsion, where casein acts as a surfactant to adsorb milk fat at its interface. Pickering emulsions have been used for controlled polymerisations, creating valuable new materials,[142] and for drug delivery purposes where the solid particles surrounding the droplets are considered as capsules.[143]

As illustrated in Figure 1.10, a particle at the interface (oil-water) exhibited a contact angle θ_{ow}, which indicates how the particle adsorbs at the interface (wettability).

Hydrophilic particles tend to make contact angles smaller than 90° (form oil-in-water emulsions) while hydrophobic particles tend to make contact angles greater than 90° (form water-in-oil emulsions). However, particles that are either too hydrophilic or hydrophobic tend to remain dispersed in the aqueous or oil phase, resulting in unstable emulsions experimentally.[144]

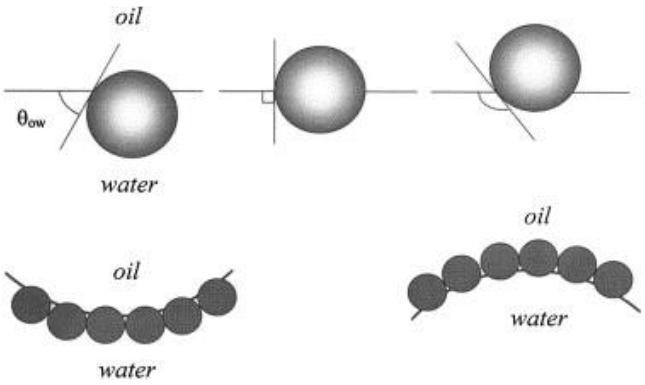

Figure 1.10 (upper) Position of a small spherical particle at a planar oil–water interface for a contact angle (measured through the aqueous phase) less than 90° (left), equal to 90° (centre) and greater than 90° (right). (lower) Corresponding probable positioning of particles at a curved interface. For θ<90°, solid stabilised o/w emulsions may form (left). For θ>90°, solid-stabilised w/o emulsions may form (right).[144] Reproduction of images from Ref. 144 with permission from Elsevier (© Elsevier 2003).

The energy required ($-\Delta_{int}G$) to remove a particle (small enough to neglect the effect of gravity) of radius *r* from an oil-water interface of tension γ_{ow} is given by Equation 1.2.[145]

$$-\Delta_{int}G = \pi r^2 \gamma_{ow}(1 - |cos\theta_{ow}|)^2 \qquad \textbf{(1.2)}$$

At room temperature, for a droplet with 1 μm of radius, θ_{ow} = 30° and γ_{ow} = 40 mN·m^{-1}, the energy required to remove the particle from the oil-water interface is approximately 10^5 kT (k is Boltzmann's constant and T is absolute temperature), which suggests that the particles are trapped on the oil-water interface (i.e. that the particles are irreversibly adsorbed at the interface). If the particles are very hydrophilic (θ_{ow} < 20°), then the particles are more likely to desorb from the interface at equilibrium. At higher temperature, the Gibbs free energy of the desorption

process becomes more negative, as the exothermic physical adsorption process is unfavourable at elevated temperature. Therefore the particles are more likely to desorb from the interface.

The plots of the relative energy of particle detachment (energy of particle detachment at θ_{ow} over the maximum energy of particle detachment, $\mathrm{RG} = -\Delta_{int}G(\theta_{ow})/-\Delta_{int}G(90°)$) versus the contact angle at oil-water interface θ_{ow} are displayed in Figure 1.11. The radius r is set to 1 μm and the surface tension γ_{ow} is set to 40 mN·m^{-1}, although the values are found to have little effect on the overall trend of the plots. In agreement with the experimental results, the amphiphilic particle ($20<\theta_{ow}<160$) irreversibly attaches to the interface and the particle adsorbs most strongly at the oil-water interface if the contact angle θ_{ow} equals to 90°.[146] The emulsion becomes unstable if the particle adsorbs and desorbs at the oil-water interface reversibly ($0<\theta_{ow}<20$, or $160<\theta_{ow}<180$).

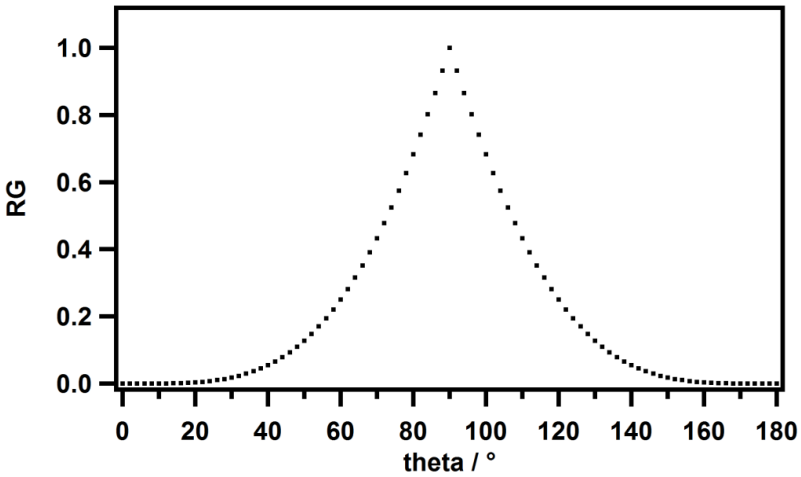

Figure 1.11 Relative energy of particle detachment calculated by Equation 1.2 versus contact angle.

While oxidation and the introduction of charged carboxylate groups to the cellulose surfaces would be expected to decrease contact angle, potentially making OCNF poorer Pickering emulsion stabilisers, OCNF still have an intermediate wettability, similar to that of hydrolysed cellulose nanocrystals.[147,148] OCNF is preferred in formulations of personal care products as the particles may be prepared by relatively low energy mechanical dispersion,[106] and have been found to give a pleasant skin

feel when used in such formulations. In addition, the thickening response of OCNF to added electrolyte and surfactants makes it a preferred formulation ingredient (rheology modifier) in some applications.[98] Thus it brings multiple functionalities (emulsion stabilization, thickening) without need for use of multiple species, reducing the number of necessary ingredients in such formulations.

The content of the particles in suspension influences the droplet size formed in the emulsion, which is essential in emulsion stabilisation. A decrease in droplet size is generally accompanied by an increase in particle concentration, since a larger interfacial area can be stabilised (smaller droplets have a higher area to volume ratio) when more particles are present.[149] The droplet diameter can be quantitatively determined by Equation 1.3:

$$\mathrm{D} = \frac{6\phi_v V}{A} \qquad \textbf{(1.3)}$$

Where ϕ_v is the volume fraction of the dispersed phase in the emulsion and A/V represents the interfacial area per unit volume fraction of emulsion.

There are several methods to measure the droplet size experimentally. Microscopic observation (optical and electron microscope) allows one to directly obtain the shape and size of the emulsion droplets.[150,151] Light diffraction (static light scattering) is one of the most common methods used to obtain the sphere equivalent diameter from submicron up to hundreds of micron size, based on the intensity change over scattering angles.[137,152] The dynamic light scattering method allows calculation of the sphere equivalent diameter of the emulsion droplet undergoing Brownian motion, using the Stokes-Einstein equation (Equation 1.4).[153,154]

$$\mathrm{D} = \frac{k_B T}{6\pi\eta r} \qquad \textbf{(1.4)}$$

Where D is diffusion coefficient in $m^2 \cdot s^{-1}$, k_B is Boltzmann's constant, T is absolute temperature in Kelvin, η is dynamic viscosity in Pa·s, r is radius of diffusing particle in m.

This method is viable for droplet sizes up to submicrons, as larger entangled particles do not follow Brownian motion. Therefore, light diffraction is used for measuring the emulsion droplets size in the thesis.

There has recently been a growing interest in Pickering emulsions studies for several reasons. First, it is essential for a wide range of applications from food to oil recovery processing, to understand the role of particles at the oil-water interface.[155] Second, particles assembled at the oil-water interface provide direct experimental models for the study of crystal orders on curved surfaces,[156] which helps to understand the interaction of particles on curved surfaces, and has potential application in direct self-assembly.[157] Third, Pickering emulsions offer novel functional scaffolds for various applications.[158,159]

Recent developments in Pickering emulsions include the use of magnetic,[158] thermal[137,161]and pH responsive[160] Pickering stabilisers, and the synthesis of new materials and structures (e.g. Janus particles[161]) driven by liquid-liquid interfacial self-assembly of solid particles. For instance, a magnetic-responsive Pickering emulsion underwent macroscopic phase separation under an external magnetic field, and the emulsion could be recovered by remixing the components by mechanical agitation.[162] A thermally responsive emulsion stabilised by silica nanoparticles with poly(2-(dimethylamino)ethyl methacrylate) brushes grafted to the surfaces became unstable above specific temperatures. This provided tuneable materials for controlled drug release applications.[161]

In addition, the use of solid particles from more renewable sources, such as natural polysaccharides, is also on the rise, playing an important role in food, cosmetic, and pharmaceutical industries.[163] The biodegradability, nontoxicity and abundant availability of these polysaccharides particles, which may be derived from agricultural by-products, and the relative ease of production are the driving factors that stimulate the use of these nanoparticles as sustainable stabilisers to replace synthetic surfactants.[164]

Non-oxidised cellulose nanofibrils, cellulose nanocrystals and modified cellulose nanocrystals have also been used to stabilise oil-in-water and water-in-oil Pickering

emulsions.[137,165,166] Oxidised cellulose was also used to stabilise o/w emulsions due to the similarity in structure with cellulose nanocrystals, although the reasons for the stabilisation by oxidised cellulose have not been studied in detail.[99,106] In addition, since the surface of the oxidised cellulose nanofibrils are negatively charged, emulsions stabilised by oxidised cellulose could have a better stability over time, due to the electrostatic repulsion.[167]

Oxidised cellulose, as the emulsifier in the Pickering emulsion, has the potential to replace the petroleum-based surfactants (e.g. sodium lauryl sulphate) used in cosmetics, which might have undesirable effects to human skin.[168] In addition, solid polymer particles typically used in Pickering emulsions could also be replaced by oxidised cellulose to provide a biodegradable,[169] non-toxic (long term toxicity on human health is yet to be verified[170]) and sustainable substitute.[19]

1.3 Organization of the Thesis

The PhD project focuses on the production of innovative nanomaterials from cellulose using 'green' and sustainable synthetic methods, and the applications of the oxidised cellulose nanofibrils for composite materials and personal care products (e.g. shampoo and creams), as a replacement for polymers from petrochemical sources and non-biodegradable materials, such as silicones.

The thesis is arranged as follows: In Chapter 1, the background to oxidised cellulose is introduced, and relevant studies pertaining to oxidised cellulose are described, with a focus on the synthesis of the oxidised cellulose and applications for MOFs immobilisation and stabilising Pickering emulsions. In Chapter 2, the methodology used in the research is presented. Chapter 3 shows the results of the experiments of voltammetry optimisation for reaction conditions. Chapter 4 shows the results of electro-oxidation of cellulose. Study on oil-in-water emulsions stabilised by oxidised cellulose is described in Chapter 5. The synthesis of MOFs/cellulose composites for gas sorption is presented in Chapter 6. In Chapter 7, a summary is provided of findings to date and future work proposed. All the supporting information is listed in Chapter 8.

1.4 References

1. J.-H. Kim, et al., *Int. J. of Precis. Eng. and Manuf.-Green Tech.,* 2015, **2**, 197-213.
2. H. G. Wiedeman; G. Bayer, *Anal. Chem.,* 1983, **55**, 1220A-1230A.
3. K. T. Meilert; D. Laub; J. Kiwi, *J. Mol. Catal. A: Chem.,* 2005, **237**, 101-108.
4. T.-H. Tsien, *JAOS,* 1973, **93**, 510-519.
5. B. Falk, *For. Prod. J.,* 2009, **59**, 6-12.
6. X. Wen, et al., *Prog. Nat. Sci.,* 2015, **25**, 197-203.
7. A. K. Bledzki; J. Gassan, *Prog. Polym. Sci.,* 1999, **24**, 221-274.
8. D. S. Hon, *Cellulose,* 1994, **1**, 1-25.
9. S. R. Collinson; W. Thielemans, *Coord. Chem. Rev.,* 2010, **254**, 1854-1870.
10. P. N. Ciesielski, et al., *ACS Nano,* 2013, **7**, 8011-8019.
11. V. Kocherbitov; S. Ulvenlund; M. Kober; K. Jarring; T. Arnebrant, *J. Phys. Chem. B,* 2008, **112**, 3728-3734.
12. A. O'Sullivan, *Cellulose,* 1997, **4**, 173-207.
13. K. M. Gupta; Z. Hu; J. Jiang, *RSC Advances,* 2013, **3**, 12794-12801.
14. L. M. J. Kroon-Batenburg; J. Kroon, *Glycoconjugate J.,* 1997, **14**, 677-690.
15. A. Isogai; T. Saito; H. Fukuzumi, *Nanoscale,* 2011, **3**, 71-85.
16. A. Dufresne, *Mater. Today,* 2013, **16**, 220-227.
17. D. Bondeson; A. Mathew; K. Oksman, *Cellulose,* 2006, **13**, 171-180.
18. P. B. Filson; B. E. Dawson-Andoh; D. Schwegler-Berry, *Green Chem.,* 2009, **11**, 1808-1814.
19. X. Miao, et al., *Carbohydr. Polym.,* 2016, **136**, 841-850.
20. M. Uhlig, et al., *Langmuir,* 2016, **32**, 442-450.
21. S. Beck-Candanedo; M. Roman; D. G. Gray, *Biomacromolecules,* 2005, **6**, 1048-1054.
22. L. Brinchi; F. Cotana; E. Fortunati; J. M. Kenny, *Carbohydr. Polym.,* 2013, **94**, 154-169.
23. E. Tkalya, et al., *ACS Macro Letters,* 2013, **2**, 157-163.
24. N. L. Garcia de Rodriguez; W. Thielemans; A. Dufresne, *Cellulose,* 2006, **13**, 261-270.
25. M. Schlesinger; W. Y. Hamad; M. J. MacLachlan, *Soft Matter,* 2015, **11**, 4686-4694.
26. M. J. Bonné, et al., *J. Phys. Chem. C,* 2008, **112**, 2660-2666.
27. S. Eyley; W. Thielemans, *Nanoscale,* 2014, **6**, 7764-7779.
28. A. Bendahou; A. Hajlane; A. Dufresne; S. Boufi; H. Kaddami, *Res. Chem. Intermed.,* 2014, **41**, 4293-4310.
29. M. Lewin, *Macromol. Symp.,* 1997, **118**, 715-724.
30. E. C. Yackel; W. O. Kenyon, *J. Am. Chem. Soc.,* 1942, **64**, 121-127.
31. K. Garves, *Holzforschung,* 1997, **51**, 526-530.
32. Z. Zhou; A. S. Jaaskelainen; T. Vuorinen, *J. Pulp Pap. Sci.,* 2008, **34**, 212-218.
33. J. Nakayama; A. Miyake, *J. Therm. Anal. Calorim.,* 2012, **110**, 321-327.
34. C. C. Unruh; W. O. Kenyon, *J. Am. Chem. Soc.,* 1942, **64**, 127-131.
35. Q. Cui, et al., *RSC Advances,* 2014, **4**, 1630-1639.
36. S. Takaichi; A. Isogai, *Cellulose,* 2013, **20**, 1979-1988.
37. K. M. Lewis, et al., *Eur Surg,* 2013, **45**, 213-220.

38. A. E. J. de Nooy; A. C. Besemer; H. van Bekkum, *Carbohydr. Res.,* 1995, **269**, 89-98.
39. M. F. Semmelhack; C. S. Chou; D. A. Cortes, *J. Am. Chem. Soc.,* 1983, **105**, 4492-4494.
40. T. Saito; S. Kimura; Y. Nishiyama; A. Isogai, *Biomacromolecules,* 2007, **8**, 2485-2491.
41. D. Ishii; T. Saito; A. Isogai, *Biomacromolecules,* 2011, **12**, 548-550.
42. Y. Okita; T. Saito; A. Isogai, *Biomacromolecules,* 2010, **11**, 1696-1700.
43. M.-C. Li, et al., *ACS Sustain. Chem. Eng.,* 2015, **3**, 821-832.
44. X. Xu, et al., *ACS Appl. Mater. Interfaces,* 2013, **5**, 2999-3009.
45. A. Isogai; Y. Kato, *Cellulose,* 1998, **5**, 153-164.
46. A. Rattaz; S. Mishra; B. Chabot; C. Daneault, *Cellulose,* 2011, **18**, 585-593.
47. Y. Kato; R. Matsuo; A. Isogai, *Carbohydr. Polym.,* 2003, **51**, 69-75.
48. B. Jiang; E. Drouet; M. Milas; M. Rinaudo, *Carbohydr. Res.,* 2000, **327**, 455-461.
49. N. Tamura; M. Wada; A. Isogai, *Carbohydr. Polym.,* 2009, **77**, 300-305.
50. D. da Silva Perez; S. Montanari; M. R. Vignon, *Biomacromolecules,* 2003, **4**, 1417-1425.
51. R. Ciriminna; G. Palmisano; C. D. Pina; M. Rossi; M. Pagliaro, *Tetrahedron Lett.,* 2006, **47**, 6993-6995.
52. M. Zhao, et al., *J. Org. Chem.,* 1999, **64**, 2564-2566.
53. S. J. Eichhorn, et al., *J. Mater. Sci.,* 2001, **36**, 2107-2131.
54. J. B. Binder; R. T. Raines, *J. Am. Chem. Soc.,* 2009, **131**, 1979-1985.
55. T. Saito; A. Isogai, *Biomacromolecules,* 2004, **5**, 1983-1989.
56. X. W. Cao; B. Ding; J. Y. Yu; S. S. Al-Deyab, *Carbohydr. Polym.,* 2012, **90**, 1075-1080.
57. T. Saito; Y. Okita; T. T. Nge; J. Sugiyama; A. Isogai, *Carbohydr. Polym.,* 2006, **65**, 435-440.
58. P. L. Bragd; A. C. Besemer; H. v. Bekkum, *J. Mol. Catal. A: Chem.,* 2001, **170**, 35-42.
59. I. Shibata; A. Isogai, *Cellulose,* 2003, **10**, 151-158.
60. M. F. Semmelhack; C. R. Schmid; D. A. Cortés, *Tetrahedron Lett.,* 1986, **27**, 1119-1122.
61. M. Yamaguchi; T. Takata; T. Endo, *Tetrahedron Lett.,* 1988, **29**, 5671-5672.
62. A. E. J. de Nooy; A. C. Besemer; H. van Bekkum, *Tetrahedron,* 1995, **51**, 8023-8032.
63. A. E. J. De Nooy; A. C. Besemer; H. Van Bekkum, *Synthesis,* 1996, **1996**, 1153-1176.
64. I. W. C. E. Arends; Y.-X. Li; R. Ausan; R. A. Sheldon, *Tetrahedron,* 2006, **62**, 6659-6665.
65. W. F. Bailey; J. M. Bobbitt; K. B. Wiberg, *J. Org. Chem.,* 2007, **72**, 4504-4509.
66. V. A. Golubev; V. N. Borislavskii; A. L. Aleksandrov, *Bull. Acad. Sci.USSR. Div. of Chem. Sci,* 1977, **26**, 1874-1881.
67. J. C. Qiu; P. P. Pradhan; N. B. Blanck; J. M. Bobbitt; W. F. Bailey, *Org. Lett.,* 2011, **14**, 350-353.
68. M. Shibuya; M. Tomizawa; I. Suzuki; Y. Iwabuchi, *J. Am. Chem. Soc.,* 2006, **128**, 8412-8413.
69. S. Iwamoto, et al., *Polym. Degrad. Stab.,* 2010, **95**, 1394-1398.

70. P. Astolfi, et al., *New J. Chem.,* 2005, **29**, 1308-1317.
71. S. Coseri, et al., *Biomacromolecules,* 2009, **10**, 2294-2299.
72. M. Hirota; N. Tamura; T. Saito; A. Isogai, *Carbohydr. Polym.,* 2009, **78**, 330-335.
73. I. Patel, et al., *Holzforschung,* 2010, **64**, 549-554.
74. P. L. Bragd; H. van Bekkum; A. C. Besemer, *Top. Catal.,* 2004, **27**, 49-66.
75. G. D. Mendenhall; K. U. Ingold, *J. Am. Chem. Soc.,* 1972, **94**, 7166-7167.
76. M. Henriksson; L. A. Berglund; P. Isaksson; T. Lindström; T. Nishino, *Biomacromolecules,* 2008, **9**, 1579-1585.
77. G. Rodionova, et al., *Cellulose,* 2012, **19**, 705-711.
78. K. Ahn; U. Hennniges; G. Banik; A. Potthast, *Cellulose,* 2012, **19**, 1149-1159.
79. R. Shinoda; T. Saito; Y. Okita; A. Isogai, *Biomacromolecules,* 2012, **13**, 842-849.
80. J. K. Dunnick; R. L. Melnick, *J. Natl. Cancer Inst.,* 1993, **85**, 817-822.
81. J. M. Hoover; S. S. Stahl, *J. Am. Chem. Soc.,* 2011, **133**, 16901-16910.
82. E. Aracri; T. Vidal; A. J. Ragauskas, *Carbohydr. Polym.,* 2011, **84**, 1384-1390.
83. T. Isogai; T. Saito; A. Isogai, *Biomacromolecules,* 2010, **11**, 1593-1599.
84. I. W. C. E. Arends; Y.-X. Li; R. A. Sheldon, *Biocatal. Biotransform.,* 2006, **24**, 443-448.
85. K. P. Katuri; S. Venkata Mohan; S. Sridhar; B. R. Pati; P. N. Sarma, *Water Res.,* 2009, **43**, 3647-3658.
86. P. Parpot; K. Servat; A. Bettencourt; H. Huser; K. Kokoh, *Cellulose,* 2010, **17**, 815-824.
87. T. Isogai; T. Saito; A. Isogai, *Cellulose,* 2011, **18**, 421-431.
88. E. Aracri; T. Vidal, *Cellulose,* 2012, **19**, 867-877.
89. D. Jaušovec; R. Vogrinčič; V. Kokol, *Carbohydr. Polym.,* 2015, **116**, 74-85.
90. K. Sato; M. Hyodo; J. Takagi; M. Aoki; R. Noyori, *Tetrahedron Lett.,* 2000, **41**, 1439-1442.
91. I. Patel; R. Ludwig; D. Haltrich; T. Rosenau; A. Potthast, *Holzforschung,* 2011, **65**, 475.
92. H. Fukuzumi; T. Saito; T. Wata; Y. Kumamoto; A. Isogai, *Biomacromolecules,* 2009, **10**, 162-165.
93. S. Fujisawa; Y. Okita; H. Fukuzumi; T. Saito; A. Isogai, *Carbohydr. Polym.,* 2011, **84**, 579-583.
94. T. Saito; A. Isogai, *Carbohydr. Polym.,* 2005, **61**, 183-190.
95. T. Saito; A. Isogai, *Tappi J.,* 2005, **4**, 3-8.
96. E. Aracri; C. Valls; T. Vidal, *Carbohydr. Polym.,* 2012, **88**, 830-837.
97. R. J. Crawford; K. J. Edler; S. Lindhoud; J. L. Scott; G. Unali, *Green Chem.,* 2012, **14**, 300-303.
98. *UK Pat.,* WO2012171725 A2, 2012.
99. A. G. Cunha; J.-B. Mougel; B. Cathala; L. A. Berglund; I. Capron, *Langmuir,* 2014, **30**, 9327-9335.
100. H. Koga, et al., *J. Mater. Chem.,* 2012, **22**, 5538-5542.
101. H. Koga; T. Kitaoka; A. Isogai, *J. Mater. Chem.,* 2012, **22**, 11591-11597.
102. S. Galland, et al., *J. Mater. Chem. C,* 2013, **1**, 7963-7972.
103. R. Bendi; T. Imae, *RSC Advances,* 2013, **3**, 16279-16282.
104. D. Sun; J. Yang; X. Wang, *Nanoscale,* 2010, **2**, 287-292.
105. R. T. Olsson, et al., *Nat. Nanotechnol.,* 2010, **5**, 584-588.

106. *UK Pat.,* WO2012139817A2, 2012.
107. A. Thirumurugan; C. N. R. Rao, *J. Mater. Chem.,* 2005, **15**, 3852-3858.
108. H. Li; M. Eddaoudi; M. O'Keeffe; O. M. Yaghi, *Nature,* 1999, **402**, 276-279.
109. O. K. Farha, et al., *J. Am. Chem. Soc.,* 2012, **134**, 15016-15021.
110. T. V. N. Thi, et al., *Adv. Nat. Sci.: Nanosci. Nanotechnol.,* 2013, **4**, 035016.
111. Z.-Z. Lu; R. Zhang; Y.-Z. Li; Z.-J. Guo; H.-G. Zheng, *J. Am. Chem. Soc.,* 2011, **133**, 4172-4174.
112. J. Lee, et al., *Chem. Soc. Rev.,* 2009, **38**, 1450-1459.
113. N. Stock; S. Biswas, *Chem. Rev.,* 2012, **112**, 933-969.
114. J. Klinowski; F. A. Almeida Paz; P. Silva; J. Rocha, *Dalton Trans.,* 2011, **40**, 321-330.
115. M. Sanchez-Sanchez, et al., *Green Chem.,* 2015, **17**, 1500-1509.
116. D. Zacher; O. Shekhah; C. Woll; R. A. Fischer, *Chem. Soc. Rev.,* 2009, **38**, 1418-1429.
117. A. Nalaparaju; J. Jiang, *J. Phys. Chem. C,* 2012, **116**, 6925-6931.
118. B. Liu, *J. Mater. Chem.,* 2012, **22**, 10094-10101.
119. J. Nemoto; T. Saito; A. Isogai, *ACS Appl. Mater. Interfaces,* 2015.
120. J. George; K. V. Ramana; S. N. Sabapathy; A. S. Bawa, *World J. Microbiol. Biotechnol.,* 2005, **21**, 1323-1327.
121. S. S.-Y. Chui; S. M.-F. Lo; J. P. H. Charmant; A. G. Orpen; I. D. Williams, *Science,* 1999, **283**, 1148-1150.
122. L. Brinda; K. S. Rajan; J. B. B. Rayappan, *J. Appl. Sci.,* 2012, **12**, 1778-1780.
123. K. Schlichte; T. Kratzke; S. Kaskel, *Microporous Mesoporous Mater.,* 2004, **73**, 81-88.
124. M. D. Allendorf, et al., *J. Am. Chem. Soc.,* 2008, **130**, 14404-14405.
125. R. Ameloot, et al., *Nat Chem,* 2011, **3**, 382-387.
126. A. Banerjee; U. Singh; V. Aravindan; M. Srinivasan; S. Ogale, *Nano Energy,* 2013, **2**, 1158-1163.
127. I. W. Hamley *Introduction to soft matter: polymers, colloids amphiphiles, and liquid crystals*, Wiley, 2000.
128. P. Walstra, *Chem. Eng. Sci.,* 1993, **48**, 333-349.
129. P. Finkle; H. D. Draper; J. H. Hildebrand, *J. Am. Chem. Soc.,* 1923, **45**, 2780-2788.
130. R. J. Hunter, Oxford University Press: Oxford, 2001.
131. P. Taylor, *Adv. Colloid Interface Sci.,* 1998, **75**, 107-163.
132. W. D. Bancroft, *J. Phys. Chem.,* 1912, **17**, 501-519.
133. T. G. Mason, *Curr. Opin. Colloid Interface Sci.,* 1999, **4**, 231-238.
134. D. Langevin, *Adv. Colloid Interface Sci.,* 2000, **88**, 209-222.
135. M.-G. Song; S.-H. Jho; J.-Y. Kim; J.-D. Kim, *J. Colloid Interface Sci.,* 2000, **230**, 213-215.
136. Y. He, et al., *ACS Appl. Mater. Interfaces,* 2013, **5**, 4843-4855.
137. J. O. Zoppe; R. A. Venditti; O. J. Rojas, *J. Colloid Interface Sci.,* 2012, **369**, 202-209.
138. S. U. Pickering, *J. Chem. Soc., Trans.,* 1907, **91**, 2001-2021.
139. S. Tarimala; L. L. Dai, *Langmuir,* 2003, **20**, 3492-3494.
140. K. L. Thompson, et al., *Langmuir,* 2012, **28**, 16501-16511.
141. Z. Li; T. Ngai, *Langmuir,* 2010, **26**, 5088-5092.

142. K. Zhang; W. Wu; H. Meng; K. Guo; J. F. Chen, *Powder Technol.,* 2009, **190**, 393-400.
143. J. Frelichowska, et al., *Int. J. Pharm.,* 2009, **368**, 7-15.
144. R. Aveyard; B. P. Binks; J. H. Clint, *Adv. Colloid Interface Sci.,* 2003, **100–102**, 503-546.
145. S. Levine; B. D. Bowen; S. J. Partridge, *Colloids Surf.,* 1989, **38**, 325-343.
146. T. S. Horozov; B. P. Binks; R. Aveyard; J. H. Clint, *Colloids Surf. Physicochem. Eng. Aspects,* 2006, **282–283**, 377-386.
147. S. Sharma, et al., *RSC Advances,* 2014, **4**, 45136-45142.
148. X. X. Sun; Q. L. Wu; S. X. Ren; T. Z. Lei, *Cellulose,* 2015, **22**, 1123-1133.
149. J. Frelichowska; M.-A. Bolzinger; Y. Chevalier, *J. Colloid Interface Sci.,* 2010, **351**, 348-356.
150. S. Sihler; A. Schrade; Z. Cao; U. Ziener, *Langmuir,* 2015, **31**, 10392-10401.
151. M. W. Patchan, et al., *ACS Appl. Mater. Interfaces,* 2015, **7**, 7315-7323.
152. H. Lindner; G. Fritz; O. Glatter, *J. Colloid Interface Sci.,* 2001, **242**, 239-246.
153. W. I. Goldburg, *Am. J. Phys.,* 1999, **67**, 1152-1160.
154. M. Z. Yates; M. L. O'Neil; K. P. Johnston, *Macromolecules,* 1997, **30**, 5060-5067.
155. E. Vignati; R. Piazza; T. P. Lockhart, *Langmuir,* 2003, **19**, 6650-6656.
156. W. Zhou; J. Cao; W. Liu; S. Stoyanov, *Angew. Chem. Int. Ed.,* 2009, **48**, 378-381.
157. W. T. M. Irvine; V. Vitelli; P. M. Chaikin, *Nature,* 2010, **468**, 947-951.
158. S. Barg, et al., *Nat Commun,* 2014, **5**, 4328.
159. T. Uragami, *Polym. J,* 2008, **40**, 485-494.
160. J. Li; H. D. H. Stöver, *Langmuir,* 2008, **24**, 13237-13240.
161. D. Suzuki; S. Tsuji; H. Kawaguchi, *J. Am. Chem. Soc.,* 2007, **129**, 8088-8089.
162. S. Melle; M. Lask; G. G. Fuller, *Langmuir,* 2005, **21**, 2158-2162.
163. Y. Qian; Q. Zhang; X. Qiu; S. Zhu, *Green Chem.,* 2014.
164. S. B. Haaj; W. Thielemans; A. Magnin; S. Boufi, *ACS Appl. Mater. Interfaces,* 2014, **6**, 8263-8273.
165. I. Kalashnikova; H. Bizot; B. Cathala; I. Capron, *Langmuir,* 2011, **27**, 7471-7479.
166. T. Winuprasith; M. Suphantharika, *Food Hydrocolloids,* 2015, **43**, 690-699.
167. J. T. G. Overbeek, *J. Colloid Interface Sci.,* 1977, **58**, 408-422.
168. M. Tsang; R. H. Guy, *Br. J. Dermatol.,* 2010, **163**, 954-958.
169. I. Homma; T. Isogai; T. Saito; A. Isogai, *Cellulose,* 2013, **20**, 795-805.
170. A. Shimotoyodome; J. Suzuki; Y. Kumamoto; T. Hase; A. Isogai, *Biomacromolecules,* 2011, **12**, 3812-3818.

Chapter 2 Experimental

2.1 Principles of Analysis

Various techniques have been used to characterise oxidised cellulose and its corresponding materials. Mediator screening for oxidised cellulose synthesis was investigated by cyclic voltammetry (CV), Fourier transform infrared spectroscopy (FTIR); and possible buffer competition mechanism was probed by nuclear magnetic resonance (NMR) study. Bulk oxidised cellulose was synthesised using electrochemistry.

Metal-organic-frameworks/oxidised cellulose composites were characterised by nitrogen adsorption, scanning electron microscope (SEM), transmission electron microscopy (TEM), X-ray diffraction (XRD), Fourier transform infrared spectroscopy (FTIR) and thermogravimetric analysis (TGA).

Characteristics of emulsion stabilised by oxidised cellulose were investigated additionally using laser diffraction, small angle scattering and rheology studies.

The theories and instrumentation used in these techniques are explained in this Chapter.

2.1.1 Cyclic Voltammetry[1]

Cyclic voltammetry (CV) is an electrochemical technique, which linearly and reversibly scans the potential of an electrode immersed in an unstirred solution, against that of a reference electrode (RE) (usually a saturated calomel electrode (SCE) or a silver/silver chloride electrode (Ag/AgCl)), and measures the corresponding current passing through the system using the counter electrode (CE) (Figure 2.1). The typical shape of the controlled potential (also known as excitation signal) over time is a triangular waveform (Figure 2.2a). The slope of the straight line in a potential *versus* time plot is defined as the scan rate (20 $mV \cdot s^{-1}$). Single or multiple cycles can be used (the second cycle is indicated by the dashed line in Figure 2.2a).

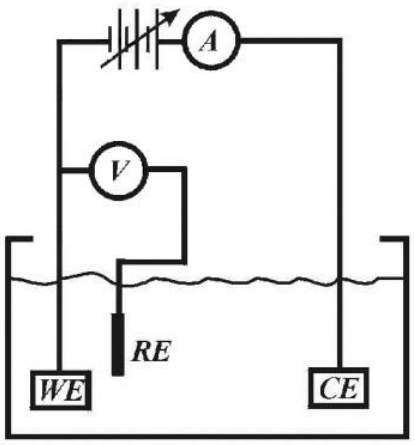

Figure 2.1 Schematic model of a three electrode system

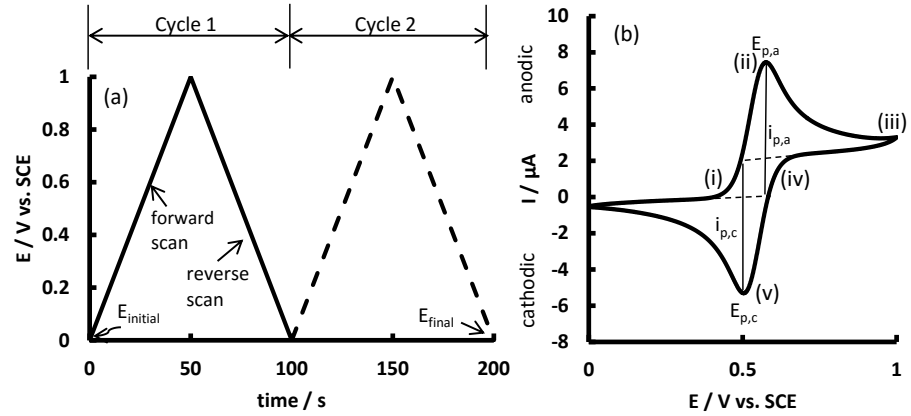

Figure 2.2 (a) Typical excitation signal for CV and (b) CV of 1 *mM* TEMPO in 0.1 *M* carbonate buffer pH 10, scan rate at 20 $mV \cdot s^{-1}$.

The cyclic voltammogram is a display of current as a function of potential measured at the working electrode. A typical cyclic voltammogram is illustrated in Figure 2.2b for a 3 mm diameter boron-doped diamond working electrode in a solution containing 1 *mM* TEMPO as the electro-active species in 0.1 *M* NaCl aqueous solution as the supporting electrolyte. In CV, mass transport of the electroactive species occurs only through diffusion. Therefore, practically, a *ca* 0.1 *M* solution of supporting electrolyte is used to avoid migration effects (charged species close to the electrode surface will be attracted or repelled by electrostatic forces, which is dependent on the ionic strength of the solution) and ensure conductivity.[2]

The potential excitation signal used to obtain this voltammogram is that shown in Figure 2.2a, with a positive switching potential of 1 V. The initial potential is set at 0 V (the redox potential of TEMPO is around 0.5 V) to avoid any electrolysis of the TEMPO radical when the electrode is switched on. The potential is then scanned positively. When the potential is sufficiently positive to oxidise TEMPO, anodic current increases, as indicated at (i) in Figure 2.2b, due to the oxidation process (Scheme 2.1).

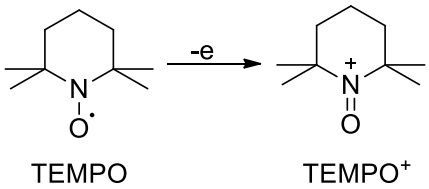

Scheme 2.1 TEMPO oxidation process

Since the electrode potential is now sufficiently strong to oxidise TEMPO to $TEMPO^+$, the anode current increases rapidly (i → ii) until the concentration of TEMPO at the electrode surface is substantially diminished, causing the current peak ii. The current then decays (ii → iii) as the solution surrounding the electrode is depleted of TEMPO due to its electrolytic conversion to $TEMPO^+$. The scan direction is switched at 1 V (the flat section around 1 V in the curve indicates the depletion of excess TEMPO close to the electrode) iii for the reverse scan. The potential is still sufficiently positive to oxidise TEMPO (iii → iv), therefore anode current remains (arising from diffusion of TEMPO to the electrode) even though the potential is now scanning back in the negative direction. When the electrode becomes a sufficiently strong reductant, $TEMPO^+$ accumulated at the surface of the electrode can now be reduced by the electrolytic process (Scheme 2.2).

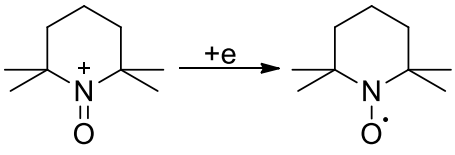

Scheme 2.2 $TEMPO^+$ reduction process

The reduction causes the rise of the cathode current (iv→v). The cathode current rapidly increases until the surface concentration of $TEMPO^+$ is diminished, causing

the current to peak v. The current then decays (the cathode process is the reverse of anode process). The single cycle is completed when the potential returns to 0 V.

Electron transfer to solution redox species at solid electrodes is a heterogeneous process. If the transfer occurs quickly, it is called electrochemically reversible ($\Delta E_p = E_{p,a} - E_{p,c} = \frac{59}{n}\, mV$, n is the number of electrons involved). Slow electron transfers are referred to as electrochemically irreversible. Intermediate rates of electron transfer are known as quasi-reversible ($\Delta E_p > \frac{59}{n}\, mV$, with the value increasing with increasing scan rate).

The redox process for TEMPO (Scheme 2.1 and Scheme 2.2) is chemically reversible, as the redox couple TEMPO/TEMPO$^+$ is stable on the time scale of the voltammetric experiment. The redox couple will become chemically irreversible if the reduced or the oxidised form cannot be converted back by direct electron transfer on the time scale of the voltammetric experiment. Limited chemically reversible reactions occur if the redox couple is converted back only very slowly by direct electron transfer.

The half wave potential ($E_{1/2}$) for a electrochemically reversible couple is the mean value of $E_{p,a}$ and $E_{p,c}$ (Equation 2.1), obtained from CV.

$$E_{1/2} = \frac{E_{p,a} + E_{p,c}}{2} \qquad \textbf{(2.1)}$$

The Nernst equation describes the relationship between the potential applied to the working electrode and the concentration of the redox species at the electrode (Equation 2.2).

$$E = E^0 + \frac{RT}{\mathrm{nF}} ln \frac{\alpha_{ox}}{\alpha_{red}} \qquad \textbf{(2.2)}$$

Where E^0 is the standard redox potential, R is the ideal gas constant (8.314 J·mol^{-1}·K^{-1}), T is the temperature in Kelvin (K), n is the number of electrons involved, F is the Faraday constant (96485.3365 C·mol^{-1}), $\frac{\alpha_{ox}}{\alpha_{red}}$ is the activity ratio of the redox species. The activity ratio is usually replaced by concentration ratio $\frac{C_{ox}}{C_{red}}$ at low

concentration of redox species, and then $E_{1/2}$ is considered to be replaceable for E^0 if the ratio of diffusion coefficient ($\frac{D_{ox}}{D_{red}}$) for the redox species is close to 1.[3]

The peak current for a reversible system is described by the Randles-Sevcik Equation 2.3.

$$i_p = 0.4463FA\left[\frac{F}{RT}\right]^{1/2} c^* D^{1/2} v^{1/2} \quad \textbf{(2.3)}$$

Where F is the Faraday constant (96485.3365 C·mol^{-1}), A is the electrode surface area (cm^2) (obtained using geometric measurement, or, more accurately, by chronocoulometry (measurement of the charge *versus* time)), R is the ideal gas constant (8.314 J·mol^{-1}·K^{-1}), T is the temperature in Kelvin (K), D is the diffusion coefficient (cm^2·s^{-1}), c^* is the concentration of the electroactive species in the bulk solution (mol·cm^{-3}) and v is the scan rate (V·s^{-1}).

The values of $i_{p,a}$ (anodic current) over $i_{p,c}$ (cathodic current) for a simple reversible (fast) electrochemistry active couple should equal 1 (Figure 2.2b).

The electrolysis reaction process, particularly that which occurs “following catalytic reaction”, is introduced here as it is an essential method used in the research.

A catalytic reaction occurring during an electrochemical process is commonly known as an EC’ reaction, where E represents for a heterogeneous electron transfer at the electrode and C’ stands for a catalytic process. The EC’ mechanism can be written as:

$$A \underset{}{\overset{n\ e^-}{\rightleftharpoons}} B$$

$$B + Y \longrightarrow A + \text{products}$$

The catalytic process is the reaction of B with substrate Y in the solution. B is oxidised/reduced back to the starting material A (catalytic cycle) yielding products.

A typical cyclic voltammogam of an EC’ reaction is illustrated in Figure 2.3.

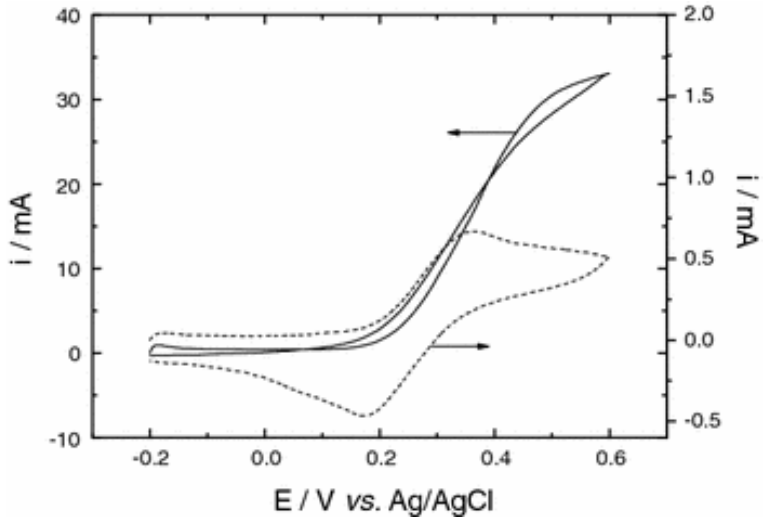

Figure 2.3 Voltammograms of a vitreous carbon electrode in 0.2 mol·L^{-1} carbonate buffer (pH 10), recorded at 50 mV·s^{-1} in the presence of TEMPO (dashed line) and TEMPO + methyl α-D-glucopyranoside (42 mmol·L^{-1}) (solid line), at 22 °C.[4] Reproduction of image from ref. 4 with permission from Springer (© Springer 2010).

In Figure 2.3, the CV of TEMPO alone (before the addition of methyl α-D-glucopyranoside) indicates a quasi-reversible process (i_c / i_a ≠ 1, but the process is still reversible). A significant increase in the current is observed after the addition of 42 mmol·L^{-1} methyl α-D-glucopyranoside. The increase of the anode current and the disappearance of the cathode peak (reduction of TEMPO$^+$ to TEMPO) indicate an electro-catalytic reaction between the TEMPO oxoammonium ion (TEMPO$^+$) and the carbohydrate. This catalytic curve is very important in analysing the reaction rate and mechanism by comparing the catalytic current with different scan rate (e.g. reaction rate can be obtained using the scan rate when the catalytic current diminishes).

2.1.2 Electron Microscopy

In an electron microscope, a beam of energetic electrons is used to examine specimens and produce magnified images. This has advantages over optical microscopy in magnification and resolution (electrons have wavelengths about 100,000 times shorter than visible light photons). The electron microscope image is recorded by a charge-coupled device (CCD) detector.

The maximum resolution, R, obtained with a light microscope is limited by the wavelength (λ) of the photons that are being used to probe the sample, and the

numerical aperture (NA, a number to characterise the range of angles over which the system can accept or emit light) of the system (Equation 2.4).

$$\mathrm{R} = \frac{\lambda}{2NA} \qquad \textbf{(2.4)}$$

As electrons have both wave and particle properties (De Broglie wavelength $\lambda = {}^{\mathrm{h}}/_{p} = {}^{\mathrm{h}}/_{mv}$ and $\mathrm{E} = \frac{1}{2}mv^2$), higher resolution can be obtained by using high energy electron beams.

Two types of electron microscopy have been used in this research, namely scanning electron microscopy (SEM) and transmission electron microscopy (TEM). Both microscopes offer higher magnification, greater depth of field and greater versatility than the light microscope.

2.1.2.1 Scanning Electron Microscope [5]

A scanning electron microscope (SEM) is a type of electron microscope that images a sample by scanning it with a focused beam of electrons (scanned electron beam rather than a fixed beam). As is illustrated in Figure 2.4, the electron beam focused by the condenser lens passes through a pair of scan coils to deflect the beam in the x and y axes and then interacts with the specimen over a rectangular area of the sample surface. The electrons interact with atoms in the sample, producing various signals that contain information about the sample's surface topography obtained by secondary electron emission (inelastic scattering of electrons by the electrons in the atom), and sample composition, by back scattered electrons (elastic scattering of electrons by nuclei of the atom) based on the average atomic number. Ideally, SEM can achieve a resolution better than 20 nm (for ideal samples under high vacuum conditions).

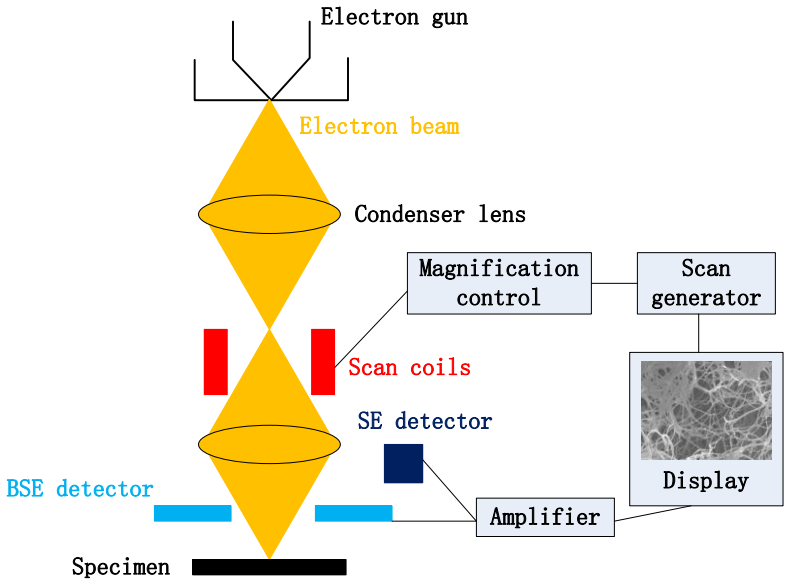

Figure 2.4 Schematic illustration of a SEM instrument.[5] Adapted from reference 5.

The advantage of using SEM is that it provides topographic information about samples down to the nano-scale. SEM is also easy to operate with minimal sample preparation and the data acquisition is fast, compared to other electron microscopy techniques.

Many variables should be considered to obtain the best image from SEM. Generally, high vacuum is still required in SEM to give good resolution as the molecules in air scatter electrons, however many samples may become unstable under very low pressure, which limits the applicable sample types. Lowering the accelerating voltage (the voltage difference between the cathode and the anode) could also provide an image with a clearer surface structure, because a higher accelerating voltage causes electrons to penetrate deeper into the sample and therefore less sample surface information is obtained.[6] Lower accelerating voltages also result in less charge-up (good for insulating samples) and thus less beam damage, despite a minor decrease in resolution.

Modern SEM is normally equipped with Energy-dispersive X-ray spectroscopy (EDX), which allows the determination of the elemental composition of a material from an area as small as 50 nm^2.

For SEM sample preparation, an electrically conductive coating (gold or chromium coating) is required for insulating samples (e.g. cellulose) at high voltage. Thus, samples measured using SEM are not reusable for other experiments. The SEM used in the MAS at the University of Bath is a JEOL SEM6480LV.

2.1.2.2 Transmission Electron Microscopy [7]

Transmission electron microscopy (TEM) was the first type of electron microscopy developed. It operates in a similar fashion to light transmission microscopes except using electrons as the focused beam instead of light to visualize the specimen, which is analogous to a slide projector.

The difference between TEM and SEM lies in the fact that electrons are transmitted through the sample in TEM rather than scattered from the sample surface (as are the electrons collected for visualisation in SEM).

The TEM can be divided into a few main components (Figure 2.5): electrons produced from the gun (typically a tungsten wire anode) are focused by the electromagnetic condenser lens system to form the probe beam transmitted through the specimen. Thin specimens are important for TEM to obtain a satisfactory result. Objective lenses are used to magnify the image (projector) on a fluorescent screen to form an image, which is recorded by direct exposure of the transmitted electrons onto a special photographic film or digitally by a CCD detector.

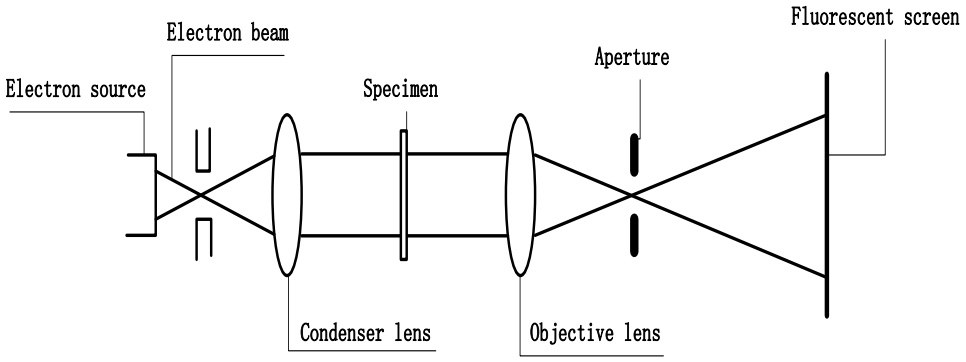

Figure 2.5 Schematic illustration of a TEM instrument.[7] Adapted from reference 7.

The TEM used in the MAS at the University of Bath is a JEOL JEM1200EXII with an accelerating voltage of 120 kV. The accelerating voltage determines the velocity,

wavelength and hence the resolution (ability to distinguish the neighbouring microstructural features) of the microscope (the higher the better). The limiting resolution for TEM is *ca* 0.22 nm.

Sample preparation for TEM requires expertise to obtain the desired results compared to other characterization techniques (i.e. light microscope). Staining of the sample with heavy metal salts or labelling with gold is normally required to give better contrast, as atoms with higher atomic weight scatter electrons more significantly than the lighter atoms. Significant sample degradation can occur during imaging, even in inorganic materials, due to the high energy of the electron beam.

2.1.3 Laser Diffraction for Particle Size Analysis[8]

Scattered patterns of light (also applied to other electromagnetic waves) can be used to determine particle size and shape as the scattering is controlled by the distribution of dipoles in the molecule.[9] A diffraction pattern from a crystalline structure alone is easy to analyse. However, there are other interactions possible when light illuminates particles (Figure 2.6), creating a complex scattering pattern.

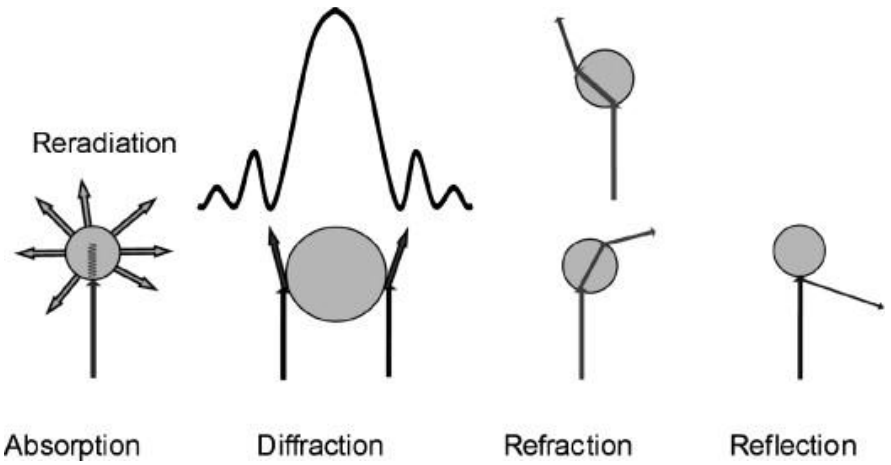

Figure 2.6 Overview of scattering phenomena which occur if a particle is illuminated with light: from left to right: absorption, diffraction, refraction and reflection.[10] Reproduction of images from Ref. 10 with permission from Elsevier (© Elsevier 2008)

Depending on the particle diameter (d) over light wavelength (λ), three distinctive scattering effects occur: Fraunhofer scattering (λ<d, strong forward scattering and a relatively weak backward scattering), Mie scattering (λ≈d, ratio of forward scattering

to backward scattering is much smaller than Fraunhofer scattering) and Rayleigh scattering (λ>d, comparable forward scattering with backward scattering). It is not possible for a detector to distinguish between these patterns. In addition, other light scattering phenomena (Figure 2.6) also need to be taken into account (e.g. adsorption of a particle is adjusted using refractive index).

Fortunately, Gustav Mie, a German physicist, developed a theory (known as Mie theory) in 1908 to describe all the phenomena. A simplified version is given in Equation 2.5, applicable to spherical particles, which is a solution to the Maxwell equation with limiting conditions (i.e. the continuity of tangential electric and magnetic fields across the boundary) to allow for analytical solutions.[10-12] Thus, a particle radius can be calculated based on the equation if the scattered angle and the optical parameters (complex refractive index) are known.

$$I\,(W) = E\{k^2A^4[J1(W)]^2W^{-1} + [K_1W]^1 + [K_2W]^3 + [K_3W]^5$$

Fraunhofer Term

$$+k^4A^6(m-1)^2W^6/8\pi^2\}$$ ← Rayleigh Term **(2.5)**

Where I is the intensity of scattered light, E is flux per unit area of incident light, k and K are constants, A is particle radius, $J1$(W) is the first order Bessel function of first kind, and W is the angle of scattering (the equation follows Keck and Müller[10]). Since laser diffraction only provides a size which gives the same diffraction pattern as a sphere, it cannot provide information for anisotropic or irregularly-shaped particles (shape, aspect ratio). Laser diffraction instead measures an equivalent sphere diameter which is the diameter of a sphere with equivalent volume as an irregularly shaped object.

Image analysis of TEM or SEM micrographs is therefore frequently used for the size measurement of anisotropic particles.[13]

Due to its simplicity and accuracy (well established technique, ISO13320), laser diffraction is used to measure particle size by measuring the angular change in scattered light at small angles. Small particles scatter light at large angles relative to the incident beam, while large particles scatter light at smaller angles (Figure 2.7).

The angular scattering intensity data is then analysed to calculate the size of the particles responsible for creating the scattering pattern, using the Mie theory.[11,12] The particle size is reported as a volume equivalent sphere diameter (D [3,2], assuming a spherical particle model, see 2.2.2.9 for reference). The range of the scattering angles measured in this study is from 0.03° to 50°.

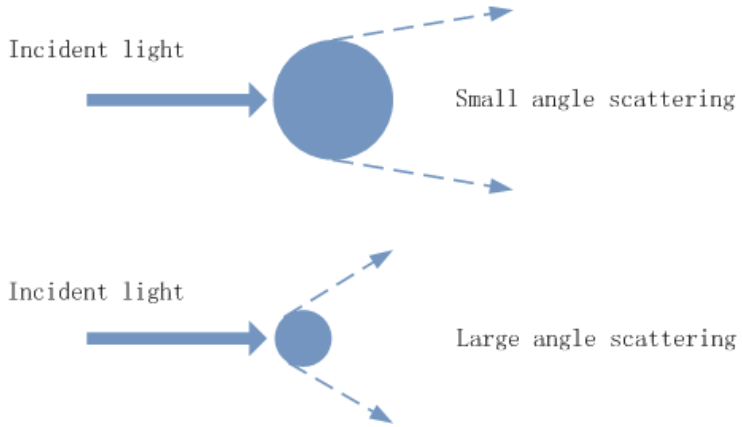

Figure 2.7 Scattering of light from small (upper) and large (lower) particle

Particle size and distribution were characterized using a Mastersizer X (Malvern, UK). The lens used can detect diameters ranging from 0.5 µm up to several mm.

2.1.4 Zeta Potential[14]

Zeta potential, ζ, is also known as the electrokinetic potential in colloidal systems. It is the potential drop across the mobile part of the double layer and is a function of surface charge density. In a colloidal system, the inner region of the liquid layer surrounding the particle is called the Stern layer, where ions absorb strongly, while the outer diffuse layer is where the ions are less firmly attached. Therefore, an electrical double layer exists for each particle. When the particle moves, there is an inner boundary where any ion beyond the boundary travels with the particle. The potential at the boundary is known as the zeta potential (Figure 2.8).

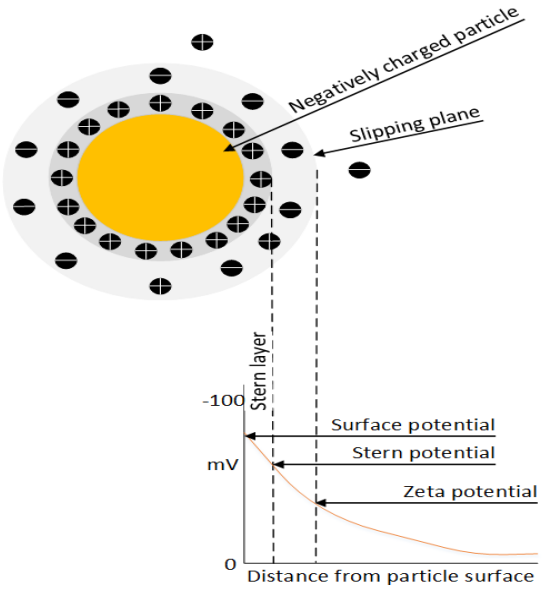

Figure 2.8 Illustration of the electrical double layer.

Zeta potential can be calculated by assuming that the particle is spherical and determining the electrophoretic mobility (U_E) of the particle (using Equation 2.6 and then Henry's equation in Equation 2.7).[15] The electrophoretic mobility is obtained by using laser Doppler velocimetry (LDV) to measure the velocity (v) at the applied potential E.

$$U_E = v/E \tag{2.6}$$

$$U_E = \frac{2\varepsilon\zeta f(ka)}{3\eta} \tag{2.7}$$

Where U_E is the electrophoretic mobility, ζ is the zeta potential, ε is the dielectric constant η is viscosity, $f(ka)$ is Henry's function (which has a value dependent on particle size a and Debye length k^{-1}). A full form of the Henry's function has been described in the literature, and the value of $f(ka)$ is calculated from the limit of a thin or thick double layer (which determines the stability, diffusional and electrostatic properties).[16] Typically, 1.5 is used for particles in polar media (with a thin double layer, $ka \gg 1$, known as the Smoluchowski approximation), or 1.0 was commonly used for particles in non-polar media (thick double layer, $ka \ll 1$, known as the Hückel approximation)). For a cylindrical particle, the alignment of the long axis or short axis with the electric field would give different mobility (the mobility becomes a

weighted sum of the two different mobility values if the particle randomly orients), but the relative change in the zeta potential is still viable. If the particles have a large positive or negative zeta potential then they tend to repel each other and remain thermodynamically stable. Particles with zeta potentials ≥ +30 mV or ≥ -30 mV are generally considered stable while particles with zeta potential between +30 mV and -30 mV may coalesce or precipitate. The most important factor that affects zeta potential is pH (pH could alter the nature of surface charge of the particles). Ionic strength (normally salt concentration) of the media also has an influence on the zeta potential by altering the charges in the double layer.

2.1.5 Thermogravimetric Analysis [17]

Thermogravimetric analysis (TGA) is a common technique used to measure the change of weight in sample as a function of temperature. A sample is heated at a constant heating rate, or held at a constant temperature, while a sensitive balance is used to monitor sample weight changes due to physical or/and chemical reactions. The atmosphere used in the TGA experiment plays an important role and can be reactive, oxidising (e.g. air) or inert (e.g. N_2).

The results are usually displayed as a curve where mass or mass percentage is plotted against temperature. A sample losing or gaining mass may be caused by the following factors: (1) Evaporation of volatile constituents (e.g. solvent); (2) Oxidation of metals in the atmosphere; (3) Oxidative decomposition of samples in air or oxygen or (4) Thermal decomposition of samples in an inert atmosphere. Thus, information about the composition of the samples can be obtained by using TGA together with other techniques (e.g. mass spectroscopy).

2.1.6 Powder X-ray Diffraction[18]

Powder X-ray diffraction (XRD) is a technique to determine the atomic and molecular structure of a crystal. Every crystalline substance gives a unique pattern. Thus, the X-ray diffraction pattern of a pure substance is the fingerprint that substance in a specific crystalline form and is used for characterization and identification of polycrystalline phases.

The basic theory behind XRD is Bragg's law (Equation 2.8). Therefore, atomic crystal structure can be obtained from the θ value.

$$n\lambda = 2dsin\theta \quad \textbf{(2.8)}$$

Where n is an integer, λ is the wavelength of incident wave, d is the spacing between the planes in the atomic lattice, and θ is the angle between the incident ray and the scattering planes.

When the periodic plane in the crystal meets Bragg's law, a sharp peak will appear on the XRD pattern. Amorphous materials produce a broad background signal, and crystallinity is determined by comparing the integrated intensity of the sharp peaks to that of the background.

2.1.7 Fourier Transform Infrared Spectroscopy [19]

Fourier transform infrared spectroscopy (FTIR) is a technique used to identify the functional groups in pure or mixed samples.

When infrared radiation (typical wavenumber ranges from 550 cm^{-1} to 4000 cm^{-1}) is passed through a sample, some of the infrared radiation is absorbed by the sample (functional groups) and some of it passes through. If the frequency of the radiation source matches the vibrational or bending frequency of the particular functional groups, the amplitude of molecular vibration will change and the radiation will be absorbed. The resulting spectrum represents the molecular absorption and transmission, creating a molecular fingerprint of the sample.

Typically, alkyl C-H stretches occur at *ca* 2900 cm^{-1} and the weak peak at *ca* 3000 cm^{-1} is the aromatic C-H stretch. A peak at *ca* 1600 cm^{-1} is the stretch of C=C bond, and the region for C=O bond is at *ca* 1700 cm^{-1}. The O-H stretches occur from 3200-3500 cm^{-1}. These values were important to identify the respective functional groups in the compounds studied in this work.

2.1.8 Small-angle scattering[20]

X-rays are a form of relatively short wavelength, high energy electromagnetic radiation, while a neutron is a subatomic particle with no net electric charge. In

quantum mechanics, X-rays or neutrons are characterised by either their energy E or frequency f, which can be interconverted by Plank's hypothesis using the following equation.

$$E = hf \tag{2.9}$$

Where h is a constant value called Planck's constant, and frequency f is the number of peaks which pass a point per second (phase velocity v of the wave divided by the wavelength λ of the wave),

$$f = {}^{v}/_{\lambda} \tag{2.10}$$

The scattering of an X-ray or a neutron by a sample is described by its change in momentum, $\boldsymbol{P}$, and energy, E.

$$\boldsymbol{P} = \hbar\boldsymbol{k_i} - \hbar\boldsymbol{k_f} = \hbar\boldsymbol{q} \tag{2.11}$$

Where $\hbar$ is known as the reduced Planck constant or Dirac constant $\hbar = \frac{h}{2\pi}$, $\boldsymbol{k}$ is the wavevector $|\boldsymbol{k}| = \frac{2\pi}{\lambda}$.

Therefore,

$$\boldsymbol{q} = \boldsymbol{k_i} - \boldsymbol{k_f} \tag{2.12}$$

Similarly,

$$E = \hbar\omega_i - \hbar\omega_f \tag{2.13}$$

Where ω is the angular frequency $\omega = \frac{2\pi}{\lambda} v$.

Small-angle scattering is used to study structures with a typical size on the order of 10 Å or larger. Information on size, shape and structure of a sample can be obtained at small angles (<10°) for scattered X-rays or neutrons. A full derivation of the small angle scattering principles is beyond the scope of this brief overview and can be found in standard textbooks.[21] However, a brief description of scattering theory is available in this section.

In the following discussions, the scattering experiment is restricted to the special case of elastic scattering ($E = 0$), where there is no energy exchange. This condition implies that the modulus of wavevector, also known as wavenumber, is also unchanged (Equation 2.13 leads to Equation 2.14).

$$|\boldsymbol{k_i}| = \left|\boldsymbol{k_f}\right| = k \tag{2.14}$$

In an elastic scattering experiment, if the scattering angle is 2θ (Figure 2.9), then Equation 2.12 is converted to

$$q = |\boldsymbol{q}| = \left|\boldsymbol{k_i} - \boldsymbol{k_f}\right| = 2ksin\theta = \frac{4\pi sin\theta}{\lambda} \tag{2.15}$$

Equation 2.15 links the magnitude of the momentum transfer to the wavelength and scattered angle.

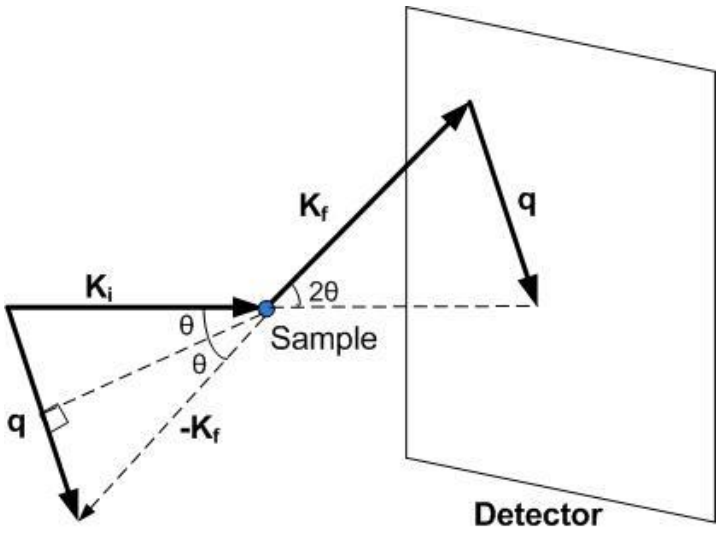

Figure 2.9 Representation of neutrons or X-rays being scattered by a sample.

Combining Equation 2.15 with Bragg's law (Equation 2.8), then

$$q = \frac{2\pi}{d} \quad \textbf{(2.16)}$$

Therefore, scattering from large scale structures is contained at small angle (typically <2°) for scattered X-rays or neutrons, which is known as small angle X-ray scattering (SAXS) and small angle neutron scattering (SANS).

In SAS experiments, the observed scattering intensity *I* from isotropic systems is described as

$$I = N_P V_P^2 (\rho_P - \rho_S)^2 P(q) S(q) + B \quad \textbf{(2.17)}$$

Where N_P is the number of particles, V_P is the volume of particles, ρ is the scattering length density (SLD) of particles P and solvent S, $P(q)$ is the form factor dependant on the particle shape, $S(q)$ is the structure factor dependant on the interactions of particles ($S(q) = 1$ at low particle concentration), and B is the background constant.

The difference between SAXS and SANS is how X-rays and neutrons interact with matter. X-ray photons interact with the electrons and so higher atomic number elements will have large interaction with X-rays, while neutrons interact with nuclei and this interaction varies randomly from isotope to isotope. The scattering interaction of X-rays or neutrons with a single “fixed” atom is quantified by the numerical constant b (scattering length). Scattering length density (SLD) from a material is calculated by

$$\rho = \frac{N_A d}{MW} \sum_i b_i \quad \textbf{(2.18)}$$

Where N_A is the Avogadro’s constant in mol^{-1}, d is the density of the compound in $g \cdot cm^{-3}$, MW is the molecular weight of the compound in $g \cdot mol^{-1}$, b_i is the scattering length of element i in cm. The unit for SLD is cm^{-2}.

One advantage of SANS is that the scattering from hydrogen is distinct from that of deuterium, which is important for the studying of soft materials using contrast variation to change the components to be highlighted in SANS, therefore selectively visualizing the structure (Figure 2.10).[22]

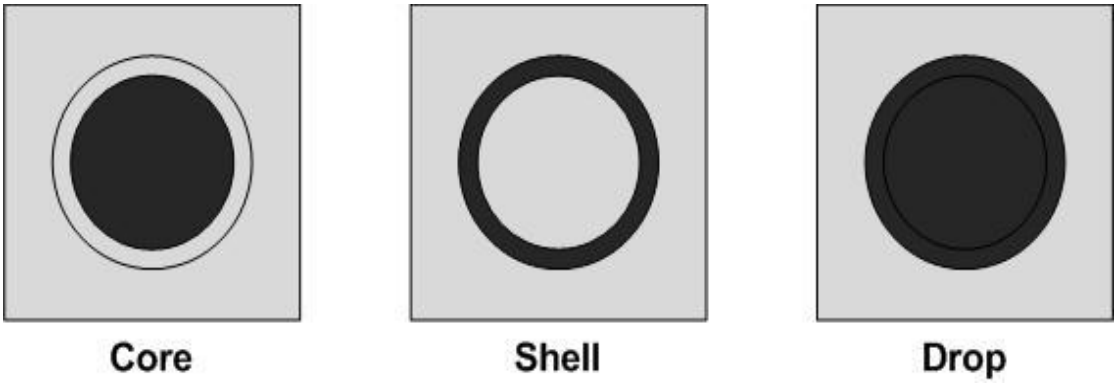

Figure 2.10 An example of contrast variation using solvent deuteration in SANS.

The models used for data fitting will be discussed below in section 2.2.2.13.

2.1.9 Nitrogen sorption[23]

Nitrogen sorption measurements are widely used determining the specific surface area (total surface area of a solid per unit of mass) and pore size distribution of solid materials.

In physical adsorption, adsorption isotherms are classified into 6 types (Figure 2.11).

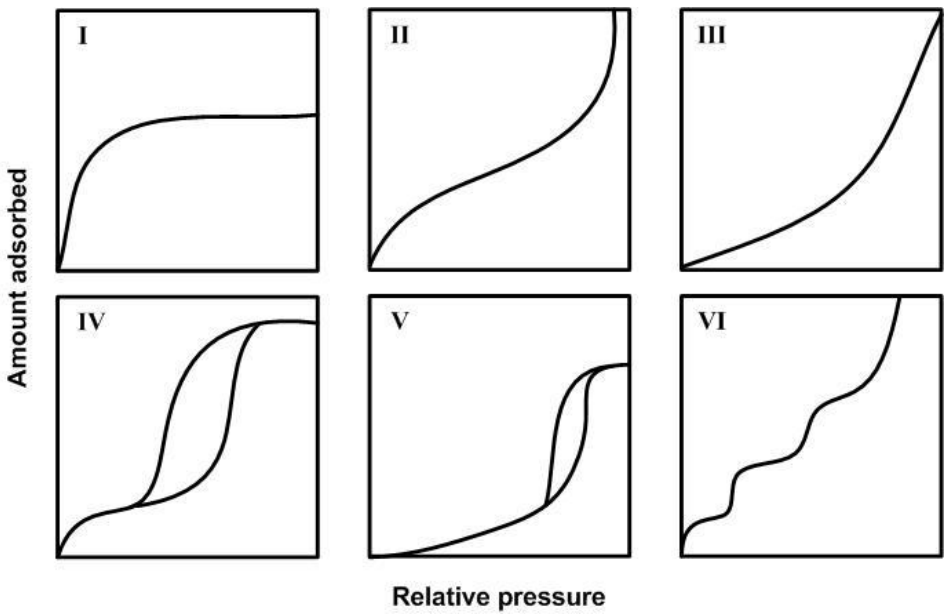

Figure 2.11 IUPAC definitions of types of physisorption isotherms.[24]

Type I isotherms are given by microporous (pore diameter up to 2 nm) solids (e.g. activated carbon); type II and type III isotherms are from nonporous materials with

strong (type II) or weak (type III) interactions between the solid surface and adsorbate; type IV isotherms are given by mesoporous (pore diameter between 2 to 50 nm) solids (e.g. silica), the hysteresis is associated with capillary condensation taking place in pores.; type V isotherms represent mesoporous or microporous materials with weak interactions with the sorbate; type VI isotherms are from nonporous solids with strong gas-solid interaction. Some actual samples do not fit into this adsorption classification, which is a result of mixed types of adsorption isotherms.

Brunauer-Emmett-Teller (BET) theory refers to multilayer physical adsorption, and is used to calculate the specific surface area of adsorbent.[25] The BET theory was based on three hypotheses: 1) Adsorption sites on the adsorbent surface have the same adsorption energy. 2) No lateral interaction occurs between adsorbed molecules. 3) Adsorption energies of layer 2 and above are equal to the condensation energy of the adsorptive (also known as heat of adsorption).

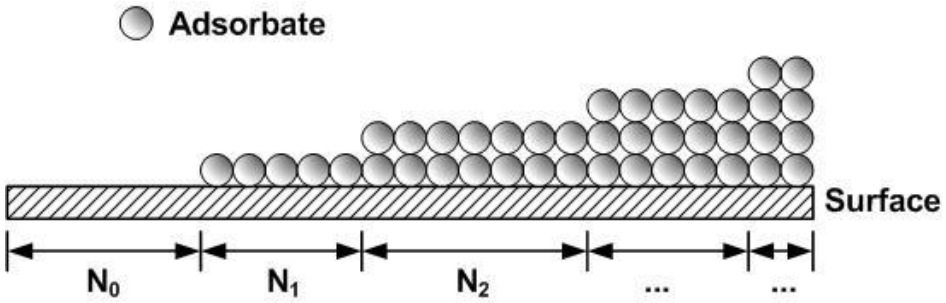

Figure 2.12 Multilayer adsorption on the surface

In Figure 2.12, N_0, N_1, N_2… N_i … are the adsorption sites covered by 0, 1, 2 … i …layers of adsorbed molecules. At equilibration, N_0, N_1, N_2… N_i … remain constant (adsorption site N_{i-1} is illustrated in Equation 2.19).

$$k_{-i}N_i = k_i p N_{i-1} \qquad \textbf{(2.19)}$$

Where k_{-i} is the rate of evaporation to form the ith layer, k_i is the rate of adsorption to form the i^{th} layer, p is the adsorbate pressure, N_i is the adsorption site with i layers of adsorbate molecules. At equilibrium, a constant x is defined such that $x = N_i/N_{i-1} = p\,k_i/k_{i-1}$, then $N_i = xN_{i-1} = cx^iN_o$ $(i \neq 1)$, and c is a constant.

The total surface coverage can be expressed by the following equation. $\mathrm{v/v_m} = \sum_{\mathrm{i=0}}^{\infty} \mathrm{iN_i} / \sum_{\mathrm{i=0}}^{\infty} \mathrm{N_i} = \mathrm{cN_0} \sum_{\mathrm{i=1}}^{\infty} \mathrm{ix^i} / \mathrm{N_0}(1 + \mathrm{c} \sum_{\mathrm{i=1}}^{\infty} \mathrm{x^i})$, and $\sum_{\mathrm{i=1}}^{\infty} \mathrm{x^i} = \mathrm{x}/(1 - \mathrm{x})$. Where v is the total volume adsorbed, v_m is the volume adsorbed when all the adsorption sites are covered with a complete monolayer. Then the surface coverage equation is written as $v/v_m = cx/(1-x)\,(1 - x + cx)$. Replacing x with p/p_0 and rearranging gives the BET equation which is then shown below.[25]

$$\frac{\mathrm{p}}{v(p_0 - p)} = \frac{1}{v_m c} + \frac{c - 1}{v_m c}\left(\frac{p}{p_0}\right) \tag{2.20}$$

Where p is the pressure of the adsorbate, p_0 is the saturation pressure, v is the adsorbed amount. Plotting $p/(v(p_0 - p))$ against p/p_0, the two constants (v_m and c can be calculated by Equation 2.21 and Equation 2.22 from the intercept (b) and slope (k) of the straight line (known as a BET plot).

$$v_m = \frac{1}{k + b} \tag{2.21}$$

$$c = \frac{\mathrm{k}}{b} + 1 \tag{2.22}$$

In practice, v_m and c are commonly evaluated in the pressure rage (p/p_0) of 0.05 to 0.35 from the BET plot because the approximations made in deriving the BET equation no longer hold above this point and the plot deviates from linearity.

The specific surface area (S_{BET}) of the solid material can be calculated by Equation 2.21 and 2.23.

$$S_{BET} = \frac{\left(\frac{v_m}{V_m} N_A \sigma\right)}{m} \tag{2.23}$$

Where is the volume of the molecules adsorbed in the solid, V_m is molar volume of the adsorbed molecules, $N_A$is the Avogadro constant, m is the mass of the solid, σ is the cross section of the adsorbed molecules ($\sigma(N_2) = 0.162\ nm^2$ at 77 K). Due to its

convenience and well known properties, nitrogen at 77 K is recommended for BET measurement.

The BJH (Barrett-Joyner-Halenda) method and DH (Dollimore-Heal) method were used to characterise the pore size distribution of the material in the capillary condensation region of an isotherm, based on different assumptions (BJH method assumes all pores are filled with liquid; DH method assumes a cylindrical pore geometry).[26]

2.1.10 Rheology[27]

Rheology, the study of deformation and flow of matter, links the macroscopic behaviour of material to its internal structure. Rheology extends the disciplines of Continuum mechanics to materials whose mechanical behaviour cannot be described with the classical (e.g. elasticity and Newtonian) theories.

In 1687, Isaac Newton proposed the postulate (Figure 2.13) to introduce viscosity as a measure of resistance to flow, obeying Equation 2.24. Later, Navier and Stokes independently developed the three dimensional theory for Newton's postulate, known as the Navier-Stokes equations.

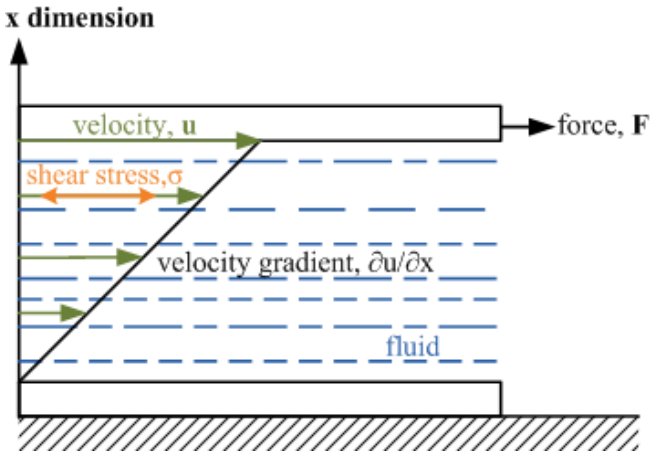

Figure 2.13 Two parallel planes of area A filled with sheared fluid. The upper plane moves at velocity u**.**

$$\sigma = {}^{F}/_{A} = \eta \frac{\partial u}{\partial x} \quad \textbf{(2.24)}$$

Where F is the external force applied to the system, σ is the shear stress, η is the viscosity (more specifically, the dynamic viscosity) of the fluid, ∂u/∂x is the shear velocity gradient at a plain with surface area A, this is referred to as the shear rate, denoted by γ.

Therefore,

$$\sigma = \eta\gamma \quad \textbf{(2.25)}$$

For Newtonian fluids (e.g. glycine and water), shear viscosity is independent of shear rate, and is sometimes called coefficient of viscosity. For most of the liquids, shear viscosity is a function of the shear rate (known as non-Newtonian fluids), and is often referred to as apparent viscosity or dynamic viscosity. Shear-thinning non-Newtonian fluids (e.g. emulsions, dispersions and polymer solutions) are when fluid viscosity decreases with increasing shear rate (shear-thinning behaviour or pseudoplasticity). Shear-thickening non-Newtonian fluids (e.g. sand in water) show behaviour where the fluid viscosity increases with increasing shear rate.

Viscoelastic materials exhibit both viscous and elastic properties under constant shear stress or shear rate. To measure the viscoelastic behaviour of materials, a sinusoidal shear deformation (ε) was induced and the resultant stress (σ) was measured, known as oscillatory rheology. The time scale of the effect is determined by the oscillation frequency, ω, over the shear deformation.

For a sinusoidal strain deformation $\varepsilon(\omega, t) = \varepsilon_0 \sin(\omega t)$, the stress response of a viscoelastic material is given by $\sigma(\omega, t) = \varepsilon_0 G'(\omega)\gamma_0 \sin(\omega t) + \varepsilon_0 G''(\omega)\gamma_0 \cos(\omega t)$. The storage modulus $G' = \frac{\sigma_0 cos\varphi}{\varepsilon_0}$ describes the elastic properties, and the loss modulus $G'' = \frac{\sigma_0 \sin\varphi}{\varepsilon_0}$ describes the viscous properties, where φ is the phase lag between stress and strain.

The visco-elastic behaviour originates from molecular rearrangement in the material. When a stress is applied to a viscoelastic material, some of the molecules change positions in order to compensate the stress, generating a back stress in the material. The material remains solid when the back stress is the same magnitude as the applied stress, and the material no longer creeps. When the external stress is taken away from the material, the accumulated back stress will cause the molecules to return to their original position.

2.2 Materials and Methods

2.2.1 Materials

Cotton samples (Phoenix Calico, US) were woven non-fluoresecent, non-desized and non-mercerised, obtained from Unilever. TEMPO (98 %), 4-acetamido-TEMPO (for EPR spectroscopy), 4-carboxy-TEMPO (97 %) and 4-hydroxy-TEMPO (97 %) were obtained from Aldrich, while 4-methoxy-TEMPO (>98 %) was from TCI. Oxidised cellulose was obtained as a freeze-dried powder from Croda, and was prepared using the method described in a previous publication.[28] Bacterial cellulose was produced by Acetobacter aceti in apple cider vinegar (Omega Nutrition,UK), using a culture medium of black tea (1g tea bag heated with 100 mL water for 30 min) and 5 vol% of sucrose. Copper (II) acetate (98%), ethanol (>99.8%) were obtained from Sigma-Aldrich, while 1,3,5-benzenetricarboxylic acid (trimesic acid, >98 %) and N,N-dimethylformamide (DMF, >99.5%) were from TCI. Hexadecane (99%) was obtained from Sigma-Aldrich and was washed thoroughly with water to remove any remaining surfactants.

All other chemicals were obtained from Sigma-Aldrich and used as received without further purification.

In Chapter 3, carbonate buffer (CBS) pH 10; borate buffer (BBS) pH 9.5, 9 and 8.5; phosphate buffer (PBS) pH 5 and 7; acetate buffer (ABS) pH 6, 5 and 4; and citrate buffer pH 7 were used to maintain the pH of the reaction solution. All the buffers were of 0.1 *M* concentration unless otherwise specified. Mediators (Chart 3.2) were of 1 *mM* concentration unless otherwise specified. Voltammetric experiments were carried out in buffered solutions prepared with ultrapure water (18.2 MΩ cm) from a

PURELAB Classic system (EGLA, UK).

2.2.2 Methods of Analysis

2.2.2.1 Cyclic Voltammetry

For voltammetric studies an Autolab PGSTAT12 system (EcoChemie, NL) was employed with a KCl-saturated calomel (SCE) counter electrode (REF401, Radiometer, Copenhagen), and a Pt counter electrode. The working electrode was a 3 mm diameter boron-doped diamond electrode (Diafilm^{TM}, Windsor Scientific).

Following a methodology developed previously,[29] a 5 mm disk of cotton fabric was placed in close contact with the working electrode, held in place with a fine nylon mesh and immobilised by an O-ring illustrated in Figure 2.14. The voltage range used was from 0 to 1 V and scan rates were as indicated for each experiment.

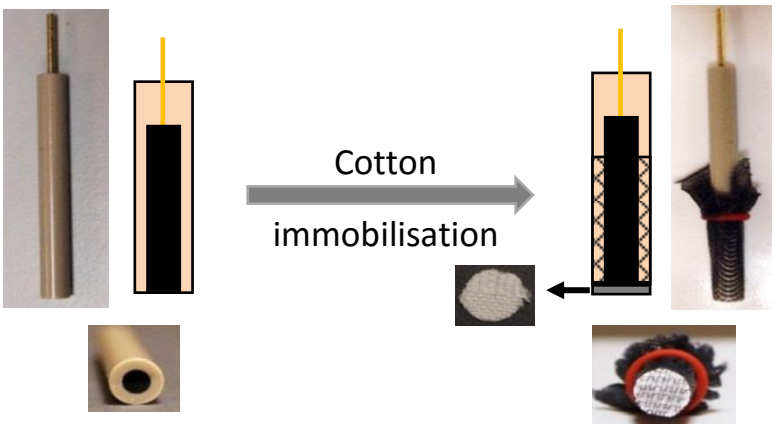

Figure 2.14 A disk of cotton fabric is placed in intimate contact with the working electrode and secured by means of a fine nylon mesh.

2.2.2.2 Fourier Transform Infrared Spectrometry

Attenuated total reflection Fourier transform Infrared spectrometry (ATR-FTIR) was used at room temperature on a diamond single-crystal parallelepiped internal reflection element in a PerkinElmer Frontier IR system to characterize freeze-dried non-oxidized and oxidised cotton derived from multiple oxidation cycles at pH 10. The spectra were recorded with a width ranging from 4000 to 600 cm^{-1}, with an accumulation of 10 scans and a 1 cm^{-1} resolution. Of particular importance was the evolution of the C=O stretching band at *ca* 1650 cm^{-1} following oxidation.

2.2.2.3 Conductometric Titration

Freeze-dried oxidised cellulose (30-40 mg) was dissolved or suspended in 20 mL 0.01 *M* aqueous HCl solution and titrated with aqueous 0.01 *M* NaOH solution in aliquots of 200 µl each time. The conductivity was measured after every addition of NaOH solution and the titration proceeded over the pH range of 2–12. The volume of NaOH solution required determined based on the conductometric titration curve and the degree of oxidation (DO) was calculated according to

$$\mathrm{DO} = \frac{162 \times \mathrm{V_{NaOH}} \times \mathrm{c}}{\mathrm{m} - \mathrm{V_{NaOH}} \times \mathrm{c} \times 36} \qquad \textbf{(2.26)}$$

Where V_{NaOH} is the used volume of aqueous NaOH solution in L, c is its concentration (mol·L^{-1}) and m is the weight of dried OC sample in g (formula weight of cellulose "monomer" = 162 and of HCl = 36).

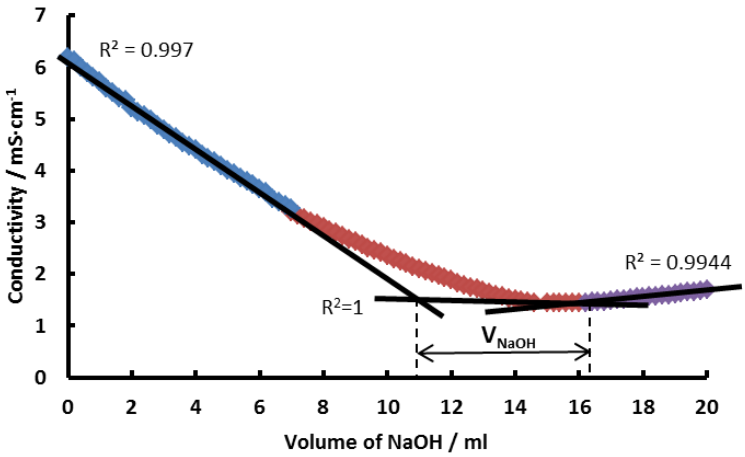

Figure 2.15 Conductometric titration curve of an oxidised cellulose sample

A typical titration curve for DO determination is presented in Figure 2.15. There are two end points in the titration curve. The first corresponds to the neutralization of HCl (at *ca* 8 mL). To discern the endpoint, the best fit straight line of scattered points from 0 mL to 7 mL is determined (the difference in the calculated carboxylate content is smaller than 0.1 mmol·g^{-1} if the experimental data is fitted over the range of 0-3 mL instead of 0-7 mL). The second endpoint corresponds to the neutralization of weak acid (at *ca* 17 mL), following which the conductivity increases due to the excess of NaOH. The transition from weak acid titration to excess strong base is

easily identified on the curve and the endpoint determined. The first straight line was fitted for the same data range (0-7 mL) for all samples in order to minimise the variation.

For the determination of aldehyde content, the TEMPO-oxidized cellulose fibres (0.2 g) were further oxidized with $NaClO_2$ (0.2 g) at pH 4-5 (20 mL HCl solution) and room temperature for 2 days to selectively convert aldehyde groups in the samples to carboxylate groups. Carboxylate content was determined directly for the TEMPO-oxidized material and then complete oxidation (of CHO groups to COOH) was achieved by further $NaClO_2$ oxidation, after which the total degree of oxidation of cellulose fibrils was determined by the above conductometric titration method. The difference between these values provides a measure of the number of aldehyde groups present in the sample.

2.2.2.4 Viscometric Degree of Polymerization

Cellulose, or oxidised cellulose samples (0.04 g each) were dissolved in 0.5 *M* copper ethylenediamine solution (CED, 20 mL) for 30 min. Intrinsic viscosities of the solutions were obtained by using a Cannon−Fenske capillary viscometer, and these values were converted to the viscometric degree of polymerization (DP_v) values by using the Mark−Houwink−Sakurada equation, for $[\eta] = 0.57 \times \mathrm{DP}_v$.[30]

The relationship between DP_v, DP_n (number-average degree of polymerization) and DP_w (weight-average degree of polymerization) can be described as $\mathrm{DP}_n = \frac{\mathrm{DP}_v}{1+a(\frac{\mathrm{DP}_w}{\mathrm{DP}_n}-1)}$ where a is the constant.[31] It has been found experimentally that the value of DP_v is very close to DP_w for OCNF.[30]

2.2.2.5 Nuclear magnetic resonance

Solutions of oxidised cellulose (0.0202g, 2 wt%) were prepared by heating a mixture of the respective oxidised cellulose, DMSO-d_6 (0.6285g, 68.5 wt%) and the ionic liquid (EMIMAc, 0.28 mL, 29.5wt%) to 100 °C with constant stirring. Upon dissolution, the samples were transferred to 5 mm quartz NMR tubes. The ^{13}C spectra were

collected at 90 °C on a Bruker AVANCE 400 NMR spectrometer operating at a ^{13}C frequency of 100.61 MHz. A total of 15 000 scans were collected. [32,33]

Other NMR experiments were recorded on Agilent 500 MHz NMR spectrometer at 298 K if not specified, and referenced to the residual solvent signals for ^{1}H NMR and ^{13}C NMR.

2.2.2.6 SEM / Field Emission-SEM and TEM

Morphology was characterised using a scanning electron microscope (JEOL SEM6480LV or JEOL FESEM6301F, Japan) equipped with an energy dispersive X-ray spectrometer (Oxford INCA X-ray analyser, UK) operating at an accelerating voltage of 5 kV. Samples were coated with chromium.

The transmission electron microscope (TEM) images were obtained on the JEOL IEM1200EXII instrument with the operating voltage of 120 kV. Before image acquisition, samples were deposited on copper grid and negatively stained using uranyl acetate.

2.2.2.7 X-ray diffraction

X-ray diffraction (XRD) patterns of the materials were recorded on a Bruker AXS D8 Advance X-ray diffractometer with Cu Kα radiation (λ = 1.542 Å), equipped with a Vantec-1 detector. The accelerating voltage was 40 kV and the applied current of 40 mA. The spectra were recorded with a step size of 0.0156° and at a scanning rate of 2°·min^{-1}. Capillary mode and flat plate mode were used for XRD contingent on the sample forms). The size of the crystallite is calculated using Scherrer equation (the smaller the crystallite, the broader the peak will be).[34]

$$D_{hkl} = K\lambda/\left(\beta_{1/2}cos\theta\right) \quad \textbf{(2.27)}$$

Where D_{hkl} is crystallite size in the direction of the lattice plane hkl, λ is the radiation wavelength ,$\beta_{1/2}$ is the half-maximum of the diffraction peak at the diffraction angle θ. K is a dimensionless shape factor, ranging from 0.62 to 2.08, depended on the shape of the crystal.[35] For cellulose materials, K was set to 0.94, a value that is widely used, based on the geometry of a cylindrical crystallite.[36,37]

The cellulose crystallinity index (CI) has been used to describe the relative quantity of crystalline material in the bulk cellulose. The cellulose crystallinity has been measured using several different techniques including XRD, solid-state ^{13}C-NMR, infrared spectroscopy and Raman spectroscopy.[38] XRD is the most widely used techniques to determine cellulose crystallinity and there have been several methods used for calculating crystallinity from the raw XRD data.

One common method, known as Segal's method, allows rapid empirical comparison of cellulose samples. CI is calculated from the ratio of the height of the 002 peak (I_{002}) and the height of the minimum (I_{am}, at ca 18.5° of 2θ for OCNF used in this work) between the 002 and the 101 peaks, $\mathrm{CI} = \frac{I_{002}-I_{am}}{I_{002}}$.[39] This method is useful for comparing the relative differences between samples from the same source, but the results should be only considered as a rough estimation.[40] The Rietveld method uses the full diffraction pattern to simultaneously fit unit cell, crystal structure, peak parameters and background, using a least-squares fitting procedure.[41]The use of the correct cell parameters for cellulose, a rigorous data collection method and good signal-to-noise ratio in the measured XRD pattern are all essential to a proper refinement.[42]

Segal's method is used in Chapter 4 to provide an estimation of the crystallinity of OCNF before and after oxidation. The Rietveld refinement was also applied here to measure the change in crystallinity of OCNF in Chapter 4, and to measure the MOF fraction in the composites in Chapter 6. The Rietveld refinement was conducted using Match! version 3.1.1, following the procedures described by Eyley *et al*.[43] The experimental data of cellulose are fitted by a polynomial background, one scale factor, two peak profile parameters and two cell dimensions (*a* and *b*).[43] The crystallinity of cellulose and MOF was calculated as described by Thygesen *et al*.[44] For the refinement, the crystallinity of the cellulose, or MOF fraction, was calculated by $\int_{s_0}^{s_1} I_c(s)\, s^2 ds / \int_{s_0}^{s_1} I\,(s) s^2 ds$, where $s = 2sin\theta/\lambda$ is the scattering vector, $I_c(s)$is the intensity at a particular vector due to crystalline material and $I(s)$ is the total intensity at a particular vector, and s_0,s_1 are the limits of the integration.The crystal structures used for fitting were I_α[45] and I_β[46] from Nishiyama *et al*, cellulose II from Langan *et*

al,[47] MOF-199 from Chiu *et al,* [48] and Ni-MOF from Zhang *et al*.[49] The Rietveld refinment patterns are attached in the appendices.

2.2.2.8 TGA

TGA experiments were performed on a Perkin Elmer TGA 4000 Thermogravimetric Analyser. The samples were heated from 45 °C to 600 °C at a heating rate of 10 °C /min, under a flow of air or nitrogen (20 mL/min).

2.2.2.9 Laser diffraction for particle size measurement

Particle sizes in the emulsions were characterized using a Mastersizer X (Malvern, UK). The optics used can detect sizes ranging from 0.5 -180 µm. The range of the scattering angles measured is from 0.03° to 50°. Each sample was measured 3 times. A liquid dispensing system was used to circulate the emulsion droplets in the laser diffraction instrument. Before each measurement, the diffraction of pure water was taken and subtracted as background.

The obtained result is displayed as a volume equivalent sphere diameter, which is calculated using the derived diameter D (m,n) defined below.

$$D\,(m,n) = \left[\frac{\sum V_i d_i^m}{\sum V_i d_i^n}\right]^{\frac{1}{m-n}} \qquad \textbf{(2.28)}$$

Where V_i is the volume of class i with the mean diameter d_i. Letters m and n are the integer values that describe the type of $D\,(m,n)$, where m denotes the type of distribution (m=1, 2, 3 for number-weighted, surface-weighted and volume-weighted respectively) and m-n denotes the type of average (arithmetic mean if m-n=1 and quadratic mean if m-n=2).[50] In this thesis, the surface weighted mean diameter D (3,2) is used to characterise emulsion droplets.

2.2.2.10 Zeta potential for droplet charge measurement

A Zetasizer Nano from Malvern Instruments was used to determine the zeta potential of the droplets in emulsions. Practically, 1 mL of the emulsion or suspension was placed in disposable capillary electrode cells, situated in the Zetasizer Nano, and the zeta potential was measured 20 times per sample.

2.2.2.11 Surface tension

The surface tension at the oil/water interface was determined using a Du Noüy ring method in a Sigma 701 instrument (Attension, Sweden).[51] A platinum ring with a radius of 9.58 mm was used in the experiment. The ring was cleaned by rinsing it in methanol followed by burning off the residues between measurements. Each experiment was performed at least 10 times. The temperature remained constant at 23 °C during the experiments.

2.2.2.12 Contact Angle

The water contact angle (WCA) and hexadecane contact angle (HCA) of spin-coated films of both salt form oxidised cellulose (Oxcell-COONa, pH *ca* 7.3) and acid-form oxidised cellulose (Oxcell-COOH, pH *ca* 4.3) on glass slides was determined using the sessile droplet method. The modified substrate was placed on the goniometer and static images were captured using a Discovery VMS-001 USB microscope (Veho). The subsequent images were used to calculate the contact angle of the droplet, utilizing Dropsnake software with the ImageJ imaging process package. Contact angle measurements were conducted at room temperature after the samples had been dried in an oven at 100 °C for 3 h.

2.2.2.13 Confocal Laser Scanning Microscopy (CLSM)

For CLSM visualization, the oxidised cellulose was stained with fluorescein. Images were acquired using a LSM510META confocal microscope (Zeiss, Gottingen, Germany) using an x60 lens with an optics section thickness around 2 μm. Experiments were carried out at room temperature.

2.2.2.14 Small Angle X-ray / Neutron Scattering (SAXS / SANS)

SAXS experiments were carried out on an Anton Paar SAXSess instrument (Graz, Austria) with a line-collimation mode on a PANalytical X-ray generator using a Cu Kα source with a wavelength of 1.54 Å at the University of Bath. 30 vol% of hexadecane and 70 vol% of H_2O with various NaCl or $CaCl_2$ concentrations were used for SAXS experiments. The q range for the experiment covered from 0.02 $Å^{-1}$ to 0.3 $Å^{-1}$. The system was maintained at 25 °C. Reusable Europium excitation based image plates

(size: 66 x 200 mm) with a 42.3 μm^2 pixel size were used to detect the scattered X-ray, and the plates were then read by a Perkin Elmer cyclone reader using OptiQuant software. SAXSquant program was used to generate SAXS profiles, data processing (background subtraction, and desmearing from a line to a point source using the Lake method).[52]

SANS experiments were carried out at the time-of-flight SANS2D instrument on Target Station II at the ISIS Spallation Neutron Source (Rutherford Appleton Laboratory, UK). Technical information about the instrument has been reported in literature by Heenan et al.[53] The q range for the experiment covered from 0.00243 $Å^{-1}$ to 0.3 $Å^{-1}$. Background correction was carried out using a quartz cell filled with the corresponding aqueous solutions (D_2O, H_2O and 50/50 vol D_2O/H_2O) for the emulsions. All the experiments were conducted at 25 °C. Mantidplot was used to process the raw data for the linearity and efficiency of the detector response.[54]

A summary of the SLD (scattering length density, refer to section 2.1.8 for details) of the materials for SAXS and SANS used in the experimental data analysis is displayed below. These were calculated using Equation 2.18.

Table 2.1 X-ray and neutron scattering length densities of materials used in this work.

Name	**Chemical formula**	**Density (g/mL)[a]**	**SANS SLD ($x10^{-6}$ $Å^{-2}$)[b]**	**SAXS SLD ($x10^{-6}$ $Å^{-2}$)[b]**
water	H_2O	1	-0.56	9.47
deuterated water	D_2O	1.11	6.39	9.45
hexadecane	$C_{16}H_{34}$	0.77	-0.43	7.52
deuterated hexadecane	$C_{16}D_{34}$	0.887	6.83	7.52
oxidised cellulose[c]	$(C_6H_{10}O_5)_n$	1.5	1.7	13.5

[a] data obtained from MSDS forms on Aldrich website.

[b] calculated by Irena SAS macros in Igor Pro software

[c] data of cellulose from as chemical compositions and the nanofibril density remain the similar.[55]

For the fitting model, the 'polyCore_and_Nshells' model[56] in the NIST SANS Analysis package within Igor Pro was found to best fit the data and give realistic results.[57] The model calculates the form factor for polydisperse spherical particles with a core-shell structure (a polydisperse core with either one or two concentric shells of constant thickness in this study). The SLD of each shell is specified individually. The polydispersity is described by a Schulz distribution because it can provide a reasonable description of the polydispersity of emulsion system.[58]

The form factor is normalized by the average particle volume shown in Equation 2.29. The structure factor was set to 1, as no interparticle interference of the emulsion droplets would be observed in this q range.

$$P(q) = a \times \frac{f^2(q)}{V_p} + B \qquad \textbf{(2.29)}$$

Where a is the scale factor (between 0 and 1), $f(q)$ is the scattering amplitude of a single particle related to the SLD of particles (detailed correlation equation was not describe here as it was not the focus for this study but it can be found in literature),[56] and V_P is the volume of particles averaged over the Schulz distribution of core radius (Equation 2.30).

$$V_P = \frac{4\pi}{3} r^3 \qquad \textbf{(2.30)}$$

$$r^3 = \frac{(z+3)(z+2)}{(z+1)} r \qquad \textbf{(2.31)}$$

$$z = \frac{1}{p^2} - 1 \qquad \textbf{(2.32)}$$

Where r is the radius of the particle, z is the width of the Schulz distribution, p is the polydispersity constrained between 0 and 1 ($p = \sigma / r_c$, where σ is the standard deviation of the radius distribution and r_c is the mean core radius).

The input parameters for the model were displayed in Table 2.2.

Table 2.2 Input variables for the 'Polycore_Nshell' model.

Parameters	Initial value	Constraint
scale	0.1	(0.0001,1)
core radius (A)	10000	hold
Core Polydispersity (0,1)	0.3	hold
Core SLD (A^{-2})	ρ_c	hold
Shell 1 thickness (t_1)	10	(0.001,100)
Mole fraction of oil (ρ_1)	0.5	(0.0001,1)
Shell 2 thickness(t_2)	10	(0.001,100)
Mole fraction of water(ρ_2)	0.5	(0.0001,1)
Solvent SLD (A^{-2})	ρ_s	hold
background (cm^{-1})	set from data	hold

The model was visualised in Figure 2.16. ρ_c and r_c are the SLD and radius of the core. ρ_1 and t_1 are the SLD and thickness of the inner shell. ρ_2 and t_2 are the SLD and thickness of the outer shell. ρ_s is the SLD of the solvent. For 'polyCore_and_1shell' model, t_1 is considered as zero.

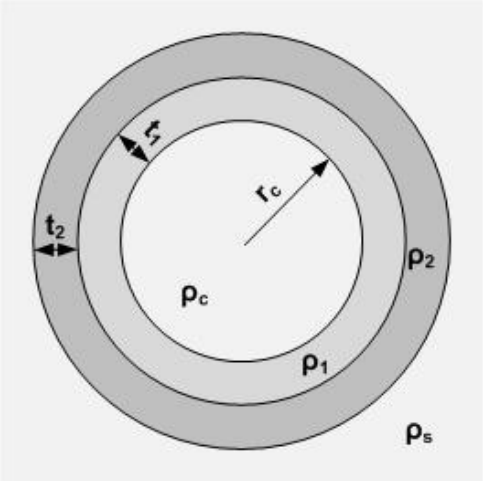

Figure 2.16 Illustration of a polydisperse core-shell sphere with two shells.

2.2.2.15 Sorption Isotherms

The sorption isotherms of N_2 at 77 or 273 K and CO_2 at 273 K were conducted by BELSORP Mini-II (BEL, Japan) instrument. The sample was pre-conditioned at 160 °C for 6 h prior to the sorption experiment. The specific surface area of the samples was calculated by the Brunauer-Emmett-Teller (BET) method in the P/P_0 range of 0.05-0.1. The selectivity of the material for CO_2 over N_2 sorption was calculated from the single gas isotherms by the CO_2 adsorption capacity over that of the N_2 at the relative pressure of 1.

The xylene sorption study was carried out in a sealed vial of mixture to be absorbed, as is illustrated in Scheme 2.3. Typically, *ca* 40 mg of MOFs were weighed and placed in a solvent containing vial where they were equilibrated for 12 hrs at room temperature (1 week for MOFs / BC composites due to slow sorption), until the weight of the particles remained constant. The particles were then taken for TGA and XRD measurements. For selectivity determination, the corresponding particles were washed with deuterated methanol and then filtrated for ^{13}C NMR.

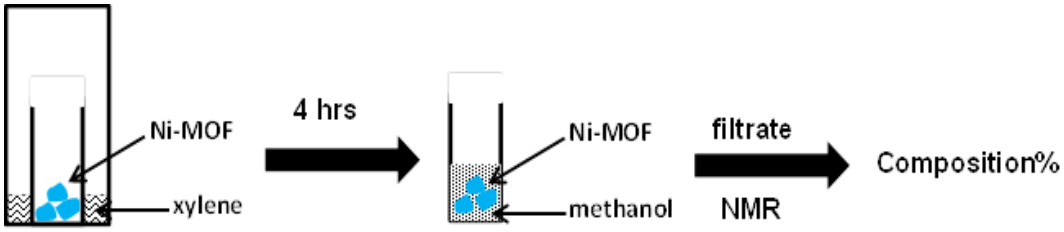

Scheme 2.3 Competitive adsorption experiment on Ni-MOF exposure to xylene mixtures.

Measurements of sorption kinetics reactions were carried out using a pre-evacuated microbalance at 25 °C (in-house purpose-built instrument in Professor Len Barbour's group at University of Stellenbosch, South Africa). The data recorded as mass vs. time were used to extract the kinetics results.

2.2.2.16 Rheology

Rheology experiments were conducted on a Bohlin C-VOR 200 range of rheometer equipped with cone–plate geometry (1° cone angle, 40 mm diameter and 0.5 mm gap). Oscillatory stress experiments were conducted over an oscillatory stress range of 0.1–10 Pa at the frequency of 1 Hz (terminated when strain exceeded 300%), with a pre-conditioning step of 20 s at zero-shear before each measurement. Shear viscosity data were collected with a conditioning step of 30 s at zero-shear and measurement over a shear rate range of 1 s^{-1} to 300 s^{-1} (15 s shearing at each shear rate and the viscosity was averaged over the last 3 s of each point. All experiments were conducted at a regulated temperature of 25 °C.

2.2.3 Electro-oxidation of cellulose

α-Cellulose (1 g) was suspended in 0.1 *M* carbonate buffer pH 10 (100 mL) containing 10 m*M* TEMPO (0.1562 g). The electro-oxidation was conducted using a three-electrode system in a single cell (Figure 2.17). For electro-mediated oxidation studies, an Autolab PGSTAT12 system (EcoChemie, NL) was employed with a KCl-saturated calomel (SCE) counter electrode (REF401, Radiometer, Copenhagen), and a platinum counter electrode. The working electrode was a 50×50 mm glassy carbon plate (Alfa Aesar, UK), 1/2 or 2/3 of the total electrode was immersed into the aqueous solution. Potential was controlled at 1.0 V *versus* SCE with continuous stirring (1000 rpm) for a certain period (2-3 h). The mixture was stirred at 600 rpm.

Upon completion, the reaction was quenched by adding an excess of ethanol. The white precipitates formed were washed thoroughly with water, ethanol and acetone 3 times each using sequential (re)suspension and centrifugation (Eppendorf Centrifuge 5804R, UK), at 11000 rpm and 20 °C for 10 min.

(a) (b)

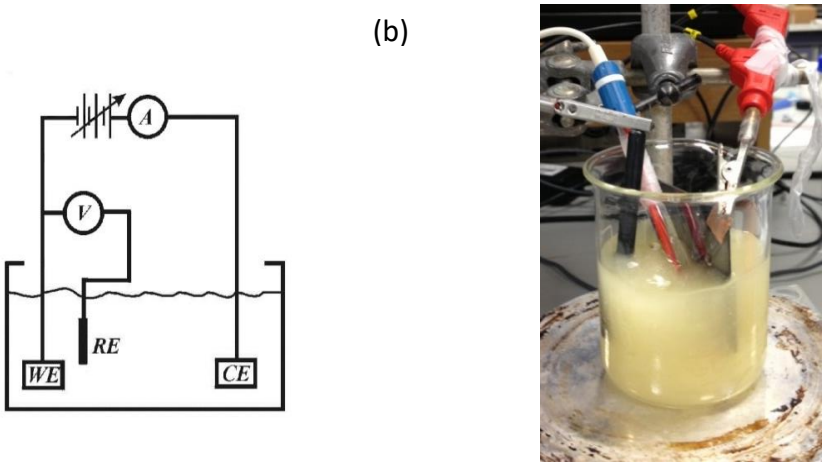

Figure 2.17 (a) Schematic model of three electrode system and (b) oxidation system set-up

2.2.4 Synthesis of MOFs / Cellulose Composites

Synthesis of MOF-199 and MOF-199 / cellulose composites: Copper acetate anhydrous (860 mg, 0.24 mmol) was mixed in 12 mL of a solvent mixture DMF:ethanol:water (1:1:1) and left overnight reacting in the presence of oxidised cellulose/bacterial cellulose (0.12 g dried sample). Then, 1,3,5-benzenetricarboxylic acid (500 mg, 0.12 mol) previously dissolved in 12 mL of the same solvent mixture was added dropwise into the previous sample (For MOF-199 synthesis, no cellulose was added in the first step) within 30 min and stirred for another 24 h.

For purification, the samples were washed subsequently with ethanol 3 times. For MOFs / oxidised cellulose composites, the washed samples were collected by centrifuge at 8000 rpm for 30min. The purified samples were then freeze-dried (composites were pressed between two porous Teflon plate) and weighed.

Synthesis of Ni-MOF: 10 mmol $Ni(NO_3)_3 \cdot 6H_2O$ (2.9g) was dissolved in 50 mL methanol and then added to 20 mmol (1.9g) KNCS. The mixture was stirred overnight and filtered to remove KCl precipitate. About 50 mL methanol was added to the filtrate to a final volume of 100 mL.

4,4'-Bipyridyl of 2 mmol (0.6248 g) was dissolved in 20 mL methanol. The prepared solution was added dropwise to 10 mL of the 0.1 M $Ni(NCS)_2$ solution and a bluish slurry was observed. The mixture was stirred at r.t. for 24 hrs, and then filtered and washed with methanol 3 times. The residue was freeze dried.

Synthesis of Ni-MOF / BC composites: 4,4'-Bipyridyl of 120 mmol (18.744 g) was dissolved in 600 mL methanol. About 200 g (99 wt% methanol retention) methanol soaked BC membrane was immersed in 300 mL of the 0.1 M $Ni(NCS)_2$ solution for a week by orbital shaker. The prepared 4,4'-Bipyridyl solution was then added dropwise to the $Ni(NCS)_2$ / BC mixture and a bluish slurry was observed. The mixture was stirred at r.t. for a week, and then washed with methanol 3 times. The membrane was freeze-dried (pressed between two porous Teflon plate) and weighed.

2.2.5 Oxidised cellulose dispersion preparation

Oxidised cellulose (2 g) was dispersed in 100 mL water and stirred for 10 min. The dispersion was then sonicated with a probe ultrasonicator (Vibracell VC300) with a tapered titanium microprobe (6.5 mm diameter) at an intensity of 10 $W \cdot cm^{-2}$ applied power determined by heat balance), alternating 1 s sonication with a 1 s standby for 4 x 15 min. Unfibrillated/partly fibrillated fractions were removed from the dispersion by centrifugation at 8000 rpm for 30 min. The dispersed fractions collected by the centrifuge were dialysed sequentially with HCl (aq), NaOH (aq) and water to remove impurities. The purified suspension was then obtained at pH *ca* 7.3.

2.2.6 Pickering emulsion preparation

The o/w emulsions were prepared using hexadecane and the oxidised cellulose suspension at the required concentration. All the emulsions were prepared using an oil/aqueous phase ratio of 30/70.

The typical procedure for emulsion preparation was: 0.3 mL of hexadecane was mixed 0.7 mL of oxidised cellulose suspension in a vial and then sonicated with an ultrasonic device (Vibracell VC300) with a 3 mm diameter tapered titanium tip at an

intensity of 17 $W \cdot cm^{-2}$ applied power, determined by heat balance), alternating 1 s sonication with a 1 s standby for 15 s.

For the preparation of the emulsions containing salts, the desired amount of the salt was premixed with oxidised cellulose suspension and then sonicated with hexadecane using the same condition described previously.

2.3 References

1. P. T. Kissinger; W. R. Heineman, *J. Chem. Educ.,* 1983, **60**, 702-706.
2. J. Heinze, *Angew. Chem. Int. Ed. Engl.,* 1984, **23**, 831-847.
3. A. J. Bard; L. R. Faulkner *Electrochemical Methods: Fundamentals and Applications*, Wiley, 2000.
4. P. Parpot; K. Servat; A. Bettencourt; H. Huser; K. Kokoh, *Cellulose,* 2010, **17**, 815-824.
5. M. T. Postek, *J. Res. Natl. Inst. Stand. Technol.,* 1994, **99**, 641-671.
6. K. Kanaya; S. Okayama, *J. Phys. D: Appl. Phys.,* 1972, **5**, 43-58.
7. J. M. Howe; B. Fultz; S. Miao, In *Characterization of Materials*, John Wiley & Sons, Inc., 2002.
8. B. Chu, *J. Chem. Educ.,* 1968, **45**, 224-230.
9. R. H. Müller; R. Schuhmann *Teilchengrößenmessung in der Laborpraxis*, Wissenschaftliche Verlagsgesellschaft mbH: Stuttgart, 1996.
10. C. M. Keck; R. H. Müller, *Int. J. Pharm.,* 2008, **355**, 150-163.
11. G. Mie, *Annalen der Physik,* 1908, **330**, 377-445.
12. H. Horvath, *J. Quant. Spectrosc. Radiat. Transfer,* 2009, **110**, 787-799.
13. P. Bowen; J. Sheng; N. Jongen, *Powder Technol.,* 2002, **128**, 256-261.
14. J. H. Masliyah; S. Bhattacharjee, In *Electrokinetic and Colloid Transport Phenomena*, John Wiley & Sons, Inc., 2005, p 105-178.
15. P. H. Wiersema; A. L. Loeb; J. T. G. Overbeek, *J. Colloid Interface Sci.,* 1966, **22**, 78-99.
16. J. W. Swan; E. M. Furst, *J. Colloid Interface Sci.,* 2012, **388**, 92-94.
17. P. Gabbott *Principles and Applications of Thermal Analysis*, Blackwell Publishing: Oxford, 2007.
18. B. E. Warren *X-Ray Diffraction*, Dover Publications: New York, 2003.
19. B. Smith *Infrared spectral interpretation : a systematic approach*, CRC: Boca Raton 1999.
20. D. S. Sivia *Elementary Scattering Theory: For X-ray and Neutron Users*, OUP Oxford, 2011.
21. O. Glatter; O. Kratky *Small Angle X-ray Scattering*, Academic Press, 1982.
22. M. J. Hollamby, *PCCP,* 2013, **15**, 10566-10579.
23. K. S. W. Sing, et al., In *Handbook of Heterogeneous Catalysis*, Wiley-VCH Verlag GmbH & Co. KGaA, 2008.
24. S. Storck; H. Bretinger; W. F. Maier, *Applied Catalysis A: General,* 1998, **174**, 137-146.
25. S. Brunauer; P. H. Emmett; E. Teller, *J. Am. Chem. Soc.,* 1938, **60**, 309-319.
26. N. Isobe; U.-J. Kim; S. Kimura; M. Wada; S. Kuga, *J. Colloid Interface Sci.,* 2011, **359**, 194-201.
27. H. A. Barnes; J. F. Hutton; K. Walters *An Introduction to Rheology*, Elsevier, 1989.
28. R. J. Crawford; K. J. Edler; S. Lindhoud; J. L. Scott; G. Unali, *Green Chem.,* 2012, **14**, 300-303.
29. S. Shariki; S. E. C. Dale; F. Marken, *Electroanalysis,* 2011, **23**, 2149-2155.
30. R. Shinoda; T. Saito; Y. Okita; A. Isogai, *Biomacromolecules,* 2012, **13**, 842-849.

31. K. G. McLaren, *The International Journal of Applied Radiation and Isotopes,* 1978, **29**, 631-635.
32. J. S. Moulthrop; R. P. Swatloski; G. Moyna; R. D. Rogers, *Chem. Commun.,* 2005, 1557-1559.
33. D. Yang; V. Kumar, *Carbohydr. Polym.,* 2012, **90**, 1486-1493.
34. F. Jiang; Y.-L. Hsieh, *Carbohydr. Polym.,* 2013, **95**, 32-40.
35. J. I. Langford; A. J. C. Wilson, *J. Appl. Crystallogr.,* 1978, **11**, 102-113.
36. C. Lee, et al., Springer Berlin Heidelberg, 2015, p 1-17.
37. B. E. Warren *X-ray Diffraction*, Courier Corporation, 1969.
38. S. Park; J. O. Baker; M. E. Himmel; P. A. Parilla; D. K. Johnson, *Biotechnology for Biofuels,* 2010, **3**, 1-10.
39. N. Masruchin; B. D. Park; V. Causin; I. C. Um, *Cellulose,* 2015, **22**, 1993-2010.
40. L. Segal; J. J. Creely; A. E. Martin; C. M. Conrad, *Text. Res. J.,* 1959, **29**, 786-794.
41. A. Thygesen; J. Oddershede; H. Lilholt; A. B. Thomsen; K. Ståhl, *Cellulose,* 2005, **12**, 563-576.
42. L. B. McCusker; R. B. Von Dreele; D. E. Cox; D. Louer; P. Scardi, *J. Appl. Crystallogr.,* 1999, **32**, 36-50.
43. S. Eyley, et al., *Nanoscale,* 2015, **7**, 14413-14421.
44. A. Thygesen; J. Oddershede; H. Lilholt; A. B. Thomsen; K. Ståhl, *Cellulose,* 2005, **12**, 563-576.
45. Y. Nishiyama; J. Sugiyama; H. Chanzy; P. Langan, *J. Am. Chem. Soc.,* 2003, **125**, 14300-14306.
46. Y. Nishiyama; P. Langan; H. Chanzy, *J. Am. Chem. Soc.,* 2002, **124**, 9074-9082.
47. P. Langan; Y. Nishiyama; H. Chanzy, *Biomacromolecules,* 2001, **2**, 410-416.
48. S. S.-Y. Chui; S. M.-F. Lo; J. P. H. Charmant; A. G. Orpen; I. D. Williams, *Science,* 1999, **283**, 1148-1150.
49. Y. Zhang; L. Jianmin; D. Wei; M. Nishiura; T. Imamoto, *Chem. Lett.,* 1999, **28**, 195-196.
50. W. Pabst; E. Gregorova, *ICT Prague,* 2007, **2007**.
51. P. Atkins; J. De Paula *Physical Chemistry*, Oxford University Press, 2006.
52. J. Lake, *Acta Crystallogr.,* 1967, **23**, 191-194.
53. R. K. Heenan, et al., *Neutron News,* 2011, **22**, 19-21.
54. A. Paul, et al., *Soft Matter,* 2010, **6**, 2552-2556.
55. G. Cheng, et al., *Biomacromolecules,* 2011, **12**, 2216-2224.
56. P. Bartlett; R. H. Ottewill, *J. Phys. Chem.,* 1992, **96**, 3306-3318.
57. S. Kline, *J. Appl. Crystallogr.,* 2006, **39**, 895-900.
58. M. Kotlarchyk; R. B. Stephens; J. S. Huang, *J. Phys. Chem.,* 1988, **92**, 1533-1538.

Chapter 3 Voltammetry Study of TEMPO Mediated Oxidation of Cellulose

3.1 Introduction

Oxidized cellulose, one of the cellulose derivatives, has the characteristics of biocompatibility, biodegradability, environmental friendliness and non-toxicity.[1,2] Oxidized cellulose has been used as a carrier in drug delivery and as a hemostat to stem bleeding in open wounds.[3,4] In addition, selective oxidation of cellulose is an effective method to produce distinctive new products and intermediates. Cellulose partially oxidised at the C2, C3 and/or C6 position (Chart 3.1) could be used as a fluorescent agent,[5] an ion exchange resin in chromatography,[6] in medical treatments,[7] reinforcement[8] and as an organic template to stably fabricate metallic nanoparticles.[9] Hence, studies on the 'green' synthesis of partially oxidized cellulose and its applications are becoming the academic frontier of cellulose studies.

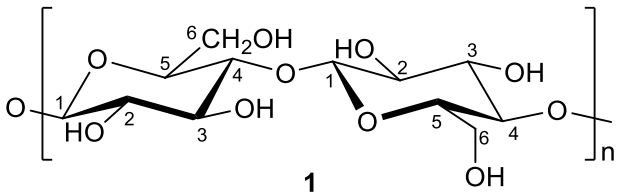

1

Chart 3.1 Structure of cellulose

TEMPO was first adopted in the TEMPO/NaBr/NaClO system to selectively oxidize soluble polysaccharides by de Nooy *et al* in 1995.[10] Later on, the TEMPO/NaBr/NaClO system and TEMPO/NaClO/$NaClO_2$ system were applied to the oxidation of water-insoluble cellulose at the C6 position under alkali conditions and acid-neutral conditions respectively.[11-16] However, depolymerisation of cellulose was unavoidable during the TEMPO mediated oxidation using chlorine-containing chemicals.[17]

An alternative approach to obtain C6-oxidized cellulose is by electrochemical oxidation, where TEMPO is continuously oxidized to the corresponding *N*-oxoammonium ion at the anode at suitable potential.[18] In the electrochemistry system, cellulose is oxidized by the direct electron transfer rather than via a chemical

oxidant such as NaClO, or $NaClO_2$. Direct transfer of electrons is considered as a sustainable route, and may also prevent cellulose depolymerisation and other possible side reactions (e.g. promoting the stability of the catalyst over time).[17,19] The existing electrochemical method of cellulose oxidation requires relatively large amounts of TEMPO and also takes a considerable amount of time for the completion of the reaction (more than 10 hours) compared to chemical oxidation (less than 2 hours) using chlorine-based oxidants,[20] which is not desirable for the evaluation of mediators on a small scale or for optimisation of reaction conditions (largely due to the need for titrimetric analytical methods to discern the degree of oxidation).

In this study, therefore, the aim was to develop a cotton modified electrode for rapid screening of mediators and optimisation of reaction conditions. TEMPO (R=H), 4-acetamido-TEMPO ($R=NHCOCH_3$), 4-methoxy-TEMPO ($R=OCH_3$), 4-carboxy-TEMPO (R=COOH) and 4-hydroxy-TEMPO (R=OH) were used here as typical mediators for evaluation (Chart 3.2). Buffer and pH were also taken as variables to investigate the impact on the reaction.

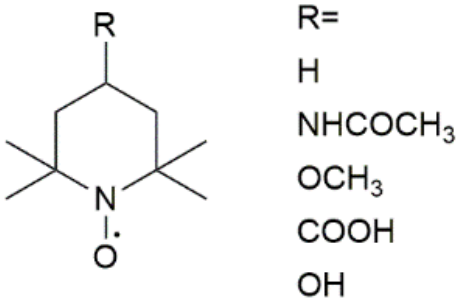

Chart 3.2 TEMPO-derivatives used in the experiment

3.2 Results and discussion

3.2.1 Fabric Voltammetry I: Reaction of TEMPO with Cellulose

Initial studies were carried out at pH 10 in aqueous carbonate buffer solution (CBS) to explore the reactivity of TEMPO with cellulose (cotton fabric with ca. 270 µm thickness) immobilised at the electrode surface. Comparison of cyclic voltammetry

traces of CBS alone, cotton fabric in CBS, TEMPO in CBS and cotton fabric in CBS with TEMPO, Figure 3.1a, revealed that the oxidation of a substrate (green curve) was readily distinguished from reversible oxidation/reduction of TEMPO alone (blue curve). The diminution of the cathode current peak in the presence of cotton and mediator was a result of reaction of the TEMPO oxoammonium cation ($TEMPO^{+}$) with cellulose, i.e. chemical rather than electrochemical reduction of $TEMPO^{+}$. A significant increase in measured current resulted from the rapid diffusion of the reduced TEMPO back to the surface of the working electrode in the confined region between the cotton and electrode interface. Indeed, it was important to ensure that the cotton was held in close proximity to the working electrode to avoid elevated noise in the measurements.

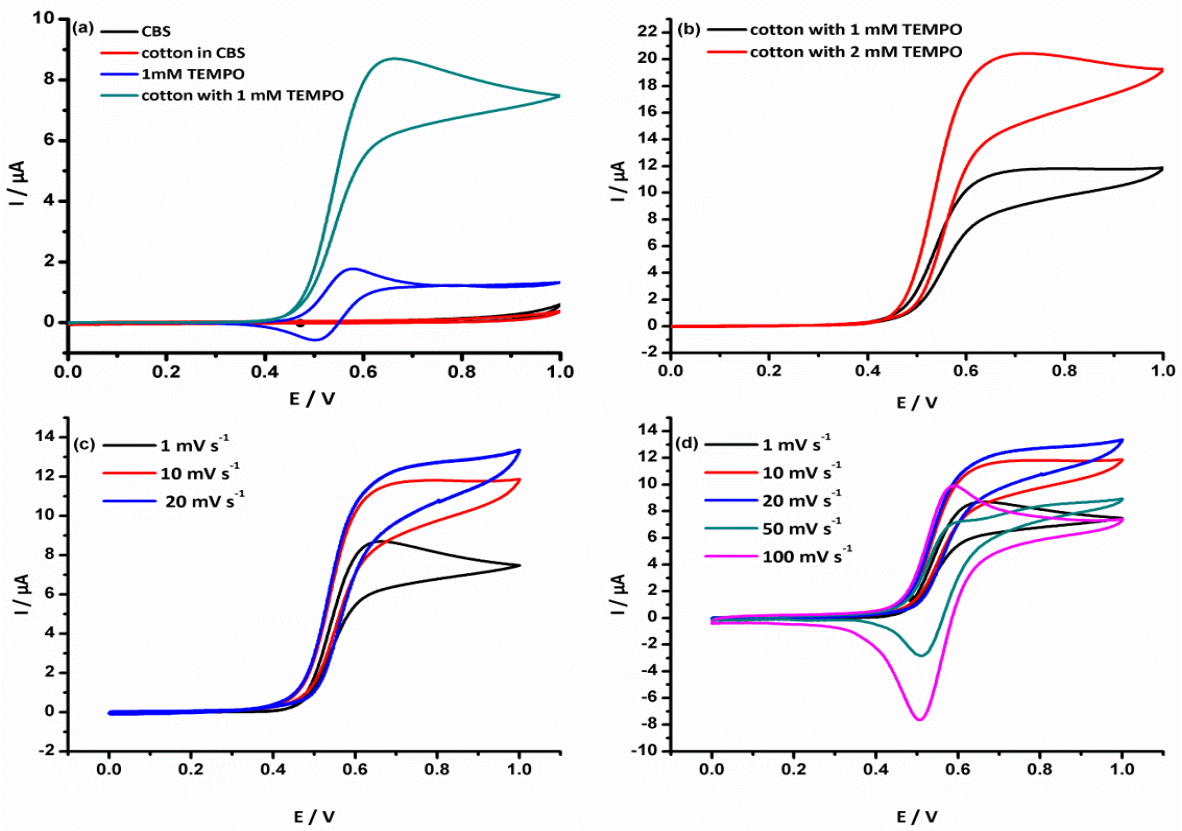

Figure 3.1 Cyclic voltammograms of (a) CBS, cotton with CBS, 1 m*M* TEMPO and cotton with 1 m*M* TEMPO at pH 10; potential scan rate 1 $mV{\cdot}s^{-1}$; (b) cotton with 1 m*M* and 2 m*M* TEMPO in CBS pH 10, potential scan rate 10 $mV{\cdot}s^{-1}$; (c) cotton with 1 m*M* TEMPO in CBS pH 10 at potential scan rates of 1 $mV{\cdot}s^{-1}$, 10 $mV{\cdot}s^{-1}$ and 20 $mV{\cdot}s^{-1}$; (d) cotton with 1 m*M* TEMPO in CBS pH 10, at potential scan rate of 1 $mV{\cdot}s^{-1}$, 10 $mV{\cdot}s^{-1}$, 20 $mV{\cdot}s^{-1}$, 50 $mV{\cdot}s^{-1}$ and 100 $mV{\cdot}s^{-1}$.

Doubling the mediator concentration resulted in an approximate doubling of the anodic current peak (Figure 3.1b), suggesting that the rate of oxidation of cellulose by TEMPO is proportional to the TEMPO concentration, in accordance with previous results for both cellulose[21] and methyl α-D-glucopyranoside.[10] Therefore, the reaction could be accelerated by increasing the concentration of mediator.

The effect of altered scan rate on voltammetric response provided a means of probing the transport processes and rate of chemical reaction. The measured current is a function of rate of reduction of $TEMPO^+$ upon reaction with cellulose and rate of diffusion of TEMPO to and from the electrode surface (and to and from the cellulose surface). Thus, a change in measured current could signify:

1. a change in the binding of $TEMPO^+$ to the cellulose surface (or release of TEMPOH from the surface);
2. a change in rate of the chemical oxidation reaction; or
3. a change in the rate of transport of $TEMPO^+$, TEMPO and/or TEMPOH through the electrolyte.

Together these processes (binding, chemical reaction, release) comprise the effectiveness of oxidation of cellulose by a given mediator. (The reasonable assumption was made that, water-soluble small-molecule mediators bearing the same charge exhibited similar rates of diffusion in water.) An increase in scan rate from 1 to 10 $mV \cdot s^{-1}$ resulted in a significant increase in measured current, but a further increase to 20 $mV \cdot s^{-1}$ had less effect (Figure 3.1c). Moreover, further increase in scan rate resulted in appearance of a reduction peak, until, at 100 $mV \cdot s^{-1}$, the shape of the reversible TEMPO voltammogram is recovered (purple curve, Figure 3.1 (d)), suggesting that the chemical reaction between $TEMPO^+$ and cellulose no longer serves to remove $TEMPO^+$ in an irreversible chemical reaction process, on the timescale of a single cycle. In other words, the reaction was slow compared to scan rate, either because it is limited by the rate of diffusion of $TEMPO^+$, or by the binding and chemical reaction with cellulose of $TEMPO^+$.

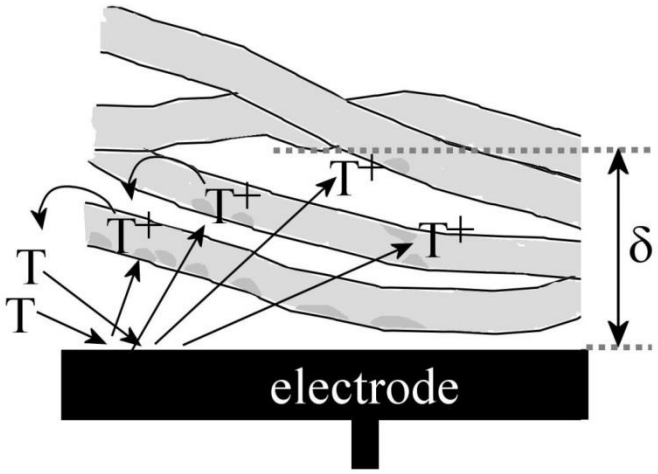

Figure 3.2 Schematic drawing of mediator generation and reaction in the cotton fabric with diffusion layer thickness δ.

The rate constant of the chemical reaction between TEMPO+ and cellulose could be quantified by comparing the diffusion layer thickness δ_{diff} and the reaction layer thickness δ_{react} using dimensionless analysis (the method to identify the relationships between different physical variables by their dimensions).

$$\delta_{diff} = \sqrt{(DRT)/(vF)} \quad \textbf{(3.1)}$$

$$\delta_{react} = D/k \quad \textbf{(3.2)}$$

Where D is diffusion coefficient in $m^2 \cdot s^{-1}$, k is reaction rate constant in $m \cdot s^{-1}$ (the units result from the definition of surface reaction rate $r = k \times c$ in $mol \cdot m^{-2} \cdot s^{-1}$, where c is the concentration of redox species in $mol \cdot m^{-3}$),[22] v is scan rate in $V \cdot s^{-1}$, R is gas constant (8.314) in $J \cdot K^{-1} \cdot mol^{-1}$, T is absolute temperature in K, F is the Faraday constant (96485) in $C \cdot mol^{-1}$. At room temperature (25 °C), RT/F can be treated as a constant in unit V.

Two limiting cases had to be considered with:

(i) Very fast scan rates where the diffusion layer thickness δ_{diff} (Figure 3.2) was too small to allow interaction with the cellulose. The smallest diffusion layer thickness was set as 4 μm, taking into consideration the possible gap between the working electrode and the cotton fabric.

From Equation 3.1, the higher limit for scan rate can be estimated as $v_{upper} < 1$ V·s^{-1}.

(ii) Very slow scan rates where the diffusion layer thickness extended beyond the fabric into solution (with δ = 270 µm, the lower limit for scan rate can be estimated as $v_{lower} > 10$ mV·s^{-1}).

Within this range of the upper and lower limits of the scan rates the competition of diffusion and reaction at the cellulose surface allowed the apparent rate constant $k_{cellulose}$ to be estimated from the change arising from changes in the transition scan rate v_{trans} for chemically irreversible to reversible voltammetric features.

For data in Figure 3.1(d) this occurred at ca. v_{trans} = 50 mV·s^{-1}, which suggested that $k_{cellulose}$ under these conditions was $k_{cellulose} = \sqrt{(Dv_{trans}F)/(RT)}$ = 4 × 10^{-5} m·s^{-1} (from Equation 3.1 and Equation 3.2, when $\delta_{diff} = \delta_{react}$). This value had to be regarded as an estimate due to the reaction front gradually moving into the cellulose fibres and thereby slowing down the apparent rate constant.

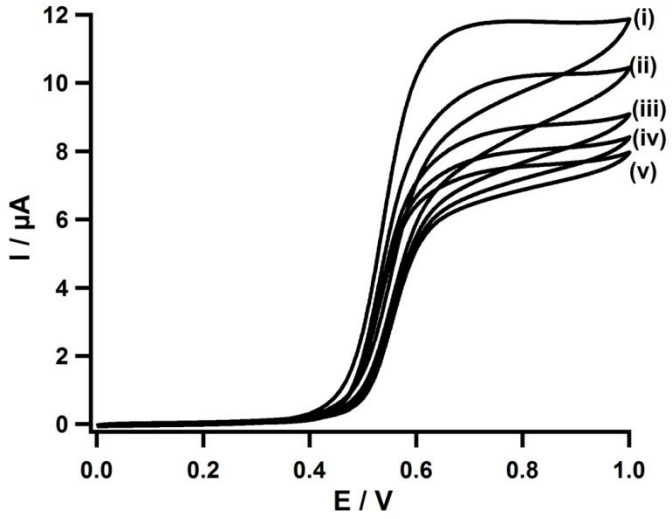

Figure 3.3 Cyclic voltammograms of first (i), second (ii), third (iii), fourth (iv) and fifth (v) cycle of cotton with 1 mM TEMPO in CBS pH10 ; potential scan rate 10mV·s^{-1}.

In Figure 3.3, the peak current decreased significantly with the increasing number of scanning cycles, showing that the chemical reaction rate slowed down over time, either due to the decreased amount of original cellulose over time (exposed primary hydroxyl groups on cellulose being consumed in the previous cycle), or due to the

reduced mobility of the $TEMPO^+$ which had interacted/neutralised with the negatively charged carboxylates formed on the cotton. Once an electron is withdrawn from TEMPO at the working electrode (electrons move towards the counter electrode), the diffusion of $TEMPO^+$ through the negatively charged cotton cloth could be reduced due to electrostatic interactions between $TEMPO^+$ ions and the cotton surface, thus reducing the measured rate of reaction (it may also shift the peak position, but the position of the peak is not distinguishable from the graph).

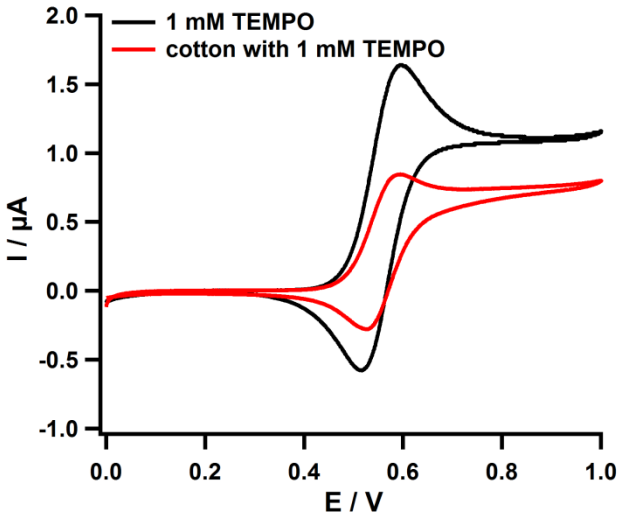

Figure 3.4 Cyclic voltammograms of 1 m*M* TEMPO (red) and cotton with 1m*M* TEMPO (black); in ABS pH 4, potential scan rate 1 $mV \cdot s^{-1}$.

The effect of change of pH on the reaction was quite marked: while the cyclic voltammagram of TEMPO was unaltered, the voltammetric response in the presence of the cotton fabric was attenuated, shown in Figure 3.4. More importantly, there was no evidence of the chemical reaction and it appeared that the cotton acted only to either absorb TEMPO/TEMPO+, or to block the diffusion of TEMPO/TEMPO+ between the bulk solution and the electrode. This presented the possibility of quick and easy scanning across a range of pHs with the aim of maximising reactivity, or, indeed, to select a mediator for use at a specific pH. Details of the pH scanning are discussed in section 3.2.3.

3.2.2 Characterisation

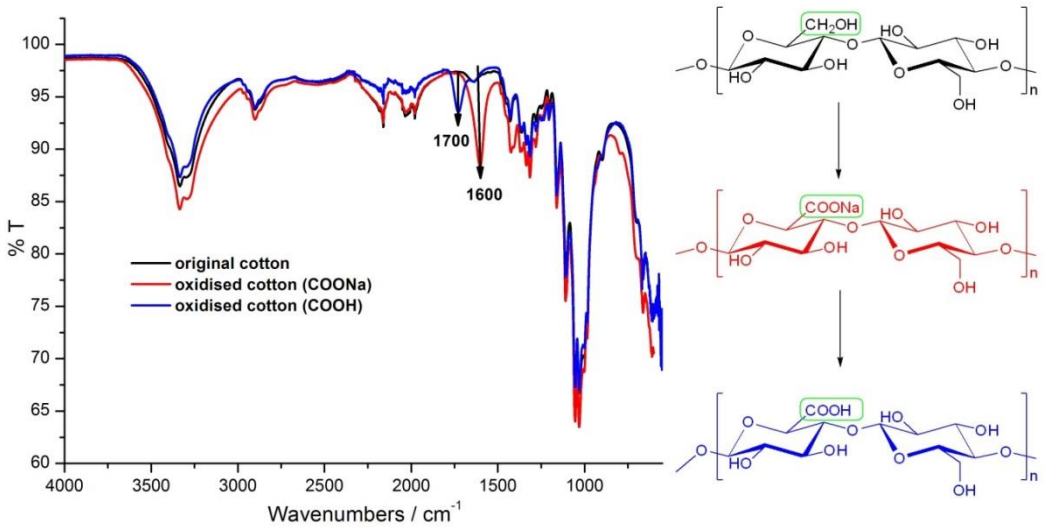

Figure 3.5 FT-IR spectra of cotton starting material (black) and cotton oxidised by TEMPO using multiple electrochemical cycles.

Evidence for the bulk-oxidation of the cotton fabric is obtained from ATR-FTIR (Figure 3.5, see peaks at 1600 or 1700 cm^{-1} corresponding to the stretching of COONa and COOH, which are in agreement with values previously reported[23]) for cotton discs removed from the electrode surface after electrochemical oxidation. Other signals may also be assigned: the broad band at 3500-3000 cm^{-1} was attributed to O-H stretching vibrations (although care must be taken to ensure that samples are rigorously dry if any significance is to be attributed to either intensity or position, due to overlap with water signals in this region); signals due to C-H stretching occurred at *ca* 2900 cm^{-1} and the band around 1400 cm^{-1} was ascribed to C-H bending vibrations. The signal observed at *ca* 1100 cm^{-1} was due to C-O stretching vibrations. In the FTIR spectra, the most significant change between the non-oxidized cotton and oxidized cotton was the appearance of the carboxyl groups (C=O) stretching band at around 1650 cm^{-1} corresponding to sodium carboxylate groups (COONa) and carboxyl groups (COOH), while the band was relatively small in the spectra of original cotton. The formation of carboxylate groups was therefore evidenced by the increase of transmittance at about 1600 cm^{-1}.

3.2.3 Fabric Voltammetry II: Comparison of TEMPO Derivatives

The effect of inclusion of various substituents at the 4 position of TEMPO (Chart 3.2) at pH 10 was compared (Figure 3.6). Mediator 4-hydroxy-TEMPO was not used because it was unstable at high pH. As expected from the results of chemical oxidation,[24] TEMPO, exhibited a higher reactivity towards cellulose at pH 10 than its substituted analogues. The sequence in reversible potentials was TEMPO < 4-carboxy-TEMPO < 4-methoxy-TEMPO < 4-acetamido-TEMPO consistent with the electron withdrawing nature of the hetero-atom substituents. Interestingly, the mildest oxidant, TEMPO, was also found to give the fastest oxidation reaction, possibly due to penetration speed of the mediator into the cellulose fibres (the diffusion coefficient of TEMPO $D = 6.1\times10^{-6}\,cm^2\cdot s^{-1}$ at pH 10 was higher than other mediators, the value was close to the literature value[25]). The detailed calculation of the diffusion coefficient of TEMPO is shown later in this section.

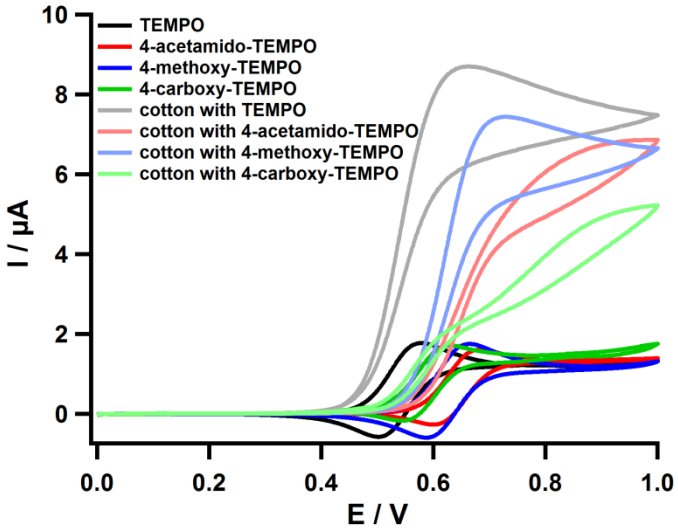

7

Figure 3.6 Cyclic voltammogram of mediators TEMPO, 4-acetamido-TEMPO, 4-methoxy-TEMPO and 4-carboxy-TEMPO (1 m*M*) without and with cotton in CBS pH 10; scan rate 1 $mV\cdot s^{-1}$.

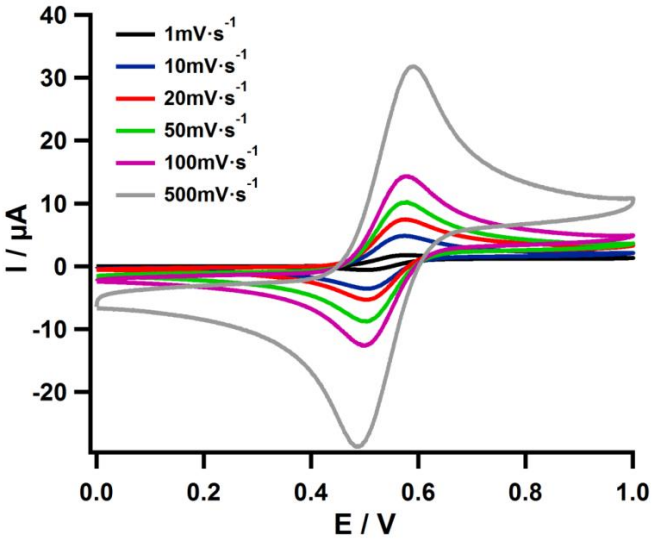

Figure 3.7 Cyclic voltammograms of 1 m*M* TEMPO in CBS pH 10, at potential scan rates of 1 mV·s^{-1}, 10 mV·s^{-1}, 20 mV·s^{-1}, 50 mV·s^{-1}, 100 mV·s^{-1} and 500 mV·s^{-1}.

Figure 3.7 shows the reversible redox reaction of TEMPO on the electrode, where the peak current can be described by the Randles-Sevcik equation (Equation 3.3).

$$i_p = 0.4463FA\left[\frac{F}{RT}\right]^{1/2} c^* D^{1/2} v^{1/2} \quad \textbf{(3.3)}$$

The diffusion coefficient D can be derived from the equation by plotting the values of $i_{p,a}$ (anodic current) and $i_{p,c}$ (cathodic current) over the square root of each scan rate ($v^{1/2}$) . The plotted data and the fitting curves are shown in Figure 3.8. The diffusion coefficient could be retrieved from the average value of the slope obtained from the fitted lines. Similarly, diffusion coefficients of other mediators can be calculated and compared (results pertaining to other mediators can be found in appendices).

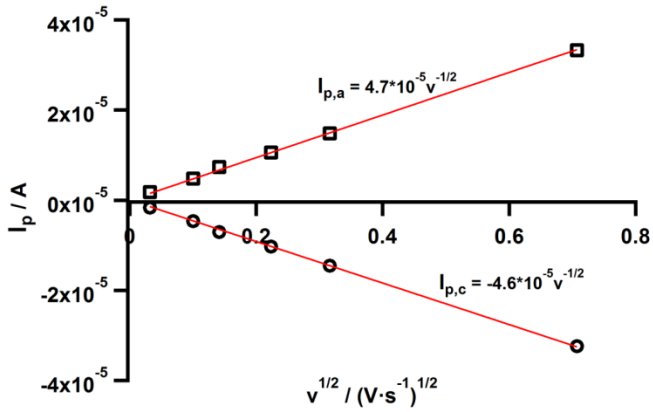

Figure 3.8 Plot of peak current over square root of scan rate; red lines represented the fitted straight lines.

The effect of inclusion of various substituents at the 4 position of TEMPO (Chart 3.2) at pH 7 was compared (Figure 3.9). Contrary to the result at pH 10, 4-acetamido-TEMPO, exhibited a higher reactivity towards cellulose than other mediators. In addition, the current of all the catalytic curves was lower compared to the reaction at pH 10, indicating that the reaction was much slower at neutral pH. This phenomenon was consistent with the results of chemical oxidation at neutral pH.[16] TEMPO, with the larger value of diffusion coefficient compared with 4-acetamido-TEMPO, was not the most effective catalyst. The reason behind this is not yet fully understood. It has been briefly discussed later in the chapter.

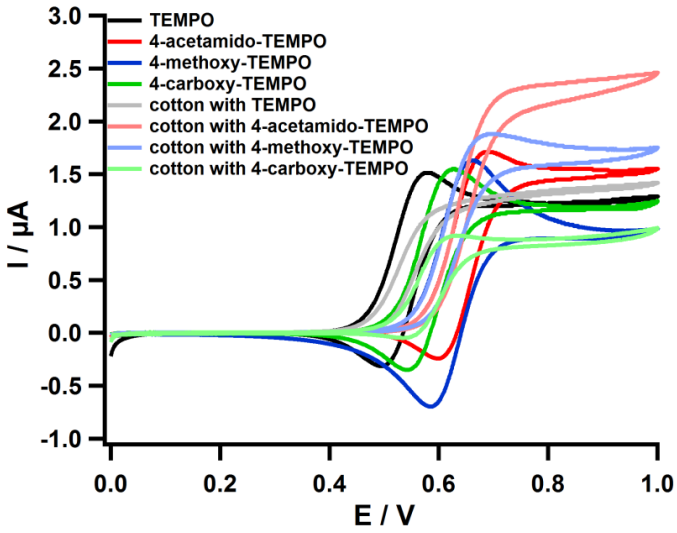

Figure 3.9 Cyclic voltammogram of mediators TEMPO, 4-acetamido-TEMPO, 4-methoxy-TEMPO and 4-carboxy-TEMPO (1 m*M*) without and with cotton in PBS pH 7; scan rate 1 mV·s^{-1}.

3.2.4 Fabric Voltammetry III: Optimisation of pH and Buffer

To allow comparison of the efficiency of cellulose oxidation by TEMPO derivatives (Chart 3.2), the ratio I_{cat}/I_{lim} was defined, where I_{cat} was the anodic peak catalytic current measured in the presence of the cotton and *N*-oxyl mediator and I_{lim} was the limiting current of the diffusion controlled anodic peak in the presence of the *N*-oxyl mediator alone. I_{lim} was determined by the peak current in the presence of cotton and TEMPO derivatives (Chart 3.2) at pH 4 (scan rate 1mV·s^{-1}), where no reaction with cotton was noted on the time scale of the voltammetric scan (Figure 3.4). This was required as the presence of the cotton, in close contact with the working electrode, resulted in attenuation of the measured current by blocking diffusion of *N*-oxyl mediator from the bulk solution.

In agreement with previous reports, all TEMPO derivatives tested exhibited a higher rate of reaction with cotton at elevated pH and all became significantly less effective as pH dropped (Figure 3.10). Mediator 4-acetamido-TEMPO retained higher activity at lower pH than either TEMPO or 4-methoxy-TEMPO, in accordance with previous reports of chemical oxidation.[12,16]

The method can be used to screen different mediators over a range of pH, allowing comparison of the catalytic efficiency. Thus, the optimum pH for a particular mediator can be easily identified.

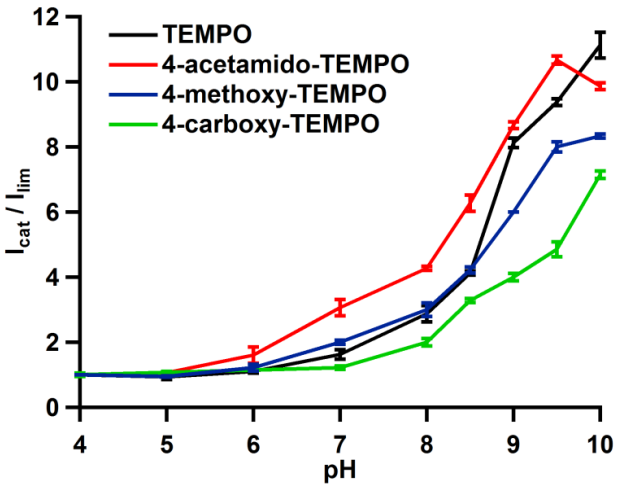

Figure 3.10 Influence of pH on efficiency of *N*-oxoammonium oxidation of cotton by electro-oxidised TEMPO (black), 4-acetamido-TEMPO (red), 4-methoxy-TEMPO (blue) and 4-carboxy-

TEMPO (green). (Lines joining points serve only to guide the eye; error bar is the standard deviation of three measurements)

The rate of oxidation of cotton did not increase monotonously with increase in pH, in accordance with the two distinctive reaction mechanisms described to occur under different pH regimes. Under basic conditions the rate of formation of the complex and subsequent elimination via a cyclic transition state are similar, while, under acidic conditions, intermolecular abstraction of the α-hydrogen atom becomes rate limiting, Scheme 3.1.[26,27] Therefore, TEMPO was found to be the most effective mediator at alkali pH due to its fast diffusion to cellulose to form the complex.

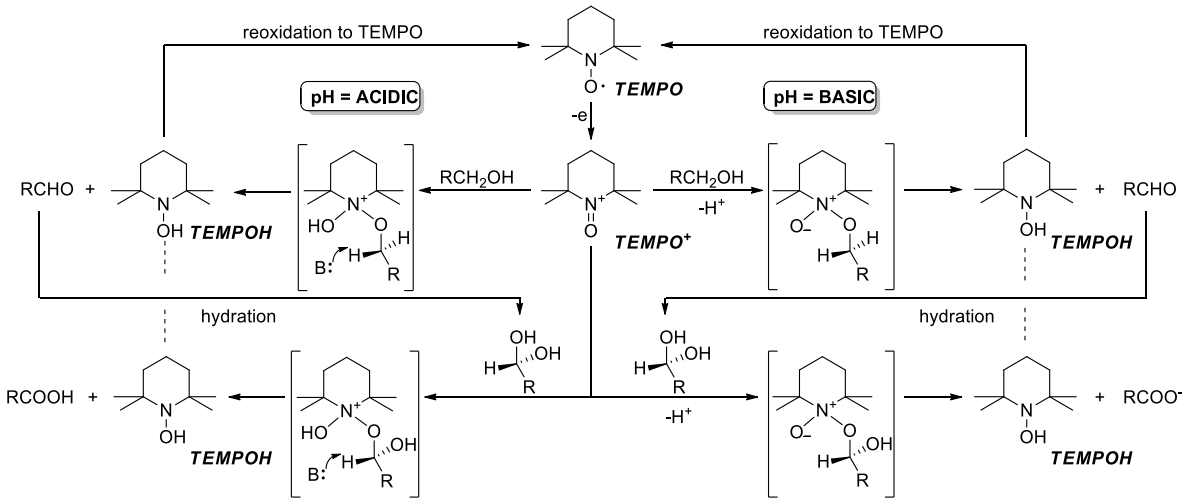

Scheme 3.1 TEMPO catalysed oxidation of primary alcohols under different pH regimes. The oxoammonium cation ($TEMPO^+$) formed by 1 electron oxidation of the *N*-oxyl radical, under basic conditions, is attacked at nitrogen by an alkoxide derived from the primary alcohol, leading to reversible formation of an oxoammonium/alkoxide complex (supported computationally[28]), followed by oxidation of the alcohol, releasing the reduced hydroxylamine form of TEMPO (TEMPOH). Under acidic conditions the accepted mechanism[27] entails proton abstraction from the complex cation by a base (the $TEMPO^+$ counterion, or a buffer component).

Further effects of increase in acidity could include: suppression of alkoxide formation that must precede (or occur with) complex formation; the effect of the counterion, which would also be the base effecting α-proton abstraction; and protonation of species derived from TEMPO at various points in the catalytic cycle. The counterion effect is further described below and protonation of TEMPOH will also serve to slow the reaction, Scheme 3.2.

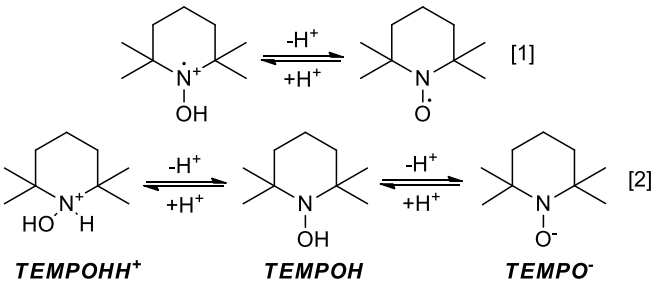

Scheme 3.2 Protonation of various species in the catalytic cycle of TEMPO like mediators, depicted for TEMPO. The protonated radical, eqn. 1, need not be considered (*pKa* = -5.8[29]), but $TEMPOHH^+$ (*pKa* = 6.9-7.5[30]), eqn. 2, serves to decrease the concentration of TEMPOH available for reoxidation, potentially slowing turnover under acidic conditions. Deprotonation of TEMPOH to $TEMPO^-$ is likely to require very strongly basic conditions (pKa assumed to be similar to H_2NOH = 13.7[30]).

The appreciable increase in rate of oxidation of TEMPO with cotton at *ca* pH 7 (Figure 3.10) agreed with a *pKa* of close to 7 for the protonated form, $TEMPOHH^+$ of TEMPOH and was in accordance with the effect noted by Israeli *et al*. in a study of comproportionation of TEMPO and 4-carboxy-TEMPO.[30] Hence, the protonated mediator was removed from the oxidation cycle so reducing the concentration of the active mediator for the reaction at low pH. The sequence of the pKa for the mediators used in this study was estimated to be 4-acetamido-TEMPO ≈ 4-methoxy-TEMPO < TEMPO < 4-carboxy-TEMPO,[31] in agreement with the catalytic trend at low pH. This correlation is useful to design new mediator reacted under neutral or acidic conditions.

In these electrochemical reactions pH is controlled by an appropriate buffer, but the buffer may not be innocuous in the reaction, particularly at acid pH where a base is implicated in proton abstraction from the intermediate complex (Scheme 3.1). To test the hypothesis, the identity of the buffer was changed from phosphate to citrate with the same concentration, at pH 7 with 4-acetamido-TEMPO as the mediator. This resulted in a decrease in efficiency of oxidation of cotton, with the change of buffers from phosphate to citrate buffer (Figure 3.11a). Similarly, doubling the concentration of the phosphate buffer also decreased the efficiency of 4-acetamido-TEMPO oxidation of cotton (Figure 3.11b), indicating that the buffer was participating in the oxidation reaction. In a multicomponent system all interactions must be considered,

including: cellulose/buffer, 4-acetamido-TEMPO$^+$/buffer, and 4-acetamido-TEMPO$^+$/cellulose. Although adsorption of positively charged moieties onto non-modified cellulose surfaces in aqueous solutions is known[32], binding between cellulose and buffer anions, in competition with 4-acetamido-TEMPO$^+$/cellulose interactions, is unlikely to lead to the observed reduction in current on increase in buffer concentration as strong electrostatic interactions are absent (cellulose starting material bears a negative surface charge which increases with oxidation[14]). In addition, the buffers, at 0.1 *M* concentration, were present in >100 times of molar excess relative to anhydroglucose units (50 mL buffer containing 5 mmol of salt anion to <0.005 g cotton containing <3 x10^{-2} mmol anhydroglucose units), thus any surface sorption sites would be saturated and doubling of concentration would be expected to have little effect. In contrast, interactions between 4-acetamido-TEMPO$^+$ and buffer anions are enhanced by electrostatic attraction and thus it is suggested that competitive binding between 4-acetamido-TEMPO$^+$ and buffer anions leads to the observed decrease in current, reflecting a decreased reaction rate.

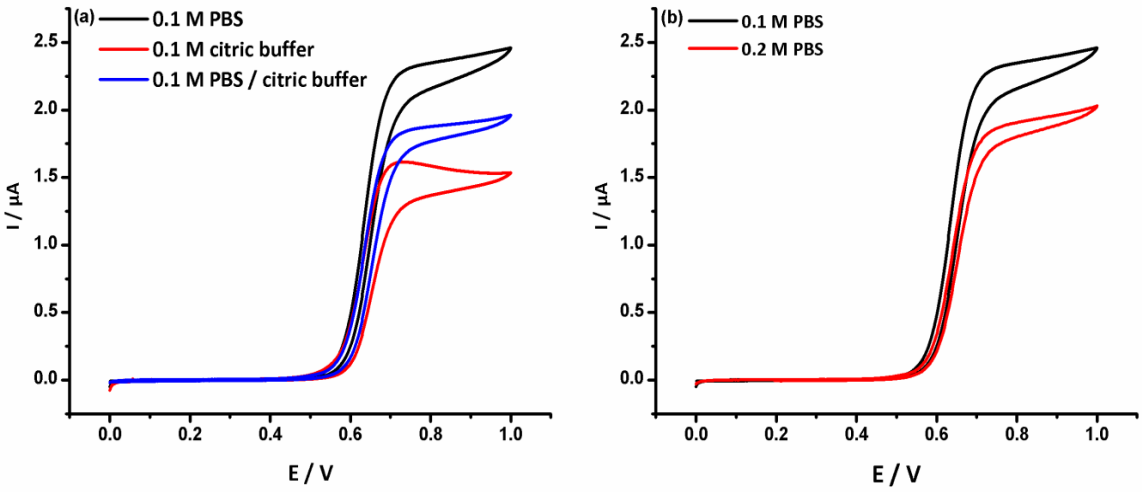

Figure 3.11 Cyclic voltammograms of cotton with 1 m*M* 4-acetamido-TEMPO in (a) 0.1 *M* phosphate buffer pH 7 (black), 0.1 *M* citrate buffer (red) and in phosphate/citrate mixed buffer pH 7 (blue); potential scan rate 1 mV·s^{-1}; (b) 0.1 *M* (black) and in 0.2 *M* phosphate buffer (red), pH 7, potential scan rate 1 mV·s^{-1}.

To investigate the buffer effect in more detail, phosphate buffer with different cations was tested. As expected, the change from potassium to sodium did not influence the catalytic activity of TEMPO significantly under the experimental conditions (Figure

3.12). The effect of buffer anions was tested by comparing the rate of oxidation in the presence of various sodium salts at pH7 (Figure 3.13)

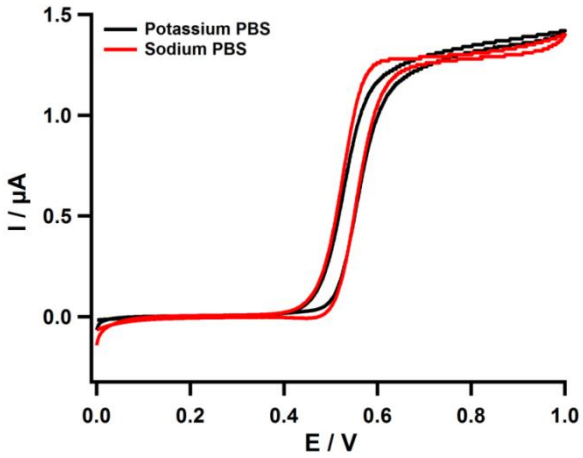

Figure 3.12 Cyclic voltammograms of cotton with 1 m*M* TEMPO in potassium phosphate buffer pH 7 (black) and in sodium phosphate buffer pH 7 (red); potential scan rate 1 mV·s^{-1}.

Having noted that the buffer anions had an impact on the oxidation reaction, the effect of addition of different anions was tested using a range of sodium salts at pH 7 and pH 10. The difference in the current of the selected salt solutions suggested that the anion effect had a significant influence on the reaction rate under neutral conditions (Figure 3.13). The potential window of $NaBr$ was controlled at 0-0.8 V to avoid the oxidation of Br^- to BrO^- (tested experimentally). The fact that the catalytic efficiency was the highest with Na_2SO_4 suggested that the anion effect was not solely a charge effect, as the measured current should be the lowest if the effect was only due to electrostatic effects (although delocalisation of the sulfate anion reduces the negative charge on the oxygen atom, sulfate still had the highest surface charge density amongst the selected anions[33]). A cathode current was observed for the $NaNO_3$ solution, suggesting that some of the 4-acetamido-TEMPO$^+$ generated did not participate in the oxidation reaction on the time scale investigated. This result was in agreement with the prevailing mechanism under neutral/acid environments (anions could affect the reaction rate, Scheme 3.1), and the same effect has been also reported in the use of oxoammonium salts with different anions (Cl^- and Br^-) for alcohol oxidation.[34] Interestingly, the current was observed to follow the Hofmeister Series (the hydration of anions in aqueous solutions, $SO_4^{2-} > Cl^- >$

$Br^- > NO_3^-$),[35] where the catalytic efficiency increased with more hydrated anions. As anions became more hydrated, the effective surface charge density of the hydrated anions would decrease and radius of the hydrated anions would increase, due to the association with more water molecules.[36] Both the decrease in effective surface charge density and the increase in size would reduce the binding of anions with 4-acetamido-TEMPO$^+$, resulting in a higher catalytic efficiency.

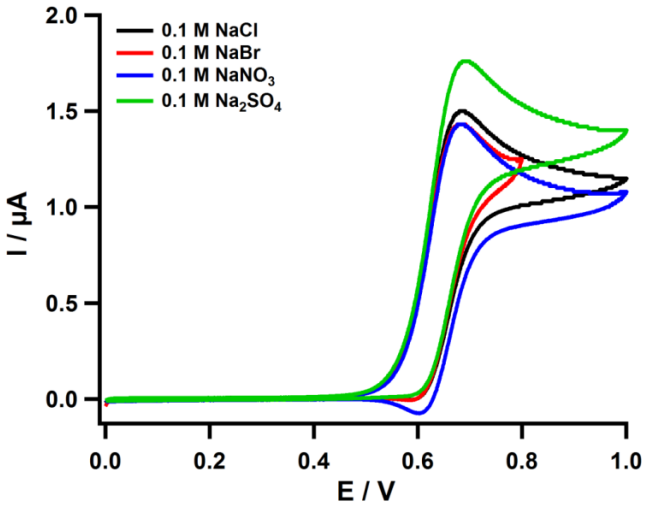

Figure 3.13 Cyclic voltammograms of cotton with 1 m*M* 4-acetamido-TEMPO in different salt solution at pH 7; potential scan rate 1 mV·s^{-1}.

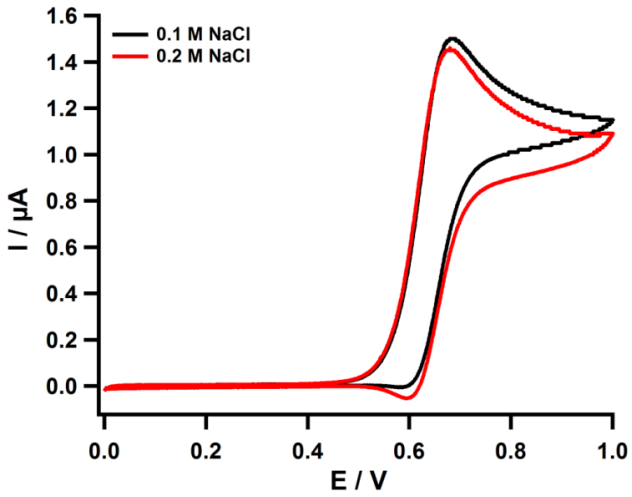

Figure 3.14 Cyclic voltammograms of cotton with 1 m*M* 4-acetamido-TEMPO in NaCl solution at pH 7; potential scan rate 1 mV·s^{-1}.

A cathode current was also observed when doubling the concentration of the salts in solution (Figure 3.14), along with a slight decrease in the catalytic current. It also suggested that the increased concentration of anions slowed the oxidation reaction between 4-acetamido-TEMPO$^+$ and cellulose.

Interestingly, the catalytic current remained the same and was almost identical for all four sodium salt solutions at pH 10 (Figure 3.15), in contrast to the result obtained at pH 7. The difference was proposed to be related to the change of the reaction pathway under a different pH regime (Scheme 3.1).

Under acidic pH, the rate limiting step was the proton abstraction from the complex cation by a base (i.e. the anion in the solution); while under a basic environment, the rate was determined by the formation of the complex and subsequent elimination via a cyclic transition state (which is identical for different salt environments). Therefore, it was expected that the counterion effect would be more significant under acidic environments, and the reaction rate was directly related to the concentration of the anions. However, it was observed from CV that the reaction rate decreased when increasing the concentration of anions, which was opposite to the proposed mechanism in Scheme 3.1. The contradiction here suggested that another hidden factor could play an important role in determining the reaction rate.

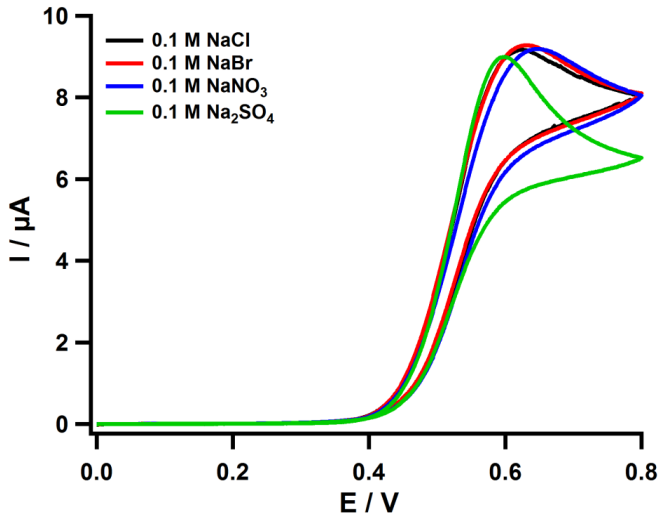

Figure 3.15 Cyclic voltammograms of cotton with 1 m*M* **TEMPO** in different salt solution at pH 10 adjusted by addition of NaOH; potential scan rate 1 mV·s^{-1}.

The counterion effect has been noted previously,[27] but not fully explored. Noting the deleterious effect of β-oxygen atoms on TEMPO mediated oxidation of alcohols[36] and the postulated formation of a complex that slows oxidation, either by reducing the positive charge on the nitrogen atom, or by forcing the hydrogen atom out of plane in the transition state,[37] it is suggested that, in addition to changes in basicity of the anions, competitive complexation by the buffer anions may also lead to decreased reactivity of the oxoammonium cation (Figure 3.16). Thus, in optimising such reactions, buffer composition could be important, especially in a low pH environment, and the voltammetric method described here allowed this to be probed with relative ease

The competitive complexation between $TEMPO^+$ and the corresponding anion in the solution could reduce the concentration of free $TEMPO^+$ available to bind with cellulose to catalyse the oxidation reaction, thereby slowing the rate of reaction. The competitive complexation effect provides a possible explanation for the difference in catalytic currents seen at pH 7, but does not account for the identical catalytic curves observed at pH 10 (Figure 3.15). It might be expected that the buffer anions would still interact with $TEMPO^+$ to slow the reaction under basic conditions, but clearly this is not the case.

This apparent contradiction may be resolved by careful consideration of the species present in solution and the reaction mechanism. It is postulated that the complexation of $TEMPO^+$ species with buffer anions is in competition with the formation of the intermediate in the rate determining step (Figure 3.16). Thus, if the equilibrium constant for the exchange of cellulose (RCH_2OH) and buffer anion (B^-) K_{acidic} is greater than K_{basic}, the concentration of reactive intermediate is reduced and the rate of conversion of alcohol to aldehyde (or aldehyde to acid/acid salt) is slowed. Based on this hypothesis, the intermediate in the rate determining step (the $TEMPO^+$/alkoxide complex) was favoured under basic pH, resulting in a higher rate of oxidation (acceleration of the rate of reaction between $TEMPO^+$ and alcohol with the increasing pH[21,38]) relative to that occurring under acidic or neutral conditions. (It is recognised that the anion speciation at the specific pH would also need to be

taken into account (e.g. $H_2PO_4^-$, HPO_4^{2-} and PO_4^{3-} for phosphate buffer), but these effects cannot be deconvoluted with the data in hand.

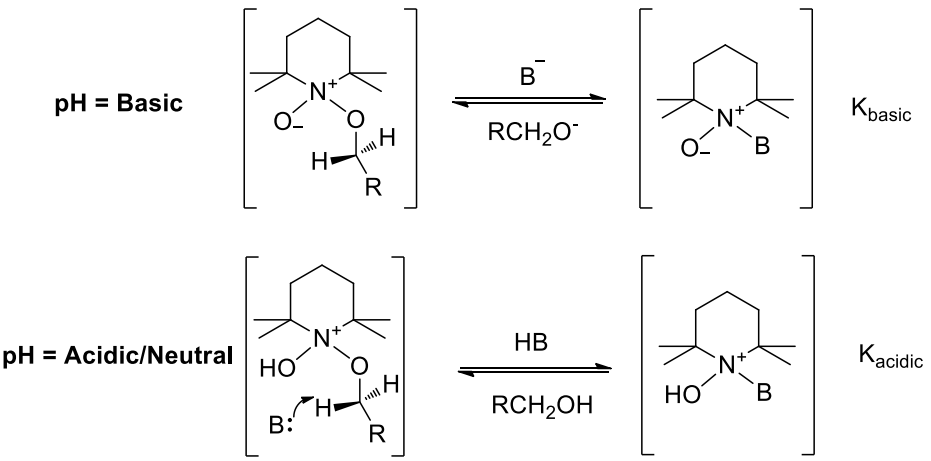

Figure 3.16 Proposed competitive complexation effect of $TEMPO^+$ with anion and cellulose. HB/B^- is the acid/base anion used, RCH_2OH represents cellulose.

The interaction of oxoammonium cation with anions has been well described in the solid state and reflected in the crystal structures of oxoammonium salts[39]), but the association constants of oxoammonium salts in aqueous solutions have not been determined. Nonetheless, if the oxoammonium cations were associated with anions this might be discerned using appropriate NMR experiments in D_2O solution. Specifically, it was considered reasonable to expect that the electronic environment of nitrogen and carbon atoms of $TEMPO^+$ would be altered upon complexation with anions. In addition to the direct charge neutralisation of the positive nitrogen atom with anion, many authors have suggested an interaction between the anion and the oxygen atom of $TEMPO^+$ due to the sterically unfavourable direct contact with a nitrogen atom surrounded by two methyl groups.[40,41]

In both situations (interaction of anion with N or O), the positive charge on N would decrease due to the charge neutralisation (the electrostatic interaction between $TEMPO^+$ and anion was not illustrated as a specific bonding, Figure 3.16). ^{13}C NMR was used to indirectly probe the changes in the electronic environment of N, as the electronic environment of the α-carbon atom was expected to be altered if the complex was formed.[42] The salts of $TEMPO^+$ with phosphate and citrate counterions were prepared by electrolysis in the corresponding (phosphate or citrate) buffer

solutions for 2 h, followed by freeze drying. These salts were then dissolved in D_2O and ^{13}C NMR spectra obtained. As the TEMPO radical cannot be detected by NMR (the free electron would accelerate the relaxation time of the coupled nuclei and broaden the signals), the signals in the NMR spectra belong to $TEMPO^+$ and the possible complex.

Two chemical shifts ascribed to the α-carbon atom were observed at 67 and 56 ppm for $TEMPO^+$ in phosphate buffer solution at pH 7 (Figure 3.17), suggesting that there were likely to be at least two different forms of $TEMPO^+$ with a mole ratio close to 1:1. The result suggested that the phosphate anions actually interacted with $TEMPO^+$ and changed the chemical environment of the entire complex (otherwise only one peak corresponding to the α-carbon should be observed as the two α-carbon atoms are chemically identical). Since there were only $TEMPO^+$, phosphate buffer (excess) and D_2O in the NMR sample, phosphate anions were the species considered most likely to interact with $TEMPO^+$. The fact that two individual signals instead of one peak were seen suggested a slow rate of interconversion, on the NMR time scale between free $TEMPO^+$ and that complexed with phosphate buffer anions.

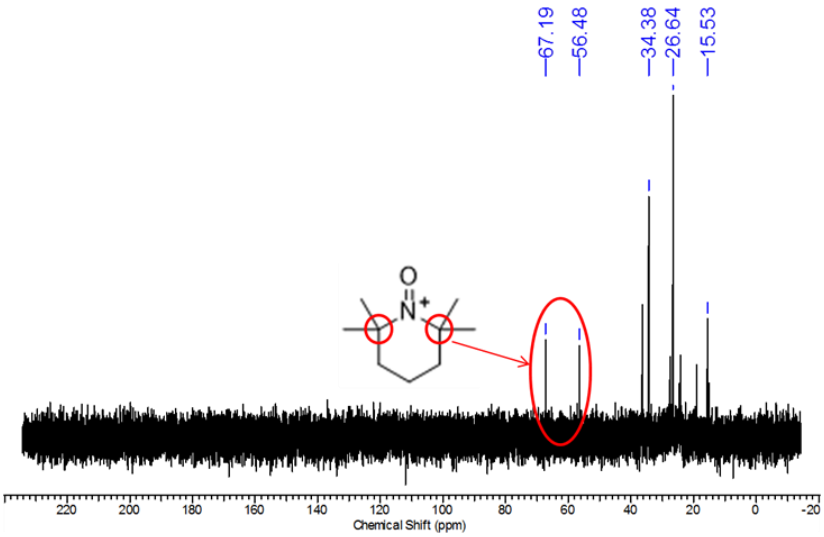

Figure 3.17 ^{13}C NMR spectrum of $TEMPO^+$ in 0.1 *M* PBS at pH7. The two α-carbon atoms are chemically identical, so the two signals in the circle suggest the presence of two distinct $TEMPO^+$ species, ascribed to free $TEMPO^+$ and $TEMPO^+$ bound with the anion.

In order to obtain more information about the chemical structure of the complex, heteronuclear multiple-bond correlation spectroscopy (HMBC), which allows

detection of heteronuclear correlations over ranges of 2–4 bonds, was used here to discern correlation of the α-carbon atom with the hydrogen atoms of the methyl groups. In practice, the ^{1}H, ^{13}C NMR-HMBC spectrum is displayed as a two-dimensional NMR spectrum (giving data on one graph using two frequency axes instead of one): the ^{1}H NMR spectrum in the horizontal direction and ^{13}C NMR spectrum in the vertical direction (Figure 3.18).

Three signals (outlined in black in Figure 3.18) are assigned to the α-carbon atoms as these indicate correlation between the α-carbon atom and protons of the methyl groups separated by 2 bonds (Figure 3.18). The presence of multiple signals suggested that more than one form of $TEMPO^{+}$ existed in the NMR sample and these are suggested to be the complexes of $TEMPO^{+}$ with HPO_4^{2-} and $H_2PO_4^{-}$ (based on pK_a values for phosphoric acid: pK_{a1}=2.16, pK_{a2}=7.21, pK_{a3}=12.32[43]).

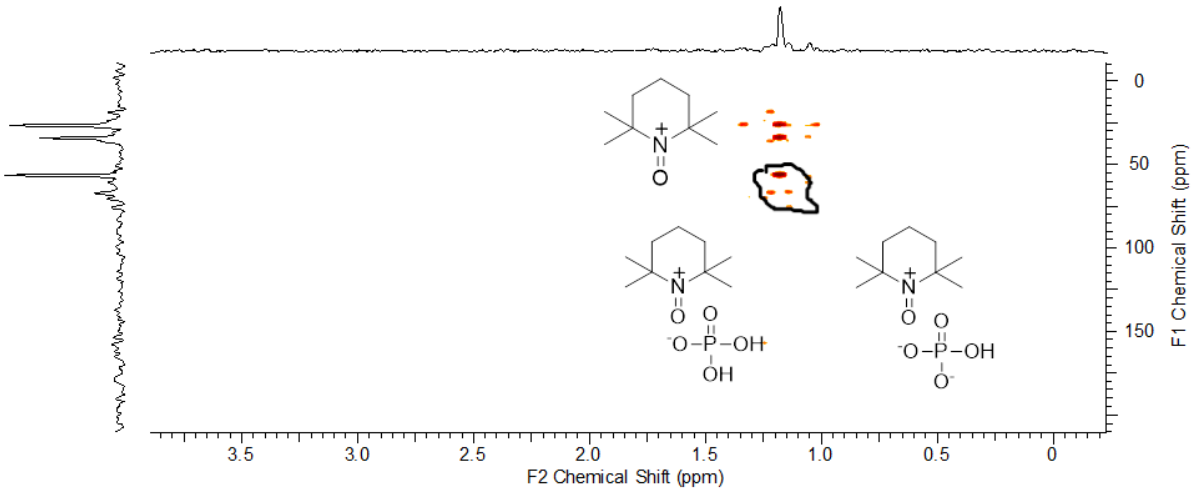

Figure 3.18 ^{1}H,^{13}C-NMR- HMBC spectrum of $TEMPO^{+}$ in 0.1 *M* PBS at pH7. The black outline highlights the three signals ascribed to the α-carbon atoms suggesting three possible discrete species in solution in the presence of excess phosphate buffer.

To discern which of the signals was associated with the complexes and which was due to free $TEMPO^{+}$, diffusion-ordered spectroscopy (pulsed field gradient NMR), also known as DOSY was employed. DOSY provides a means to separate the NMR signals of different species according to their diffusion coefficient, which is an indicator of molecular weight. Molecules or complexes with smaller weight move faster, therefore a higher diffusion coefficient value would be measured for free

TEMPO$^+$ versus TEMPO$^+$ complexes in the DOSY experiment.[44]

Analysis of the diffusion coefficients associated with the three signals ascribed to α-carbon atoms of various complexed and uncomplexed TEMPO$^+$ identities allow these to be deconvoluted (Figure 3.19). Two species with larger molecular weights (and similar diffusion coefficients) were postulated to be TEMPO$^+$ associated with the phosphate buffer derived anions (TEMPO$^+$/ HPO_4^{2-} and/or TEMPO$^+$/ $H_2PO_4^-$ complexes) and the species with the faster diffusion coefficient ascribed to free TEMPO$^+$. Thus, the results of both ^{13}C NMR (Figure 3.17) and HMBC (Figure 3.18), analysis both suggested that anions could interact with TEMPO$^+$ leading to formation of TEMPO$^+$/anion complexes, as proposed and illustrated in Figure 3.16.

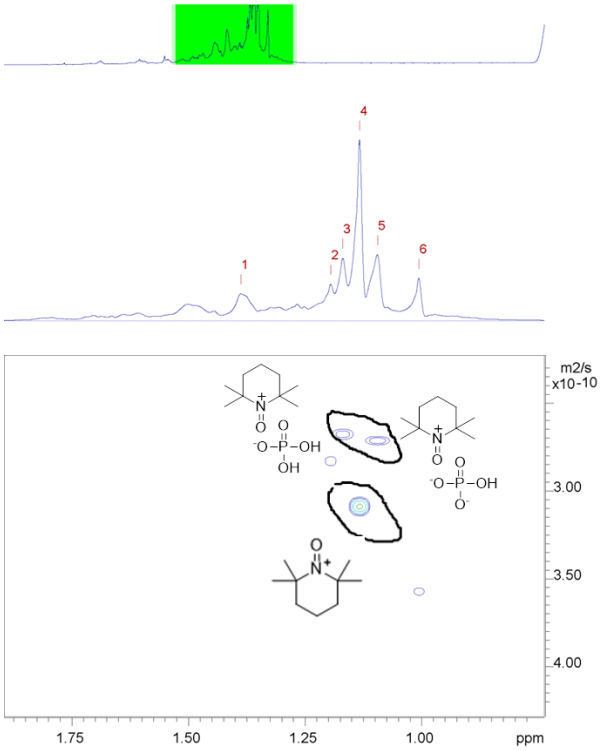

Figure 3.19 2D DOSY spectrum showing TEMPO$^+$ in PBS characterised by different diffusion coefficients.

A similar study was also made for TEMPO$^+$ in citrate buffer solution (CBS), in order to compare the results with the phosphate buffer. For TEMPO$^+$ in CBS at pH 7 (Figure 3.17), only one peak at about 56 ppm was visible in the ^{13}C NMR spectrum. This could imply either that only one form of TEMPO$^+$ existed in the solution, or that

the concentration of other forms was too low to be detected using this relatively insensitive spectral technique. It was safe to say that one $TEMPO^+$ form was dominant in the solution, based on the peak intensity.

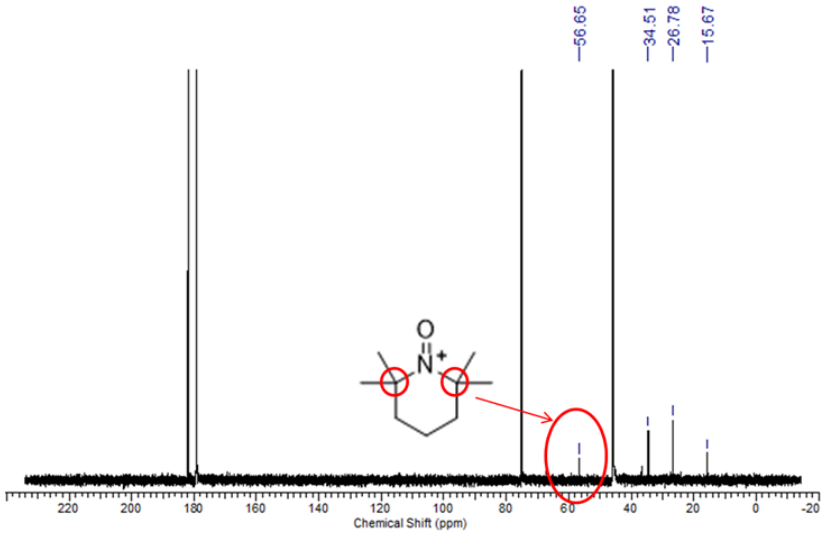

Figure 3.20 ^{13}C NMR spectrum of $TEMPO^+$ in 0.1 *M* CBS at pH7. The strong signals at *ca* 46, 76 and 180 ppm are due to citrate buffer, which is present in large excess.

Similarly, $^{1}H,^{13}C$-NMR-HMBC for $TEMPO^+$ in the presence of citrate showed only one peak in the correlated area, and the possible chemical structure was drawn on the spectrum (Figure 3.21), confirming that one $TEMPO^+$ form was dominant in the solution.

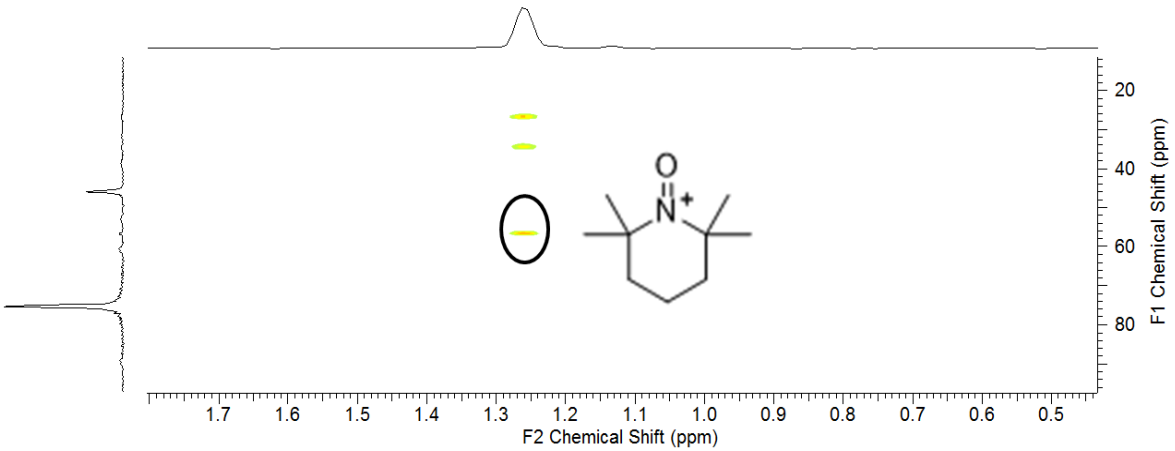

Figure 3.21 $^{1}H,^{13}C$-NMR- HMBC spectrum of $TEMPO^+$ in 0.1 *M* CBS at pH7.

The DOSY NMR obtained (Figure 3.22) showed 3 peaks for possible $TEMPO^+$ identities (similar to the DOSY NMR for $TEMPO^+$ in PBS), with the free $TEMPO^+$ diffusing faster than the suggested $TEMPO^+/C_6H_5O_7^{3-}$ and/or $TEMPO^+/C_6H_6O_7^{2-}$ complexes ($C_6H_5O_7^{3-}$ and $C_6H_6O_7^{2-}$ were the two possible anions in CBS at pH7; pK_a for citric acid[43]: pK_{a1}=3.13, pK_{a2}=4.76, pK_{a3}=6.4). The NMR results for $TEMPO^+$ in CBS suggested that citrate anions also interacted with $TEMPO^+$, but that the free $TEMPO^+$ was the dominant form in the solution.

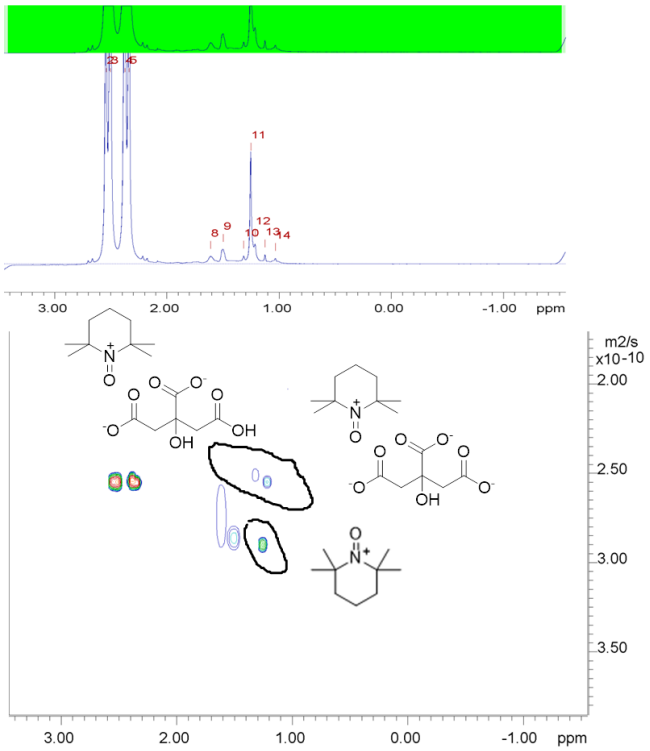

Figure 3.22 2D DOSY spectrum showing $TEMPO^+$ in CBS. The three signals assigned to the α-carbon atoms of $TEMPO^+$ are characterised by different diffusion coefficients, suggesting three discrete forms (two larger species with similar molecular weights and one smaller species) present in solution.

The NMR results suggested that both phosphate and citrate anions could interact with $TEMPO^+$, which is consistent with the postulate illustrated in Figure 2.16. The anion effect has also been observed for TEMPO mediated oxidation of hyaluronan.[45] It was not possible to derive association constants for $TEMPO^+$ and buffer anions from the NMR data obtained here, and significant further detailed experimentation would be required to correlate these with the rates of reaction derived from cyclic

voltammetry.

3.2.5 Fabric Voltammetry IV: Robustness of TEMPO Derivatives

Finally, the cotton modified electrode could be used for the evaluation of the stability of the mediators as side reactions modify the shape and reproducibility of the cyclic voltametric trace recorded. 4-Hydroxy-TEMPO, was reported to be unstable under basic conditions[24] and comparison of voltammograms recorded at pH 6, 7 and 8 clearly showed the transition to an irreversible reaction at higher pH (Figure 3.23a). Increasing the scan rate allowed recovery of the reversible *N*-oxyl/oxommonium equilibrium (Figure 3.23b) with no evidence of mediator decomposition, suggesting that it was possible to select conditions such that the relatively slow decomposition reaction did not deleteriously affect the use of this mediator.

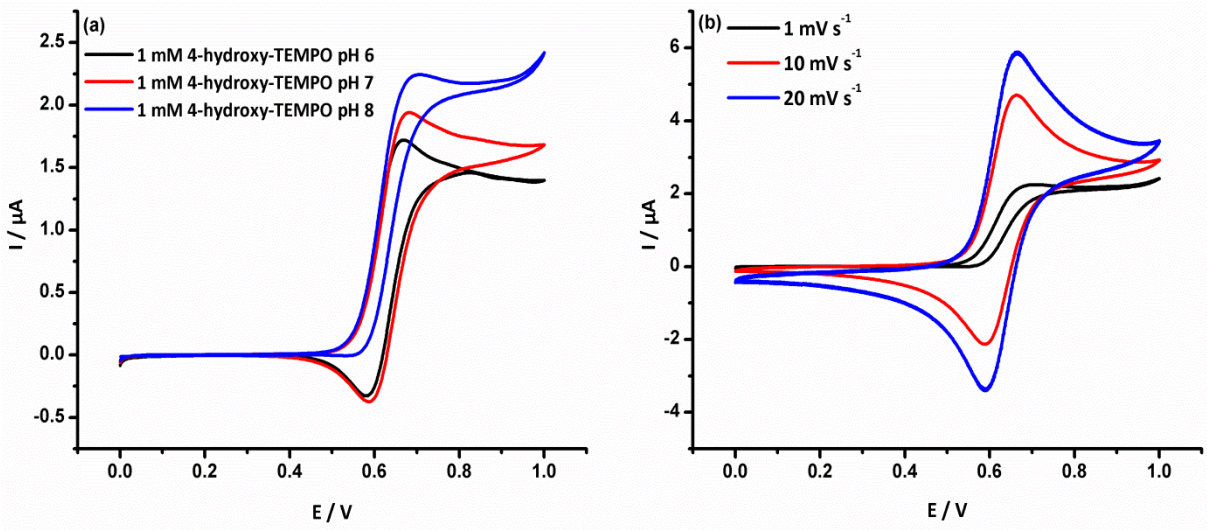

Figure 3.23 Cyclic voltammograms of cotton with 1 m*M* 4-hydroxy-TEMPO at (a) pH 6, 7 and 8; potential scan rate 1 mV·s^{-1}; (b) at pH 8; potential scan rates 1, 10 and 20 mV·s^{-1}.

3.3 Conclusions

Here, a simple voltammetric method is demonstrated for screening the efficacy of mediators in TEMPO electro-mediated oxidation. The voltammetric method, applied here to TEMPO and its derivatives, is sensitive, easy to deploy and yields information pertaining to relative rates of substrate oxidation, as well as stability of mediators under a range of conditions. As very small amounts of mediator are required for testing, this provides a means for fast screening of new synthetic or

natural mediators and selection of optimal conditions of pH and buffer.

From the results of cyclic voltammetry, the buffer (counterion) effect was believed to have a significant impact on the catalytic efficiency of mediator at neutral pH, and no counterion effect was observed in a basic environment, as the kinetics of the TEMPO mediated reaction of alcohols accelerated with the increase of the pH value. The counterion effect was probed by NMR spectroscopy and an interaction between $TEMPO^+$ and anions was shown to be likely to exist. The details of the competitive binding, $TEMPO^+$/cellulose *versus* $TEMPO^+$/buffer anions, could not be deconvoluted using the techniques here. Meanwhile, CV results illustrated that the buffer used could alter the rate of the oxidation reaction under neutral/acid conditions, in agreement with the accepted mechanism (Scheme 3.1) and the use of CV provided valuable information for new buffer screening.

While oxidation of cellulose is of wide interest due to developing applications of oxidised cellulose nanofibrils, the method described is also applicable to a range of other insoluble substrates (e.g. chitin) and need not be limited to polysaccharides.

3.4 References

1. C. Delattre; P. Michaud; R. Elboutachfaiti; B. Courtois; J. Courtois, *Cellulose,* 2006, **13**, 63-71.
2. W. K. Son; J. H. Youk; W. H. Park, *Biomacromolecules,* 2003, **5**, 197-201.
3. M. Singh, et al., *J. Biomed. Mater. Res.,* 1981, **15**, 655-661.
4. K. M. Lewis, et al., *Eur Surg,* 2013, **45**, 213-220.
5. S. Barazzouk; C. Daneault, *Cellulose,* 2011, **18**, 643-653.
6. T. Saito; A. Isogai, *Carbohydr. Polym.,* 2005, **61**, 183-190.
7. R. Gazzeri; M. Galarza; A. Alfieri; M. Neroni; R. Roperto, *World Neurosurgery,* 2011, **76**, 173-175.
8. R. K. Johnson; A. Zink-Sharp; S. H. Renneckar; W. G. Glasser, *Cellulose,* 2009, **16**, 227-238.
9. S. Ifuku; M. Tsuji; M. Morimoto; H. Saimoto; H. Yano, *Biomacromolecules,* 2009, **10**, 2714-2717.
10. A. E. J. de Nooy; A. C. Besemer; H. van Bekkum, *Carbohydr. Res.,* 1995, **269**, 89-98.
11. A. Isogai; Y. Kato, *Cellulose,* 1998, **5**, 153-164.
12. M. Hirota; N. Tamura; T. Saito; A. Isogai, *Carbohydr. Polym.,* 2009, **78**, 330-335.
13. T. Saito; S. Kimura; Y. Nishiyama; A. Isogai, *Biomacromolecules,* 2007, **8**, 2485-2491.
14. T. Saito, et al., *Biomacromolecules,* 2009, **10**, 1992-1996.
15. T. Saito; Y. Nishiyama; J.-L. Putaux; M. Vignon; A. Isogai, *Biomacromolecules,* 2006, **7**, 1687-1691.
16. R. Tanaka; T. Saito; A. Isogai, *Int. J. Biol. Macromol.,* 2012, **51**, 228-234.
17. T. Isogai; T. Saito; A. Isogai, *Biomacromolecules,* 2010, **11**, 1593-1599.
18. T. Isogai; T. Saito; A. Isogai, *Cellulose,* 2011, **18**, 421-431.
19. I. Patel, et al., *Holzforschung,* 2010, **64**, 549-554.
20. P. Parpot; K. Servat; A. Bettencourt; H. Huser; K. Kokoh, *Cellulose,* 2010, **17**, 815-824.
21. B. Sun; C. Gu; J. Ma; B. Liang, *Cellulose,* 2005, **12**, 59-66.
22. X. Zhang; J. Leddy; A. J. Bard, *J. Am. Chem. Soc.,* 1985, **107**, 3719-3721.
23. X. X. Sun; Q. L. Wu; S. X. Ren; T. Z. Lei, *Cellulose,* 2015, **22**, 1123-1133.
24. S. Iwamoto, et al., *Polym. Degrad. Stab.,* 2010, **95**, 1394-1398.
25. R. L. Donkers; D. G. Leaist, *J. Phys. Chem. B,* 1997, **101**, 304-308.
26. A. E. J. De Nooy; A. C. Besemer; H. Van Bekkum, *Synthesis,* 1996, **1996**, 1153-1176.
27. I. W. C. E. Arends; Y.-X. Li; R. Ausan; R. A. Sheldon, *Tetrahedron,* 2006, **62**, 6659-6665.
28. W. F. Bailey; J. M. Bobbitt; K. B. Wiberg, *J. Org. Chem.,* 2007, **72**, 4504-4509.
29. V. D. Sen; V. A. Golubev, *J. Phys. Org. Chem.,* 2009, **22**, 138-143.
30. A. Israeli, et al., *Free Radical Biol. Med.,* 2005, **38**, 317-324.
31. V. D. Sen', et al., *J. Phys. Org. Chem.,* 2015, **28**, 17-24.
32. M. Ertaş; B. Acemioğlu; M. H. Alma; M. Usta, *J. Hazard. Mater.,* 2010, **183**, 421-427.
33. K. D. Collins; M. W. Washabaugh, *Q. Rev. Biophys.,* 1985, **18**, 323-422.
34. Y. Liu; H. Guo; Z. Liu, *Acta Chim. Sinica,* 1991, **49**, 187-192.

35. N. V. Nucci; J. M. Vanderkooi, *J. Mol. Liq.,* 2008, **143**, 160-170.
36. M. Yamaguchi; T. Takata; T. Endo, *J. Org. Chem.,* 1990, **55**, 1490-1492.
37. Z. Ma; J. M. Bobbitt, *J. Org. Chem.,* 1991, **56**, 6110-6114.
38. J. F. Thaburet; N. Merbouh; M. Ibert; F. Marsais; G. Queguiner, *Carbohydr. Res.,* 2001, **330**, 21-29.
39. Y. Yonekuta; K. Oyaizu; H. Nishide, *Chem. Lett.,* 2007, **36**, 866-867.
40. J. M. Bobbitt; A. L. Bartelson; W. F. Bailey; T. A. Hamlin; C. B. Kelly, *J. Org. Chem.,* 2014, **79**, 1055-1067.
41. J. M. Bobbitt; C. BrüCkner; N. Merbouh, In *Organic Reactions*, John Wiley & Sons, Inc., 2004.
42. M. Judith Percino, et al., *J. Mol. Struct.,* 2016, **1103**, 254-264.
43. *CRC Handbook of Chemistry and Physics*, 90th ed., Taylor & Francis, 2009.
44. D. Li; I. Keresztes; R. Hopson; P. G. Williard, *Acc. Chem. Res.,* 2009, **42**, 270-280.
45. B. Jiang; E. Drouet; M. Milas; M. Rinaudo, *Carbohydr. Res.,* 2000, **327**, 455-461.

Chapter 4 Electro-oxidation of cellulose

4.1 Introduction

Selective oxidation of cellulose in an NaClO/NaBr/TEMPO aqueous solution was proved to be able to selectively oxidise primary hydroxyl groups in the presence of secondly hydroxyl groups under mild reaction conditions,[1,2] resulting in a stably dispersed nanofibril suspension following ultra-sonication.[3] However, chlorine based oxidants used in the chemical oxidation are deemed undesirable for a variety of reasons (e.g. concerns from consumers over using chlorinated chemicals in personal care products;[4] stoichiometric quantities of chlorinated oxidant are undesirable in industrial processes[5]), and a chlorine-free primary oxidant is desired (Figure 4.1).

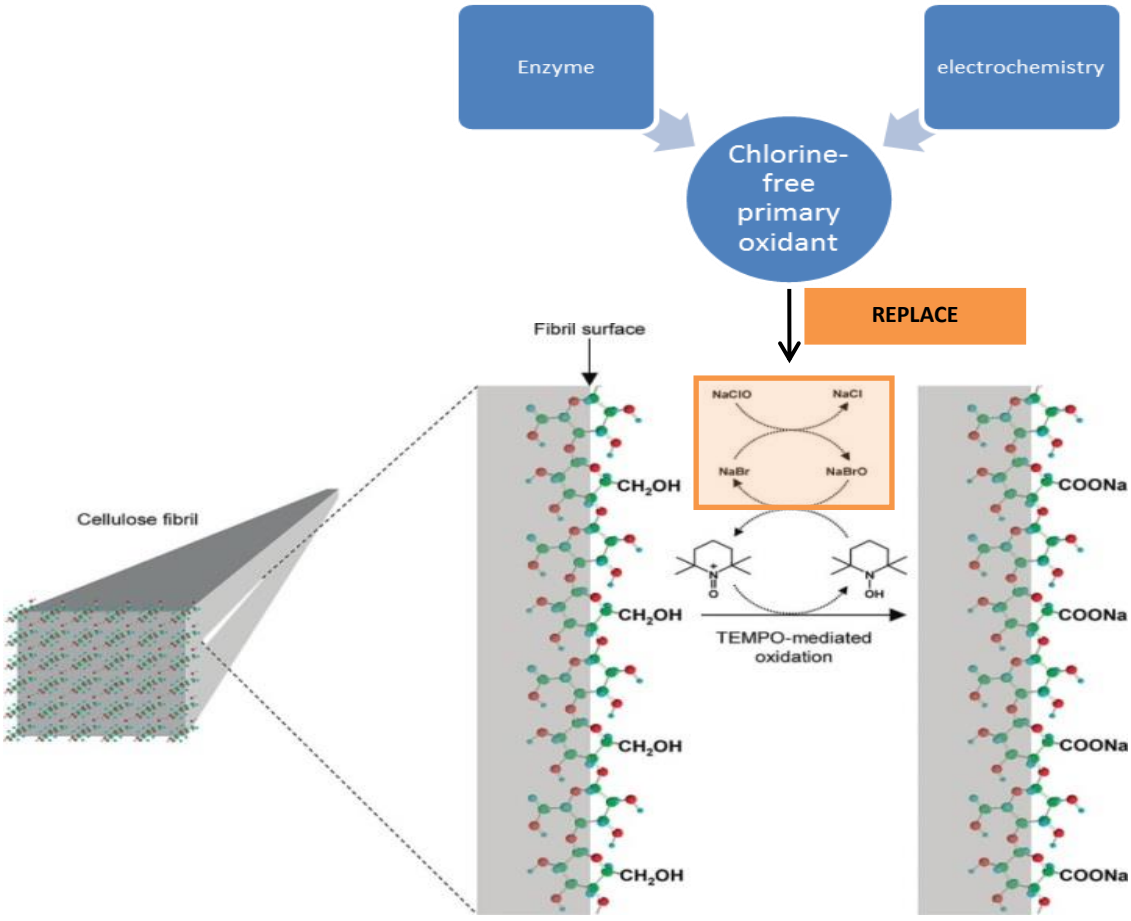

Figure 4.1 Schematic model of oxidation of C6 primary hydroxyl on cellulose microfibril surfaces.[6] Reproduction of image from Ref. 6 with permission from Elsevier (© Elsevier 2004).

Reported chlorine-free oxidation systems, allowing selective oxidation of the cellulose C6 primary alcohol groups, include those relying on enzymatic process (e.g. with laccases,[7] a possible reaction pathway is displayed in Scheme 4.1), or electrochemical oxidation of a mediator (e.g. TEMPO being oxidised by an electrochemical reaction[8]). Other methods (e.g. NO_2-HNO_3[9] or CuCl/TEMPO[10] oxidation systems), have also been shown to be effective to selectively oxidise the primary hydroxyl groups in the presence of other hydroxyl groups, but concern over toxicity and sustainability of the regents involved limits a wider application. The enzymatic- or electro-oxidation may also prevent cellulose degradation by depolymerisation, during the oxidation process, as NaClO used in the reaction may attack the end groups on cellulose chains.[8] Between these two alternatives, electrochemistry seems to be an more attractive option, obviating the issues of inhibition of enzyme by some metal impurities in the starting material, enzyme stability during reaction and high cost of the enzyme,[9,10] while providing a “clean” and sustainable oxidation method. In addition, the enzymatic reaction requires a long oxidation time to produce reasonable density of carboxyl groups on the cellulose surface,[11] as both the reaction rate of enzyme oxidising TEMPO and cellulose oxidation by $TEMPO^+$ at low pH were too slow (refer to Chapter 3).[12,13] Previously described electrochemical methods for cellulose oxidation required relatively large concentration of TEMPO (400 $mmol \cdot L^{-1}$) compared to that required in the chemical oxidation (1 $mmol \cdot L^{-1}$ for TEMPO), and also required considerable periods of time (more than 24 hours) for the completion of reaction,[14] which is not efficient, and not practical for industrial applications. A kintecis study of the elctro-mediated TEMPO oxidation has been conducted on a soluble substrate and a possible mechanism was proposed: the reaction pathway was similar to the oxidation reaction in the NaClO/NaBr/TEMPO system, with the exception that the aldehyde groups formed in electro-oxidation needed to be hydrated before being converted into carboxylate groups, while the aldehydes could be directly oxidised by NaClO, or NaBrO in the latter.[15] A similar result was also observed for electro-oxidation of benzyl alcohol in ionic liquid using TEMPO as catalyst, where the forming aldehyde intermediate remained unhydrated, and benzyl aldehyde with 100% chemical selectivity was obtained.[16] This mechanism could also explain the reason for forming higher

aldehyde/carboxylate ratio of cellulose in laccase- and electro-oxidation compared to chemcial oxidation, as water diffuses slowly into the crystlline region of cellulose and slows down the hydration of the aldehyde groups.[17]

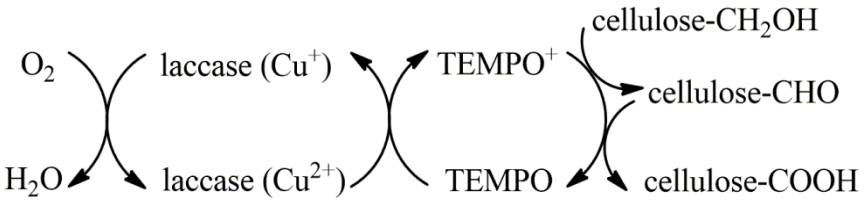

Scheme 4.1 laccase/TEMPO oxidation of cellulose.[18]

Therefore, a more efficient method that completes the reaction in a reasonable time period (preferably within several hours or less) and reduces the quantity of mediator used is essential to make the reaction cost effective, while minimising possible side reactions. It was considered that the previously published long reaction times and apparently inefficient electrochemically mediated oxidation were probably due to the small area of the working electrode,[8,19] or excess starting material,[14] and modification of these parameters in this study has allowed development of a more viable process. Based on the results in Chapter 3, the optiumum reaction conditions (TEMPO in 0.1 M carbonate buffer) was identified by cyclic voltammetry and used here to produce oxidised cellulose in bulk quantities.

4.2 Results and discussion

Electro-oxidation at elevated pH (pH 10) using TEMPO (chosen as the most efficient catalyst at pH 10 from the results of the cyclic voltammetry study in Chapter 3) as the mediator for cellulose oxidation was carried out for varying periods of reaction time and consumption of charge measured as a first approximation of the likely degree of oxidation. A much larger working electrode was adopted here, compared to the previous study in Chapter 3, to provide more surface area for the electron transfer between TEMPO and the electrode and so reduce the reaction time. Temperature was also investigated here to evaluate the influence on the reaction. The relative quantities of carboxylate and aldehyde groups were determined by conductometric titration of material as recovered and post $NaClO_2$ treatment (to convert aldehyde to carboxylate) respectively.[20] Analyses of crystallinity and degree of polymerisation

(DP) of cellulose and its corresponding oxidised form were evaluated by XRD and viscosity measurements to reveal the structure change of cellulose before and after electro-oxidation.

4.2.1 Variation of the reaction time

The initial reaction time was set to 2 h (Figure 4.2), comparable to the reaction period in chemical oxidation using the NaClO/NaBr/TEMPO system, in order to test the viability of producing oxidised cellulose by electro-oxidation. The surface area of the working electrode in contact with the mixture was *ca.* 25 cm^2. The steady current over the reaction period implied a continuous generation of $TEMPO^+$ on the working electrode to react with cellulose. Electro-oxidation systems reported in literatures using 1 *mM* TEMPO took more than 20 h to reach completion, which was not practical and probably resulted in undesired side reactions.[17,19] Therefore, the concentration of TEMPO used was set at 10 *mM* to keep the reaction time within a reasonable period, based on the concentration effect results measured in the cyclic voltammetry study (increased concentration of mediator resulted in increased reaction rate).

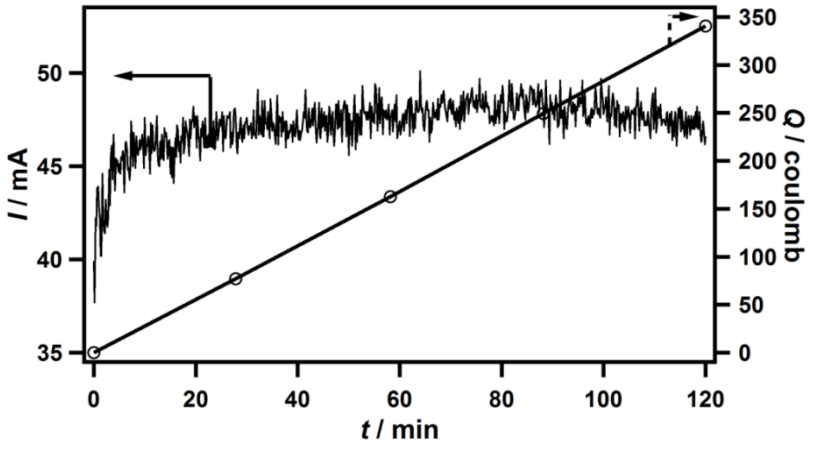

Figure 4.2 Relationship between 10 m*M* TEMPO electro-mediated oxidation current of 1 g α-cellulose in CBS at pH 10 over the corresponding time (left axis) ,and quantities of consumed charge versus oxidation time (right axis).

The total consumed charge for 2 h electro-oxidation was 341 C. The carboxylate groups and aldehyde groups formed in the oxidised cellulose were 0.8 $mmol \cdot g^{-1}$ and 0.3 $mmol \cdot g^{-1}$ as determined by conductometric titration. The Faraday efficiency for

the production of carboxyl groups was 86 % (calculated based on the number of electrons required for the resulting carboxyl formed over the number of electrons consumed during the process), which was higher than the reported value for similar electrochemical oxidation of cellulose. The efficiency gradually decreased as the time evolved, due to the current loss by the electrolytes and gases formed during the reaction.[21] Therefore the reduction of the overall reaction time was very important to increase the efficiency.[17] The mass recovery was 93 % (ratio of solid sample weight before and after oxidation), which was comparable to the value in NaClO/NaBr/TEMPO system (over 90%), so the oxidised cellulose from the electro-oxidation could be recovered in the same way as chemically oxidised cellulose.[22]

The carboxylate content of the oxidised cellulose formed in the electro-oxidation system was lower and a higher content of aldehyde groups was measured, compared the NaClO/NaBr/TEMPO system. This indicated that NaClO may not only act to oxidise TEMPO, but also served to convert aldehyde (hydrated or non-hydrated) to carboxylic groups more effectively in the chemical oxidation system,[23] as was mentioned previously in the introduction.

In order to increase the carboxylate content of electro-oxidised cellulose (a greater density of the negative charge on the fibril surface), thus improving the dispersibility of the OCNF,[22] a longer oxidation time or higher current (faster reaction rate) would be required and this was tested in this Chapter.[8]

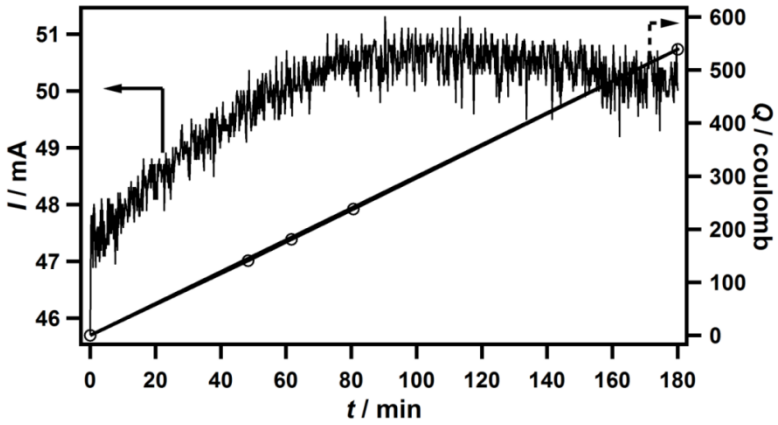

Figure 4.3 Relationship between 10 m*M* TEMPO electro-mediated oxidation current of 1 g α-cellulose in CBS at pH 10 over the corresponding time (left axis), and charge consumed against oxidation time (right axis).

The total consumed charge for a 3 h electro-oxidation was 539 C (Figure 4.3). The surface area of the working electrode was ca 30 cm^2.The current and reaction time were higher and longer than the previous experiment to evaluate the effect on the oxidised product. The carboxylate groups and aldehyde groups formed in the oxidised cellulose were 1.1 $mmol \cdot g^{-1}$ and 0.5 $mmol \cdot g^{-1}$, determined by conductometric titration. The Faraday efficiency for the production of carboxyl groups was 89 %. The mass recovery ratio was 91 %.

The carboxylate content was comparable to that achieved in the NaOCl/NaBr/TEMPO chemical oxidation process in a similar time scale, but the aldehyde content was higher, suggesting that that electro-oxidation may require a "polishing step" post oxidation to convert aldehyde groups to carboxylate via further oxidation of aldehydes by oxidants,[24] if low aldehyde content is required (the aldehyde groups may actually be beneficial to some application, e.g., protein immobilisation).[25,26] The results showed that electro-oxidation may be a promising "clean" alternative to chemical oxidation, producing oxidised cellulose within reasonable time without adopting chlorine-based chemicals.

It was noticeable that, although the current varied between the 2 h and 3 h electro-oxidation, which could be adjusted by the area of the working electrode or stirring speed, the consumption of charge *versus* time was always a linear relationship and it was shown from cyclic voltammetry study that turnover of TEMPO occurred at a constant rate dependent on applied potential, which in turn suggested the oxidation of $TEMPO^+$ with cellulose was the rate limiting step in the reaction rate law under the conditions tested.

Focus now turned to determining the reproducibility of the process with samples subjected to the consumed charge and measured with respect to carboxylate and aldehyde contents.

Therefore, the charge consumption was monitored and controlled here. The total consumed charge was 535 C (Figure 4.4). The electro-oxidation was conducted at a lower current to evaluate the effect of time on oxidation (it was not purposely set to react at the lower current, but this occurred due to the variance of electrode surface

area in the mixture and was not able to controlled precisely with the set-up here, The surface area of the working electrode was ca 22 cm^2). It was obvious from the graph that the reaction took a much longer time to complete due to a lower current, compared to the reaction shown in Figure 4.3. Therefore, a higher current was desirable to complete the reaction within a short time, and this could be achieved by increasing the surface area of the working electrode.

The carboxylate groups and aldehyde groups formed in the oxidised cellulose were 1.1 $mmol \cdot g^{-1}$ and 0.5 $mmol \cdot g^{-1}$ determined by conductometric titration. The result was similar to the reaction shown in Figure 4.3. Therefore, it was the consumed charge affecting the conversion ratio of cellulose within short period of the reaction time (< 3 h).

The Faraday efficiency for the production of carboxyl groups was 85 %. Noticeably, an increase in temperature was also observed after the reaction (temperature measured at the end of the reaction was 30 °C), suggesting that some efficiency loss was due to energy conversion. The mass recovery ratio was 80%, lower than the previous results, probably due to the increased amounts of soluble substrates formed at higher temperature, led by the degradation of cellulose chains.[27]

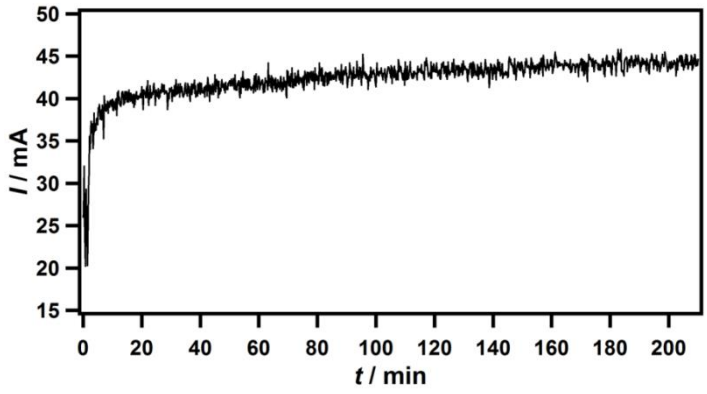

Figure 4.4 Measured oxidation current for 10 m*M* TEMPO electro-mediated oxidation of 1 g α-cellulose in CBS at pH 10 over the corresponding time.

4.2.2 Variation of the total consumed charge

Since it has been determined that the carboxyl contents of electro-oxidised cellulose was influenced by the total consumed charge, the focus was to correlate the

carboxylate and aldehyde contents of the oxidised cellulose with different total amounts of consumed charge, and its impact on the degree of polymerisation (DP) and the crystallinity of the oxidised cellulose. The method for DP value determination has been described in Chapter 2.

Both the carboxylate and aldehyde contents in Figure 4.5 increased with the increasing consumption of charge as expected (higher charge consumption, more conversion). Although the change in carboxyl content did not follow a linear relationship with the consumption of charge, it was still possible to estimate the carboxyl content if the charge consumption is known. It was also noticed that the DP_v value of the oxidised cellulose dropped significantly during the beginning of the reaction (probably due to the removal of amorphous cellulose region) and remained relative stable afterwards. The DP_v value was found to be in a positive relationship to the length of the OCNF, and hence the decrease in the DP_v value here suggested that OCNF shortened during the reaction.[28]

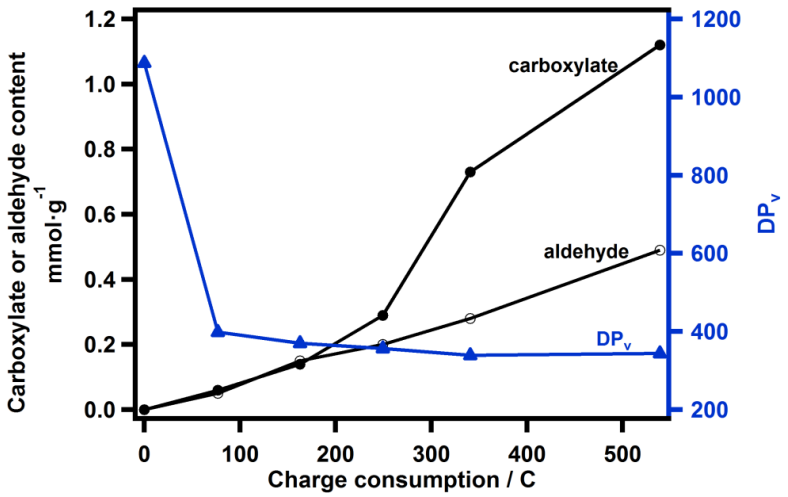

Figure 4.5 Carboxylate and aldehyde contents (left axis), viscosity-average degree of polymerization (right axis, DP_v) of the oxidized cellulose *versus* charge consumption by electro-mediated TEMPO oxidation at ambient temperature in CBS at pH 10. Lines here are only for guidance.

4.2.3 Other variables

Two variables (counter electrode type and temperature) were also probed here to determine the impact on the reaction and the oxidised product, although it was also

noticed that type and form of the working electrode,[29] and the geometry and form of the electrochemistry cell would also change the efficiency of the reaction. [30]

The set-up of the electro-oxidation system was the same as above, with the exception that the cathode was replaced by a glassy carbon electrode of 3 mm in diameter instead of a platinum electrode. The surface area of the working electrode was ca 35 cm^2. Since glassy carbon is much cheaper than platinum, it was deemed useful to determine whether a change in cathode material would greatly influence the outcome of the reaction (the function of the cathode here was to allow current to flow through the system and hydrogen was produced on the glassy carbon), and it was expected that the chemically inert carbon electrode should not change the TEMPO oxidation. All the other parameters were the same as was mentioned above.

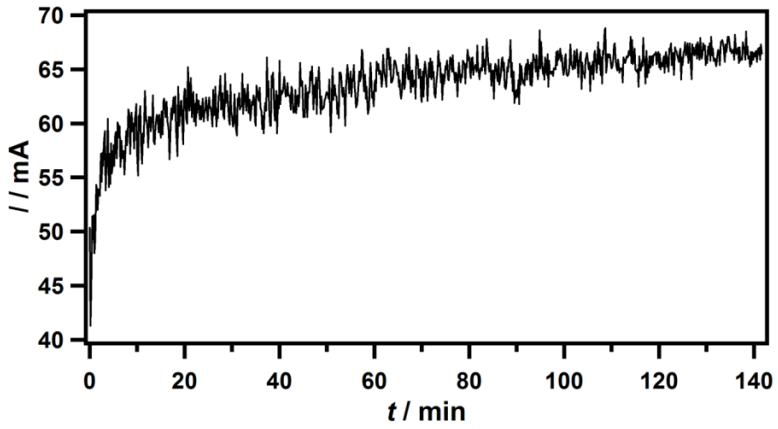

Figure 4.6 Relationship between 10 m*M* TEMPO electro-mediated oxidation current of 1 g α-cellulose at CBS pH 10 over the corresponding time.

The reaction was ended when the total charge consumption reached 540 C (Figure 4.6). There were 1.1 $mmol \cdot g^{-1}$ carboxylate content and 0.5 $mmol \cdot g^{-1}$ aldehyde content formed in the oxidised cellulose, as determined by conductometric titration. The Faraday efficiency for the production of carboxyl groups was 85 %, and the mass recovery ratio was 87%. The resultant product is comparable to that obtained in the 3 hour electro-oxidation process using a Pt counter electrode with respect to the COOH and CHO content, but the reaction proceeds more rapidly (complete within 2.5 hours), due to the higher current. Therefore, replacement of Pt electrode with glassy carbon was considered viable. A similar oxidised product resulted and

the cheaper electrode led to slightly more rapid reaction. A slight increase in temperature was also observed (30 °C at the end of the reaction).

It was suggested from other research result that cooler temperatures might avoid the depolymerisation reaction (with increasing temperature in the chemical oxidation, the reaction produced oxidised cellulose with lower DP_w).[31] Therefore, temperature variation was also investigated here with an expectation that the reaction would slow down at lower temperature, thus increasing the reaction time.

Set-up of the temperature controlled electro-oxidation system was configured by immersing the electro-oxidation cell used at ambient temperature into an ice bath equipped with a thermometer, to monitor temperature change of the reaction mixture, and so maintain the temperature at ca 4°C. When the temperature was higher than a set value (*ca* 4 °C) and the ice in the bath melted, extra ice was added into the bath to reduce and maintain the temperature. The cathode used here was a glassy carbon electrode. The effect of higher temperature was not tested here, as it was suggested that both the crystallinity and the yield of the product would decrease at a higher temperature.[27]

The total consumed charge was 350 C (Figure 4.7), and the surface area of the working electrode was ca 30 cm^2. The charge value was set lower than 540 C, as the reaction rate was too slow to consume such amount of charge within a reasonable time scale.

It was expected that the electro-oxidised cellulose contained ca 0.8 $mmol \cdot g^{-1}$ and 0.3 $mmol \cdot g^{-1}$ for carboxylate and aldehyde content respectively, based on the results in Figure 4.5. Meanwhile, it was surprising to observe increase in both carboxylate and aldehyde contents to 0.9 $mmol \cdot g^{-1}$ and 0.5 $mmol \cdot g^{-1}$, as determined by conductometric titration. The carboxyl content was much higher than the oxidation with same charge consumption at ambient temperature, and the Faraday efficiency for the production of carboxyl groups reached 97 %, which was much higher than the experiment at ambient temperature. The mass recovery ratio was 88 %. The DP_v of the oxidised cellulose was about 385, which was also higher than the reaction taking place at ambient temperature.

These results suggested that the electro-mediated TEMPO oxidation resulted in a higher efficiency of the reaction and longer polymer chains of the oxidised cellulose under lower temperature conditions. This occurred because the absolute reaction rate of the low temperature reaction, reflected by the speed of charge consumption, was much slower compared to the reaction rate at ambient temperature. This was consistent with other results of TEMPO mediated electro-oxidation of alcohols, as lowering the temperature resulted in an increase in selectivity of primary hydroxyl groups over secondary ones,[32] thus increasing the electrical efficiency.

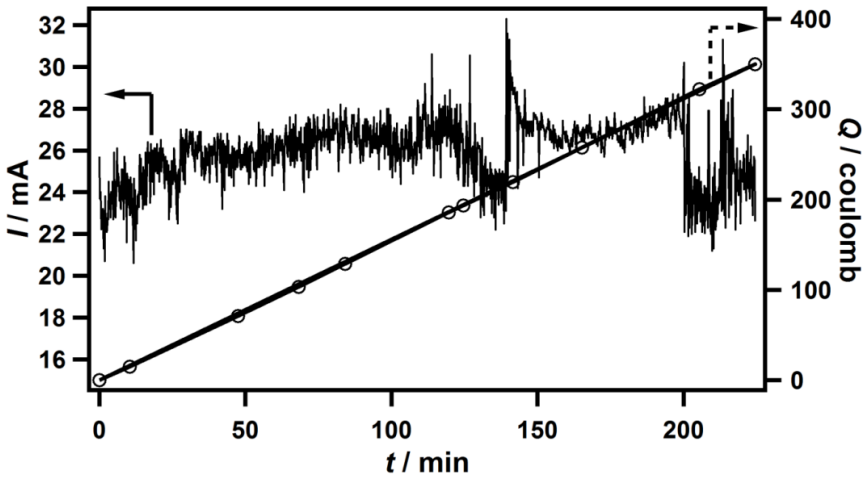

Figure 4.7 Relationship between 10 m*M* TEMPO electro-mediated oxidation current of 1 g α-cellulose in CBS at pH 10 over the corresponding time (left axis), and charge consumed against oxidation time (right axis).

4.2.4 Characterisation of electro-oxidised cellulose

The formation of carboxylate groups at C6 primary hydroxyl alcohol groups during electro-oxidation was confirmed by ^{13}C NMR experiments (Figure 4.8), using oxidised cellulose completely dissolved in EMIM AC/DMDO-d6 with data collected at 90 °C to compensate for the high viscosity of the solution at lower temperatures (a detailed sample preparation method for ^{13}C NMR can be found in Chapter 2). The signals due to the EMIMAC must be disconnected, as the ionic liquid used to achieve full dissolution of cellulose also resulted in signals in the ^{13}C NMR (but did not overlap with the signals of cellulose, Figure 4.8). As the achievable cellulose concentration was low, the signal to noise ratio was poor in the ^{13}C NMR, and the

signal of aldehyde groups was too poor to be observed.[33] Existence of aldehyde groups formed in the oxidised cellulose could be identified by reacting the oxidised cellulose with 2,4-dinitrophenylhydrazine, followed by spectrophotometric measurement.[34]

The signal at 158.84 ppm indicated the formation of C6 carboxylate groups, while the signal for non-oxidised C6 carbon atoms was detected at 60.14 ppm.[35] The C1 carbon signal occurred at 102.29 ppm. The C4 carbon signal was observed at 78.70 ppm and the C2, C3 and C5 signals were between 73.66-76.51 ppm (Scheme 4.2). Therefore, the selective TEMPO mediated electro-oxidation at C6 hydroxyl groups of cellulose was confirmed by ^{13}C NMR and was in consistent with the spectrum of the chemically oxidised cellulose.[36]

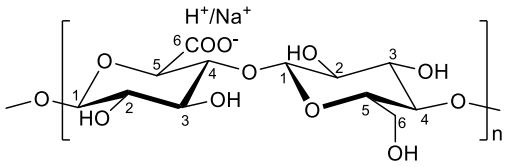

Scheme 4.2 Molecular structure of C6 partially oxidised cellulose.

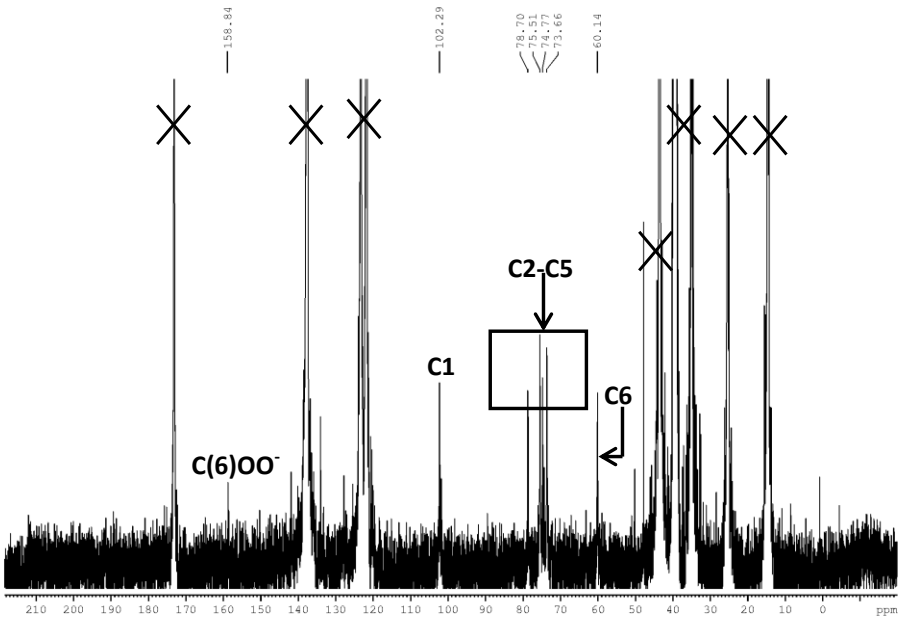

Figure 4.8 ^{13}CNMR spectrum of 2 wt% oxidised cellulose in EMIMAc/DMSO-d_6 measured at 90 °C.

Crystallinity of the cellulose before and after electro-oxidation reaction was compared to determine the influence of the reaction on the cellulose structure (Figure 4.9). The original cellulose was labelled as α-cellulose (cellulose type I), obtained from Sigma. However, the XRD spectra suggested that it was actually cellulose type II (Rietveld refinement in the later section below shows that it was a mixture of type I and II), as determined by the difference in the peak position.[37,38] This cellulose was used as the starting material in electro-oxidation, noting that the difference in the hydrogen bonding between cellulose I and II would affect the reaction rate (different accessibility of crystalline region of cellulose to mediator).[39] Mediator would diffuse faster into cellulose II, therefore it was expected that both cellulose I and II would show a similar trend in the change of reaction rate (faster in cellulose II), carbonyl content (higher in cellulose II), crystallinity (lower in cellulose II). The crystallinity was 56% for the original cellulose and 65% for the oxidised cellulose (1.1 mmol·g^{-1} carboxylate groups and 0.5 mmol·g^{-1} aldehyde groups, Figure 4.9), calculated by Segal's method.[40] Rietveld refinement was also applied here to compare the crystallinity change following the method of Thygesen *et al*.[41] The Rietveld fitting for the cellulose starting material was illustrated in Figure 5.10 (see appendices for the result of the oxidised cellulose). This method is considered to give more realistic results than Segal's method, allowing comparison of cellulose from different sources. The proportion of different cellulose polymorphs could also be extracted from the data. The crystallinity was determined to be 41% for the original cellulose sample (cellulose II : I_α : I_β = 3 : 2 : 2, and 58% for electro-oxidised cellulose (where cellulose II : I_α: I_β = 1 : 1 : 1). The increase in the crystallinity of cellulose after electro-oxidation, which was confirmed by both Segal's method and Rietveld refinement, was in agreement with the result of the decrease DP_v value after the reaction, showing that some amorphous cellulose was removed during the reaction (probably due to the formation of water soluble products resulting from a higher degree of oxidation in the amorphous regions of cellulose[42]) and therefore a higher degree of crystallinity was observed. The change in proportion of different cellulose polymorphs, determined by Rietveld refinement before and after electro-oxidation, suggested that the cellulose II has reacted with TEMPO more rapidly than cellulose I, yielding a water soluble product.

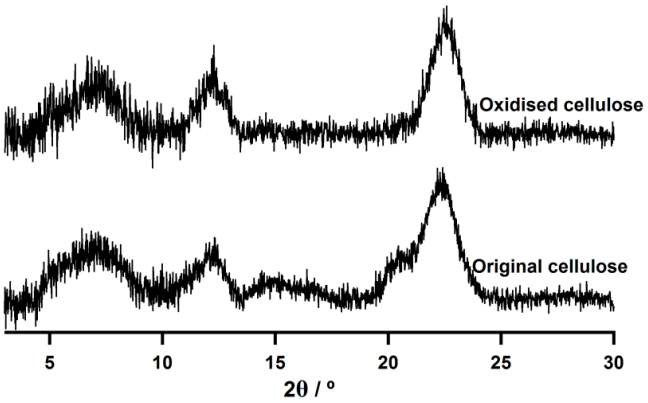

Figure 4.9 X-ray diffraction patterns of original cellulose and oxidised cellulose.

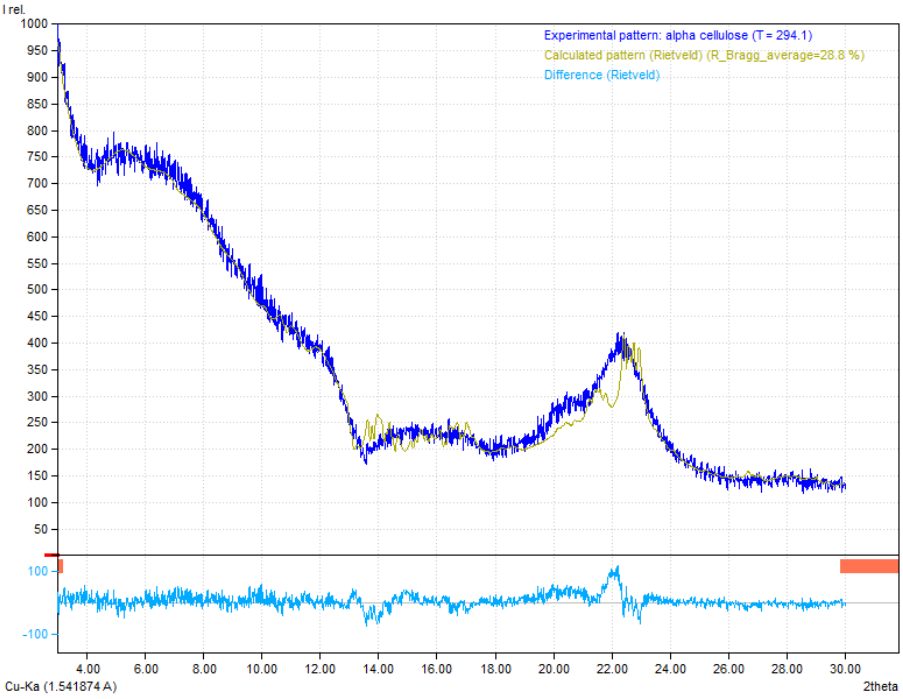

Figure 4.10 Rietveld refinement pattern of the X-ray diffraction data for alpha cellulose. Dark blue line shows the experimental profile and yellow line shows the calculated profile. The light blue line at the bottom shows the residual difference.

The morphology of OCNF obtained from electro-oxidation was studied by TEM, in order to compare it with the OCNF using chemical oxidation. The cellulose after electro-oxidation process (1.1 mmol·g^{-1} carboxylate groups and 0.5 mmol·g^{-1} aldehyde groups) was further oxidised using $NaClO_2$, to convert all aldehyde groups to carboxylate groups, then diluted and ultra-sonicated to yield 0.1 wt% OCNF aqueous suspension.[38] The sonicated suspension was centrifuged to remove large

particles at 8000 rpm. TEM images of OCNF suspensions obtained from electro-oxidation and chemical oxidation were displayed in Figure 4.11. Both OCNF from electro-oxidation and chemical oxidation processes presented fibril-like structure with a high aspect ratio, and the nanofibrils entangled with others. The electro-oxidised OCNF resulted in an average fibril width of *ca* 7nm, corresponding to the crystallite size in Figure 4.9, calculated by the use of Scherrer equation.[43] Therefore, it was demonstrated for the first time that the electro-oxidation process could produce OCNF comparable to chemically oxidised cellulose, with similar morphology.

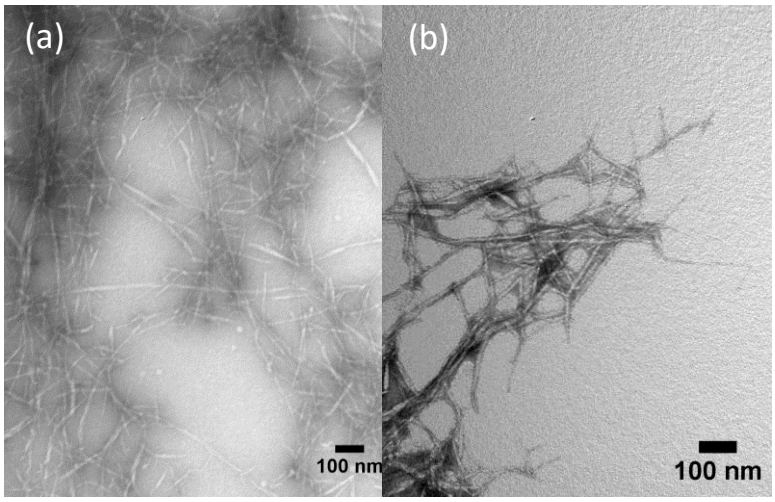

Figure 4.11 TEM of OCNF obtained from (a) electro-oxidation and (b) NaClO/NaBr/TEMPO oxidation.

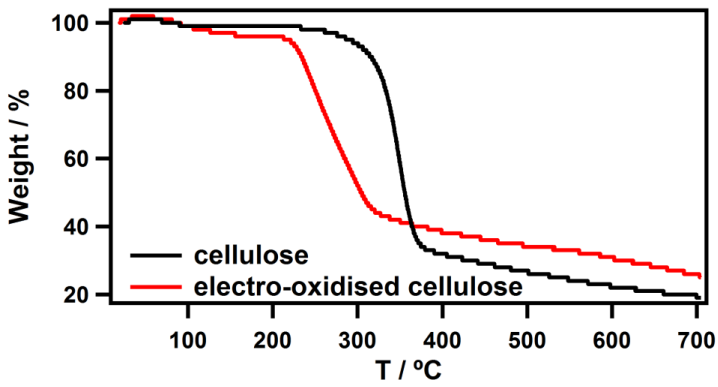

Figure 4.12 TGA of cellulose before and after electro-oxidation.

The thermal stability of the electro-oxidised cellulose (1.1 mmol·g^{-1} carboxylate groups and 0.5 mmol·g^{-1} aldehyde groups) after the $NaClO_2$ "polishing" process is shown in Figure 4.12. The mass loss at *ca* 100 °C for both samples was ascribed to

the loss of free water moieties. The degradation temperature of electro-oxidised cellulose (*ca* 220 °C) was lower than that of the original cellulose, but similar to that of the chemically oxidised cellulose (*ca* 222 °C).[44] The higher residue of the electro-oxidised cellulose was ascribed to the incomplete carbonization of the oxidised cellulose in the presence of sodium atoms in the sample, as the acid treated oxidised cellulose resulted in a similar residue value as the original cellulose.[45]

4.3 Conclusions

A simple, clean electro-oxidation method for the selective oxidation of cellulose under chlorine-free conditions has been established. With the working electrode surface area / cellulose weight at *ca* 30 cm^2 / 1 g, potential at 1 V and 10 $mM \cdot g^{-1}$ of TEMPO to cellulose in 100 mL 0.1 M carbonate buffer at pH 10, electro-oxidation of cellulose was accomplished with controllable carboxyl content in a reasonable time (2-5 hours). The reaction rate was reflected by the measured current level: higher current indicated a faster reaction. Faraday efficiency of the electro-oxidation was significantly improved by lowering the temperature, although a slower reaction rate was inevitable.

The DP, carboxylate/aldehyde content, Faraday efficiency, mass recovery ratio and crystallinity for selected samples are summarised in Table 4.1. The results were obtained using a platinum counter electrode at room temperature, unless specified in the table. Generally, the DP decreased (from 1088 to 340) and the crystallinity increased (from 41% to 58% as determined by Rietveld refinement) as the oxidation proceeded. The amorphous phase and type II cellulose was partially removed during oxidation, suggesting that these were oxidised more completely with TEMPO, yielding some water soluble products. This is reflected in the change in the relative quantities of cellulose polymorphs (the ratio of cellulose II : I_α : I_β changed from 3:2:2 to 1:1:1) derived from Rietveld refinement. Lowering the temperature could help to increase the efficiency, but it would also slow the reaction and extra energy would also be required to maintain the low temperature. The change of the counter electrode from platinum to glassy carbon resulted in no significant difference in the

conversion of C6 hydroxyl groups, which could be used when scaling up the reaction as glassy carbon is much cheaper than platinum.

In addition, the carboxylate and aldehyde contents were shown to be identical when the charge consumption was *ca* 540 C using platinum or glassy carbon counter electrodes. This result suggested that the degree of oxidation could be controlled by the charge consumption, based on Figure 4.5. The carboxylate/aldehyde ratio formed in the electro-oxidation increased with increasing charge consumption (from 1 to 2), but the value was lower than that in the NaClO/NaBr/TEMPO system (carboxylate/aldehyde is typically >5[46]) and post-oxidation polishing process may be required to convert the aldehyde groups into carboxylate groups if necessary. Quantitative analysis of ^{13}C NMR signals was not conducted to evaluate the carboxylate/aldehyde content (calibration of the carbon signal would be required to correlate the peak intensity to the carboxylate/aldehyde content). It was used to qualitatively compare the conversion of C6 hydroxyl groups to carboxylates based on comparison to previously published data,[31] but this could be applied in the future to cross-check with the results from conductometric titration.

Table 4.1 Summary of the electro-oxidation results for α-cellulose in the presence of 10 m*M* TEMPO in 0.1 *M* carbonate buffer at pH 10

Charge consumption / C	Carboxylate / g·mol^{-1}	Aldehyde / g·mol^{-1}	Carboxylate /Aldehyde	DP_v	Mass recovery / %	Faraday efficiency / %	Crystallinity / %	
							Segal's method	Rietveld refinement
0	0	0	-	1088	100	-	56	41
77	0.1	0.1	1	399	-	-	-	-
163	0.1	0.2	1	370	-	-	-	-
249	0.3	0.2	1	356	-	-	-	-
341	0.7	0.3	3	339	93	86	-	-
350 (t=4 °C)	0.9	0.5	2	385	88	97	-	-
539	1.1	0.5	2	344	91	89	65	58
540 (glassy carbon counter electrode)	1.1	0.5	2	340	85	87	-	-

The potential limitation for this method to be scaled up would be the intial investment in the electrodes used in the system and the replacement cost of the electrodes after the life cycle. Meanwhile, the expensive platinum cathode could be replaced by a cheaper glassy carbon electrode, leading to a similar result of carbonyl content and

efficiency. It is also worth mentioning that membrane separation is necessary between the cathode chamber and the anode chamber to avoid reduction of $TEMPO^+$ (or other side reactions) when the reaction is scaled up, otherwise a significant decrease in efficiency would be expected[47].

Oxidised cellulose produced by electro-oxidation and chemical oxidation showed similar fibrils morphology and thermal stability. The difference between electro-oxidation and the chemical oxidation in the NaClO/NaBr/TEMPO system was a higher content of aldehyde groups formed on the surface using electrochemistry, due to the lack of efficient oxidant converting aldehydes into carboxylate. Therefore, a post-polishing step is necessary if low aldehyde content is essential for the final product.

4.4 References

1. A. E. J. de Nooy; A. C. Besemer; H. van Bekkum, *Carbohydr. Res.,* 1995, **269**, 89-98.
2. A. E. J. de Nooy; A. C. Besemer; H. van Bekkum, *Tetrahedron,* 1995, **51**, 8023-8032.
3. Y. Okita; S. Fujisawa; T. Saito; A. Isogai, *Biomacromolecules,* 2011, **12**, 518-522.
4. S. C. Rastogi; S. Heydorn; J. D. Johansen; D. A. Basketter, *Contact Dermatitis,* 2001, **45**, 221-225.
5. R. A. Sheldon; I. W. C. E. Arends; G.-J. ten Brink; A. Dijksman, *Acc. Chem. Res.,* 2002, **35**, 774-781.
6. Y. Okita; T. Saito; A. Isogai, *Biomacromolecules,* 2010, **11**, 1696-1700.
7. J. Liu; R. Pelton; J. M. Obermeyer; A. Esser, *Biomacromolecules,* 2013, **14**, 2953-2960.
8. T. Isogai; T. Saito; A. Isogai, *Biomacromolecules,* 2010, **11**, 1593-1599.
9. S. Sadhasivam; S. Savitha; K. Swaminathan; F.-H. Lin, *Process Biochem.,* 2008, **43**, 736-742.
10. I. W. C. E. Arends; Y.-X. Li; R. A. Sheldon, *Biocatal. Biotransform.,* 2006, **24**, 443-448.
11. E. Aracri; T. Vidal; A. J. Ragauskas, *Carbohydr. Polym.,* 2011, **84**, 1384-1390.
12. J. Kulys; R. Vidziunaite, *J. Mol. Catal. B: Enzym.,* 2005, **37**, 79-83.
13. Y. Jin; K. J. Edler; F. Marken; J. L. Scott, *Green Chem.,* 2014, **16**, 3322-3327.
14. P. Parpot; K. Servat; A. Bettencourt; H. Huser; K. Kokoh, *Cellulose,* 2010, **17**, 815-824.
15. T. Saito, et al., *Biomacromolecules,* 2009, **10**, 1992-1996.
16. R. Barhdadi, et al., *J. Appl. Electrochem.,* 2007, **37**, 723-728.
17. D. O. Carlsson; J. Lindh; L. Nyholm; M. Stromme; A. Mihranyan, *RSC Advances,* 2014, **4**, 52289-52298.
18. A. Marjasvaara; M. Torvinen; P. Vainiotalo, *J. Mass Spectrom.,* 2004, **39**, 1139-1146.
19. T. Isogai; T. Saito; A. Isogai, *Cellulose,* 2011, **18**, 421-431.
20. T. Saito; I. Shibata; A. Isogai; N. Suguri; N. Sumikawa, *Carbohydr. Polym.,* 2005, **61**, 414-419.
21. W. Hug; J. Divisek; J. Mergel; W. Seeger; H. Steeb, *Int. J. Hydrogen Energy,* 1992, **17**, 699-705.
22. T. Saito; S. Kimura; Y. Nishiyama; A. Isogai, *Biomacromolecules,* 2007, **8**, 2485-2491.
23. G. Holst, *Chem. Rev.,* 1954, **54**, 169-194.
24. D. Jaušovec; R. Vogrinčič; V. Kokol, *Carbohydr. Polym.,* 2015, **116**, 74-85.
25. L. S. Wong; F. Khan; J. Micklefield, *Chem. Rev.,* 2009, **109**, 4025-4053.
26. H. Koga; T. Kitaoka; A. Isogai, *J. Mater. Chem.,* 2012, **22**, 11591-11597.
27. L. Dai, et al., *Fibers Polym,* 2015, **16**, 319-325.
28. R. Shinoda; T. Saito; Y. Okita; A. Isogai, *Biomacromolecules,* 2012, **13**, 842-849.
29. J. Rossmeisl; A. Logadottir; J. K. Nørskov, *Chem. Phys.,* 2005, **319**, 178-184.
30. Y. Fan; H. Hu; H. Liu, *J. Power Sources,* 2007, **171**, 348-354.
31. A. Isogai; Y. Kato, *Cellulose,* 1998, **5**, 153-164.

32. M. F. Semmelhack; C. S. Chou; D. A. Cortes, *J. Am. Chem. Soc.,* 1983, **105**, 4492-4494.
33. I. Shibata; A. Isogai, *Cellulose,* 2003, **10**, 335-341.
34. I. Dalle-Donne; R. Rossi; D. Giustarini; A. Milzani; R. Colombo, *Clin. Chim. Acta,* 2003, **329**, 23-38.
35. J. S. Moulthrop; R. P. Swatloski; G. Moyna; R. D. Rogers, *Chem. Commun.,* 2005, 1557-1559.
36. M. Hirota; K. Furihata; T. Saito; T. Kawada; A. Isogai, *Angew. Chem. Int. Ed.,* 2010, **49**, 7670-7672.
37. M. Hirota; N. Tamura; T. Saito; A. Isogai, *Cellulose,* 2012, **19**, 435-442.
38. T. Saito; A. Isogai, *Biomacromolecules,* 2004, **5**, 1983-1989.
39. B. Sun; C. Gu; J. Ma; B. Liang, *Cellulose,* 2005, **12**, 59-66.
40. C. Lee, et al., Springer Berlin Heidelberg, 2015, p 1-17.
41. A. Thygesen; J. Oddershede; H. Lilholt; A. B. Thomsen; K. Ståhl, *Cellulose,* 2005, **12**, 563-576.
42. D. da Silva Perez; S. Montanari; M. R. Vignon, *Biomacromolecules,* 2003, **4**, 1417-1425.
43. K. Benaissi; L. Johnson; D. A. Walsh; W. Thielemans, *Green Chem.,* 2010, **12**, 220-222.
44. X. X. Sun; Q. L. Wu; S. X. Ren; T. Z. Lei, *Cellulose,* 2015, **22**, 1123-1133.
45. H. Fukuzumi; T. Saito; Y. Okita; A. Isogai, *Polym. Degrad. Stab.,* 2010, **95**, 1502-1508.
46. T. Saito; Y. Nishiyama; J.-L. Putaux; M. Vignon; A. Isogai, *Biomacromolecules,* 2006, **7**, 1687-1691.
47. H. Liu; B. E. Logan, *Environ. Sci. Technol.,* 2004, **38**, 4040-4046.

Chapter 5 Pickering emulsion stabilised by oxidised cellulose Nanofibrils

5.1 Introduction

Pickering emulsions rely on solid particles (the emulsifier), adsorbed at the interface between two immiscible phases, to stabilise the emulsion.[1] Pickering emulsions are kinetically stable due to the steric hindrance or/and electrostatic repulsion of solid particles acting as barriers between droplets to prevent coalescence.[2] The difference in wettability of particles (hydrophilic or hydrophobic nature of the surfaces) changes the formation of emulsions significantly. Oil-in-water (o/w) emulsions form favourably when the emulsifiers are more hydrophilic, while water-in-oil (w/o) emulsions are stabilised if the emulsifiers are hydrophobic.[3]

O/w emulsions stabilised by surfactants or solid particles (e.g. polymers, proteins) occur widely in daily life. However, common surfactants add burden to waste water treatment and suitable polymers tend to be expensive and synthetic, so may not be environmental friendly and bio-compatible.[4] Some natural polymers can be used as alternatives, but they are generally from food competitive sources or hard to process.[5,6] Oxidised cellulose nanofibrils (OCNF), prepared by selective oxidation of cellulose via chemical-, electro-, or enzymatic-oxidation, followed by mild mechanical treatment, is a new type of renewable bio-material. It is used as a rheology modifier, an alternative emulsifier to surfactants from petrochemical sources and can replace non-biodegradable materials, such as silicones.[7-9] While OCNF cost will depend on economies of scale, production processes are currently being scaled up (Nippon Paper), or have been tested at scale (Croda), so the cost is expected to become more competitive. Full cost/benefit analyses would need to be conducted before OCNF are used in formulations to replace polymers, but this is beyond the scope of this thesis.

O/w Pickering emulsions stabilised solely by OCNF have not been reported so far. One patent by Unilever described the use of OCNF to form an emulsion along with other surfactants, but the role of OCNF in the emulsion was not fully investigated.[10] Most papers regarding Pickering emulsions stabilised by cellulose derived materials

concern the use of microfibrillated cellulose (also referred to as nanofibrillated cellulose), hydrophobised OCNF (to form a w/o emulsion) or cellulose nanocrystals which have very different aspect ratios and surface properties to OCNF.[11,12] The morphology of the cellulose fibrils or rods at the oil/water interface also has not been explored in the real environment. Most investigations used SEM, or AFM on dried emulsion samples, where the drying process could potentially change the morphology. Optical microscopy does not give high enough resolution to identify the individual particles at the interface.[13,14]

In this work, an OCNF suspension, prepared by TEMPO mediated oxidation followed by ultrasonication, was used to stabilize the hexadecane/water interface to form o/w Pickering emulsions. The stability of the emulsions, droplet sizes, and shell thicknesses under different conditions were investigated to provide a clear understanding of the structure of the emulsions and to elucidate the effects of addition of formulation ingredients.

5.2 Results and discussion

5.2.1 OCNF characterisation

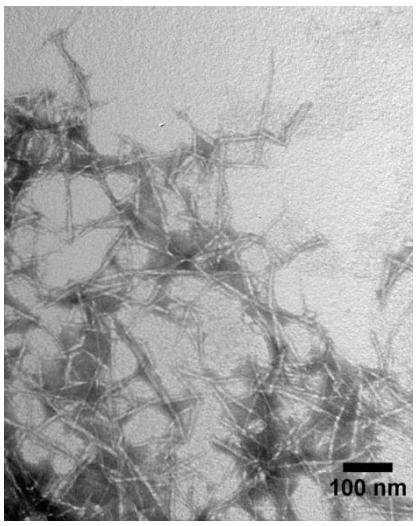

Figure 5.1 TEM image of 0.01 wt% OCNF dispersion, negatively stained by uranyl acetate.

Analysis of the dimensions of OCNF particles, visualised using TEM (Figure 5.1), yields a number average value of the width of 4.5 ± 1.5 nm (Figure 5.2) and several microns in length. This result is in accordance with most other authors working on

OCNF who reported sizes for the individual nanofibres.[7,15] Characteristic features of the OCNF dispersion are the negatively charged fibrils, large aspect ratios and entangled interactions which cause formation of a mesh of nanofibrils upon drying onto the TEM grid, compared to cellulose nanocrystals, which dry as individual rods.[16-18]

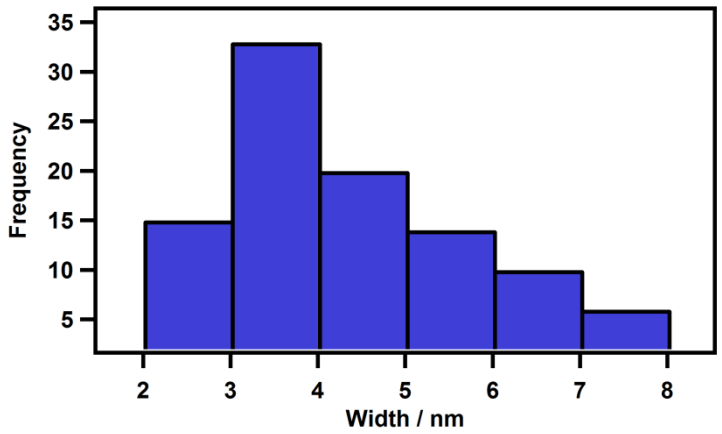

Figure 5.2 Histogram of width distributions of OCNF from TEM image analysis using imageJ, a total measurement of 100 particles was conducted.

5.2.2 Emulsion characterisation

A range of o/w emulsions were formed at a 30 to 70 volume ratio of oil (hexadecane) to aqueous OCNF dispersion, with no added surfactant. The aqueous dispersions consisted of OCNF at concentrations ranging from 0 to 15 $g \cdot L^{-1}$ and emulsification was achieved by ultrasonication, resulting in stable o/w Pickering emulsions (Figure 5.3). The emulsion pH remained at *ca* 7 (matching that of the input OCNF dispersions) and was not adjusted.

The stability of the emulsion, droplet size, and thickness of the OCNF shell at the hexadecane-water interface were investigated. Centrifugal force was used to accelerate the creaming process of the emulsion. The excess aqueous phase was excluded from the emulsion after this process, resulting in close packing of the droplets (Figure 5.3). A rotational speed of 4000 revolutions per minute (rpm) was found suitable for the emulsion stability test. The volume change of the emulsion layer was recorded before and after centrifugation.

Before centrifugation, the emulsion layer (Figure 5.3a) increased gradually with the increased concentration of OCNF in the suspension (illustrated by the white layer formed in the Eppendorf tubes in the figure), indicating that oil droplets were effectively surrounded by OCNF at higher solid particle content and that these were effectively distributed throughout the continuous phase. After centrifugation (Figure 5.3b), excess OCNF aqueous dispersion was excluded from the emulsion, and the concentrated emulsion layer formed was resistant to the force induced by centrifugation for all except the lowest concentrations of OCNF. The emulsion layer remained stable after centrifugation for all concentrations above 3 $g \cdot L^{-1}$ OCNF, suggesting strong adsorption of OCNF at the oil-water interface. The critical OCNF concentration for stabilising the emulsion is dependent on the effective surface coverage of the solid particles on the oil droplet surface. This variable has been extensively studied by the group of Capron *et al* (*ca* 44% coverage value was essential for the emulsion stabilised by CNC,[13] and this value decreased with increasing crystal length[19]). The critical surface coverage was calculated to be *ca* 45% for Pickering emulsion stabilised by OCNF, similar to the value for CNC.

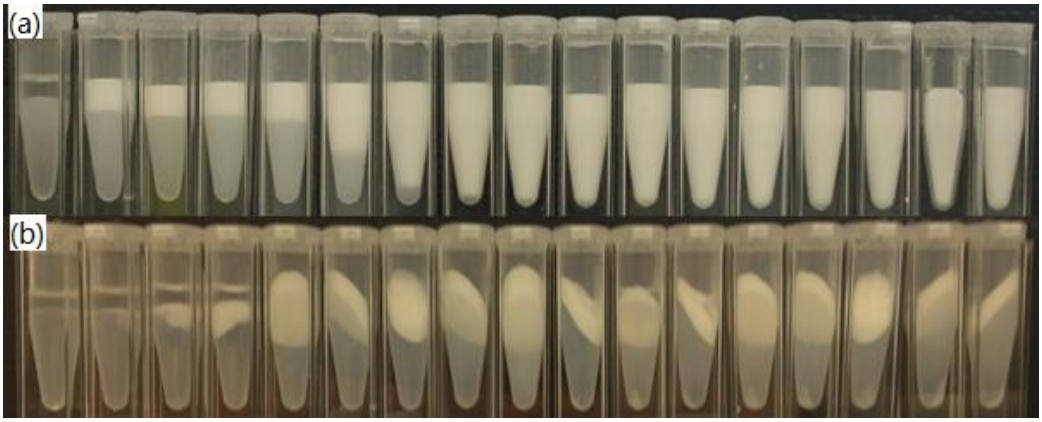

Figure 5.3 Photographs of o/w emulsions with increasing concentrations of OCNF in the aqueous phase from 0 to 15 $g \cdot L^{-1}$ taken (a) 24 h after emulsification and (b) after centrifugation at 4000 rpm for 30 min.

Droplet diameter measurements (Figure 5.4) indicated the occurrence of coalescence at low concentration of oxidised cellulose, which supports the appearance of an un-emulsified oil phase following centrifugation (Figure 5.3b). A

favoured droplet size of *ca* 1.9 ± 0.2 µm was observed for the stable emulsions containing more than 3 $g \cdot L^{-1}$ OCNF in the aqueous phase (the droplet size is an indicator of emulsion stability which is also dependent on the size of the solid particles and the viscosity of the mixture).[20]

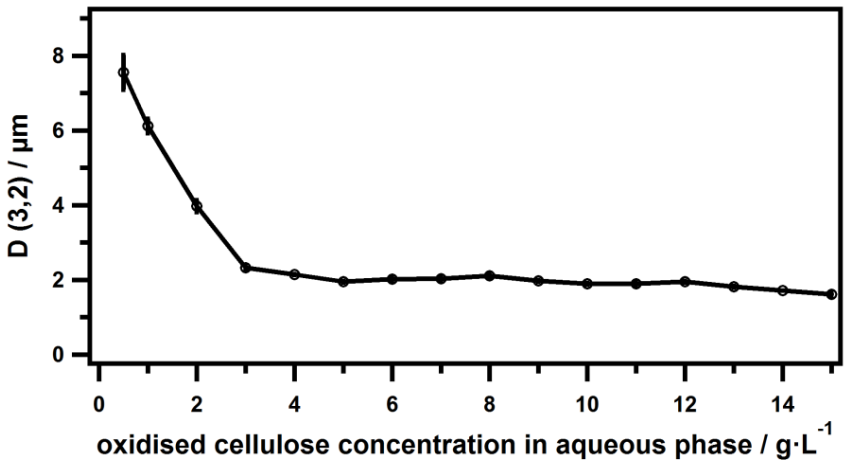

Figure 5.4 Droplet diameter D(3,2) measured as a function of OCNF concentration in the aqueous phase.

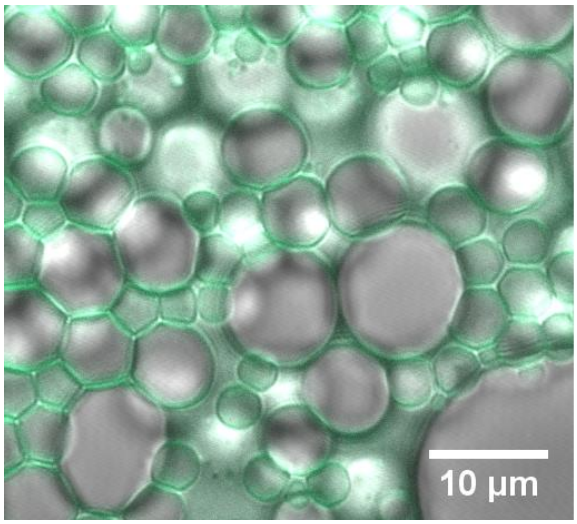

Figure 5.5 Confocal laser scanning micrograph of droplets stabilized by OCNF with fluorescent staining. The sample is taken from the emulsion layer produced post centrifugation of an emulsion formed using 8 $g \cdot L^{-1}$ of CONF.

The assembly of oxidised cellulose at the oil/water interface was probed by confocal laser scanning microscopy (CLSM). Fluorescent staining of OCNF allowed the existence of the OCNF particles adsorbed at the hexadecane/water interface to be

clearly identified, visualized as green particles using CLSM. In Figure 5.5, the green boundaries indicated the formation of the OCNF shell, preventing the oil droplets from coalescence. It should be noted that the image was taken using the condensed emulsion layer after centrifugation. An as-made emulsion was also taken for CLSM and the green boundaries were observed visually, but the difference in colour was not distinguishable using the CCD camera.

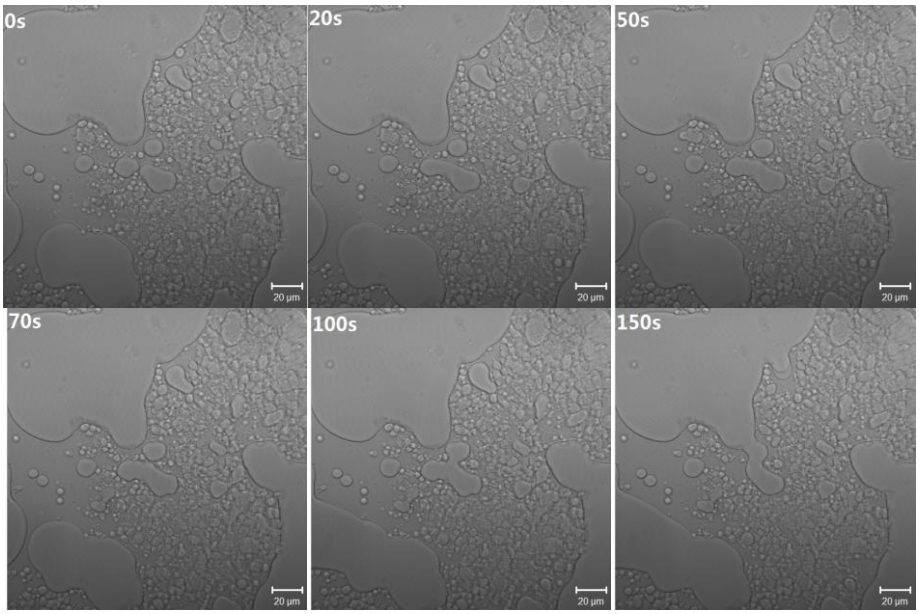

Figure 5.6 Time-lapse image of emulsion stabilised by OCNF upon adding 1 vol% ethanol.

When small amount of ethanol was added into the emulsion (after the emulsion formed), the emulsion droplets became unstable and merged together over a short time (Figure 5.6). The result indicated that the OCNF shells, formed on the surface of the emulsion droplets, were porous and permeable (ethanol dissolved hexadecane and formed a miscible solution). This will be further discussed in detail in the later section.

In order to determine the emulsion type (o/w or w/o), the contact angle of OCNF at the hexadecane/water interface was calculated using Young's equation (Equation 5.1). The result confirmed that an o/w emulsion (contact angle $\theta < 90°$) was formed in the presence of OCNF.[21,22]

$$\cos\theta_{ow} = \frac{\gamma_{os} - \gamma_{ws}}{\gamma_{ow}} = \frac{\gamma_{wv}\cos\theta_{WCA} - \gamma_{ov}\cos\theta_{HCA}}{\gamma_{ow}}$$

$$= \frac{72\cos 33 - 27\cos 12}{44} = 0.77 \qquad \textbf{(5.1)}$$

$$\theta_{ow} = 39°$$

Where θ_{ow} is the contact angle of OCNF at the oil/water interface, γ_{wv} is the surface tension at water/air interface, γ_{ov} is the surface tension at the oil/air interface and γ_{ow} is the surface tension at the water/oil interface in the presence of OCNF. The surface tension for OCNF suspensions was determined by the Du Noüy ring method (see Chapter 2 section 2.2.2.11).

5.2.3 Droplet diameter response to NaCl and pH

To test the stability of the emulsion in the presence of salt (commonly used in formulations for personal care products), different amounts of NaCl were added into the emulsion to make the required concentration in the aqueous solution (0.1 *M*, 0.5 *M* and 1.0 *M*). The stability of the emulsion was evaluated by measuring the diameter of the emulsion droplets via laser diffraction. For a stable emulsion the droplet diameter should be constant and would be expected to be similar to that of the emulsion stabilised by OCNF without NaCl, i.e. ca 2 μm, based on the results shown in Figure 5.4.

The diameter of the emulsion droplets changed rapidly in the low oxidised cellulose concentration region (from 0.5 g·L^{-1} to 5 g·L^{-1}) in the presence of NaCl in the aqueous phase, similar to the phenomenon observed in the salt-free emulsion (Figure 5.7). Once the concentration of OCNF reached a critical value, the droplet diameter remained constant despite the increasing OCNF content (the diameter was dependant on the interfacial tension, the power input and the viscosity of the continuous phase),[23,24] and the emulsions were stable against centrifuge force (see appendices). The diameter of the emulsion droplets in the presence of salt followed a sequence of: D (0.1 M NaCl) > D (0.5 M NaCl) > D (1 M NaCl) > D (0 M NaCl), which corresponds to the surface tension of the oxidised cellulose suspension at

hexadecane/water interface (Figure 5.8). The result was in agreement with Tolman's study suggesting that the droplet size increased with increasing surface tension.[25]

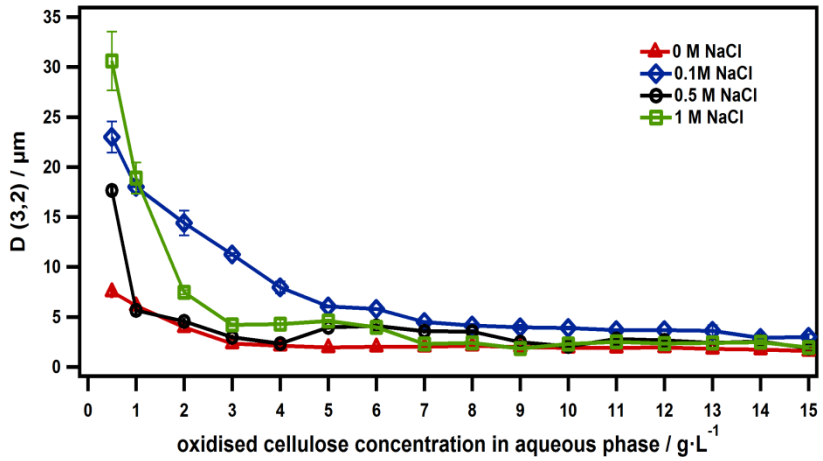

Figure 5.7 Droplet diameter measured as a function of salt concentration in the aqueous phase and oxidised cellulose concentration in the suspension.

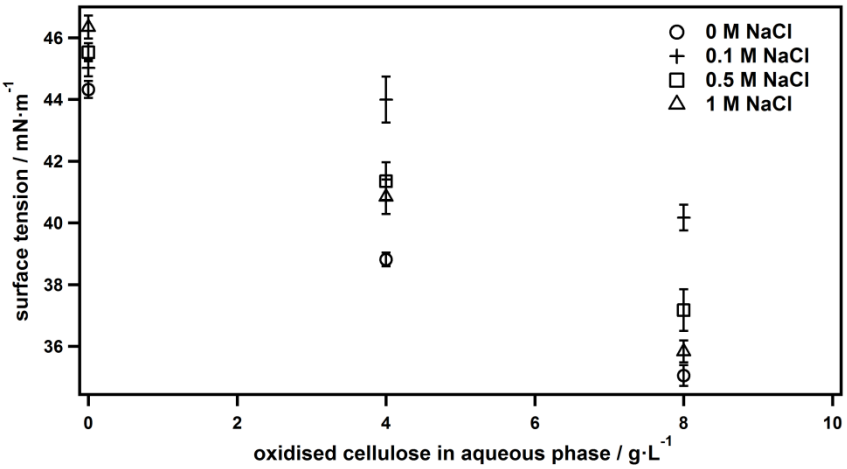

Figure 5.8 Surface tension at the hexadecane/water interface measured as a function of OCNF and NaCl concentration in the aqueous phase.

With the increased concentration of NaCl, it was expected that the surface tension should increase accordingly due to the increasing attraction among surface particles.[26] However, the presence of OCNF at the hexadecane/water interface, resulted in lowered surface tension (Figure 5.8), probably due to the disruption of hydrogen bonding of water. It was noted that the highest surface tension in the presence of OCNF was measured at 0.1 *M* NaCl rather than at higher salt concentrations. The surface tension decreased gradually with increasing amounts of

salt, due to charge screening of OCNF. This suggested that OCNF became both less hydrophilic and more able to overlap with other OCNF fibrils at the interface. At the highest salt concentrations flocculation was expected, which would remove material from the interface due to sedimentation under gravity, allowing surface tension to increase, although this was not observed at the salt concentrations measured here. We noted that non-oxidised cellulose nanofibrils were reported to flocculate when exposed to 0.1 *M* NaCl,[27] while CNC underwent sedimentation when the concentration of NaCl exceeded 0.05 *M*.[28] It is hypothesised that these phenomena could be ascribed to direct repulsion and a charge neutralisation mechanism. It is suggested that the repulsion between Cl^- and negatively charged OCNF but lower charge density particles "pushed" the entangled oxidised cellulose fibrils towards the interface,[8] hence lowering the surface tension. A similar effect has also been observed for graphene oxide (GO) at the toluene / water interface, where the GO became more hydrophobic and decreased the interfacial tension when the pH dropped.[29] In addition, increased ionic strength (more Na^+ and Cl^- in the aqueous phase) resulted in the screening of the surface charge on the fibrils, causing a decrease in the Debye length (Figure 5.9). Thus more fibrils diffused to the interface thus lowering the surface tension more significantly. To test these hypotheses, SEM, AFM were used to visualize the evolution of OCNF at oil/water interface, while SAS and rheology experiments were used to *in situ* investigate the OCNF at the interface, under various NaCl concentrations.

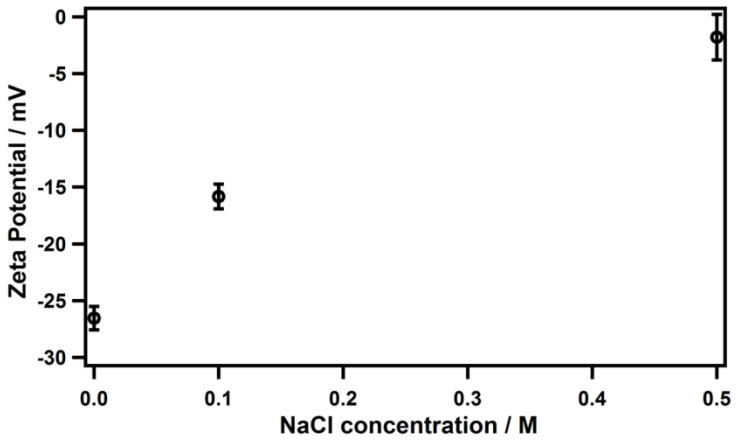

Figure 5.9 Zeta potential of 8 $g \cdot L^{-1}$ OCNF suspension with varying NaCl concentration.

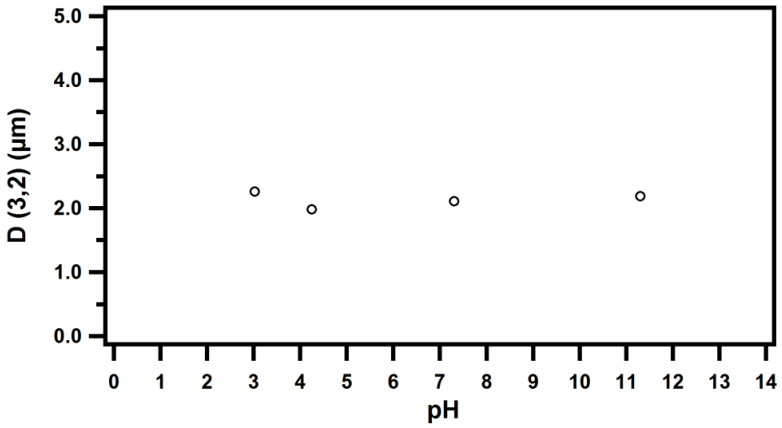

Figure 5.10 Droplet diameter in emulsions of hexadecane in water stabilised by OCNF (8 g·L^{-1}) measured as a function of pH, with error bars reflecting variation in triplicate measurements (too small to be visible).

The effect of pH on the droplet size in the emulsion was also investigated, as many formulations required different acidic/basic environments. The droplet size remained stable over the pH values tested (Figure 5.10), suggesting the adsorption behaviour of OCNF at the hexadecane/water interface remains the same under the conditions tested (the functional groups on the OCNF surface are changed from COO^- at neutral/basic pH to COOH at acidic pH). Emulsions at the four different pHs all maintained a condensed emulsion layer against centrifuge force, indicating the emulsion droplets' stability against coalescence. This stability is ascribed to the similar amphiphilicity of OCNF over the pH tested, as the contact angle of OCNF at the hexadecane/water interface remained similar ($\theta_{ow} = 40°$ at pH 2, $\theta_{ow} = 39°$ at pH 7, as calculated by Equation 5.1).

5.2.4 Shell Thickness of Emulsion Droplets

The OCNF boundaries at the oil/water interface were also visualised by SEM. In this experiment, hexane was used as the oil phase as its low boiling point facilitated removal by freeze drying, and the emulsion droplet diameter was *ca* 2.5 µm. The sphere-like continuous shell, remaining after removing oil and water out of the system, confirmed that the OCNF formed a shell structure on the emulsion droplets surfaces (Figure 5.11a). The bigger droplet size (*ca* 4 to 10 µm) observed in the SEM image was ascribed to some merging of multiple smaller droplets (coalescence) during the drying process. Some sheet-like structures were also observed in the

SEM images, suggesting some OCNF remained in the aqueous phase (similar structures have been reported in OCNF gels without oil droplets[30]).

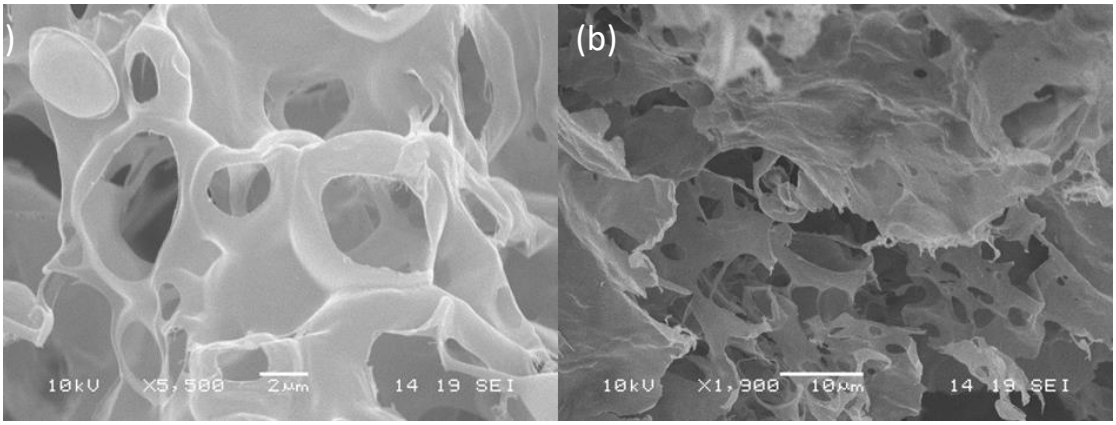

Figure 5.11 SEM images of a freeze-dried Pickering emulsion stabilised by 8 g·L^{-1} OCNF (a) showing spherical structures remaining once oil and water are removed and (b) showing the presence of some sheet like structures.

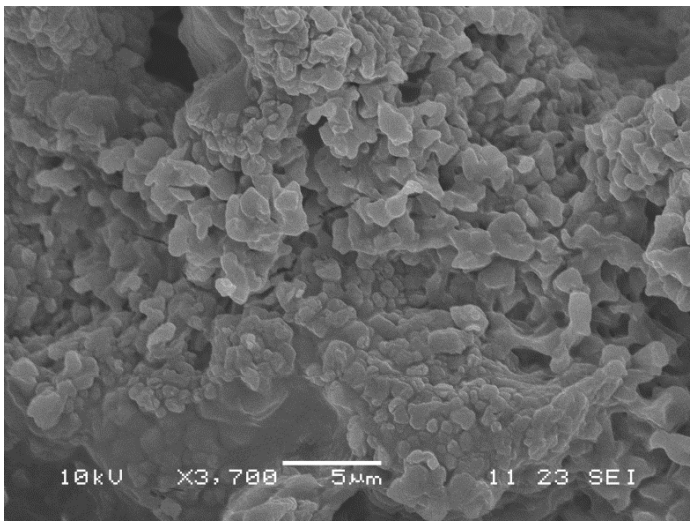

Figure 5.12 SEM image of an emulsion stabilised by 8 g·L^{-1} OCNF with 1 *M* $CaCl_2$ after the freeze-drying process.

The SEM image of the freeze-dried emulsion in the presence of salt ($CaCl_2$ was used here to form a stronger interconnected network via ionic cross-linking,[31] compared to the aggregation induced by NaCl[28]) indicated that thicker shells formed at the hexadecane/water interface at high salt concentration (Figure 5.12), as the OCNF shell did not break up during the drying process. However, as mentioned previously, these images may not demonstrate the real structure of the shell before

drying as drying is known to induce formation of aggregated and sheet-like structures in dried OCNF dispersions.[32]

Neither CLSM nor SEM represented the real morphology of the fibrils at the interface due to the low resolution for CLSM and aggregation effects of the fibrils in the shell during freeze-drying for SEM. To obtain a better understanding of the morphology of the OCNF shell at the emulsion surface, atomic force microscopy (AFM) was used to examine the emulsion with polymerizable styrene as the oil phase. OCNF showed a similar ability to stabilise styrene and hexadecane droplets, so it was assumed that the styrene/water emulsion could represent the hexadecane/water system (the diameter of the emulsion droplets was comparable, *ca* 2.5 µm for styrene/water emulsion).[33] Since the oil phase was polymerized once the emulsion formed, the OCNF assembled at the emulsion droplet surface would be immobilised, showing a more realistic morphology of the shell. The AFM image illustrated that the OCNF shell did not form a continuous film at the emulsion surface as determined by the roughness of the oval surface, but entangled together as a flexible mesh bending onto the interface. The morphology of the OCNF was similar to that reported in the existing literature where Kalashnikova *et al* reported the morphology of OCNF on a flat surface,[34] (Figure 5.13). This was similar to the TEM image of the OCNF suspension observed in Figure 5.1, but different from the morphology of a Pickering emulsion stabilised by cellulose nanocrystals. OCNF has a much larger aspect ratio and more flexibility compared to cellulose nanocrystals, which allow the fibrils to become entangled.[35,36]

It was noted that the diameter of the emulsion droplet observed in AFM (Figure 5.13) was much smaller than that determined by laser diffraction (*ca* 2.5 µm), which was the ascribed to the shrinkage of the polystyrene droplets during polymerisation and during the drying process (although possible also due to the formation of smaller droplets in the initial stage after sonication).[37] The apparently oval shape of the droplets were due to shape artefacts of the AFM tips on curved surfaces,[38] which can be improved by adopting a shaper tip (with much higher cost).[39] Combining this images with the results from confocal microscopy, laser diffraction and SEM, the AFM image was able to illustrate the assembly of OCNF on the droplet surface.

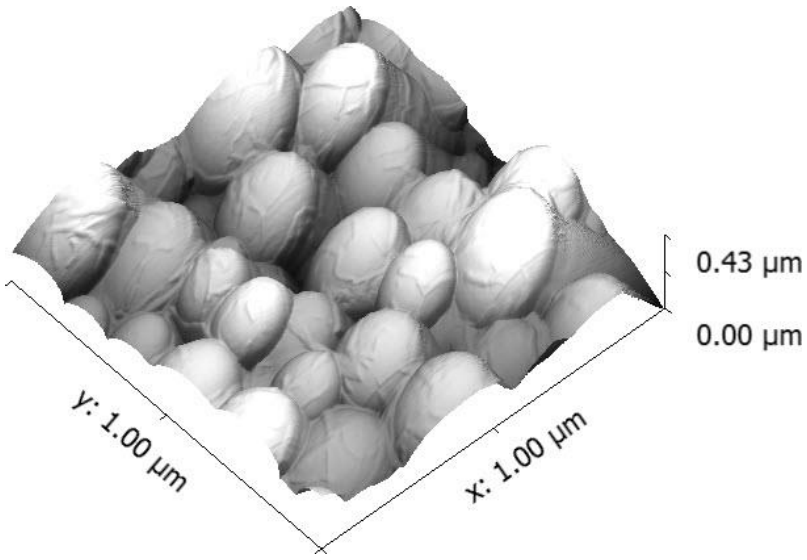

Figure 5.13 AFM image of a dried polymerized styrene/water emulsion stabilized by 8 $g \cdot L^{-1}$ OCNF in the absence of salt.

Based on the previous results of the emulsion characterisation and the SEM images of freeze-dried emulsion with or without salt, it was proposed that, the OCNF shell, adsorbed at the oil/water interface, responded positively to the increase in ionic strength in solution. That is, the higher the salt concentration, the thicker the shell formed. The salt-responsive phenomenon of the OCNF shell is very interesting and has practical application for tuning emulsion stability and drug delivery.

The focus here is to determine the evolution of the shell thickness in response to the increasing ionic strength (NaCl concentration). However, it was not viable to quantitatively determine the shell thickness by CLSM, SEM or AFM analysis, due to the low resolution, or the morphology change of the shell during the drying process.

Small angle scattering (SAS) is a very reliable technique to probe core-shell structured systems based on the scattering length density (SLD) difference.[40] In addition, SAS is a non-invasive technique to obtain in-situ structural information from a solution, which allows studies of the sample in its real environment. Therefore, the change of the OCNF shell thickness was probed directly using SAS in the presence of different NaCl concentrations.

The physical model for the emulsion shell used to fit the data is illustrated in Figure 5.14, based on the AFM study. The OCNF particles entangled with each other onto

the surface of the emulsion droplet as a mesh, where oil and/or water could penetrate into the pores of the mesh network.

Figure 5.14 Cartoon of OCNF morphology on the emulsion droplet surface.

The SAS data from the emulsion system was fitted using the "PolyCore_and_NShells" model in the NCNR SANS Analysis package within IGOR Pro which describes a sphere having a polydisperse core, surrounded by up to four shells of different SLD.[41,42] For this data, a model containing two shells was used as it was envisaged that OCNF could be found at the interface, but largely in the aqueous phase, or at the interface and penetrated into the oil phase. The SLD for the shell was modified, (refer to Chapter 2 for details), since the OCNF was postulated to exist in both oil and aqueous phases due to its amphipathic nature, so the inner shell was described an OCNF/oil mixture, while the outer shell was composed of OCNF with water.

In the model, as the size of the emulsion droplets was outside of the detection range of the SAS instrument, the fitting is insensitive to the size of the droplet core and the core radius was set at a constant value of 10000 Å. The core polydispersity was set as 0.3 (refer to Chapter 2 for the calculation), based on the laser diffraction pattern in Figure 5.15. It should be noted that the distribution patterns of the diameter varied among samples, affecting the corresponding polydispersity values. However, altering the polydispersity above 0.3 had little influence on the fitting results.

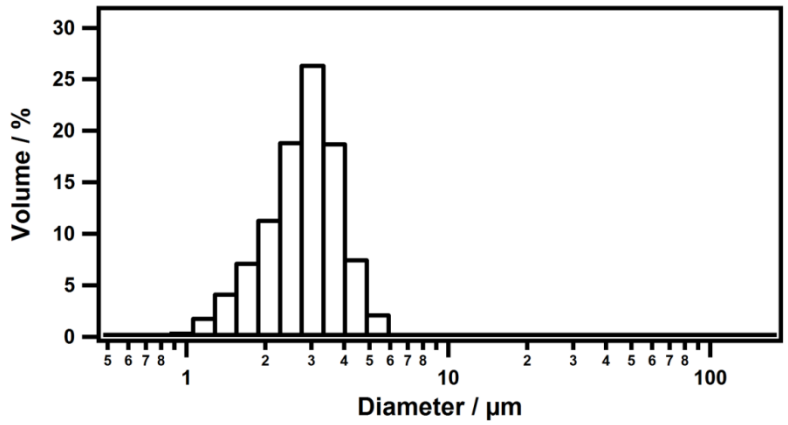

Figure 5.15 Histogram of diameter distribution of emulsion droplets from laser diffraction used to set the polydispersity value used in modelling of the SAS data.

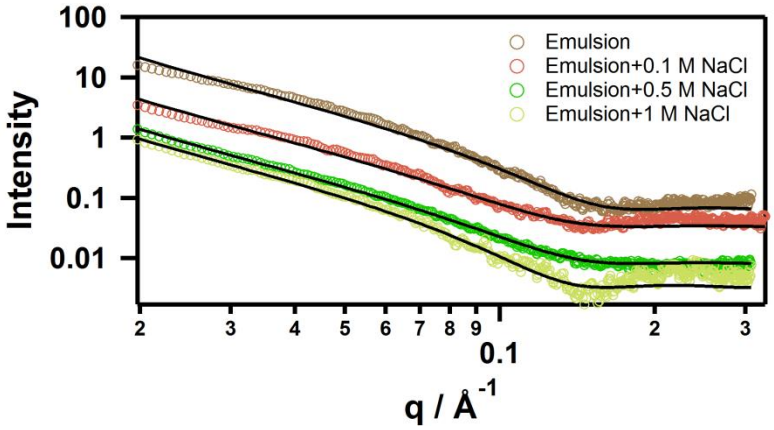

Figure 5.16 SAXS patterns of the hexadecane/water emulsion stabilised by ONCF (8 g·L^{-1}) at different NaCl concentrations (the scattered curves are offset for clarity); solid lines are the fits to the data using the model described above.

Small angle X-ray scattering (SAXS) was initially adopted to evaluate the evolution of the OCNF shell in the presence of various amounts of NaCl, as the SAXS instrument was easier to access compared to SANS. In addition, the SAXS experiments provided rapid results, providing some preliminary information on the emulsion system.

The SAXS data and the corresponding fitting curves are displayed in Figure 5.16. The fitting model in this case required only one shell of solvent/OCNF around the polydisperse droplet core instead of two shells, as the SLD for hexadecane and water is similar for X-rays therefore no difference would be observed for the two

shells. Fitting using a two shell model was also attempted, achieving a similar result, but was disregarded due to the extra parameters required to fit two shells, which were not justified for these data (only one dataset was available for each NaCl concentration). The fitting results showed that the OCNF shell thickness increased gradually (from 33 to 39 Å), which was not significant due to the poor contrast between the shell and aqueous phase, and the value of the water fraction in the shell was not reasonable (ca 1 vol%, suggesting the formation of a condensed shell). Therefore SAXS may not be sensitive enough to probe the structure changes in the shell composition.

Small angle neutron scattering (SANS) is a very commonly used technique to characterise such core-shell structures, as it highlights contrast between a H-rich material and a D-rich solvent.[43] Therefore, selective deuteration of the different components is frequently used to obtain a more detailed structural picture (Figure 2.9).[44] In Figure 5.17, the increase in intensity at low q, is correlated with increased NaCl concentration. The SLDs of the deuterated hexadecane and D_2O were similar, therefore they were contrast matched and only OCNF was visible at this contrast. Thus the increase in intensity suggests increasing thickness or density in regions containing OCNF, i.e. that the shell between oil and aqueous phases became thicker. This was in agreement with the SAXS results.

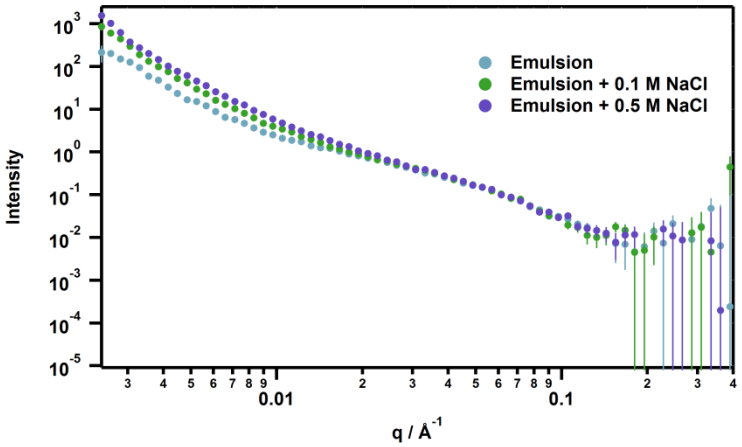

Figure 5.17 Experimental SANS patterns from a deuterated hexadecane/D_2O emulsion stabilised by ONCF (8 g·L^{-1}) at different NaCl concentrations (scattered points).

SANS measurements using different contrasts (exploiting the differences in SLD for H and D) were conducted to provide more reliable fitting, using two or three data sets of data to simultaneously fit a single model for each NaCl concentration. For instance, deuterated hexadecane/D_2O emulsion "detected" the structure of the shell as the SLDs were similar for the oil and aqueous phase, hexadecane/50wt % D_2O emulsion highlighted the droplet core and hexadecane/H_2O emulsion illustrated the entire droplet. Quantitative analysis of the change of the shell thickness was conducted for each NaCl concentration by fitting a model to the data. Figure 5.18 illustrates the SANS pattern and the corresponding fitting curves using the two shell sphere model for the emulsion in the absence of NaCl (refer to appendices for more SANS data in the presence of NaCl).

The evolution of the OCNF shell with increasing ionic strength, based on the SANS fitting results (Table 5.1) is illustrated in Figure 5.19. When there was no salt present in the emulsion system, the OCNF tended to be located in the aqueous phase due to its hydrophilic nature, and formed a single layer of OCNF/water in the outer shell. At low ionic strength (0.1 *M* NaCl), a more thicker but still hydrated shell formed (Table 5.1) and more OCNF moved to the hexadecane/water interface, as indicated by the decreased surface tension (Figure 5.8) and surface charge (Figure 5.9). At high ionic strength (0.5 *M* NaCl), the outer shell compressed into a denser state and part of the OCNF diffused into the oil phase creating a second OCNF/oil inner shell. A similar result has also been shown for Pickering emulsions stabilised by CNC, using SANS, where a charged CNC monolayer of thickness 70 Å formed at the oil-water interface (but the water fraction and the shell response to ionic strength were not determined in that case).[45] The densification of the shell by CNC aggregation was also demonstrated using uncharged CNC, which showed a very similar effect to the charge screening of OCNF, resulting in aggregation at the interface at high ionic strength.[45] This result was in good agreement with the SEM results, which indicated more OCNF was located at the interface on the droplet surfaces with increasing ionic strength, forming thicker shells.

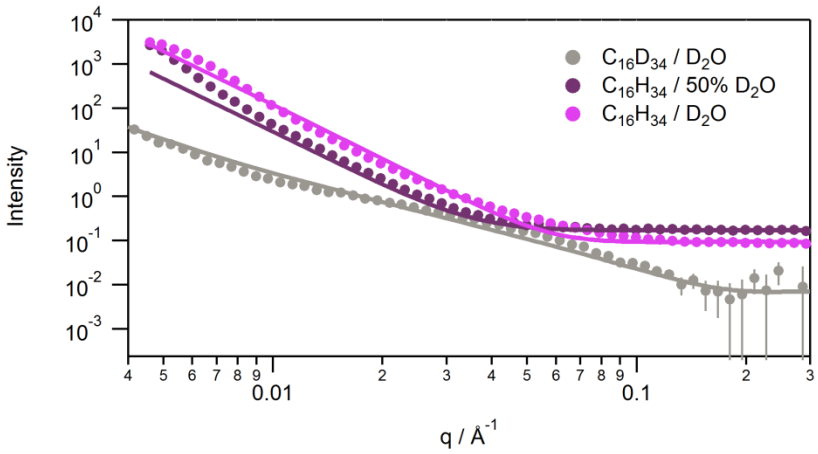

Figure 5.18 Experimental SANS patterns from a hexadecane/water emulsion stabilised by OCNF (8 g·L^{-1}) with different deuterated composition (circles); solid lines are the fitted curves.

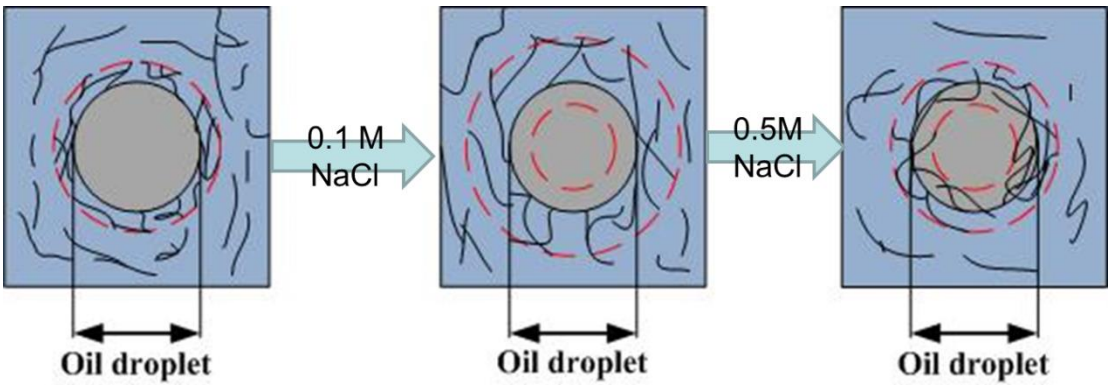

Figure 5.19. Evolution of ONCF shell thickness with increasing NaCl concentration. The red dashed circles show the boundaries for OCNF layers at the oil water interface. The OCNF formed a single-layer in the aqueous phase when no salt was added (left); in the presence of 0.1 *M* NaCl the OCNF shell became thicker and more hydrated, but did not penetrate into the oil phase (middle); while, in 0.5 *M* NaCl, the aqueous shell compressed and a second shell was formed when some of the OCNF moved into the oil phase (right).

Table 5.1 OCNF Shell thickness at hexadecane/water interface, T=25 °C.

sample	shell thickness at oil phase (Å)	Oil fraction in inner shell	shell thickness at aqueous phase (Å)	water fraction in outer shell
emulsion	0	1	26 ± 2	0.22 ± 0.05
emulsion + 0.1 M NaCl	0	1	63 ± 1	0.85 ± 0.01
emulsion + 0.5 M NaCl	14 ± 2	0.96 ± 0.13	22 ± 1	0.54 ± 0.04

5.2.5 Rheology

When NaCl was present in the emulsion, the sample started to gel. The rheological properties of the Pickering emulsions stabilised by OCNF at various ionic strength (different NaCl concentrations) are displayed in Figure 5.20a. The NaCl containing emulsions showed shear thinning behaviour, allowing them to easily spread across a surface under force and forming a thin layer of film when settled (similar to the personal care products used in daily life), which was consistent with the rheology behaviour of OCNF suspension (as OCNF was the actual rheology modifier in the emulsion that altered the viscosity).[46] The viscosity of the emulsion increased with increased OCNF (Figure 5.20b), due to the formation of a more rigid OCNF network.[47] In addition, the shear-thinning curve (Figure 5.20) can be divided into three distinctive regions over the shear rate: In region I, OCNF started to orient along the shear direction under the low shear force, resulting in a decrease in viscosity. In region II, a viscosity plateau was observed at low median rates, which was ascribed to the formation of a more entangled network due to the long aspect ratio of OCNF.[48] In region III, another shear thinning region at high shear rates corresponded to the disruption of the entangled network into more individual fibrils..[49] Therefore, the use of OCNF emulsions stabilised by various OCNF concentrations under different formulations could increase the viscosity of the products by adjusting the aqueous network,[19] and reduce the use of surfactants significantly.

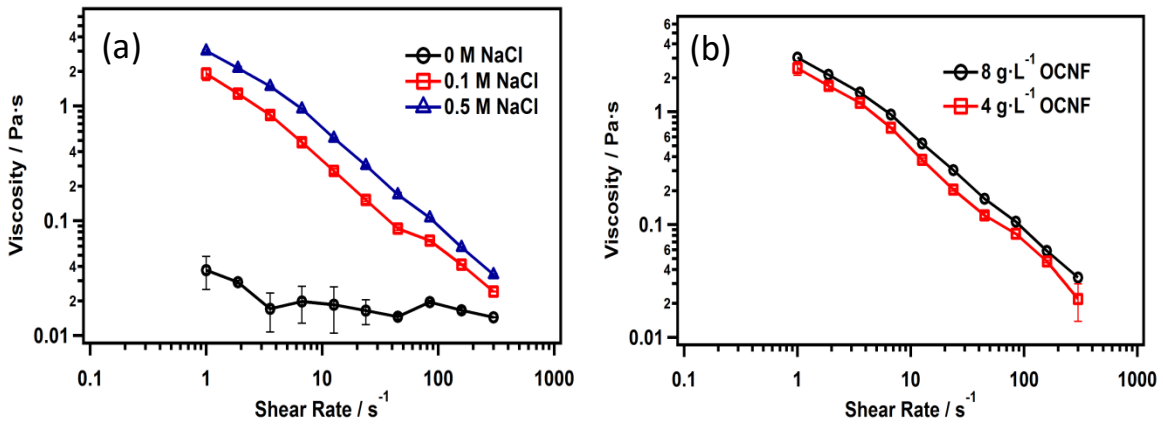

Figure 5.20 Steady shear viscosity versus shear rate of (a) hexadecane/water emulsions stabilised by 8 g·L^{-1} OCNF at various NaCl concentrations, and (b) hexadecane/water emulsion stabilised by 4 g·L^{-1} or 8 g·L^{-1} OCNF with 0.5 *M* NaCl.

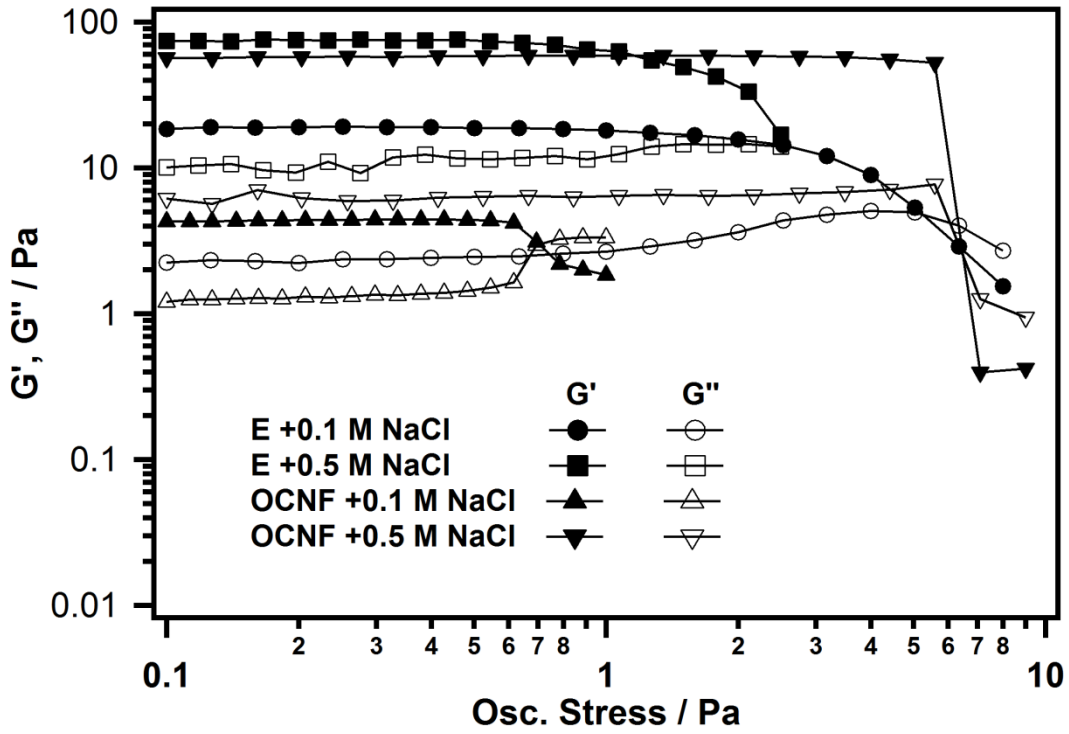

Figure 5.21 Storage modulus (G') and loss modulus (G'') versus stress curves for an 8 g·L^{-1} OCNF dispersion and hexadecane-in water emulsion stabilised by 8 g·L^{-1} OCNF with varying quantities of NaCl.

Oscillatory rheology was conducted here to study the OCNF network in the aqueous phase in the presence of NaCl (Figure 5.21). The crossover point of storage modulus (G') and loss modulus (G'') showed the yield stress of the sample deformation,[50] when the emulsion gel changed from an elastic-like solid to viscous liquid. For an OCNF dispersion (with no added oil), the yield stress increased with increased salt concentration (from 0.695 Pa at 0.1 *M* NaCl to 6.35 Pa at 0.5 *M* NaCl), implying that a stronger network formed due to the charge screening effect, which allowed greater contact interaction between fibrils at high ionic strength (Figure 5.9).[46] Similarly, the storage modulus and the yield stress increased with increased OCNF content, as a more rigid network formed.[51] However, the yield stress of the emulsion system decreased as the NaCl concentration increased (from 5.04 Pa at 0.1 *M* NaCl to 2.53 Pa at 0.5 *M* NaCl), in contrast to the behaviour of the OCNF dispersion alone. This contrary effect indicates a weaker network in the emulsion system in a higher ionic strength environment. At first this appears to be counterintuitive, but this phenomenon would actually be expected if the interpretation of the SANS results is

correct. At higher ionic strength, more fibrils were to be found at the hexadecane/water interface, therefore fewer fibrils would remain in the continuous aqueous phase to hold the emulsion network structure. Since the rheology is dominated by that of the continuous phase, a weaker gel results. The rheology results were in good agreement with the results from SANS studies; in both cases, the results were consistent with a larger fraction of the fibrils located at the oil-water interface at higher salt concentration. In contrast, in OCNF dispersions without added oil, all the fibrils remained distributed throughout the aqueous phase and charge shielding led to greater interfibrillar interaction and a stronger gel. The change in the amount of OCNF remaining in the aqueous phase with increasing NaCl concentration is illustrated in Figure 5.22, based on the rheology results.

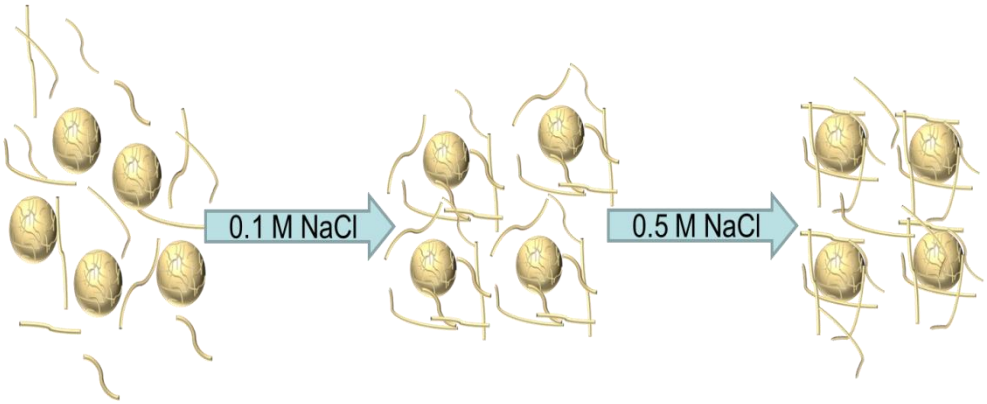

Figure 5.22 Evolution of ONCF in the aqueous phase of a hexadecane/water emulsion with increasing NaCl concentration.

5.2.6 Applications

5.2.6.1 Drug release

OCNF not only formed protective shells surrounding oil droplets creating stable emulsions, but also thickened the emulsion continuous phase leading to opportunities to tune rheology for various applications (e.g. lotions, creams) when adding salts, or surfactants (which were shown to enhance the stability of the emulsion[52]), in formulations. The responsive characteristics of the emulsion droplet shells, which exhibit thickening with altered ionic strength, have interesting potential applications in drug release control from emulsion formulations This proposal was

tested here by altering the NaCl content in a drug containing aqueous OCNF/oil emulsion and studying the effect on drug release rate.

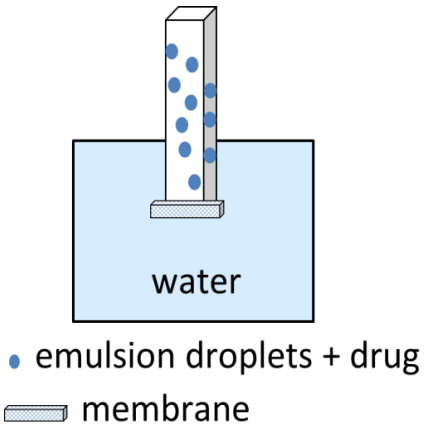

Figure 5.23 Set-up of the release experiment carried out using an emulsion containing an active ingredient.

To test the release control property of the emulsion, salicylic acid (7 $g \cdot L^{-1}$) dissolved in soybean oil (hexadecane was not used here due to the solubility problem of salicylic acid in hexadecane) was emulsified with an OCNF suspension (9 $g \cdot L^{-1}$ with different NaCl concentrations) at an oil/aqueous phase ratio of 30/70 vol%, to prepare an emulsion containing the active ingredient (salicylic acid). A set quantity of the resulting emulsion (1.5 mL) was placed in a 1.5 mL container sealed with a dialysis membrane, and dialysed against a fixed volume of water, or the corresponding NaCl solution to avoid the influence of osmosis (water moves from a lower solute concentration region into a region of higher concentration through a semi-permeable membrane),[53] with constant stirring (Figure 5.23). The concentration of salicylic acid in the external aqueous phase was measured over an extended period of time. The salicylic acid loaded emulsions at two different NaCl concentrations were evaluated for the release study. For the control experiment, salicylic acid (7 $g \cdot L^{-1}$) dissolved in soybean oil alone (at an oil/water, or oil/saline ratio of 30/70 vol% and total volume of 1.5 mL in the container, to match the emulsion volume) was dialysed against water or saline.

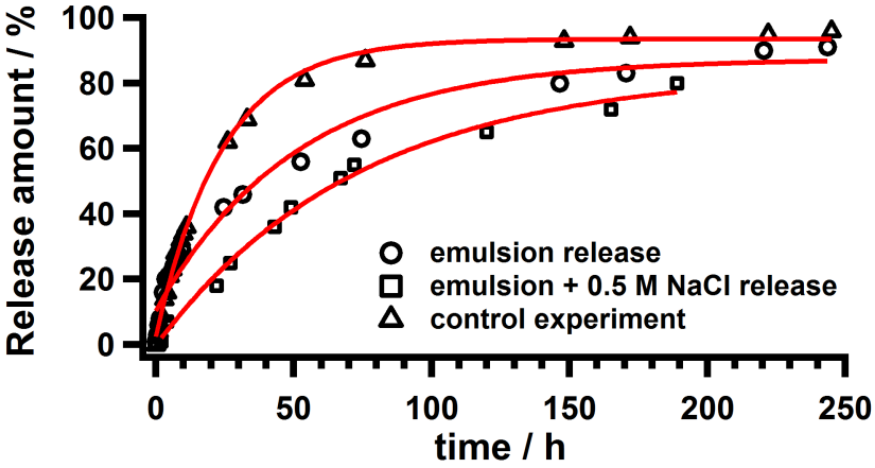

Figure 5.24 Combined release profiles of salicylic acid over time (scatter plots); red lines are the fitted curves using a first order reaction rate law.

The amount of salicylic acid released from the emulsion system was recorded over time recorded by UV measurements, as illustrated in Figure 5.24. The release kinetics followed first order kinetics and the rate constant was calculated by Equation 5.2.

$$\ln(Q_0 - Q) = lnQ_0 - kt \qquad \textbf{(5.2)}$$

Where Q_0 is the maximum released amount of the salicylic acid at equilibrium, Q is the released amount at time t and k is the calculated rate constant.

As the concentration of the salicylic acid the acceptor chamber (*ca* 0.05 g·L^{-1}) was much lower than the saturation concentration at 25 ºC (*ca* 3 g·L^{-1}),[54] the movement of the salicylic acid solution in the acceptor chamber was regarded as simple dilution and the diffusion coefficient of the salicylic acid was considered unchanged under the various experiment conditions.[55] Therefore, the rate difference observed was ascribed to the network of OCNF formed on the oil droplet surface and in the aqueous phase. The rate coefficients from the fitted release profiles were calculated to be 0.041 h^{-1} (control experiment) > 0.020 h^{-1} (emulsion) > 0.014 h^{-1} (emulsion with 0.5 *M* NaCl) respectively. The results are summarised in Table 5.2. In other words, with increasing salt concentration, a delayed release of salicylic acid from the emulsion into the receptor chamber occurred, indicating that the salicylic acid was trapped in the emulsion droplets due to the thicker shells. The maximum release of

salicylic acid from the emulsion was calculated to be 94 % (control experiment), 87 % (emulsion) and 83 % (emulsion with 0.5 *M* NaCl). This was probably related to the partitioning (concentration of a molecule in the oil phase over that in the aqueous phase) of the salicylic acid between the oil and aqueous phase (an increased ionic strength decreased the solubility of salicylic acid in the aqueous phase, therefore more salicylic acid remained in the oil phase).[56] The maximum release phenomenon was not investigated further, as the release rate provided more direct information on the permeability of the OCNF in the presence/absence of NaCl, which was used to demonstrate the shell responsive behaviour. Meanwhile, the maximum release phenomenon could be used to encapsulate the active ingredient in the oil phase by adding preservative electrolytes, especially when the active ingredient was unstable in the aqueous phase (e.g. vitamin C[57]).

Table 5.2 Summary of rate constant and maximum release for drug release experiment.

	k / h^{-1}	**maximum release %**
control experiment	0.041	94
emulsion	0.02	87
emulsion + 0.5 *M* NaCl	0.014	83

Similar sustained release behaviour has also been observed for emulsions stabilised by silica nanoparticles, where the silica layer formed at the oil-water interface changed from permeable to semi-permeable in the presence of increasing NaCl concentrations.[58] The change of the rate constant with increasing NaCl concentration in this study is very similar to that reported for emulsions stabilised by silica nanoparticles under low or high NaCl concentration, showing the possibility of formulating OCNF emulsions for sustained release.[58]

5.2.6.2 Scaffolds for composite materials

OCNF can also be used as a scaffold for composite materials, providing good mechanical performance.[59] OCNF can be used to form an anisotropic foam (Figure 5.25), which has a potential application in thermal insulators,[59] or electro-mechanical devices,[60] as the structure of the foam would provide distinctive flow, mechanical and electrical performances in different directions.[61] The Pickering emulsion of hexane

stabilised by 8 g·L^{-1} OCNF suspension was poured into a silicone or Teflon mould sitting on the surface of a copper rod in contact with a liquid-nitrogen bath, in a sealed container following the method of uni-directional freeze-drying applied to OCNF dispersions.[59,62] This resulted in a temperature gradient and the emulsion started to freeze from the bottom of the mould, eventually forming a frozen material consisting of anisotropic ice crystals surrounded by "walls" formed by the free OCNF and frozen OCNF-coated oil droplets (Figure 5.28). The ice-templating process resulted in an ultra-light structured emulsion foam with a porosity of higher than 99%. The calculation of the porosity is based on the density of the freeze-dried foam (ρ_{foam}) and the density of OCNF (ρ_{OCNF}, 1.6 g·cm^{-3}), $\text{porosity} = 1 - \rho_{foam}/\rho_{OCNF}$.[63] The resulting emulsion foam is biocompatible and biodegradable due to the properties of OCNF,[64] making it an interesting scaffold suitable for some novel applications in biotechnology, such as tissue engineering for cell generation.[65,66]

The aim here was to demonstrate the viability of producing the anisotropic emulsion form via ice-templating process, and to explore the possibility of attaching particles onto OCNF.

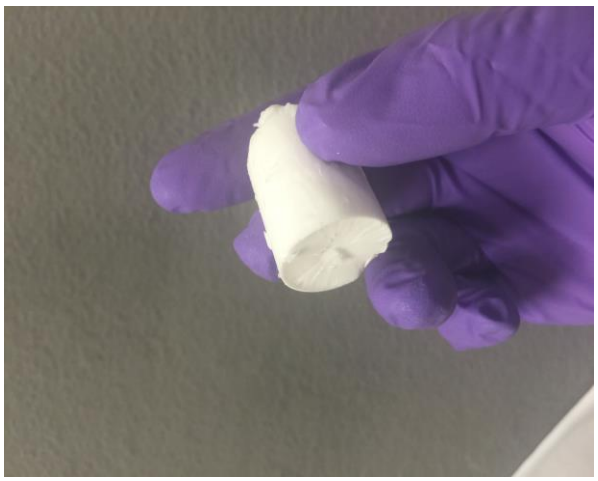

Figure 5.25 Photo of uni-directionally freeze-dried Pickering emulsion stabilised by OCNF

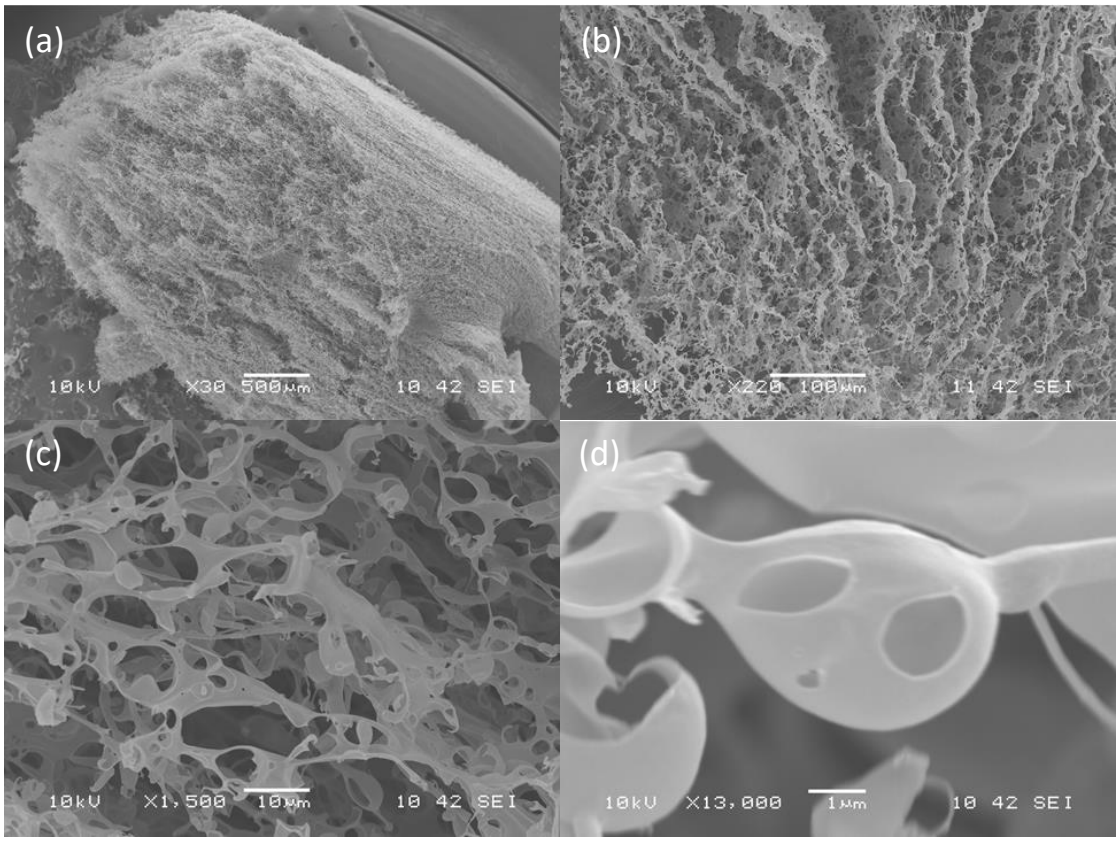

Figure 5.26 SEM images of uni-directionally freeze-dried Pickering emulsion of hexane stabilised by 8 g·L^{-1} OCNF at magnifications of (a) x30, (b) x220, (c) x1500 and (d) x13000.

Following the freeze-drying process, ice and oil crystals were removed from the emulsion to leave the OCNF network (Figure 5.26a). The aligned cylindrical pores of *ca* 30 µm (Figure 5.26b) were the positions where elongated ice crystals formed. Figure 5.26d shows the shell of the emulsion droplet. However, the emulsion droplets were not well connected as, at this low concentration, not enough OCNF remained in the aqueous phase to bind the droplets together. This could be improved by increasing the amount of OCNF used to stabilise the Pickering emulsion. When the Pickering emulsion was stabilised by 18 g·L^{-1} OCNF, more organized cylindrical pores were observed (Figure 5.27b-c). Emulsion droplets were pushed together during the freezing process and spherical pores of *ca* 5 µm formed on the walls after removing oil and ice crystals from the frozen emulsion.

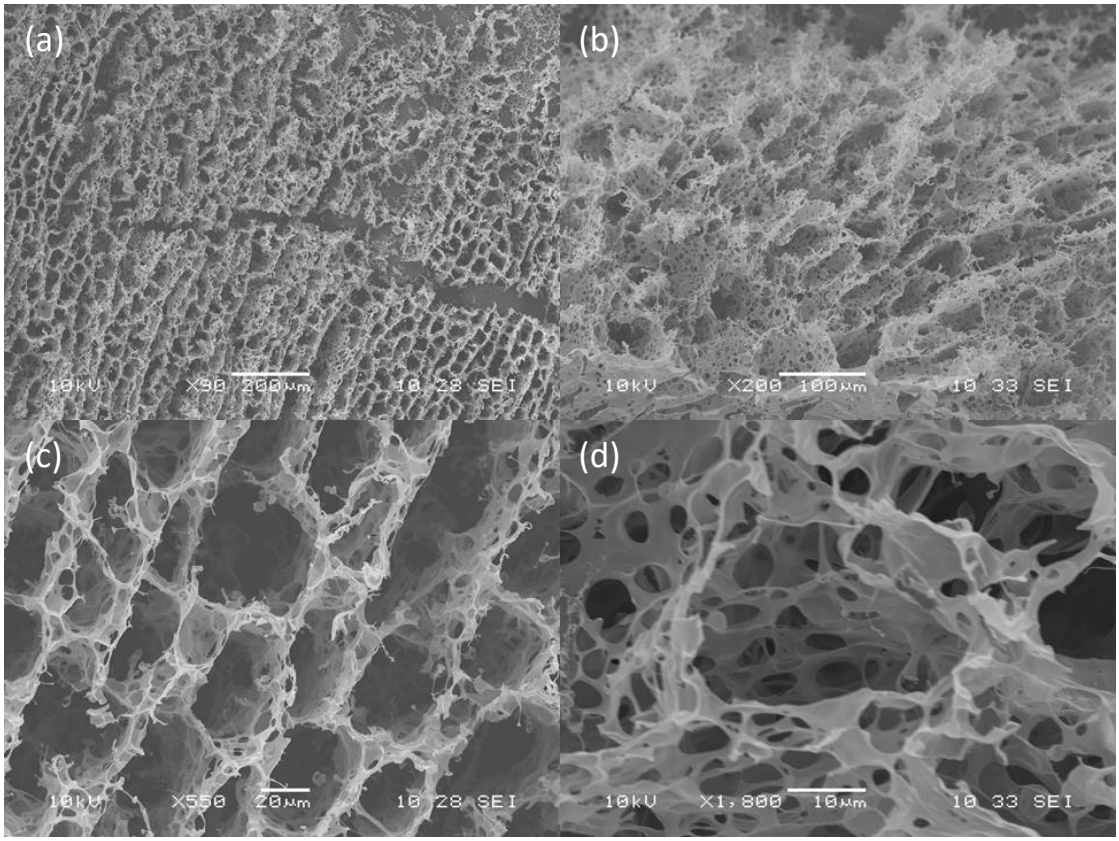

Figure 5.27 SEM images of uni-directional freeze-dried Pickering emulsion of hexane stabilised by 18 g·L^{-1} OCNF at magnifications of (a) x90, (b) x200, (c) x500 and (d) x1000.

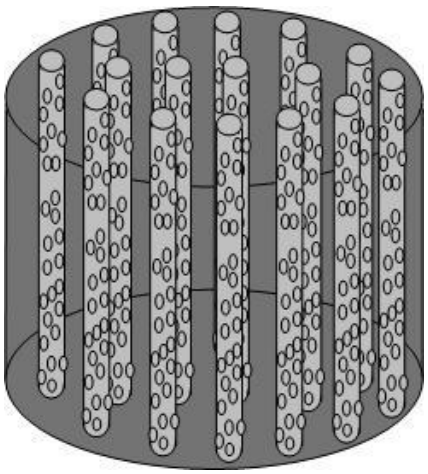

Figure 5.28 Cartoon of the uni-directional freeze-dried emulsion stabilised by OCNF.

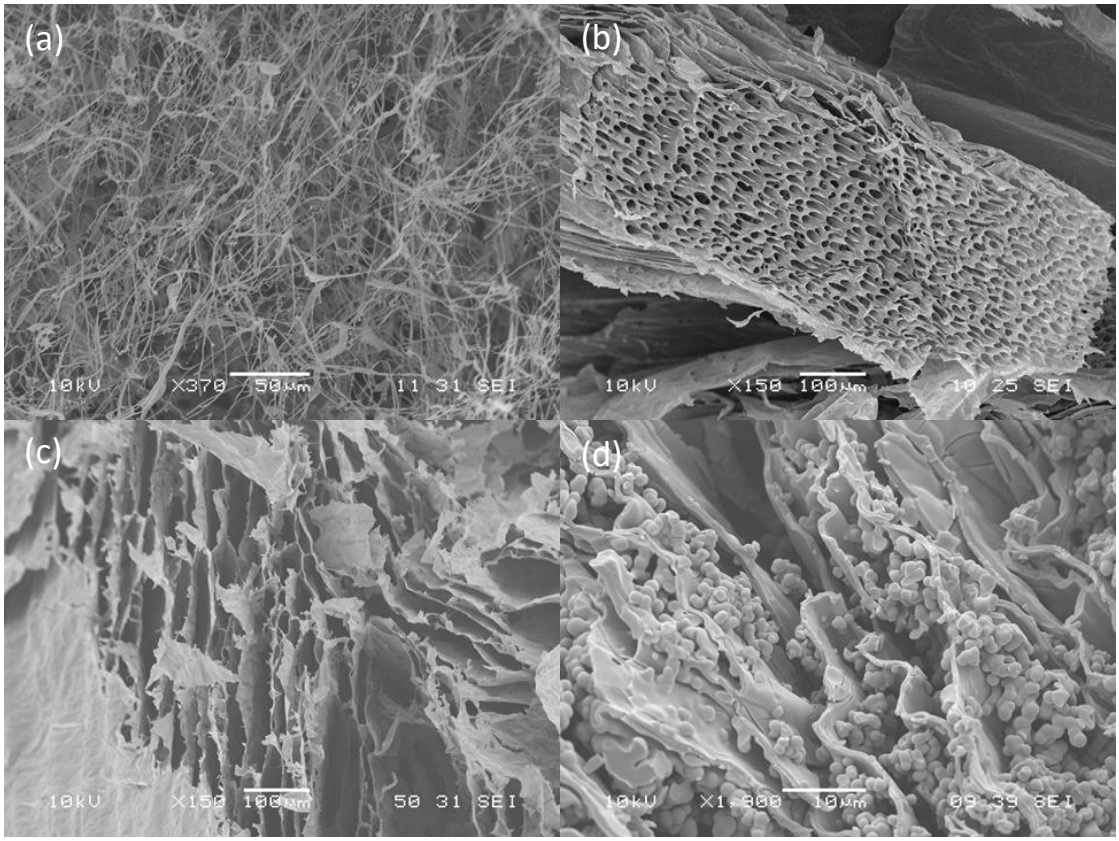

Figure 5.29 SEM images of uni-directional freeze-dried suspension containing (a) 5 g·L^{-1} OCNF (b) 8 g·L^{-1} OCNF (c) 18 g·L^{-1} OCNF and (d) 18 g·L^{-1} OCNF then modified with TiO_2.

The impact of OCNF content on the foam structure was also observed for a uni-directionally freeze-dried OCNF suspension. When the OCNF concentration was low (5 g·L^{-1}), only fibrous structures remained after freeze-drying (Figure 5.29a). When OCNF concentration was medium (8 g·L^{-1}), aligned cylindrical structure existed with some defects (pores) in the walls after freeze-drying (Figure 5.29b). When OCNF concentration was high enough (18 g·L^{-1}), aligned cylindrical structures with thick walls were noted after freeze-drying (Figure 5.29c). Therefore, it could be concluded that a more defined cylindrical structure formed with higher OCNF concentration in the aqueous phase, which was useful to design stronger freeze dried emulsion foams.

Attachment of titania particles onto OCNF was examined using uni-directionally freeze-dried OCNF suspensions (Figure 5.29C), since it was easier to visualise the TiO_2 particles on the smooth surface of the OCNF foam, compared to the emulsion foam. The advantage of using OCNF as a template to grow nanoparticles was that

all the cellulose would decompose into CO_2 and H_2O during the calcination, and leave a network of sintered nanoparticles with large porosity, unidirectional macropores and high surface area.[67] Hierarchically structured titania of this type could have potential applications in photocatalysis[68] and dye sensitised solar cells[69] arising from the specific band gap of the anatase form of titania. Calcination of the OCNF foam produced by directional freezing provided more uniform and directional macropores than were present in OCNF or CNF dispersions. This could allow greater mass transfer through the pores in the final materials. Thus preparation of porous TiO_2 on the OCNF foam scaffold was attempted. To prepare the materials the OCNF foam was soaked in neat titanium (IV) butoxide overnight, and then exposed to water vapour over a week to allow the precursor to hydrolyse and condense to form TiO_2 slowly (Figure 5.29d). The resulting composite was then calcined at 500 °C for 2 h to form anatase TiO_2 nanoparticles, as determined by XRD.[70] It was interesting that the OCNF in the composites did not decompose entirely after the calcination (some OCNF was carbonized, giving a black colour to the sample), probably due to insufficient air flow in the oven. This result did however show that it was possible to attach particles onto the OCNF scaffold and, indeed, to carbonise the delicate structures formed, which could lead to other opportunities e.g. in porous catalyst supports. Research has shown that the cellulose network with a porous structure can enhance the transport of oxygen and electrons, which is a desirable candidate for a catalyst or catalyst supporter in lithium-oxygen battery.[71]

5.3 Conclusions

In this work, o/w Pickering emulsions were successfully prepared using OCNF as the stabilizer for the first time. The behaviour of OCNF emulsions and the structures of OCNF at the oil-water interface were investigated using surface tension, laser diffraction, contact angle, confocal microscopy, TEM, SEM, AFM, SAS, zeta potential and rheology.

The OCNF was found to be surface active on the hexadecane-water interface, as determined by surface tension measurement, due to the amphiphilicity of the nanofibrils. The stability of the Pickering emulsion was investigated as a function of OCNF content in the aqueous phase and the resistance to centrifugal force, based

on the results from laser diffraction for particle size measurement. OCNF aggregation on the oil/water interface was visualised by confocal microscope, SEM and AFM measurements, providing essential information on the OCNF shell morphology. SAXS and SANS results indicated that the OCNF shell thickened with the increased salt concentration due to the screening of surface charge on the OCNF surface, and the oscillatory rheology results also confirmed the shell thickening phenomenon (weak network of OCNF in the aqueous phase at high NaCl concentration, as most OCNF migrated to the oil/water interface).

It was also demonstrated that the Pickering emulsion stabilised by OCNF can potentially be used in drug delivery applications by controlling drug release rate via different shell thickness. A decrease in the maximum release of salicylic acid was observed with the increased NaCl concentration, which was due to the partitioning of salicylic acid between oil and aqueous phase, resulting in a higher content of the oil soluble encapsulated in the oil droplets. The self-assembled structure of OCNF in the Pickering emulsion could be used for making light-weight composite scaffolds with anisotropic mechanical properties for various applications.[72]

5.4 References

1. S. U. Pickering, *J. Chem. Soc., Trans.,* 1907, **91**, 2001-2021.
2. S. Tcholakova; N. D. Denkov; A. Lips, *PCCP,* 2008, **10**, 1608-1627.
3. R. Aveyard; B. P. Binks; J. H. Clint, *Adv. Colloid Interface Sci.,* 2003, **100–102**, 503-546.
4. F. Muller; J. Degrouard; J. Jestin; A. Brulet; A. Salonen, *Soft Matter,* 2012, **8**, 10502-10510.
5. S. Tesch; C. Gerhards; H. Schubert, *J. Food Eng.,* 2002, **54**, 167-174.
6. N. Lavoine; I. Desloges; A. Dufresne; J. Bras, *Carbohydr. Polym.,* 2012, **90**, 735-764.
7. T. Saito; S. Kimura; Y. Nishiyama; A. Isogai, *Biomacromolecules,* 2007, **8**, 2485-2491.
8. R. J. Crawford; K. J. Edler; S. Lindhoud; J. L. Scott; G. Unali, *Green Chem.,* 2012, **14**, 300-303.
9. Y. Jin; K. J. Edler; F. Marken; J. L. Scott, *Green Chem.,* 2014, **16**, 3322-3327.
10. *UK Pat.,* WO2012139817A2, 2012.
11. T. Winuprasith; M. Suphantharika, *Food Hydrocolloids,* 2015, **43**, 690-699.
12. J. O. Zoppe; R. A. Venditti; O. J. Rojas, *J. Colloid Interface Sci.,* 2012, **369**, 202-209.
13. I. Kalashnikova; H. Bizot; B. Cathala; I. Capron, *Langmuir,* 2011, **27**, 7471-7479.
14. K. Xhanari; K. Syverud; G. Chinga-Carrasco; K. Paso; P. Stenius, *J. Colloid Interface Sci.,* 2011, **356**, 58-62.
15. A. Rattaz; S. Mishra; B. Chabot; C. Daneault, *Cellulose,* 2011, **18**, 585-593.
16. X. Yang; E. Bakaic; T. Hoare; E. D. Cranston, *Biomacromolecules,* 2013, **14**, 4447-4455.
17. J. Araki; M. Wada; S. Kuga, *Langmuir,* 2000, **17**, 21-27.
18. M. Salajkova; L. A. Berglund; Q. Zhou, *J. Mater. Chem.,* 2012, **22**, 19798-19805.
19. I. Kalashnikova; H. Bizot; P. Bertoncini; B. Cathala; I. Capron, *Soft Matter,* 2013, **9**, 952-959.
20. R. Chanamai; D. J. McClements, *Colloids Surf. Physicochem. Eng. Aspects,* 2000, **172**, 79-86.
21. T. Young, *Philosophical Transactions of the Royal Society of London,* 1805, **95**, 65-87.
22. B. P. Binks; L. Isa; A. T. Tyowua, *Langmuir,* 2013, **29**, 4923-4927.
23. G. I. Taylor, *Proceedings of the Royal Society of London A: Mathematical, Physical and Engineering Sciences,* 1934, **146**, 501-523.
24. T. S. H. Leong; T. J. Wooster; S. E. Kentish; M. Ashokkumar, *Ultrason. Sonochem.,* 2009, **16**, 721-727.
25. R. C. Tolman, *J. Phys. Chem.,* 1949, **17**, 333-337.
26. G. Jones; W. A. Ray, *J. Am. Chem. Soc.,* 1941, **63**, 3262-3263.
27. K. Sim; J. Lee; H. Lee; H. Youn, *Cellulose,* 2015, **22**, 3689-3700.
28. F. Cherhal; F. Cousin; I. Capron, *Langmuir,* 2015, **31**, 5596-5602.
29. J. Kim, et al., *J. Am. Chem. Soc.,* 2010, **132**, 8180-8186.
30. S. W. Chook, et al., *RSC Adv.,* 2015, **5**, 88915-88920.
31. N. Masruchin; B. D. Park; V. Causin; I. C. Um, *Cellulose,* 2015, **22**, 1993-2010.

32. D. Bendahou; A. Bendahou; B. Seantier; Y. Grohens; H. Kaddami, *Ind. Crop. Prod.,* 2015, **65**, 374-382.
33. E. Perrin; H. Bizot; B. Cathala; I. Capron, *Biomacromolecules,* 2014, **15**, 3766-3771.
34. S. Iwamoto, et al., *Polym. Degrad. Stab.,* 2010, **95**, 1394-1398.
35. I. Kalashnikova; H. Bizot; B. Cathala; I. Capron, *Biomacromolecules,* 2011, **13**, 267-275.
36. A. G. Cunha; J.-B. Mougel; B. Cathala; L. A. Berglund; I. Capron, *Langmuir,* 2014, **30**, 9327-9335.
37. G. Yin; Z. Zheng; H. Wang; Q. Du; H. Zhang, *J. Colloid Interface Sci.,* 2013, **394**, 192-198.
38. K. A. Brown; J. Berezovsky; R. M. Westervelt, *Appl. Phys. Lett.,* 2011, **98**, 183103.
39. S. Akamine; R. C. Barrett; C. F. Quate, *Appl. Phys. Lett.,* 1990, **57**, 316-318.
40. D. Beyer; W. Lebek; W. D. Hergeth; K. Schmutzler, *Colloid. Polym. Sci.,* 1990, **268**, 744-748.
41. S. Kline, *J. Appl. Crystallogr.,* 2006, **39**, 895-900.
42. P. Bartlett; R. H. Ottewill, *J. Phys. Chem.,* 1992, **96**, 3306-3318.
43. K. A. Dill, et al., *Nature,* 1984, **309**, 42-45.
44. M. J. Hollamby, *PCCP,* 2013, **15**, 10566-10579.
45. F. Cherhal; F. Cousin; I. Capron, *Biomacromolecules,* 2016, **17**, 496-502.
46. H. Fukuzumi; R. Tanaka; T. Saito; A. Isogai, *Cellulose,* 2014, **21**, 1553-1559.
47. E. Lasseuguette; D. Roux; Y. Nishiyama, *Cellulose,* 2008, **15**, 425-433.
48. F. Martoia, et al., *Soft Matter,* 2015, **11**, 4742-4755.
49. M.-C. Li, et al., *ACS Sustain. Chem. Eng.,* 2015, **3**, 821-832.
50. H. A. Barnes; J. F. Hutton; K. Walters *An introduction to rheology*, Elsevier, 1989.
51. N. Quennouz; S. M. Hashmi; H. S. Choi; J. W. Kim; C. O. Osuji, *Soft Matter,* 2015, **12**, 157-164.
52. Z. Hu; S. Ballinger; R. Pelton; E. D. Cranston, *J. Colloid Interface Sci.,* 2015, **439**, 139-148.
53. R. Mezzenga; B. M. Folmer; E. Hughes, *Langmuir,* 2004, **20**, 3574-3582.
54. F. L. Nordström; Å. C. Rasmuson, *J. Chem. Eng. Data,* 2006, **51**, 1668-1671.
55. J. Buffle; Z. Zhang; K. Startchev, *Environ. Sci. Technol.,* 2007, **41**, 7609-7620.
56. M. M. Miller; S. P. Wasik; G. L. Huang; W. Y. Shiu; D. Mackay, *Environ. Sci. Technol.,* 1985, **19**, 522-529.
57. S. Farahmand; H. Tajerzadeh; E. S. Farboud, *Pharm. Dev. Technol.,* 2006, **11**, 255-261.
58. C. A. Prestidge; S. Simovic, *Int. J. Pharm.,* 2006, **324**, 92-100.
59. B. Wicklein, et al., *Nat Nano,* 2015, **10**, 277–283.
60. R. Zhang, et al., *ACS Appl. Mater. Interfaces,* 2015, **7**, 19145-19152.
61. J. Fu; R. B. Schoch; A. L. Stevens; S. R. Tannenbaum; J. Han, *Nat Nano,* 2007, **2**, 121-128.
62. C. Suwanchawalit; A. J. Patil; R. K. Kumar; S. Wongnawa; S. Mann, *J. Mater. Chem.,* 2009, **19**, 8478-8483.
63. Y. Kobayashi; T. Saito; A. Isogai, *Angew. Chem. Int. Ed.,* 2014, **53**, 10394-10397.
64. I. Homma; T. Isogai; T. Saito; A. Isogai, *Cellulose,* 2013, **20**, 795-805.

65. E. Entcheva, et al., *Biomaterials,* 2004, **25**, 5753-5762.
66. H. Luo, et al., *Mater. Chem. Phys.,* 2013, **143**, 373-379.
67. L. Zhaodong; Y. Chunhua; W. Fei; C. Zhiyong; W. Xudong, *Nanotechnology,* 2014, **25**, 504005.
68. X.-Y. Li, et al., *J. Colloid Interface Sci.,* 2012, **368**, 128-138.
69. Y. Xiong; D. He; Y. Jin; P. J. Cameron; K. J. Edler, *J. Phys. Chem. C,* 2015, **119**, 22552-22559.
70. C. Su; B. Y. Hong; C. M. Tseng, *Catal. Today,* 2004, **96**, 119-126.
71. S. Tong, et al., *Chem. Commun.,* 2015, **51**, 7302-7304.
72. M. Mashkour; M. Tajvidi; F. Kimura; H. Yousefi; T. Kimura, *ACS Appl. Mater. Interfaces,* 2014, **6**, 8165-8172.

Chapter 6 Metal-organic Frameworks on Cellulose for Chemical Sorption

6.1 Introduction

Metal-organic frameworks (MOFs) are microporous (pore diameter<2 nm) crystalline compounds with high surface area, consisting of transition metal ions coordinating with organic linkers,[1] with various applications from gas storage or separation to catalysts for chemical reaction.[2,3]

MOFs occur commonly as polycrystalline powders, therefore they are very difficult to handle in practise and attaching MOF particles onto certain substrates (e.g. silicon, gold) via physical or chemical binding is often required.[4] MOFs immobilised on cellulose (where the MOFs could potentially attach and either totally cover a fibril, or grow on the surface of a fibril or in the gaps between fibrils, Figure 6.1) could be used as sustainable self-standing membranes for continuous gas sorption and separation (e.g. of CO_2, O_2 and N_2), or sensing applications, with low manufacturing cost, compared to the metal substrates used in MOFs devices at the moment.[5,6] The MOF/cellulose composite membrane is expected be strong (high tensile strength) and could be easily scaled up to any size and shape on demand, based on the results from other cellulose based composites.[7,8]

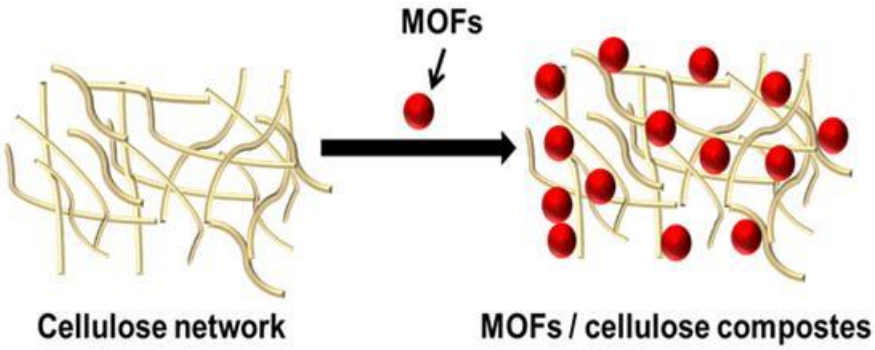

Figure 6.1 Cartoon of the attachment approach of MOFs onto cellulose.

Two types of cellulose, oxidised cellulose nanofibrils (OCNF) and bacterial cellulose (BC), were adopted here to make MOF/cellulose composites. OCNF was chosen due to the large surface area, and active sites for binding to MOF particles (the

carboxylate groups with negative charge would be expected to interact with metal ions with positive charge, thus the MOF crystals could grow from the surface). BC has high surface area (due to its sub-micron sized fibril width) and high tensile strength,[9] therefore it was expected that the combination of MOFs with BC would allow rapid flux through the macroporous (d>50 nm) structure of BC, while retaining good selectivity from the microporous structure of MOFs.

In this chapter, a proof-of-concept method was developed to prepare MOFs/cellulose composites as self-standing membranes for gas sorption and separation (e.g. CO_2 and N_2) via facile synthesis (in-situ synthesis of MOFs onto cellulose). In order to test the feasibility of attaching various MOFs onto cellulose, two types of MOFs with different metal ions and organic linkers were adopted here.

MOF-199, $[Cu_3(\textit{benzene-1,3,5-tricarboxylate})_2]_n$, was selected here due to the ease of synthesis and widely investigated properties, and the presence of MOF-199 on cellulose can be easily confirmed optically (change of the dried membrane colour from white to blue).[10] MOF-199 consists of copper dimer units and benzene-1,3,5-tricarboxylate linkers, forming a 3D framework (Figure 6.2).

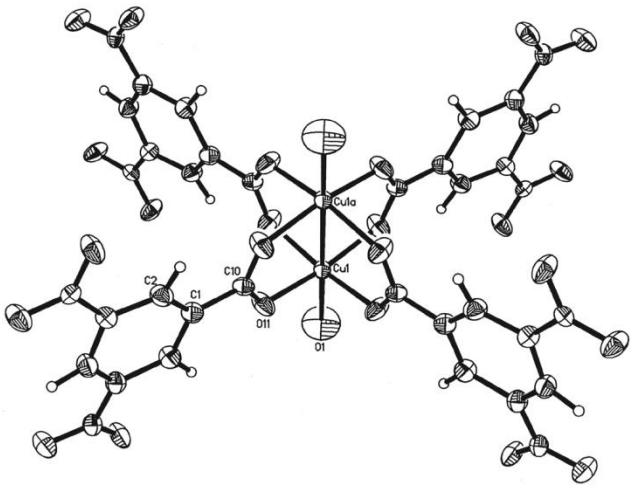

Figure 6.2 Dicopper(II) tetracarboxylate building block for MOF-199 (atom shown as labelled).[11] Reprinted with permission from AAAS.

$[Ni(NCS)_2(\textit{4,4'-bipyridyl})_2]_n$ (Ni-MOF) was used here as a nickel-based MOFs to form self-standing MOFs/cellulose membrane for xylene sorption and separation (a combined effect of xylene separation by binding to the Ni site, high surface area from

the porous MOF structure and fast flow through the cellulose membrane). This work was inspired by the study of xylene separation using a single Werner clathrate ($Ni(NCS)_2$(*para-phenylpyridine*)$_4$ that was shown to absorb the xylene isomers into a crystalline material and then desorb them, by Professor Len Barbour's group.[12] Currently, industrial methods for xylene separation involve slow, energy-intensive and multi-step distillative processes.[13] In the Ni-MOF, nickel coordinates with two 4,4'-bipyridyl units and forms a 2D square network (Figure 6.3). The Ni-MOF was obtained by mixing $Ni(NCS)_2$ and 4,4'-bipyridyl in methanol at ambient temperature, and is described in detail in Chapter 2. It was expected that the Ni-MOF would increase the adsorption of xylene and remain selective for different isomers. This work originated from the collaboration between Professor Len Barbour's group and our own.

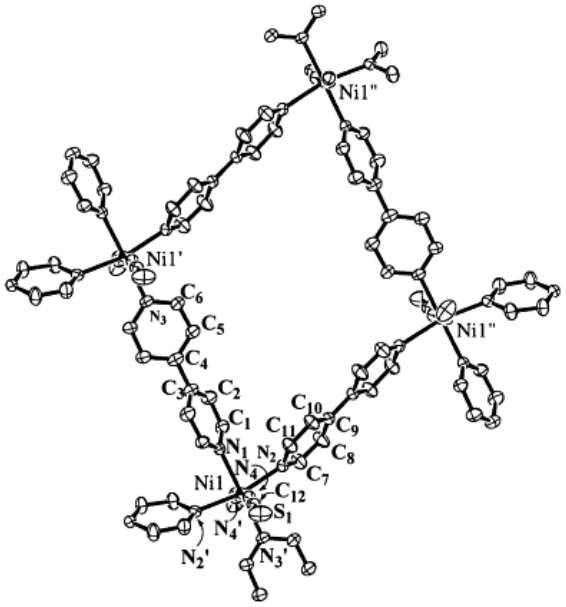

Figure 6.3 Building block for $[Ni(NCS)_2$(*4,4'-bipyridyl*$)_2]_n$ (atom shown as labelled).[14] Reproduction of images from Ref. [14] with permission from Elsevier (© Elsevier 2000).

The moisture content remaining in the cellulose fibrils could have a huge effect on the stability of a water sensitive MOF (e.g. MOF-5), so this narrowed the scope of the MOFs that could be used.[15] MOF-199 used in this study and other MOFs reported in literatures are relatively resistant to water and the synthetic media for these MOFs may also contain water,[16] therefore, it is possible to combine those water tolerant MOFs with cellulose to form the composite materials.

The presence of the MOFs on cellulose was confirmed optically, and studied using XRD, SEM, TEM, TGA and FTIR. The selectivity of the MOF/cellulose membrane for different gases or xylenes isomers was investigated using sorption studies and NMR.

6.2 Results and Discussion

6.2.1 MOF-199/Oxidised Cellulose Nanofibrils Composites

The XRD of the MOF-199 synthesised here was identical to the simulated pattern from the crystal structure of MOF-199,[11] confirming the formation of the same MOF structure using the method described in Chapter 2. The formation of MOF-199/OCNF composites was confirmed optically and using XRD (Figure 6.4). The typical peak for oxidised cellulose (around 22°) was not obvious in the composites patterns, as it may be obscured by the much stronger MOF signals. The crystallinity of MOF-199 was obtained by Rietveld refinement and the MOF fraction in the composite (the sum of crystalline and amorphous MOF fractions) was also extracted, assuming no change in the crystallinity of cellulose when forming the composite (cellulose was only exposed to a water/solvent mixture). Cellulose I_β was used here as this was the predominant form as judged from Rietveld refinement. The crystallinity of the bulk MOF-199 was 43%, and that of the OCNF starting material 44%. In the composite, the crystallinity of the MOF-199 was calculated to be 61% and the MOF-199 fraction was 84%. In addition, it was noticed that the crystallite size of MOF-199 determined using the Scherrer equation, applied to the signal at *ca* 12°, was larger in the presence of OCNF (6.8 nm) than the bulk MOF-199 (2.3 nm) alone, indicating that OCNF provided a preferential crystallization site for MOF-199 under the synthesis conditions. The refinement results of the peak broadening were also used to determine the crystallite size here for comparison, and the result was 5.3 nm for MOF-199 in the presence of OCNF and 3.2 nm for the bulk MOF, which was in agreement with the results from Scherrer equation. The carboxylate groups on the OCNF could provide nucleation sites for crystallization,[17] and promote the formation of bigger MOFs crystals by competitive complexation of metal cations (by reducing the concentration of metal cations in the solution, thereby slowing the nucleation rate).[18,19]

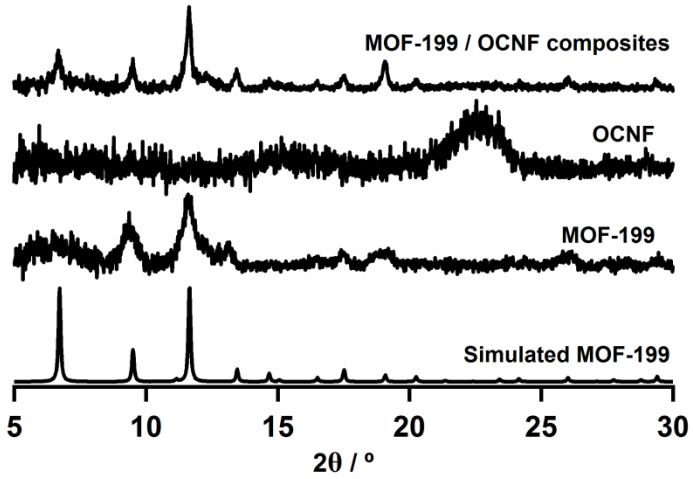

Figure 6.4 XRD patterns of simulated MOF-199, MOF-199, OCNF and MOF-199/OCNF composites.

In order to characterise the morphology of the MOF-199/OCNF composites, SEM was used. As illustrated in Figure 6.5, aggregate MOF particles around 50 nm were observed, but it proved impossible to discern the sizes of individual crystallites. The particles tended to aggregate during the drying process and no nanofibril could be observed in the SEM images (the fibres were about 4 nm in width, and not visible at this magnification – in all previous studies TEM was required to detect the OCNF). It should be noted that the crystallite size measured by XRD (Figure 6.4) is not directly comparable with these results from SEM (Figure 6.5) or TEM (Figure 6.6), as in all cases aggregates of small MOF crystallites are detected and in these samples, MOF crystallite size is clearly not the same as the aggregate particle size.

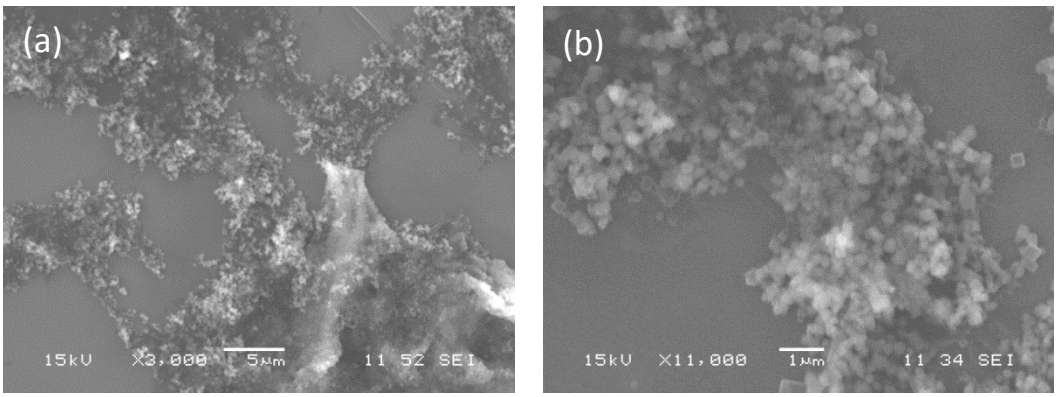

Figure 6.5 SEM images of the MOF-199/OCNF composites at (a) 3,000x, (b) at 11,000x magnification.

TEM was used to visualise MOF-199 particles grown on the OCNF (Figure 6.6). MOF particles appeared to grow along the fibre direction (although some particles also existed separately), which was different to the form of MOF-199 alone,[20] indicating the attachment of MOF-199 onto the oxidised cellulose surface. The absence of metal nanoparticles and presence of MOF-199 is clear from inspection of the XRD trace in Figure 6.4, and the crystallinity of the MOF-199 was determined to be 61% by Rietveld refinement. A similar result was previously obtained for functionalization of silicon nanowire surfaces with MOF-199, where particles were visualised along the wire using energy dispersive spectroscopy (EDS) elemental mapping.[21] However, in this case, it was not possible to separate MOF-199 signals from those of the OCNF, as the MOF was finely divided and spread out all over the cellulose thus it did not prove possible to achieve good spatial resolution.

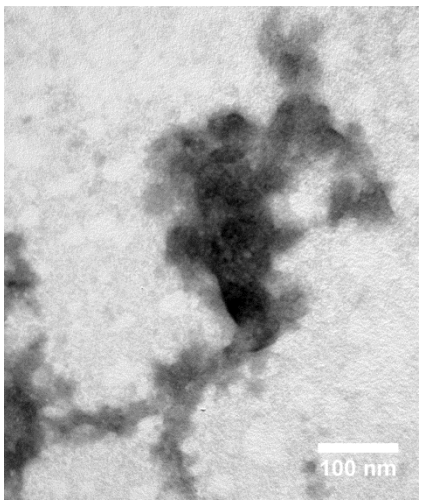

Figure 6.6 TEM image of MOF-199/OCNF composites.

6.2.2 MOF-199/Bacterial Cellulose Composites

6.2.2.1 Characterisation

Since the characterisation of MOF-199/OCNF composites was difficult due to the size of the OCNF and limited by current techniques, BC was chosen as an alternative substrate due to its larger width (allowing visualisation using SEM, Figure 6.7) compared to OCNF, and similar surface properties to OCNF (rich in hydroxyl groups which could coordinate with metal ions). Oxidised bacterial cellulose was also investigated and no significant difference was found for the MOF-199 attachment on

the oxidised and non-oxidised BC, therefore non-modified BC was used here as this required minimal treatment for the starting material.

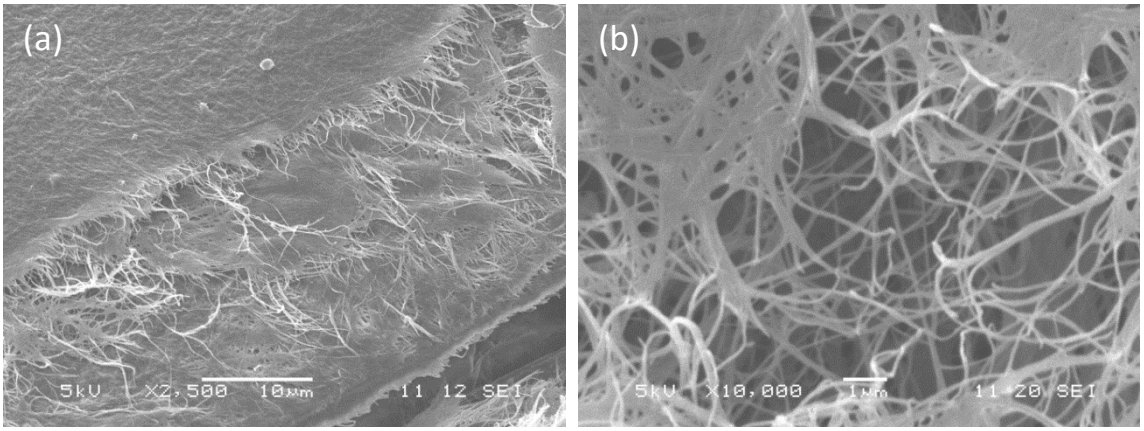

Figure 6.7 SEM images of (a) the layered structure of dried bacterial cellulose and (b) nanofibres of bacterial cellulose. The BC membrane was dried at 90 °C for 6 h.

The MOF-199/BC composite was synthesised under the same conditions as MOF-199/OCNF. A bluish jelly-like membrane was obtained after the reaction (Figure 6.8a), and SEM analysis showed widely distributed MOF-199 particles on the bacterial cellulose membrane after thermal drying (Figure 6.8b). The particle size of MOF-199 (*ca* 100 nm in SEM, Figure 6.8b) was larger than that of the MOF-199 formed on OCNF (*ca* 50 nm in TEM, Figure 6.6), as OCNF provided more nucleation sites for the MOF.[22] However, the MOF on OCNF tended to be aggregated (Figure 6.5) after drying due to the high surface energy, while the MOF on BC remained separated due to the robust network of BC.[23,24]

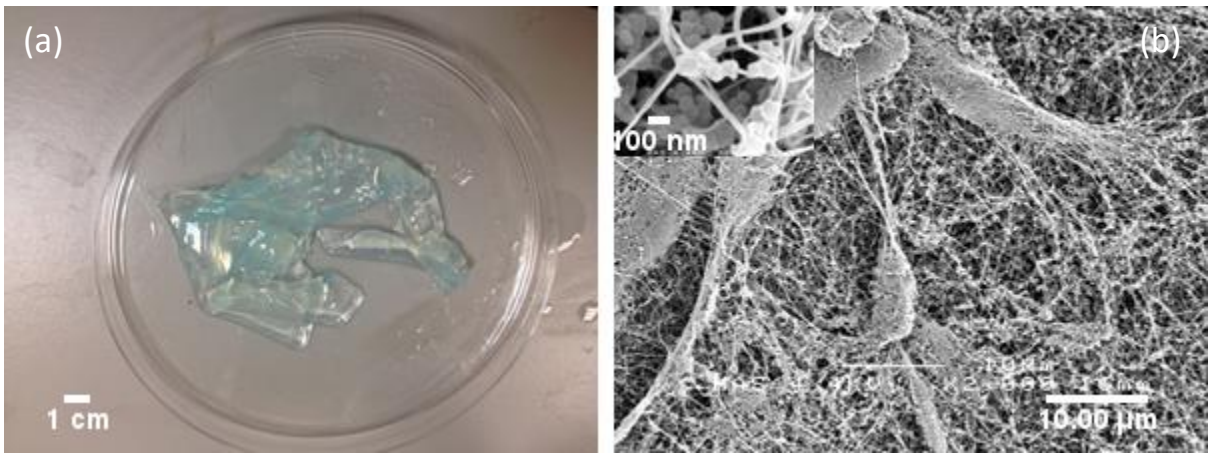

Figure 6.8 (a) Optical image and (b) FE-SEM image of MOF-199/BC membrane. The inset in (b) shows the composite at a higher magnification, where MOF particles are clearly visible on the cellulose fibres.

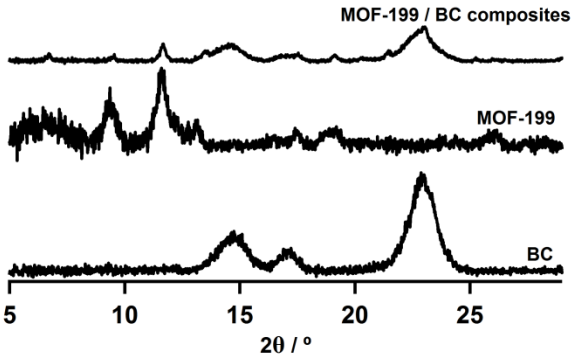

Figure 6.9 XRD patterns of BC, MOF-199 alone and synthesized MOF-199/BC composite.

XRD patterns also confirmed the formation of MOF-199 particles in the presence of bacterial cellulose (Figure 6.9). Similar to the MOF-199/OCNF composite, the crystallite size of MOF-199 was larger in the presence of BC (4.8 nm determined using the Scherrer equation, and 4.3 nm by Rietveld refinement) than the bulk MOF-199 alone (2.3 nm determined using the Scherrer equation, and 3.2 nm by Rietveld refinement), indicating that non-modified BC also provided proper crystallization sites for MOF-199 under the synthesis conditions used. The bulk MOF particles precipitated from the solution were more likely to be ill-defined due to the lack of crystallization time,[25,26] while the BC membrane acted as a barrier during the synthesis to reduce the effective concentration of the precursors (the crystallite size can also be controlled by varying the amount of starting materials) and the time for mass transport, resulting in slowing the nucleation and forming larger crystallites.[27,28] The crystallinity of MOF-199 was obtained by Rietveld refinement, and the MOF fraction in the composite (the sum of crystalline and amorphous MOF proportion in the composite) was also extracted, assuming no change in the crystallinity of cellulose when forming the composite. The crystal structure information used here has been described in Chapter 2. The crystallinity of the bulk MOF-199 was 43%, and the crystallinity of the bacterial cellulose starting material was 86%. In the composite, the crystallinity index of the MOF-199 was calculated to be 50%. The

MOF-199 fraction in the composite calculated by this method, was 33 wt%, comparable to the result of 28 wt% from TGA analysis (Figure 6.11).

The introduction of MOF-199 onto the BC membrane was also confirmed by FTIR analysis. The strong absorbance in the region of 1300-1600 cm^{-1} (red curve, Figure 6.10) was due to the C-C stretching in the aromatic ring and the C=O stretching from the benzene-1,3,5-tricarboxylate in MOF-199, while the peak at ca 730 cm^{-1} corresponds to the out of plane C-H bending on the benzene ring of MOF-199.

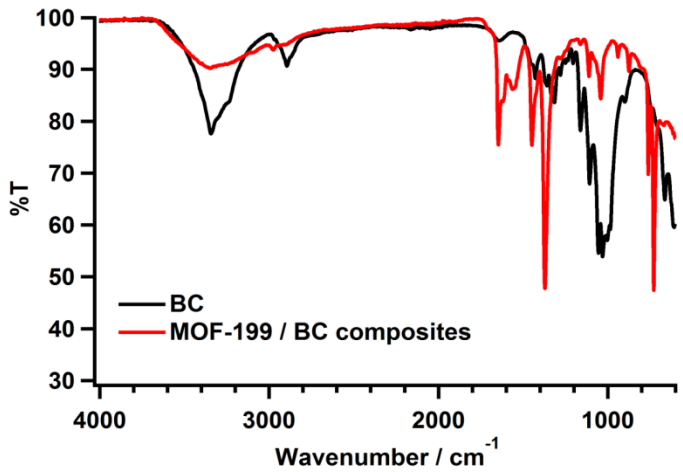

Figure 6.10 FTIR of BC (black) and MOF-199/BC (red).

The thermal stability of the MOF-199/BC composite membrane in air was studied by TGA (Figure 6.11). Loading of MOF-199 on the composite membrane was determined by the remaining weight fraction of the sample at 600 °C (*ca* 30 wt% MOF-199, Equation 6.1). It was assumed that the remaining residue was CuO (not Cu_2O since the colour of the ashes was black and Cu_2O is not stable under heating) as all the organic parts should have been lost as CO_2 and H_2O. Determination of the composition of the residue may be required to obtain the loading with better precision, but it was not essential in this study as the loading here was only used as an indication of the successful attachment of MOF-199 onto the cellulose support.

Variation of the loading of the MOFs in the composites could be achieved by changing the ratio of the metal salt, and organic linker to cellulose in the synthesis (the composite's performance for gas uptake and separation may improve with the higher MOF loading). Since the focus of this work was to examine the feasibility of

in-situ synthesis of MOFs on the cellulose surface and investigate the sorption property of the corresponding composites, loading of the MOF-199 particles was not explored in this study. However it is reported in the literature that optimised syntheses can produce loadings of nanoparticles up to 95% on cellulose supports.[24]

$$
\begin{aligned}
Loading\% &= \frac{m_{residue}\%}{\mathrm{M}_{CuO}} \times M_{MOF-199} \\
&= \frac{1}{3} \times \frac{m_{residue}\%}{\mathrm{M}_{CuO}} \times M_{\mathrm{Cu_3}(benzene-1,3,5-tricarboxylate)_2} \\
&= \frac{1}{3} \times \frac{11\%}{80} \times [(64 \times 3) + (210 - 3) \times 2] = 28\%
\end{aligned}
\qquad \textbf{(6.1)}
$$

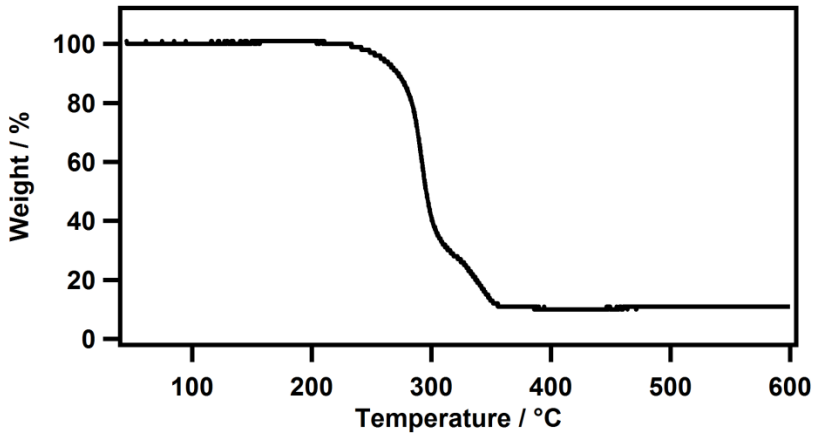

Figure 6.11 TGA measurement of MOF-199/bacterial cellulose composite membrane under air over the temperature rage range 30-600 °C.

6.2.2.2 Sorption study

Nitrogen sorption measurements shown in Figure 6.12 revealed the microporosity of MOF-199 (microporosity was inferred from the significant adsorption at low relative pressure). The isotherm obtained was a type I adsorption isotherm in the IUPAC nomenclature.[29] The micropore size was calculated to be 0.66 nm, by t-plot fitting. The hysteresis loop which occurs in the range of 0.5–1 relative pressure illustrates the existence of interparticle void space in the MOF-199 powder due to the packing of the particles. The nitrogen sorption behaviour of the MOF-199 made here was similar to that of MOF-199 prepared via hydrothermal synthesis, although the specific surface area of the MOF-199 made at room temperature (920 $m^2 \cdot g^{-1}$) was much smaller than the MOFs made under elevated pressure and temperature,

calculated from BET analysis, probably due to the poor crystallinity of the MOF-199 made at room temperature (as discussed above, the MOF-199 supported on BC has a crystallinity of 50% determined by the Rietveld analysis).[30]

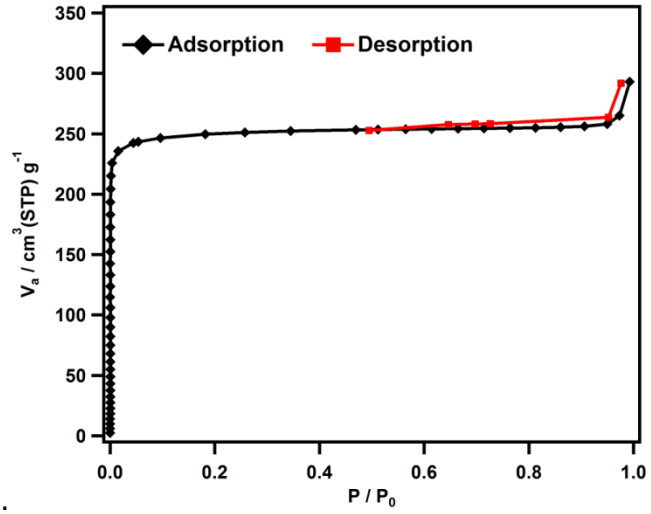

Figure 6.12 Nitrogen adsorption isotherm for MOF-199 at 77 K.

Interestingly, the nitrogen sorption isotherm for MOF-199/BC composites illustrated in Figure 6.13 is significantly different from that of MOF-199 alone. In the low relative pressure region ($P/P_0<0.01$), significant adsorption occurs related to the micropore adsorption. The hysteresis loop is characteristic of a typical capillary condensation phenomenon for type IV mesoporous material in the IUPAC categories.[29] The micropore size was calculated to be 0.66 nm by t-plot fitting demonstrating that the micropores of the MOF did not change when deposited on the cellulose surface. The mesopore size, calculated using the BJH method, however showed a broad size distribution ranging from 2-100 nm, with a maximum centred around 24 nm. The fact that the isotherm did not level off at relative pressures close to 1 indicates the presence of interparticle pores in these materials, of the size on the borderline between the mesopore and macropore ranges (in the magnitude of μm). The MOF-199/BC composite showed a BET specific surface area of *ca* 358 $m^2 \cdot g^{-1}$.

The specific surface area of the thermally dried BC alone was negligible (*ca* 0.5 $m^2 \cdot g^{-1}$) using BET (see appendices), therefore, the increase in the specific surface area for the MOF-199/BC composites was mainly attributed to MOF-199 particles. It is noted that freeze-drying processing could form a BC aerogel with significant

increase in the surface area,[31] however this is not currently easily scalable in industry, therefore thermal drying was used here. Based on the loading of MOF-199 in the composites (*ca* 30%) and the specific surface area of the MOF-199 (920 $m^2 \cdot g^{-1}$), the theoretical specific surface area of the MOF-199/BC composites should be 276 $m^2 \cdot g^{-1}$. The increase in the actual specific surface area for the MOF-199/BC composites (358 $m^2 \cdot g^{-1}$) was ascribed to the improved crystallinity of MOF-199 in the composites (the crystallinity changed from 43% for MOF-199 to 50% for MOF-199/BC composite according to the Rietveld analysis, Figure 6.9). The specific surface area of the composite is 360 $m^2 \cdot g^{-1}$ mainly due to the addition of MOF particles (thermally dried BC has a specific area lower than 1 $m^2 \cdot g^{-1}$), representing a significant increase in surface area upon formation of the composite, which is only 30% by weight MOF-199.

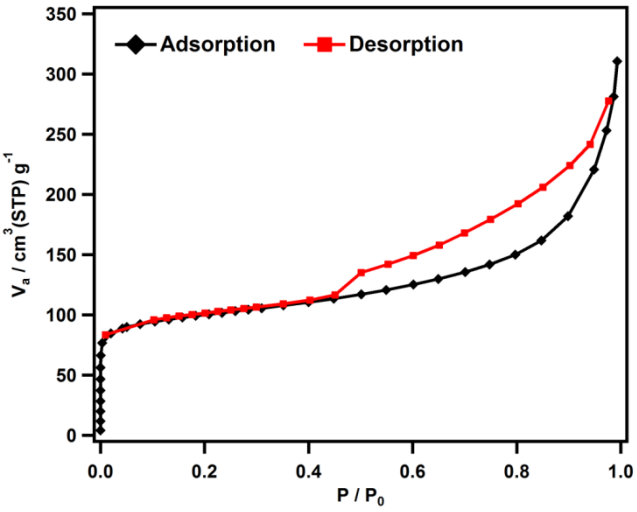

Figure 6.13 Nitrogen adsorption isotherm for MOF-199/BC composite at 77 K.

Selectivity of CO_2 and N_2 sorption properties for MOF-199 (Figure 6.14) and MOF-199/BC composite (Figure 6.15) was carried out at 273 K. The selectivity result was important to evaluate the performance of the material for gas separation (the separation performance of a material improves as the selectivity increases). Although the absolute uptake of CO_2 and N_2 for MOF-199/BC composites was much lower than the uptake for MOF-199 (as the content of the MOF-199 particles decreased in the composites), the selectivity of CO_2 over N_2 for MOF-199/BC composite actually doubled compared to the MOF-199 alone (Table 6.1). This was

probably due to the increase of the polar groups (which enhance the sorption of CO_2 via dipole Interaction) on the surface of MOF-199 with the decreasing particle size.[22] Although it might be argued that water adsorbed to the surface of the BC could potentially also increase CO_2 absorption, these samples were thoroughly activated by drying at 160 °C for 6 hours under vacuum prior to immediate measurement in airtight containers, so this was unlikely. MOF-199 particles grown in the presence of the larger diameter BC cellulose fibres were shown to be larger than those grown on cotton used in literature,[32] or on the OCNF investigated here, therefore it may be possible to tune the size of MOFs in the composites in order to improve the separation performance. The results here showed that it might prove promising to explore the application of MOF-199/BC composites for gas separation.

Table 6.1 Summary of CO_2 and N_2 sorption data for the MOFs based materials at 273 K.

Sample	CO_2 uptake (mmol·g^{-1})	N_2 uptake (mmol·g^{-1})	Selectivity[a]
MOF-199	3.4	0.34	10
MOF-199/BC membrane	0.9	0.04	22.5

[a]: The selectivity was calculated from the single gas isotherms by dividing the CO_2 adsorption capacity over that of N_2 at the relative pressure of 1. P_0 is 101.33 kPa.

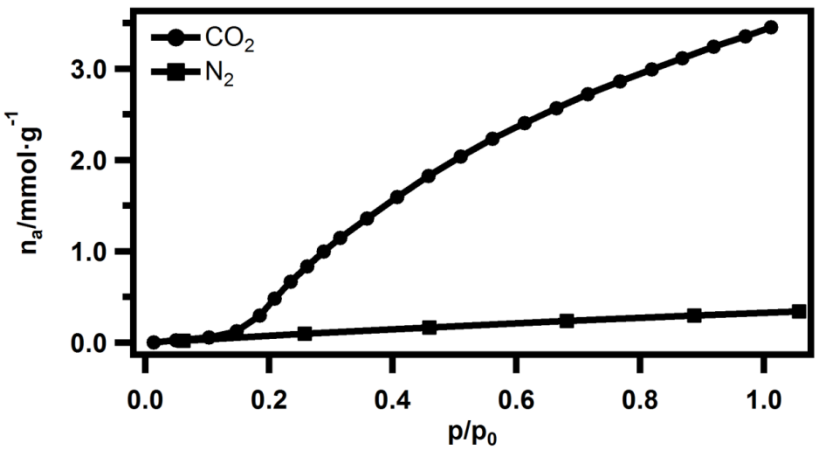

Figure 6.14 CO_2 and N_2 sorption of the MOF-199 at 273 K.

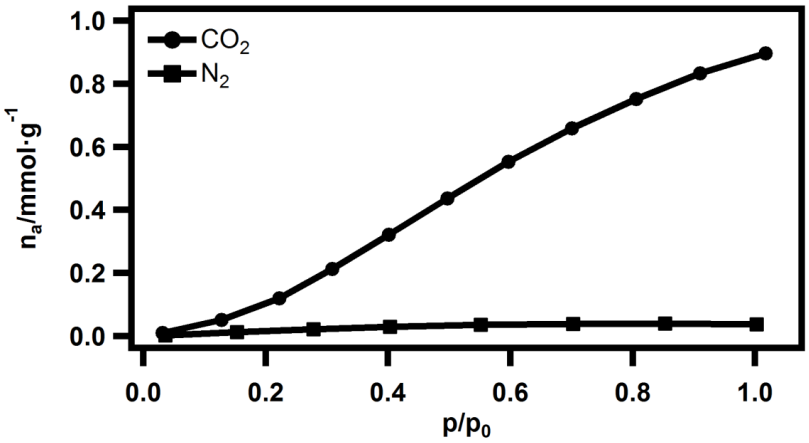

Figure 6.15 CO_2 and N_2 sorption of the MOF-199 BC composites at 273 K.

It should be noted that the selectivity measurement was not conducted in a real environment, and future experiments should evaluate the performance of the MOF-199/BC composites in a real mixed gases environment rather than in separate measurements.

6.2.3 Ni-MOF/Bacterial Cellulose Composites

Since MOF-199 has been successfully immobilised onto the cellulose substrate to form composites and there was indication of the potential for gas separation using the MOF-199/BC composites, the following study focused on the attachment of a different MOF, $[Ni(NCS)_2(\textit{4,4'-bipyridyl})_2]_n$ (Ni-MOF), to the cellulose network and evaluation of the selectivity in separation of isomers.

6.2.3.1 Characterisation

Ni-MOF has been previously prepared via hydrothermal synthesis[33] and the structure has been fully characterized. In this study, a facile method was developed to form Ni-MOF at room temperature, and the bulk Ni-MOF prepared by the new method was compared with the Ni-MOF prepared via hydrothermal synthesis using XRD, SEM, FTIR and TGA.

The XRD patterns of the polycrystalline Ni-MOF prepared by $Ni(NCS)_2$ and 4,4'-bipyridyl in methanol at room temperature matched the simulated pattern from the literature (Figure 6.16).[33] The crystallinity of Ni-MOF was determined to be 43% by Rietveld refinement. The crystallite size was calculated to be 2 nm using the

Scherrer equation (2.1 nm by the Rietveld refinement) for the peak at 2θ of *ca* 20°. Since Ni-MOF was obtained under similar synthesis conditions as that used for MOF-199, a direct comparison could be carried out to evaluate the viability of this approach to attach different MOFs to the composite materials.

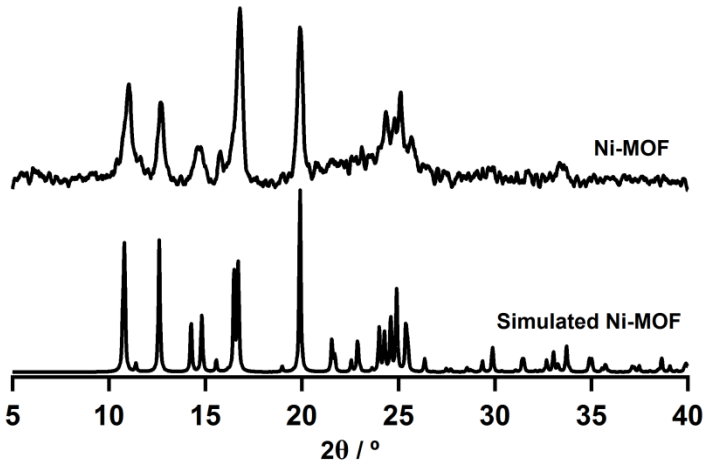

Figure 6.16 XRD patterns of the Ni-MOF made at r.t. and the simulated Ni-MOF.

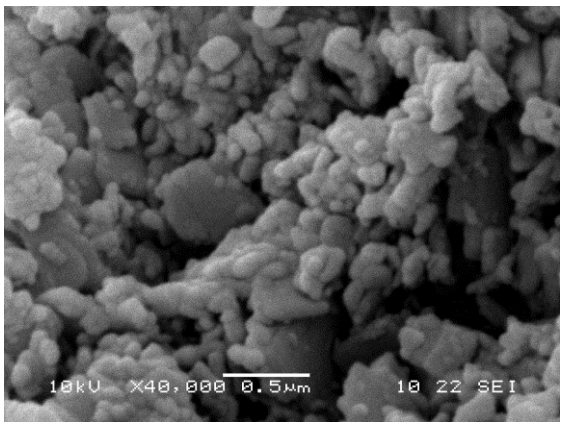

Figure 6.17 SEM of the freeze-dried Ni-MOF.

SEM images show the aggregates of Ni-MOF particles after an oven-drying process (Figure 6.17). This shows a morphology typically seen in many nano-sized materials, which develops over time as the particles tend to aggregate in order to reduce the surface area and minimise the surface free energy.[34] It was expected that the aggregation phenomenon would be significantly reduced in the MOF/BC composites (e.g. MOF-199/BC composites), as the MOFs are locally crystallized and were physically or chemically deposited on the fibre surfaces (which should prevent the

particles merging and aggregating after growth). The reduction in the aggregation behaviour of the MOFs particles could potentially increase the activity for chemical sorption and improve the shelf life of the composite materials.

The TGA result showed a similar two-step thermogravimetric behaviour, but a better thermal stability of the Ni-MOFs (stable up to 250 °C, Figure 6.18), compared to $[Ni(NCS)_2(ppp)_4]$, which was stable up to 170 °C.[35]

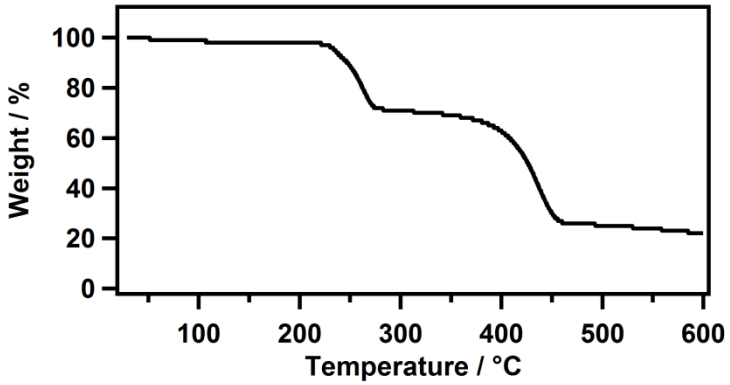

Figure 6.18 TGA of freeze dried Ni-MOF under nitrogen.

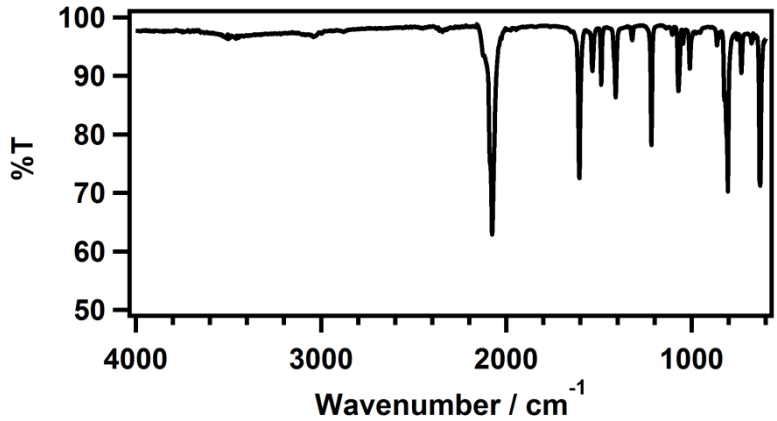

Figure 6.19 FTIR of the freeze dried Ni-MOF.

In the FTIR spectrum (Figure 6.19), the adsorption at *ca* 2100 cm^{-1} indicated the existence of thiocynate groups (-N=C=S) in the synthesised material, and the peak at *ca* 1600 cm^{-1} corresponds to the stretch of C=C bond (the weak peak at *ca* 3000 cm^{-1} is the aromatic C-H stretch). The FTIR pattern is in agreement with the expected chemical constitution of the Ni-MOF.

As the Ni-MOF was successfully synthesized using a room temperature method and the structure was confirmed, it was then introduced to the BC matrix using a similar method as that used to prepare the MOF-199/BC composites discussed above.

After drying of the Ni-MOF/BC composites (Figure 6.20), the gel-like composites shrank to a thin membrane (the membrane could be rigid or flexible contingent on the thickness of the original BC membrane).

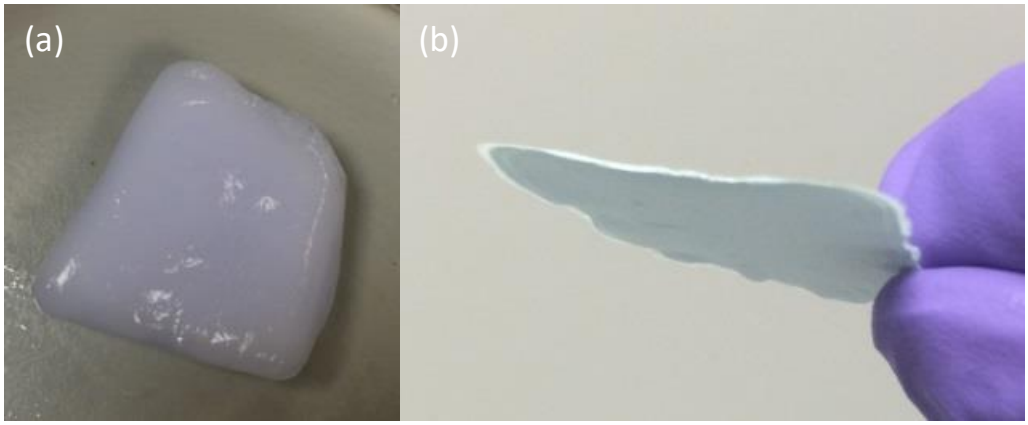

Figure 6.20 Images of (a) as-made and (b) freeze-dried Ni-MOF/BC composites.

Analysis of XRD patterns confirmed the formation Ni-MOF particles onto the BC membrane, with a similar peak at *ca* 20° from Ni-MOF and at *ca* 22° from BC (Figure 6.21). The crystallinity of Ni-MOF in the composite was determined to be 61%, and the Ni-MOF fraction was calculated to be 58 wt%. The Ni-MOF fraction calculated by XRD is comparable to the result obtained from TGA (65 wt%). The crystallite size of the Ni-MOF in the composites was slightly larger than the size of Ni-MOF alone (calculated to be 2.4 nm using the Scherrer equation, and 2.2 nm by Rietveld refinement on the peak at 2θ of *ca* 20°), indicating that the existence of BC promoted the crystallization process of Ni-MOF in the composites (in agreement with the result of MOF-199/BC composites discussed above). It was also noticed that the relative peak intensity ratios of Ni-MOF changed significantly in the composite, indicating a preferential growth direction of the Ni-MOF crystals in the presence of BC.

It should be noted that the peak at *ca* 29° of the BC pattern does not belong to the signal of BC, and it was likely to be a contaminant in the PXRD instrument as the peak was not observed when the using other instruments.

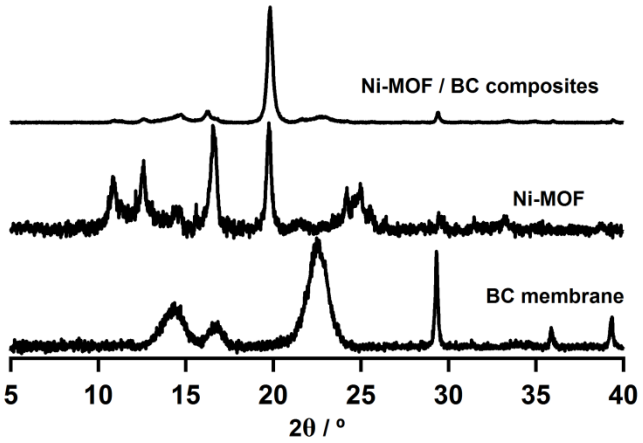

Figure 6.21 XRD patterns of BC, Ni-MOF and Ni-MOF/BC composites.

FTIR spectra (Figure 6.22) also confirmed the existence of both BC (-OH group shift at *ca* 3400 cm^{-1}) and Ni-MOF (-NCS group at *ca* 2000 cm^{-1}) in the composite. It did not, however, illustrate the nature and strength of the binding between Ni-MOF and BC. X-ray photoelectron spectroscopy could potentially be used to probe the nature of the binding of the Ni-MOF to the BC surface based on the characteristic binding energy values that correspond to the configuration of electrons within the atoms,[36] and atomic force microscopy could be useful to measure the strength of the particle binding on the cellulose by measuring the force required to pull the particle away from the cellulose surface.[37]

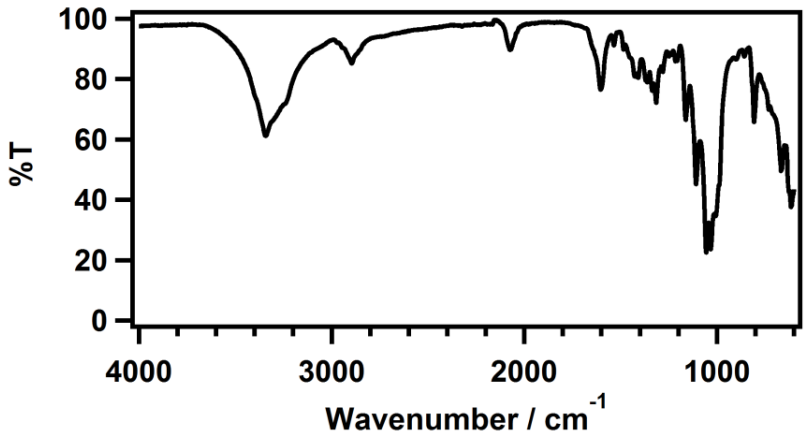

Figure 6.22 FTIR of Ni-MOF/BC composites.

TGA analysis showed the decreased thermal stability of the Ni-MOFs/BC composites when heated under nitrogen, compared to BC and Ni-MOF alone (Figure 6.23). It is

difficult to determine the loading of Ni-MOFs in the composites, based on the weight percentage loss of the composite at ca 250 °C, as BC in the composite also started to decompose. Therefore, the loading calculation was carried out using results from TGA under air (Figure 6.24), using the same method as used for MOF-199/BC composites. The calculated loading for the Ni-MOF in the composites was *ca* 65% (Equation 6.2).

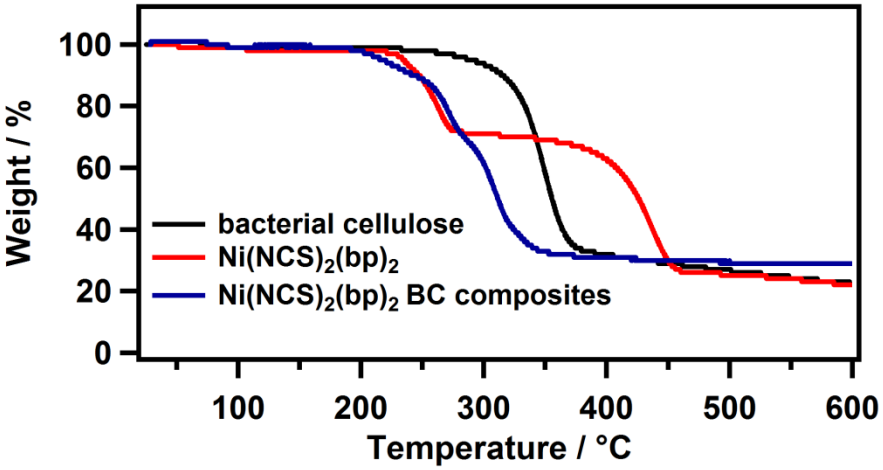

Figure 6.23 TGA of Ni-MOF, BC and Ni-MOF/BC composites under nitrogen.

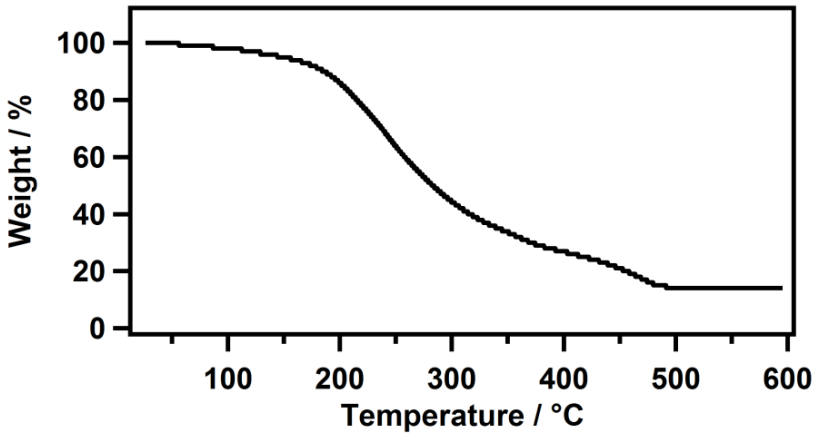

Figure 6.24 TGA of Ni-MOF / BC composite under air flow.

$$Loading\% = \frac{m_{residue}\%}{\mathrm{M}_{Ni_2O_3}} = \frac{m_{residue}\%}{\mathrm{M}_{NiO}} \times M_{\mathrm{Ni}(NCS)_2(4,4'-bipyridyl)_2} = \frac{10\%}{75} \times 487 = 65\% \quad \textbf{(6.2)}$$

SEM images showed a change in the morphology of the BC membrane after the incorporation of Ni-MOF particles (Figure 6.25). Some small particles were observed on the cellulose fibres and merging of the fibres occurred. Based on the XRD results and the SEM image, it was proposed that the Ni-MOF particles may coat the cellulose fibres and grow as uniform layers on the surface of the fibres rather than as isolated particles as seen in the case of the MOF-199/BC composite above.

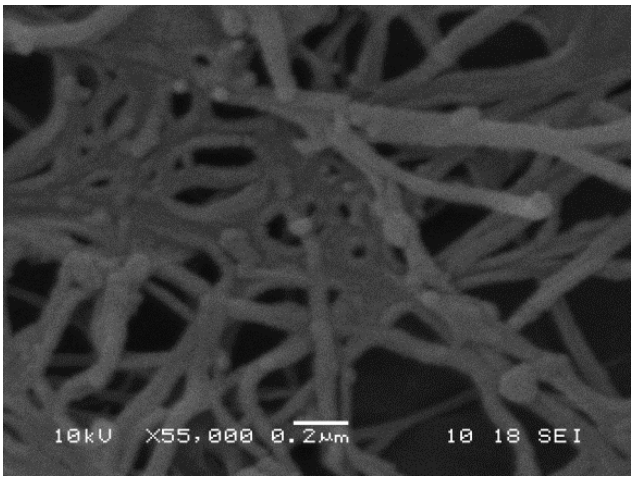

Figure 6.25 SEM image of the Ni-MOF/BC composites.

6.2.3.2 Sorption Study—Single Guest Sorption

Adsorption of guest species (adsorbates) was initially studied using methanol, as it was observed that the colour of the as-made MOF from methanol was different to the freeze-dried MOF (Figure 6.26).

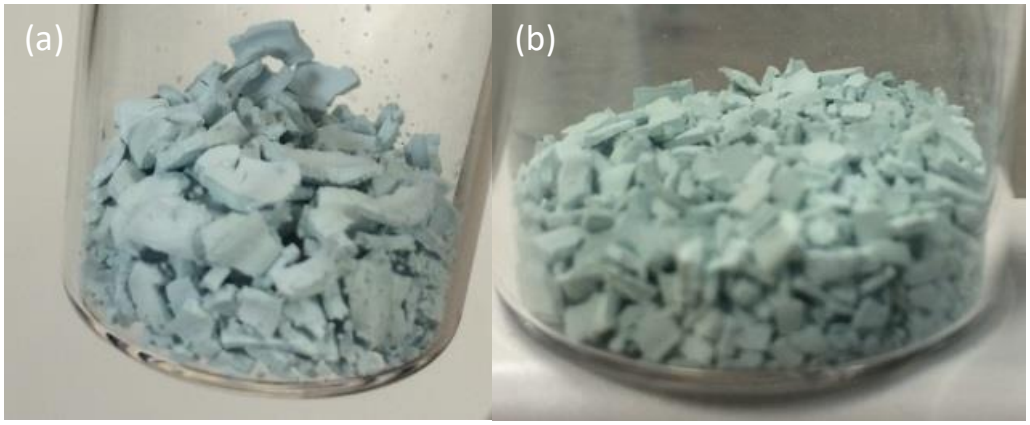

Figure 6.26 Image of the (a) as made from methanol and (b) freeze dried Ni-MOF

After 12 hours equilibration under methanol vapour in a sealed vial until the weight of the Ni-MOF stopped changing, the amount of methanol adsorbed was determined by TGA (Figure 6.27). TGA analysis showed *ca* 12 wt% of methanol was absorbed by MOFs (determined by the weight loss between 30 and 100 °C). The inclusion ratio of methanol in the Ni-MOF alone (not supported on bacterial cellulose) was calculated to be 2, forming the complex Ni-MOF·2methanol (see appendices for calculation).

It is interesting that the Ni-MOF can take up methanol into the porous structure, as the Werner clathrates $Ni(NCS)_2(ppp)_4$ did not adsorb methanol during the synthesis.[12] This result was promising for the study of xylene sorption by Ni-MOF, since the pores of Ni-MOF demonstrated the capability of adsorbing organic molecules.

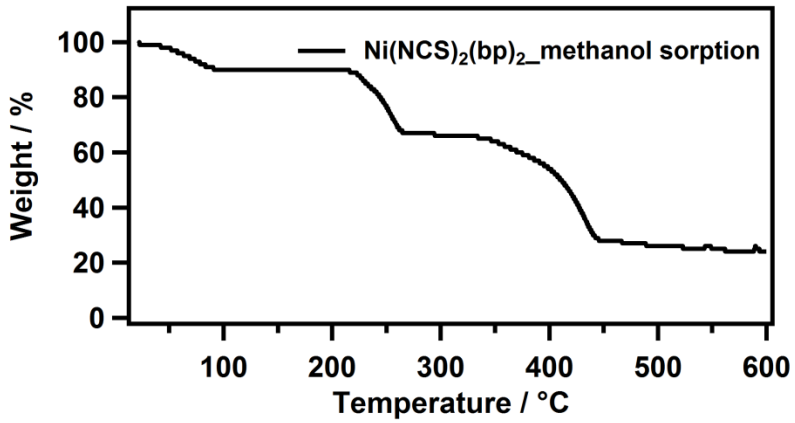

Figure 6.27 TGA of Ni-MOF with adsorbed methanol

To compare the xylene sorption performance of the synthesized Ni-MOFs with $Ni(NCS)_2(ppp)_4$, the Ni-MOF polycrystals were subject to isometric xylene sorption (i.e. the volume of vapour remained constant). Three Ni-MOF samples, after exposure to *ortho*-xylene (o-xylene), *meta*-xylene (m-xylene) or *para*-xylene (p-xylene), were then taken to investigate structural change of the complex and the guest release phenomenon from the complex as a function of temperature using TGA.

The TGA results of Ni-MOF with three xylene isomers adsorbed are displayed in Figure 6.28. Ni-MOF could uptake *ca* 40 wt% xylene isomers, which was almost double the amount adsorbed by $Ni(NCS)_2(ppp)_4$. Among the three xylene isomers, p-xylene seemed to be the least strongly adsorbed in the Ni-MOFs (since this guest was released from 50 °C), o-xylene was the most stable guest molecule (released from 150 °C) and m-xylene was intermediate between the two (released from 100 °C). Interestingly, a two-step desorption behaviour was observed for m-xylene and p-xylene, indicating two possible binding sites of different strength in the complex. In addition, the thermal stability of the Ni-MOF remained after adsorption and removal of the xylene guest molecules.

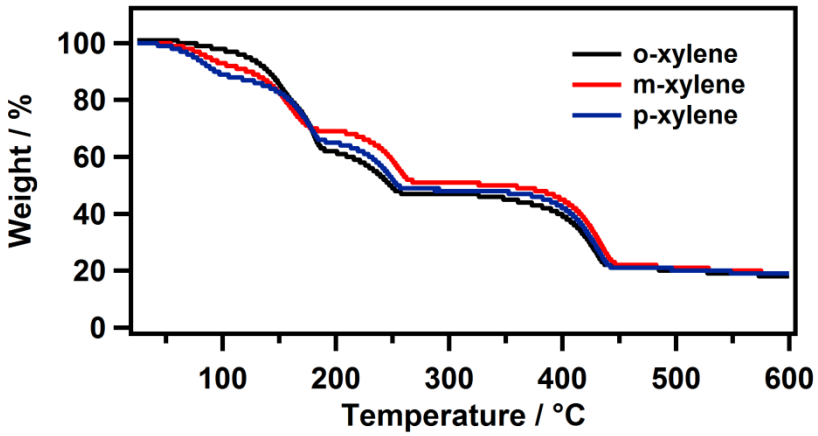

Figure 6.28 TGA of Ni-MOF adsorbed with o-xylene, m-xylene and p-xylene under N_2.

The inclusion ratio of xylene in the Ni-MOF complex was calculated from TGA data and the respective Ni-MOF complexes were Ni-MOF·3o-xylene, MOF·2m-xylene and MOF·2.5p-xylene (see appendices for calculation). The distinctive inclusion ratio

indicated that Ni-MOF adsorbed selectively of one xylene isomer over the others, which is potentially useful for the application of xylene separation.

XRD patterns illustrated the guest responsive behaviour of the Ni-MOF upon sorption of different molecules (Figure 6.29), where the adsorbed guest molecules seemed to expand the pore space within Ni-MOF since the observed diffraction peaks shifted to lower angle (increase in d-spacing). In the presence of o-xylene, the crystal structure became more symmetric, which may contribute to the strongest binding occurring between Ni-MOF and o-xylene. In addition, the structure change of Ni-MOF was reversible after removal of the guest molecules (see appendices), indicating that the adsorption-desorption process of xylene in Ni-MOF could undergo multiple cycles. Similarly, the change of MOF structure upon adsorption of xylene isomers has also been observed in the past, and was ascribed to the different host-guest interactions.[38]

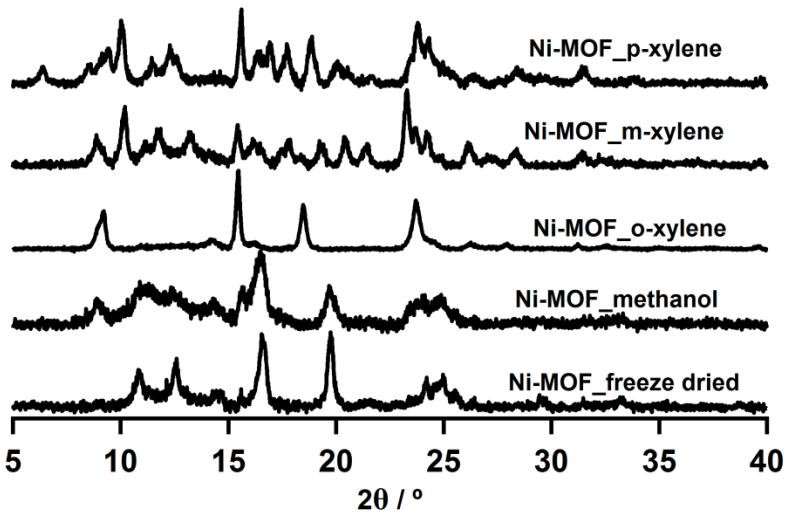

Figure 6.29 XRD patterns of freeze dried Ni-MOF, Ni-MOF after exposure to methanol, o-xylene, m-xylene and p-xylene.

The sorption kinetics curves of uptake of xylenes by Ni-MOF are shown in Figure 6.30. The sorption process was fitted using a first order reaction rate law (the best fit was found empirically and rate constants were extracted). The first order kinetics equation is derived from the Langmuir adsorption isotherm when the initial concentration of the adsorbate is low and this is considered valid for gas-solid sorption processes.[39] The rate constants fitted showed a similar trend to that of the

TGA results and showed that the guest molecules that adsorbed more rapidly into Ni-MOF also bound more strongly. Xylene isomers diffused into Ni-MOF more quickly compared to diffusion of the same isomers into $Ni(NCS)_2(ppp)_4$,[12] possibly due to the open pores in Ni-MOF.

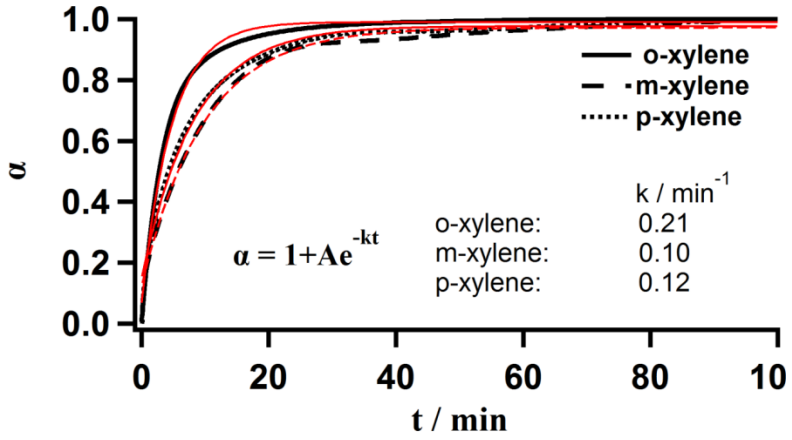

Figure 6.30 Sorption kinetics showing sorption progress, α, as a function of time for the sorption of the xylene isomers. Solid lines are the fitted curves using first order reaction rate law.

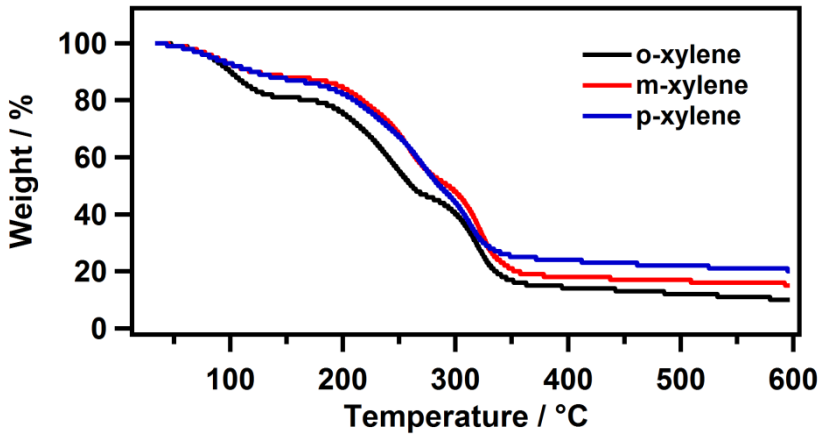

Figure 6.31 TGA of Ni-MOF/BC composites adsorbed with o-xylene, m-xylene and p-xylene under N_2.

A different binding trend for xylene isomers adsorbed in Ni-MOF was observed for the Ni-MOF/BC composites (Figure 6.31). Among the three xylene isomers, o-xylene seemed to be weakly adsorbed in the Ni-MOF/BC composites (since the guest molecule was released from 50 °C), m-xylene and p-xylene showed similar binding

strength. The Ni-MOF/BC composites could uptake *ca* 20 wt% xylene isomers, proportional to the Ni-MOF loading in the composites.

The guest responsive behaviour of the Ni-MOF upon sorption of different molecules, demonstrated by the XRD patterns persisted in the composites (Figure 6.32), and the adsorbed xylene molecules caused an expansion in the pore space of the Ni-MOF, similar to that observed for the pure Ni-MOF samples.

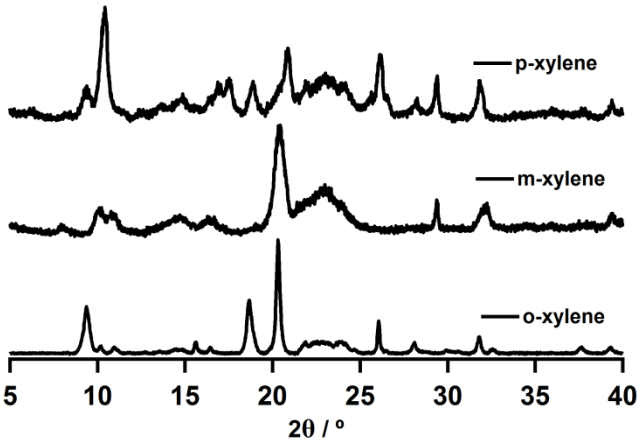

Figure 6.32 XRD patterns of Ni-MOF/BC composites after exposure to o-xylene, m-xylene and p-xylene.

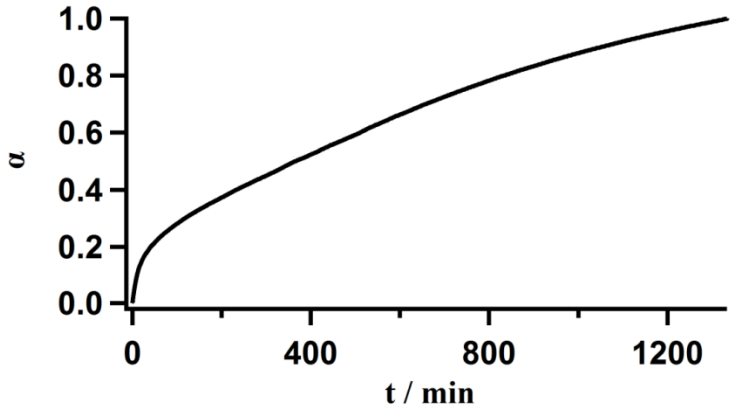

Figure 6.33 Sorption kinetics showing sorption progress, α, as a function of time for the sorption of o-xylene.

The sorption kinetics of xylene uptake by Ni-MOF/BC composites is shown in Figure 6.33. The sorption process was not completed even after 20 h. The slow sorption process may arise due to the requirement for the gas to move from the surface into

the composites. The uptake of o-xylene was *ca* 15 wt% at the end of the sorption experiment, so it was not practical to measure the kinetics rate of this reaction (as the rate was too slow to measure).

6.2.3.3 Sorption Study—Competition Experiment

Competitive adsorption was initially studied by exposing the Ni-MOF to the vapours from binary or tertiary liquid mixtures of the xylene isomers in a sealed environment. The changes in thermal stability and crystal structure of Ni-MOF after adsorption from different mixtures of xylene isomers were investigated.

When o-xylene was present in the liquid mixture, only single step desorption behaviour (a second desorption step was not clear) was observed for the Ni-MOF·xylene complex (Figure 6.34), similar to the desorption behaviour of o-xylene and p-xylene alone (Figure 6.28). When the liquid mixture consisted of m- and p-xylene (mp), a clear two-step desorption behaviour was observed for these species adsorbed into the Ni-MOF complex (Figure 6.34), similar to the desorption behaviour of m-xylene and p-xylene alone (Figure 6.28). The results indicated there was a possible selective sorption when o-xylene was present. It was noticed that the maximum capacity of Ni-MOF for xylene uptake (either a single guest vapour or a mixture) was *ca* 40 wt%.

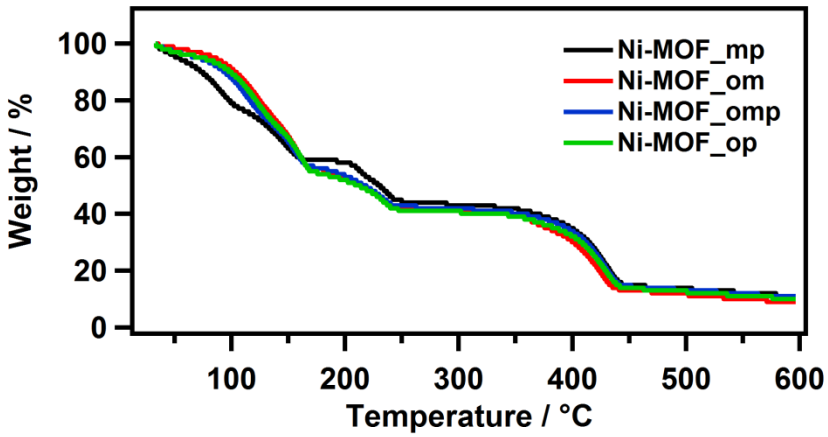

Figure 6.34 TGA of Ni-MOF competition sorption with mixtures of xylene isomers under N_2.

The XRD patterns of the Ni-MOF complexes after adsorption from xylene mixtures all seemed to be surprisingly similar (Figure 6.35) and matched the pattern of Ni-

MOF with adsorbed o-xylene (Figure 6.29), which may be ascribed to the most thermodynamically stable structure. It was not obvious from the XRD results whether a selective sorption had occurred, as the structure of the different Ni-MOF samples became similar upon sorption of the mixtures, different from that of adsorption of individual xylene isomers (Figure 6.29).

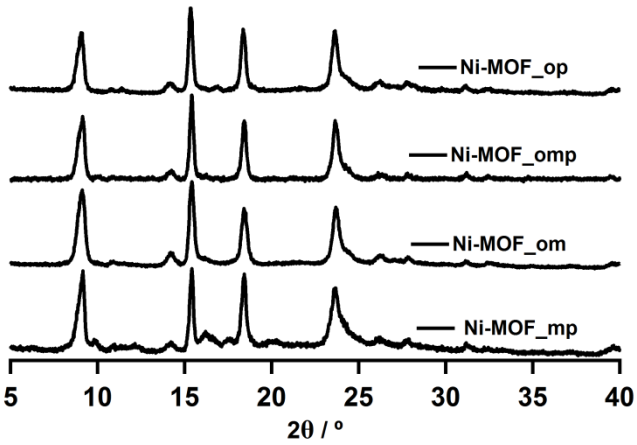

Figure 6.35 XRD patterns of Ni-MOF competition sorption with mixtures of xylene isomers.

Similarly, in competitive adsorption experiments Ni-MOF/BC composites were exposed to the vapours from the liquid mixtures of the xylene isomers under the same conditions as used for the Ni-MOF alone. The change of thermal stability and crystal structure of Ni-MOF within the composite upon adsorbing different mixtures of xylene isomers was investigated.

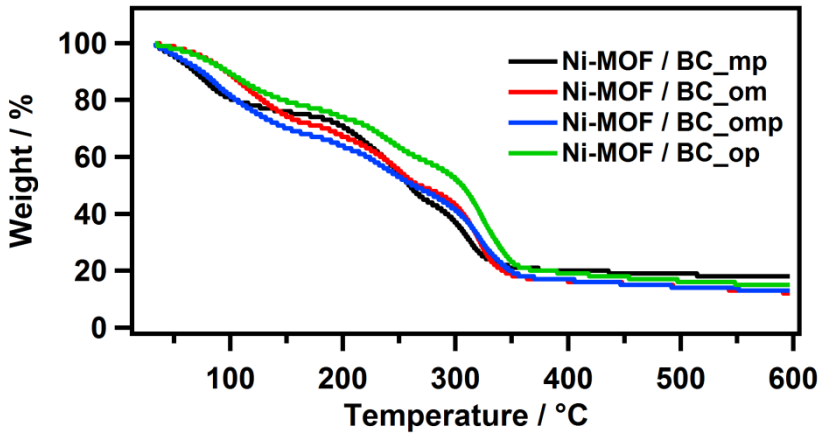

Figure 6.36 TGA of Ni-MOF/BC composite competitive sorption with mixtures of xylene isomers under N_2.

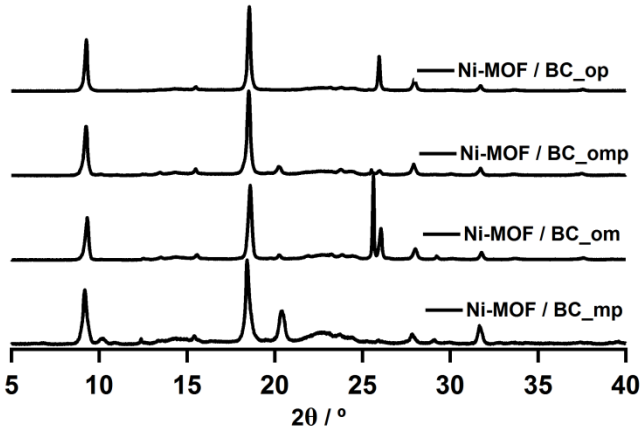

Figure 6.37 XRD patterns of Ni-MOF/BC composite competitive sorption with mixtures of xylene isomers.

The thermal stability of Ni-MOF/BC composites containing mixtures of xylene isomers can be divided into two groups. Mixtures of m- and p-xylene and mixtures of o-, m- and p-xylene were released from the structure at lower temperature, (Figure 6.36), and the respective XRD patterns of the Ni-MOF/BC complexes also seemed to be similar (Figure 6.37). Mixtures of o- and m-xylene and mixtures of o- and p-xylene were released from the structure at higher temperature, with similar peaks at *ca* 26° in the XRD patterns. It was also noticed that the maximum capacity of Ni-MOF/BC composites for xylene uptake (single guest vapour or mixture) was *ca* 20 wt% for the composite (65 wt% Ni-MOF loading in the composites). However, it was not possible to determine the selectivity from these results.

Based on the previous results, quantitative measurements of the competition experiments were undertaken to evaluate the selectivity of Ni-MOF for xylene isomers, using ^{13}C NMR since the selectivity was not able to be determined using TGA and XRD. It should be noted that no sorption of xylene isomers was observed by on BC alone, therefore the uptake of xylene isomers was due to the presence of Ni-MOF in the composite. The results are summarized in Table 6.2.

The ratio of xylene isomers in the mixtures did not change significantly before or after the competitive adsorption experiment for either Ni-MOF or Ni-MOF/BC composites, showing that Ni-MOF particles adsorbed xylene isomers non-selectively in contrast to $Ni(NCS)_2$(*para-phenylpyridine*)$_4$. The isometric sorption of Ni-MOF was

possibly determined by the size of the guest molecules, rather than kinetic (the rate constant of o-xylene was the largest) or thermodynamic factors (o-xylene was released at the highest temperature).

Table 6.2 Summary of competition sorption of xylene isomers.

Solution	omp	om	op	mp
o-xylene:m-xylene:p-xylene	1:1:1	1:1:0	1:0:1	0:1:1
in liquid (starting)	39:29:32	58:42:00	54:00:46	00:47:53
in Ni-MOF	35:30:35	54:46:00	53:00:47	00:47:53
in Ni-MOF/BC	36:29:34	54:46:00	56:00:44	00:48:52

6.3 Conclusions

A facile method for growth of MOF particles onto BC surfaces has been developed by in-situ synthesis at room temperature, and the method could be applied to other MOFs. The existence of MOFs attached to the BC membrane was confirmed optically, and also by use of SEM. TGA was used to calculate the loading of MOFs onto the BC membrane supports.

The separation performance of MOF-199 for CO_2/N_2 was improved in the composites due to the decreasing particle size. Future experiments should be focused on the performance of the MOF-199/BC composites with different MOF-199 loadings, tested in a real mixed gases environment.

Ni-MOF was synthesized at room temperature for the first time, and the structure was shown to be the same as that of the Ni-MOF prepared via hydrothermal synthesis, as characterised by XRD, TGA, FTIR and SEM. The Ni-MOF demonstrated an increased uptake of xylene isomers, compared to $Ni(NCS)_2$(*para-phenylpyridine*)$_4$. However, no selectivity was observed for this Ni-MOF with respect to xylene sorption, due to the non-selective pores introduced. The kinetic and

thermodynamic behaviour of the three xylene isomers adsorbed individually were varied, but in sorption of mixtures showed no preference.

Robust MOFs (MOF-199, no distortion of the frameworks upon sorption) seemed to maintain their structure in the composites, while flexible MOFs (Ni-MOF, distortion of the frameworks upon sorption) adopted a polycrystalline structure which formed uniform coatings on the substrate used. The separation performance of MOF/BC composites was mainly dependant on the functionality of the MOFs attached, and separation of different chemical mixtures could be achieved by varying the MOFs used in the composites.

6.4 References

1. H. Li; M. Eddaoudi; M. O'Keeffe; O. M. Yaghi, *Nature,* 1999, **402**, 276-279.
2. J. Lee, et al., *Chem. Soc. Rev.,* 2009, **38**, 1450-1459.
3. J.-R. Li, et al., *Nat Commun,* 2013, **4**, 1538.
4. B. Liu, *J. Mater. Chem.,* 2012, **22**, 10094-10101.
5. L. E. Kreno, et al., *Chem. Rev.,* 2011, **112**, 1105-1125.
6. A. Bétard; R. A. Fischer, *Chem. Rev.,* 2012, **112**, 1055-1083.
7. Y. Oishi; M. Nakaya; E. Matsui; A. Hotta, *Composites Part A,* 2015, **73**, 72-79.
8. S. Galland, et al., *J. Mater. Chem. C,* 2013, **1**, 7963-7972.
9. J. George; K. V. Ramana; S. N. Sabapathy; A. S. Bawa, *World J. Microbiol. Biotechnol.,* 2005, **21**, 1323-1327.
10. D. J. Tranchemontagne; J. R. Hunt; O. M. Yaghi, *Tetrahedron,* 2008, **64**, 8553-8557.
11. S. S.-Y. Chui; S. M.-F. Lo; J. P. H. Charmant; A. G. Orpen; I. D. Williams, *Science,* 1999, **283**, 1148-1150.
12. M. Lusi; L. J. Barbour, *Angew. Chem. Int. Ed.,* 2012, **51**, 3928-3931.
13. L.-D. Shiau; C.-C. Wen; B.-S. Lin, *Ind. Eng. Chem. Res.,* 2005, **44**, 2258-2265.
14. Y. Zhang; L. Jianmin; M. Nishiura; T. Imamoto, *J. Mol. Struct.,* 2000, **519**, 219-224.
15. J. J. Low, et al., *J. Am. Chem. Soc.,* 2009, **131**, 15834-15842.
16. M. Sanchez-Sanchez, et al., *Green Chem.,* 2015, **17**, 1500-1509.
17. D. Jiang; A. D. Burrows; R. Jaber; K. J. Edler, *Chem. Commun.,* 2012, **48**, 4965-4967.
18. S. Diring; S. Furukawa; Y. Takashima; T. Tsuruoka; S. Kitagawa, *Chem. Mater.,* 2010, **22**, 4531-4538.
19. T. Uemura; Y. Hoshino; S. Kitagawa; K. Yoshida; S. Isoda, *Chem. Mater.,* 2006, **18**, 992-995.
20. L. Brinda; K. S. Rajan; J. B. B. Rayappan, *J. Appl. Sci.,* 2012, **12**, 1778-1780.
21. N. Liu, et al., *Nano Res.,* 2012, **5**, 109-116.
22. D. Jiang; A. D. Burrows; K. J. Edler, *CrystEngComm,* 2011, **13**, 6916-6919.
23. E. Rabani; D. R. Reichman; P. L. Geissler; L. E. Brus, *Nature,* 2003, **426**, 271-274.
24. R. T. Olsson, et al., *Nat. Nanotechnol.,* 2010, **5**, 584-588.
25. J.-L. Zhuang; D. Ceglarek; S. Pethuraj; A. Terfort, *Adv. Funct. Mater.,* 2011, **21**, 1442-1447.
26. J. Gascon; S. Aguado; F. Kapteijn, *Microporous Mesoporous Mater.,* 2008, **113**, 132-138.
27. P. Li, et al., *Chem. Commun.,* 2015, **51**, 10925-10928.
28. A. M. Sokolnicki; R. J. Fisher; T. P. Harrah; D. L. Kaplan, *J. Membr. Sci.,* 2006, **272**, 15-27.
29. K. S. W. Sing, et al., In *Handbook of Heterogeneous Catalysis*, Wiley-VCH Verlag GmbH & Co. KGaA, 2008.
30. D. Jiang; T. Mallat; F. Krumeich; A. Baiker, *Catal. Commun.,* 2011, **12**, 602-605.
31. L. Heath; W. Thielemans, *Green Chem.,* 2010, **12**, 1448-1453.
32. M. Silva Pinto; C. Sierra-Avila; J. Hinestroza, *Cellulose,* 2012, **19**, 1771-1779.

33. Y. Zhang; L. Jianmin; D. Wei; M. Nishiura; T. Imamoto, *Chem. Lett.,* 1999, **28**, 195-196.
34. J. Li; Y. Lin; B. Zhao, *J. Nanopart. Res.,* 2002, **4**, 345-349.
35. E. Batisai; M. Lusi; T. Jacobs; L. J. Barbour, *Chem. Commun.,* 2012, **48**, 12171-12173.
36. Y. A. Teterin, et al., *Physical Review B,* 2014, **89**, 035102.
37. L. Gross, et al., *Science,* 2012, **337**, 1326-1329.
38. R. El Osta, et al., *Chem. Mater.,* 2012, **24**, 2781-2791.
39. Y. Liu; L. Shen, *Langmuir,* 2008, **24**, 11625-11630.

Chapter 7 Conclusions and Future Work

7.1 Conclusions

In this thesis it is demonstrated that oxidised cellulose nanofibrils (OCNF) can be obtained from an electro-oxidation process, thus reducing the environmental impact of the oxidation process by adopting a more sustainable primary oxidant (electrical energy, where the renewable energy sources could be derived from wind, nuclear power and tidal energy[1]). OCNF possess a number of properties (e.g. large aspect ratio, negative charge on the fibril surface, and flexible nanofibrils) that render them useful in a range of applications (e.g. as the basis for composites or emulsifiers), replacing chemicals from petrochemical sources, potentially irritating surfactants (e.g. sodium lauryl sulfate) and non-biodegradable materials (e.g. silicones) used in personal care products and composite materials. The methods for optimising the electro-oxidation reaction conditions have been presented, and the potential applications of OCNF were explored.

A facile voltammetric method using a cotton-covered electrode has been developed to optimise the reaction conditions of TEMPO-mediated electro-oxidation of cellulose, and the method described could be applied to other water insoluble substrates (e.g. chitin), using the corresponding substrate-fabric/film electrode. The method is very useful in fast screening of potential new mediators for cellulose oxidation, where only a small quantity of the mediator (*ca* 0.05 mmol) is required for the initial experiment, and the results can be achieved in less than a minute. This allows exploration of new catalysts, especially when the synthesis is difficult and only small amounts of the mediator are available to test, minimising labour and reducing energy consumption during the research process.

It was found that the reaction rate of the cellulose oxidation accelerated at elevated pH, for all the mediators tested. At pH 10, TEMPO was found to be the most efficient catalyst in the oxidation of cellulose. On the other hand, 4-acetamido-TEMPO was more effective than TEMPO in the oxidation of cellulose under acid or neutral conditions. The results of the catalytic efficiency tests carried out in this study were in accordance with previous research, demonstrating that this novel, rapid method can

be used to replace the slower and more laborious chemical methods for catalyst testing.

In neutral/acidic environments, the rate of the oxidation was found to be controlled by the disassociation constant of the mediator. When the pH was close to the pK_a of $TEMPOHH^+$ ($pK_a \approx 7$), a significant decrease in the reaction rate occurred. The pK_a of 4-acetamido-$TEMPOHH^+$ was *ca* 6, therefore a higher catalytic efficiency was observed for 4-acetamido-TEMPO under the same conditions as TEMPO at pH 7. The finding is useful to design new mediators which perform better under neutral or acidic conditions, where depolymerisation of cellulose during the oxidation can be avoided.[2]

The anions of buffers, which were used during the electro-oxidation reactions, were also found to significantly alter the reaction rate under neutral conditions. This finding is very important, as all of the TEMPO mediated electro-oxidation reactions require buffer to stabilise the pH, or as background electrolyte (e.g. NaCl) during the reaction process, however the effect of the differing structure of these added electrolytes has not been investigated in detail before. This finding is especially useful for the enzyme driven laccase-TEMPO oxidation of cellulose, where citrate buffer is commonly used to stabilise laccase under acidic environments[3] and the implications of this is discussed further in section 7.2.

Buffer anions were found to participate in the cellulose oxidation reaction at neutral pH, affecting the efficiency of the mediator through electrostatic and steric effects:

1) Direct interaction of the buffer anion with $TEMPO^+$ was identified from NMR studies and the anion effect on the catalytic efficiency was shown to follow the Hofmeister Series (a combination of the effective surface charge and the diameter of the hydrated anion), based on the results of CV.
2) Reducing the accessibility of $TEMPO^+$ to cellulose. When the buffer concentration was increased, the equilibrium would be shifted towards the $TEMPO^+$/anion salts or complexes with these anions effectively screening the $TEMPO^+$ charge, reducing the interaction between $TEMPO^+$ and cellulose,

which bears an increasing density of negative charge as the oxidation reaction proceeds.

The reaction rate at neutral pH is a complex result that results from the balance between the electrostatic and steric effects, therefore an extensive study would be required to combine these factors into a single equation. However, it was possible to probe the effect of different buffers, or electrolytes, on the cellulose oxidation rate, using CV. Under basic conditions, the reaction rate between TEMPO and cellulose accelerated, suggesting that the competing equilibria (complexed $TEMPO^+$ *versus* reactive intermediate $TEMPO^+$/cellulose) were shifted towards the reactive complex with cellulose, such that the effect of the anions was negligible, therefore all anions resulted in an identical reaction rate at pH 10.

Using the optimal reaction conditions obtained from the CV study (using a TEMPO mediator in carbonate buffer at pH 10), electro-oxidation of cellulose resulted in a controllable degree of oxidation of cellulose as this could be followed by monitoring the consumed electricity, and, most importantly, the reaction could be completed within a relatively short duration (*ca* 2 h, comparable to the NaClO/NaBr/TEMPO chemical oxidation route). The OCNF produced by electro-oxidation exhibited similar fibril morphology and thermal stability compared to the OCNF obtained from the chemical oxidation in the NaClO/NaBr/TEMPO system. However, the content of aldehyde groups formed on the OCNF surface using electro-oxidation was much higher than that formed during the NaClO/NaBr/TEMPO oxidation. The carboxylate to aldehyde ratio can be increased during the synthesis by lowering the reaction temperature, but the reaction rate will also be slowed. Thus, a post-reaction polishing step is necessary if low aldehyde content is undesirable for the final product. However, it is desirable to have *high* aldehyde contents for some applications, such as paper strength improvement[4] and enzyme immobilization.[5]

It was shown that the OCNF were able to stabilise o/w Pickering emulsions, using various formulations with different salt concentrations. The critical concentration of OCNF required to stabilise a hexadecane/water emulsion of 30/70 phase volume ratio was found to be *ca* 3 $g \cdot L^{-1}$ of OCNF suspension in the aqueous phase, which is ascribed to the efficient coverage of the oil droplet surface by OCNF. The OCNF was

found to form a mesh-like shell at the oil-water interface, determined by AFM, and the shell thickness responded to the ionic strength in the aqueous phase as indicated by SEM. However, the drying methods of the emulsions for AFM and SEM resulted in the aggregation of OCNF, therefore did not provide accurate information about the OCNF shell structure in the real (wet) environments.

The shell responsive behaviour was then studied *in situ* by small angle scattering, without drying the samples. It was found that the evolution of the OCNF shell underwent 3 stages: from the formation of single layer of OCNF mesh to a hydrated network, and eventually compressed to a more densely packed network, with increasing ionic strength in the aqueous phase. This finding was also confirmed by the rheology results, where a less connected network of the emulsion was observed at high ionic strength, indicating that fewer OCNF remained in the aqueous phase to support the network. Exploitation of the salt responsive behaviour was illustrated in a potential application of delayed drug delivery, and the freeze-dried emulsions resulted in structured porous networks which could be used as scaffolds for catalysts, supports for MOF crystals, or (following carbonization) for electrode applications.

Oxidised cellulose was, for the first time, used to support MOFs onto the fibril surfaces. For the convenience of characterisation in the initial investigation, a self-standing bacterial cellulose (BC) membrane was used as alternative to oxidised cellulose nanofibrils for MOF attachment. BC was used in a non-oxidised form, as the large surface area on the fibrils was able to form metal-oxygen coordination bonds, allowing the growth of MOFs on the site. However, for the production of OCNF, it was essential to form enough carboxylate groups on the cellulose surfaces, in order to facilitate fragmentation of the large initial cellulose fibres into nanoscale fibrils to provide a high functionalized surface area for MOF growth. These cellulose-based MOF composites complement other metal- or polymer-based materials and can be produced at relatively low cost (compared to metal based substrates). BC provides a strong substrate for the production of self-supporting membranes or films and, as it is known that OCNF can also be fabricated into films, there are opportunities for production of various materials for specific applications. If the MOF components are environmentally acceptable, the biodegradability of the cellulose

substrates would allow for innocuous end of life treatment potentially improving sustainability of the composites. The effect of the MOF components on biodegradability would need to be ascertained if biodegradable materials are desired (see section 7.2).

The successful immobilisation of two MOFs (MOF-199 and Ni-MOF) onto bacterial cellulose was visualised by colour changes of the membranes and SEM images. MOF-199 maintained the structure in the composites, while the Ni-MOF adopted a preferential growth which formed uniform coatings on the substrate, determined by XRD. The separation performance of MOF-199/BC composites with respect to CO_2/N_2 separation was improved due to the formation of smaller MOF particles, and the size of MOF particles was demonstrated to be adjustable, depending on the diameter of the cellulose fibres used. The Ni-MOF and Ni-MOF/BC composite did not show selectivity for xylene isomers, as the pores in the Ni-MOF were too large and therefore able to accommodate all xylene isomers without incurring any energy penalty. However, the uptake of xylene was *ca* 40 wt% due to the large pores present in the MOF – the potential for exploiting this is discussed in section 7.2.

In summary, the reaction conditions of TEMPO electro-mediated oxidation of cellulose have been optimised using cyclic voltammetry, and possible impact of different buffer identities was elucidated. OCNF have been produced in bulk quantities (gram scale) by electro-oxidation in the lab. OCNF demonstrate promising applications for stabilising Pickering emulsion and making composite materials.

7.2 Future work

Increasing awareness of the importance of using sustainable materials for various applications (e.g. automotive parts, personal care products) in combination with the desire for low cost, light weight and high mechanical performance, has stimulated extensive research on biopolymer based materials. Cellulose derived materials are particularly attractive as cellulose is the most abundant biopolymer and is renewed rapidly in nature.[6] In addition, it is obtainable from waste sources (e.g. food processing waste[7]) and is not a human food stuff, so the food *versus* chemicals or materials issue does not arise.[8] There are few examples of OCNF commercial

products in the market at the moment, as the uptake may be hampered by the cost and availability of OCNF commercially (e.g. while Croda has tested production of OCNF at tonne scale for applications in personal care products, the product is not yet available at large scale; Nippon Paper Group produces OCNF pre-commercially, potentially for use in high end markets for electronics, composite and personal care products, although the focus is believed to be on the use of OCNF in films[9]). However, with the increasing market demand for sustainable products, it is expected that the price of OCNF will significantly reduce to a level low enough to compete with some synthetic polymers, due to improved economies of scale and investment from government and industry (this has already occurred in the UK *via* TSB and Innovate UK funding for collaborative research projects). In addition, new techniques developed for production will also contribute to the cost reduction and improved performance of new materials (e.g. Omya patented the production of CNF via mineral grinding, which could reduce the energy consumption and resulted in a better performance of the final product[10]). Therefore, it is also possible to combine disintegration of the OCNF during the TEMPO oxidation process, or *in-situ* nanofibrillate with polymer to form composites, and the combined synergetic effects of such processes should be investigated to optimize the manufacturing process.

A long-term ambition of the research is to produce OCNF commercially (both the electrochemical method and the co-grinding method, described above, could be explored) and to apply OCNF to products beyond traditional paper applications, based on the fundamental understanding of properties and challenges of OCNF (e.g. mechanical, rheological, biological and optical performance). OCNF has potential for use in high end paper products, e.g., in specialty paper to increase paper strength, but there are also various new promising applications mentioned in Chapter 1. In future, OCNF may be used in many products in our daily life from creams and lotions (such as the Pickering emulsions described here) to composite materials, and some possible works are highlighted later in this section. Development of such applications requires understanding of the opportunities and limitation of OCNF in the specific materials and further developments to improve the performance. For instance, OCNF can be used as filler in plastics and this application would be particularly beneficial in plastics intended to be composted at end-of-life, such as polylactide.[11]

However, the hydrophilic characteristics of cellulose would lead to the inhomogeneous distribution of OCNF in the composite, resulting in poor mechanical performance.[11] Therefore, further modification of OCNF would be required to increase the hydrophobicity of OCNF, either chemically or physically (e.g. by the adsorption of lignin, or by chemical modification of surfaces, including grafting of appropriate moieties[12]). Solvent exchange of OCNF in organic solvent (e.g. DMSO[13]) followed by mixing with polymer may also help to increase the homogeneity of the composite. For all of these large scale applications, cost effective, efficient productions of OCNF are required and it is suggested that the electrochemical route described here might be developed into a continuous process using flow cells.

Transportation of OCNF suspension from the manufacturing plant to customer is a common requirement at present, but this is inconvenient and very costly, as over 90 wt% of the sample is just water (OCNF suspensions would also require large areas for storage and the supply of such dilute dispersions limits the scope available to the formulator – most water in the formulation is already in the OCNF dispersion). Some research focused on the improvement of the redispersibility of de-watered CNF using different methods (e.g. freeze-drying,[14] reducing aldehyde content[15]), and other possible drying methods (e.g. combination of freeze-drying with surface modification[16]) could also be explored. Evaluation of the rheological and/or mechanical performance of the rehydrated OCNF would then be required in the future.

Last, but not least, different methods for cellulose research should be standardized and made comparable amongst the literature. For instance, reporting of crystallinity indices using powder XRD data, different fitting methods may lead to the discrepancies in results. Although the Rietveld method is considered to be accurate and comparable with results obtained from other measurements,[17] the quality of the collected XRD data and the use of different crystal parameters in the fitting could also lead to differing results,[18] FITR and solid state ^{13}C NMR have also been demonstrated as methods applicable to the evaluation of the crystallinity of cellulose, but the differences in results obtained from different methods are often neglected (the trend of the crystallinity change may be consistent, but the absolute value is

often not).[19] Therefore, a comparable and standard method is essential to understand and validate the results published in the cellulose research area. Cross-checking of different methods used would be a useful way to correlate the results and evaluate the reliability of the method used.

In this thesis, the possibility of producing OCNF by electro-oxidation has been demonstrated and thus OCNF obtained from electro-oxidation can be used as a green alternative to chemically oxidised cellulose for various applications. Furthermore, many possible research directions based on the results in this study are worthy of further investigation and these are listed:

1) The effect of buffer type on laccase/mediator oxidation reactions of cellulose should be explored, as the results gained in this electrochemical oxidation study showing that the use of citrate buffer results in a much slower reaction rate compared to that of reactions buffered with phosphate buffer at pH 7. Thus, one would suggest that the use of citrate buffer is good for laccase stability, but not desired for cellulose oxidation. Therefore, a better buffer for laccase-TEMPO oxidation of cellulose is required. The rapid screening method described here could be used to test a range of buffers to optimise conditions for enzymatic oxidation.
2) The impact of cellulose crystallinity on the electro-oxidation reaction should be investigated by CV, quantifying the relationship between crystallinity and reaction rate. The rates of oxidation of highly crystalline cellulose nanowhiskers *versus* OCNF, which contains both crystalline and amorphous segments, would provide insights into how important penetration into cellulose particles is in this process. This study could be extended, by considering cellulose with different degrees of crystallinity, which can be obtained by regenerating ionic liquid dissolved cellulose using different anti-solvents (e.g. methanol, ethanol and water).[20] This will help to understand how the accessibility of cellulose functional groups alters the overall reaction rate, accurately and efficiently.
3) Screening of a variety of buffers, or salts, in the TEMPO mediated cellulose oxidation reaction under neutral or acidic environments should be undertaken

to optimise the reaction rate. Concentration effects of the buffer should be further investigated using larger variations (e.g. from 1 *mM* to 0.1 *M*). TEMPO cations associated with different anions should be prepared and studied at different pH using NMR to better understand the interaction of TEMPO cations and salt anions.

4) Testing of new mediators, with low pK_a, which could be synthesised based on structures predicted using computational methods (e.g. DFT)[21] would be facilitated by the rapid screening methodology described here. These mediators could be designed to increase the oxidation rate at low pH, thus avoiding depolymerisation of cellulose during the reaction under basic conditions.
5) For the electro-oxidation, NaCl could be used as electrolyte in the system for *in-situ* generation of NaClO,[22] which could act as an oxidant to oxidize TEMPO, and also to convert aldehydes into carboxylates. This avoids the addition of stoichiometric amounts of the NaClO, therefore reduces the hazards associated with transport and use of hypochlorite solutions.
6) Grinding oxidised cellulose together with solid catalysts could be explored to convert cellulose into a valuable renewable chemicals.[23] The process is expected to consume less energy than the direct conversion of un-modified cellulose, as oxidised cellulose requires much less energy to break down into smaller fragments compared to the un-modified cellulose, providing higher surface area for the reaction.[24] However, as the oxidation process itself will add cost to the process, focus should be on relatively high value products.
7) Emulsion foams stabilized by OCNF could be used as precursors to prepare porous carbon electrodes via pyrolysis.[25] The emulsion can be formulated with other metal salts (e.g. $Ni(NO_3)_2$) or polymers (e.g. hyaluronan) to give different particle loadings or elemental doping for carbon electrodes used in sensor and energy storage applications. These foams also provide opportunities for templating metal oxides, such as TiO_2, allowing modulation of bulk structure as the proof of concept results in chapter 5 illustrate.

8) Polymerizable resin emulsions stabilised by OCNF could be used as environmentally friendly aqueous based formulations for painting and coating, reducing the use of irritating and volatile organic solvents.
9) Further studies of controlled delivery are necessary if these OCNF stabilised emulsions are to prove useful in for such applications, such as for delivery of agrochemicals, or flavours & aromas as well as pharmaceutically active compounds. The fact that the OCNF is biodegradable[26] means that degradation of OCNF, as well as the changes of shell thickness in ionic strength, could be used to modulate release of actives from the emulsions.
10) The CO_2/N_2 separation performance of the MOF-199/BC composite should be tested in a real mixture of gases to evaluate the selectivity. Variation of the MOF loading should be carried out to enhance the uptake/separation of the gases. Attempts should be made to immobilise different MOFs onto the BC membrane to test the scope of the particles that can be attached. In addition, the mechanical performance, lifetime, recyclability and the permeability of the composites towards various mixtures should also be investigated in order to optimise the composites for separations at an industrial level.

11) The use of Ni-MOF and Ni-MOF/BC composite as hydrogenation catalyst for molecules of similar size to xylene could be further explored (the productions of aromatic-free solvents are desired due to environmental legislation),[27] as the uptake of xylene was *ca* 40 wt% due to the large pores of MOF. The biodegradability of this composite and any others tested should also be investigated, or other end of life options (e.g. pyrolysis and metal recovery) tested.

The main outcome of the project results in a more environmentally friendly electro-mediated TEMPO oxidation of cellulose compared to the chemical oxidation system. This contributes to a partial replacement of polymers from fossil resources used in composites, in order to establish a sustainable society based on renewable resources. Clearly, further attention to the safety-issues and the biodegradability of the oxidised cellulose based composites is the current focus, to evaluate the overall impact of OCNF on the human society.

7.3 References

1. Q. Schiermeier; J. Tollefson; T. Scully; A. Witze; O. Morton, *Nature,* 2008, **454**, 816-823.
2. M. Hirota; N. Tamura; T. Saito; A. Isogai, *Carbohydr. Polym.,* 2009, **78**, 330-335.
3. S. S. More, et al., *Enzyme Research,* 2011, **2011**, 7.
4. E. Aracri; C. Valls; T. Vidal, *Carbohydr. Polym.,* 2012, **88**, 830-837.
5. N. Isobe, et al., *Cellulose,* 2011, **18**, 1251-1256.
6. X. W. Cao; B. Ding; J. Y. Yu; S. S. Al-Deyab, *Carbohydr. Polym.,* 2012, **90**, 1075-1080.
7. B. M. Cherian, et al., *J. Agric. Food. Chem.,* 2008, **56**, 5617-5627.
8. R. J. Moon; A. Martini; J. Nairn; J. Simonsen; J. Youngblood, *Chem. Soc. Rev.,* 2011, **40**, 3941-3994.
9. A. Isogai, Personal Communication, 2014.
10. *UK Pat.,* WO2014009517 A1, 2014.
11. S. Fujisawa; T. Saito; S. Kimura; T. Iwata; A. Isogai, *Biomacromolecules,* 2013, **14**, 1541-1546.
12. S. Eyley; W. Thielemans, *Nanoscale,* 2014, **6**, 7764-7779.
13. Y. Okita; S. Fujisawa; T. Saito; A. Isogai, *Biomacromolecules,* 2011, **12**, 518-522.
14. F. Jiang; Y. L. Hsieh, *ACS Appl. Mater. Interfaces,* 2014, **6**, 20075-20084.
15. S. Takaichi; T. Saito; R. Tanaka; A. Isogai, *Cellulose,* 2014, **21**, 4093-4103.
16. Z. Hu; H. S. Marway; H. Kasem; R. Pelton; E. D. Cranston, *ACS Macro Letters,* 2016, **5**, 185-189.
17. L. Jasmani; S. Eyley; R. Wallbridge; W. Thielemans, *Nanoscale,* 2013, **5**, 10207-10211.
18. S. Park; J. O. Baker; M. E. Himmel; P. A. Parilla; D. K. Johnson, *Biotechnol. Biofuels,* 2010, **3**, 1-10.
19. D. O. Carlsson; J. Lindh; M. Strømme; A. Mihranyan, *Biomacromolecules,* 2015, **16**, 1643-1649.
20. X. Geng; W. A. Henderson, *RSC Advances,* 2014, **4**, 31226-31229.
21. T. Matsui; T. Baba; K. Kamiya; Y. Shigeta, *PCCP,* 2012, **14**, 4181-4187.
22. G. F. Qin; Z. Y. Li; X. D. Chen; A. B. Russell, *J. Food Eng.,* 2002, **54**, 111-118.
23. S. Van de Vyver; J. Geboers; P. A. Jacobs; B. F. Sels, *ChemCatChem,* 2011, **3**, 82-94.
24. A. Isogai; T. Saito; H. Fukuzumi, *Nanoscale,* 2011, **3**, 71-85.
25. Y.-R. Rhim, et al., *Carbon,* 2010, **48**, 1012-1024.
26. I. Homma; T. Isogai; T. Saito; A. Isogai, *Cellulose,* 2013, **20**, 795-805.
27. S. Toppinen; T. K. Rantakylä; T. Salmi; J. Aittamaa, *Ind. Eng. Chem. Res.,* 1996, **35**, 1824-1833.

Chapter 8 Appendices

8.1 Summary of diffusion coefficient of mediator

Table 8.1 Diffusion coefficient of mediator at different pH

Mediator	pH 5	pH 6	pH 7	pH 8	pH 9	pH 10
TEMPO	4.3E-06	-	5.6E-06	5.2E-06	5.6E-06	6.1E-06
4-acetamido-TEMPO	-	-	3.47E-06	3.86E-06	-	4.8E-06
4-carboxy-TEMPO	-	-	-	3.09E-06	-	4.6E-06
4-hydroxy-TEMPO	-	5.0E-06	5.0E-06	-	-	-

8.2 Nitrogen Sorption of BC

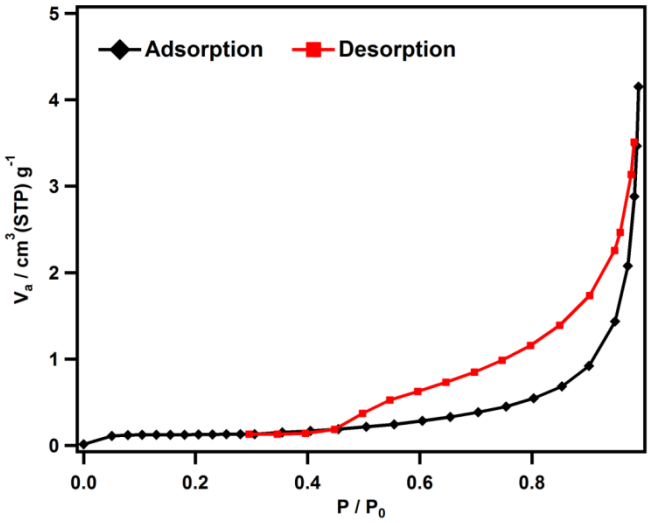

Figure 8.1 Nitrogen adsorption isotherm for thermally dried BC measured at 77 K. The specific surface area was *ca* 0.5 $m^2 \cdot g^{-1}$ using BET.

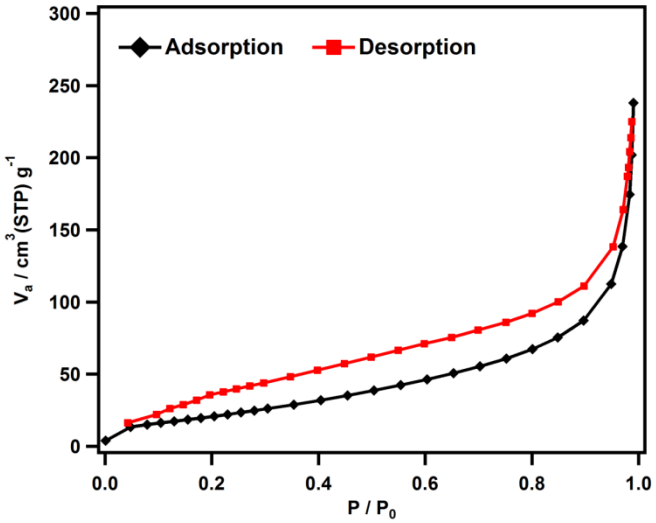

Figure 8.2 Nitrogen adsorption isotherm for freeze-dried BC measured at 77 K. The specific surface area was *ca* 70 $m^2 \cdot g^{-1}$ using BET.

8.3 TGA Calculation of Inclusion Ratio

Table 8.2 Summary of inclusion ratio of Ni-MOF· $\boldsymbol{a}$A ($\boldsymbol{a}$ is inclusion ratio, X is inclusion compound)

A	methanol	o-xylene	m-xylene	p-xylene
M(Ni-MOF)	487			
M(A)	32	106		
$\boldsymbol{a}$	2	3	2	2.5

$$a = \frac{\frac{m_{loss}\%}{\mathrm{M}_A}}{\frac{(1-m_{loss})\%}{\mathrm{M}_{Ni-MOF}}} \quad \textbf{(8.1)}$$

Where m_{loss} is the weight loss of the complex at 100 °C (for methanol) or 200 °C (for xylene isomers, M_A is the molecular weight of the inclusion compound, M_{Ni-MOF} is the molecular weight of the Ni-MOF.

8.4 Photos of Pickering Emulsion

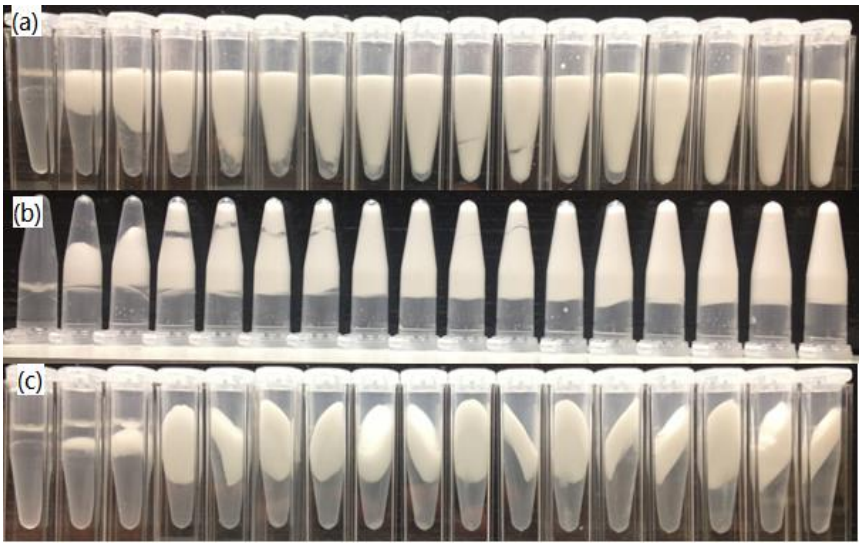

Figure 8.3 Photo of o/w emulsions with 0.1 *M* NaCl (a) before centrifugation (taken one day after emulsified), (b) upside down before centrifugation (taken one day after emulsified) and (c) after centrifugation at 4000 rpm for 30 min with an increasing concentration of oxidised cellulose in aqueous phase from 0 to 15 g·L^{-1}.

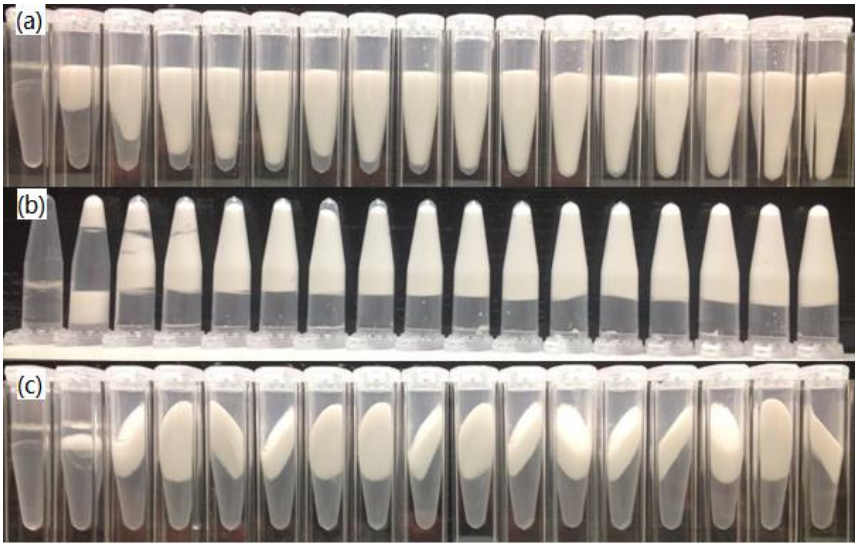

Figure 8.4 Photo of o/w emulsions 0.5 *M* NaCl (a) before centrifugation (taken one day after emulsified), (b) upside down before centrifugation (taken one day after emulsified) and (c) after centrifugation at 4000 rpm for 30 min with an increasing concentration of oxidised cellulose in aqueous phase from 0 to 15 g·L^{-1}.

Figure 8.5 Photo of o/w emulsions with 1 *M* NaCl (a) before centrifugation (taken one day after emulsified), (b) upside down before centrifugation (taken one day after emulsified) and (c) after centrifugation at 4000 rpm for 30 min with an increasing concentration of oxidised cellulose in aqueous phase from 0 to 15 $g \cdot L^{-1}$.

8.5 SANS fitting of Pickering Emulsion

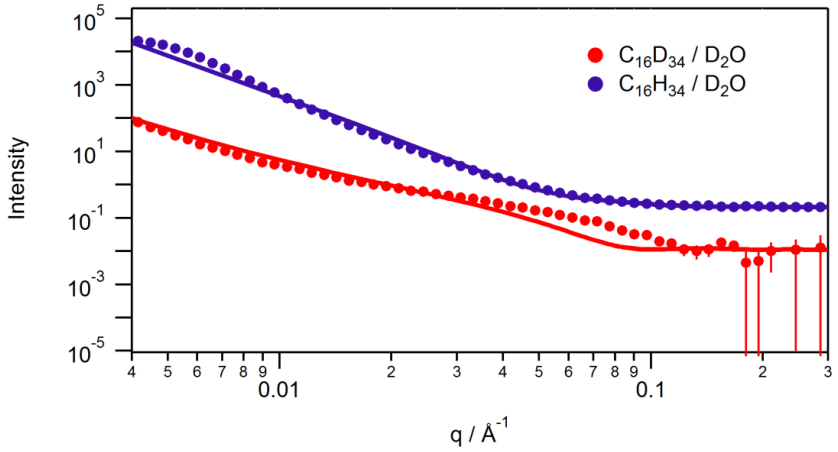

Figure 8.6 Experimental SANS spectra of hexadecane / water emulsion stabilised by ONCF (8 g·L^{-1}) at 0.1 *M* NaCl concentration with different deuterated composition (scattered points); solid lines are the fitted curves.

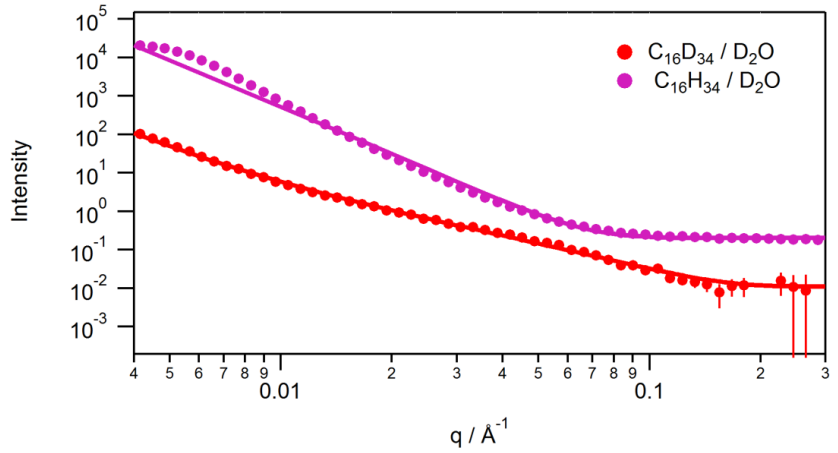

Figure 8.7 Experimental SANS spectra of hexadecane/water emulsion stabilised by ONCF (8 g·L^{-1}) at 0.5 *M* NaCl concentration with different deuterated composition (scattered points); solid lines are the fitted curves.

8.6 XRD of Ni-MOF

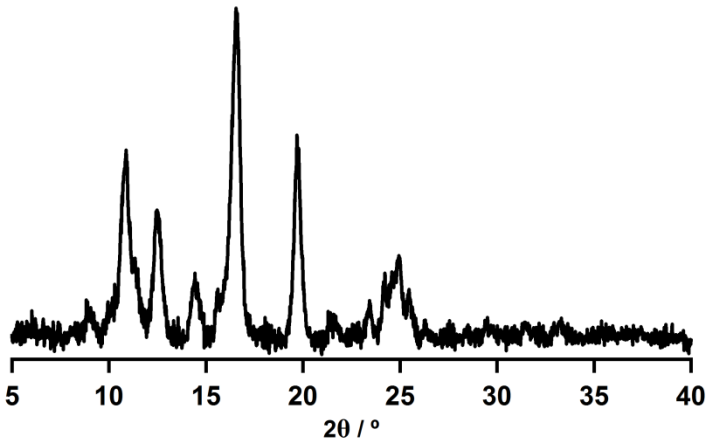

Figure 8.8 XRD pattern of Ni-MOF exposed to m-xylene and then re-evacuated.

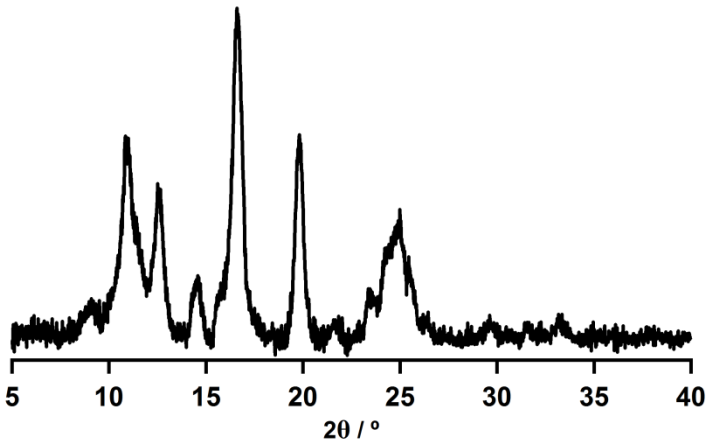

Figure 8.9 XRD pattern of Ni-MOF exposed to p-xylene and then re-evacuated.

8.7 Rietveld Refinement Patterns

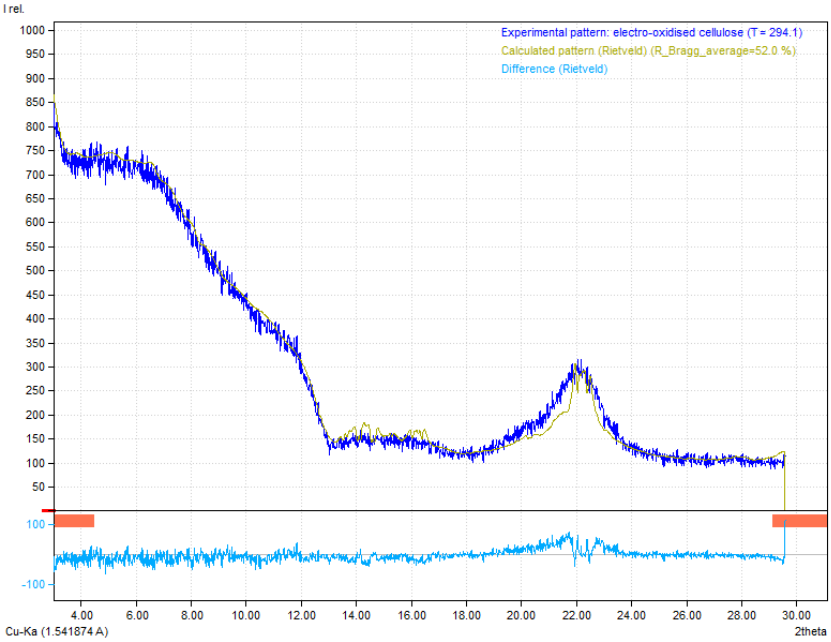

Figure 8.10 Rietveld refinement pattern of the X-ray diffraction data for electro-oxidised cellulose. Dark blue line shows the experimental profile and yellow line shows the calculated profile. The light blue line at the bottom shows the residual difference.

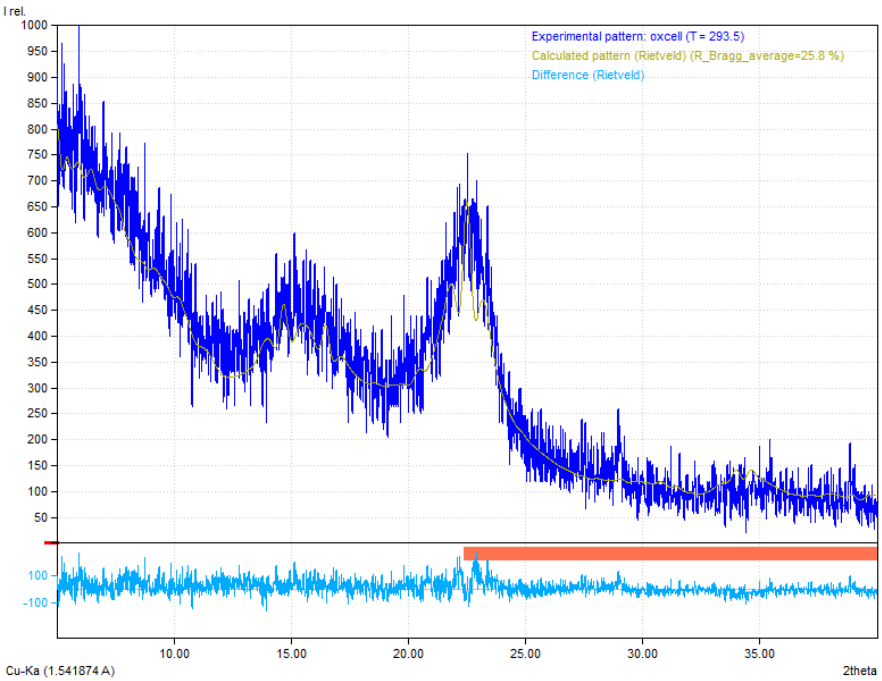

Figure 8.12 Rietveld refinement pattern of the X-ray diffraction data for OCNF. Dark blue line shows the experimental profile and yellow line shows the calculated profile. The light blue line at the bottom shows the residual difference.

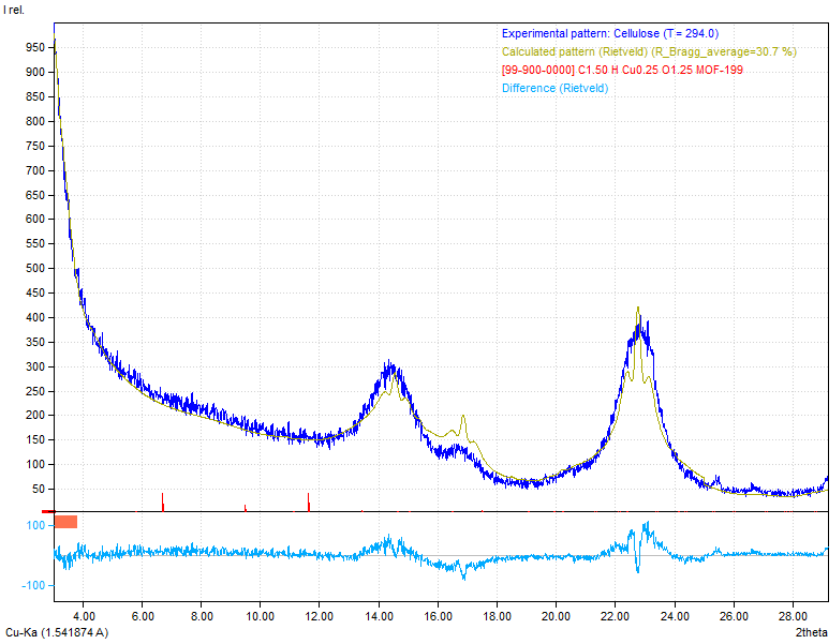

Figure 8.13 Rietveld refinement pattern of the X-ray diffraction data for BC. Dark blue line shows the experimental profile and yellow line shows the calculated profile. The light blue line at the bottom shows the residual difference.

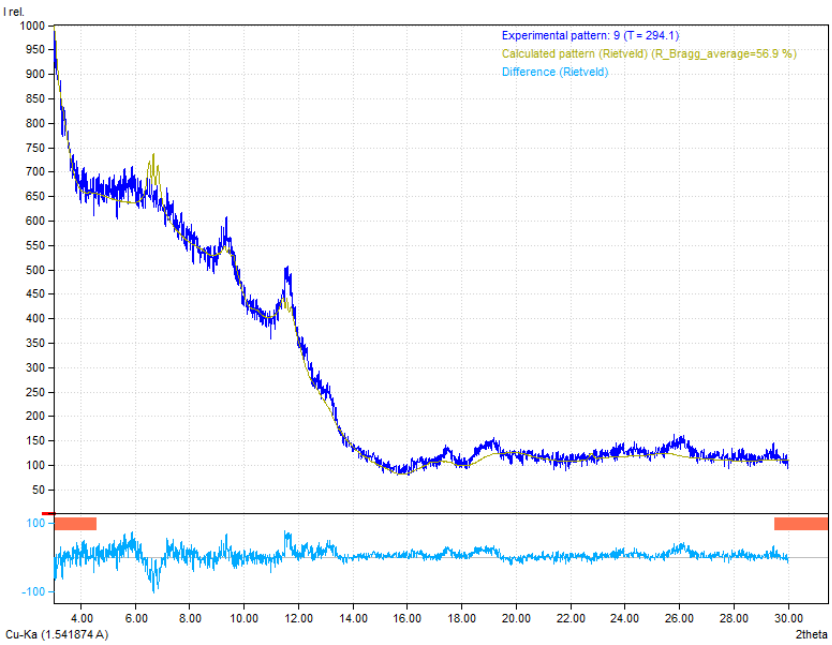

Figure 8.14 Rietveld refinement pattern of the X-ray diffraction data for MOF-199. Dark blue line shows the experimental profile and yellow line shows the calculated profile. The light blue line at the bottom shows the residual difference.

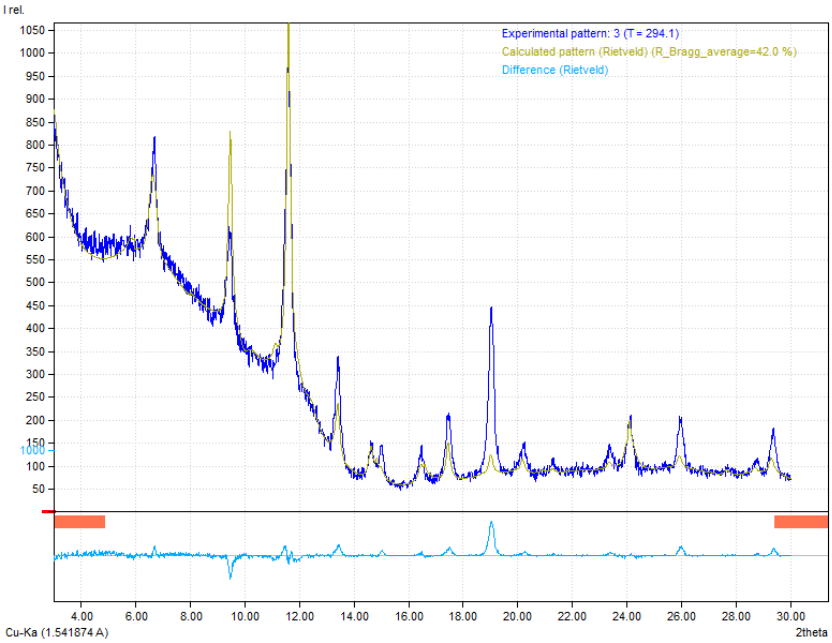

Figure 8.15 Rietveld refinement pattern of the X-ray diffraction data for MOF-199/OCNF composite. Dark blue line shows the experimental profile and yellow line shows the calculated profile. The light blue line at the bottom shows the residual difference.

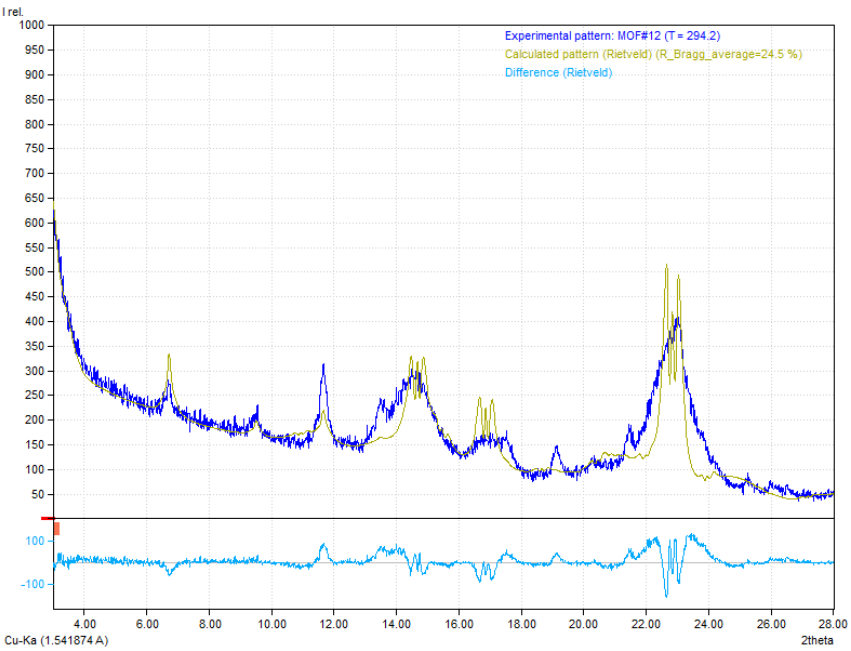

Figure 8.16 Rietveld refinement pattern of the X-ray diffraction data for MOF-199/BC composite. Dark blue line shows the experimental profile and yellow line shows the calculated profile. The light blue line at the bottom shows the residual difference.

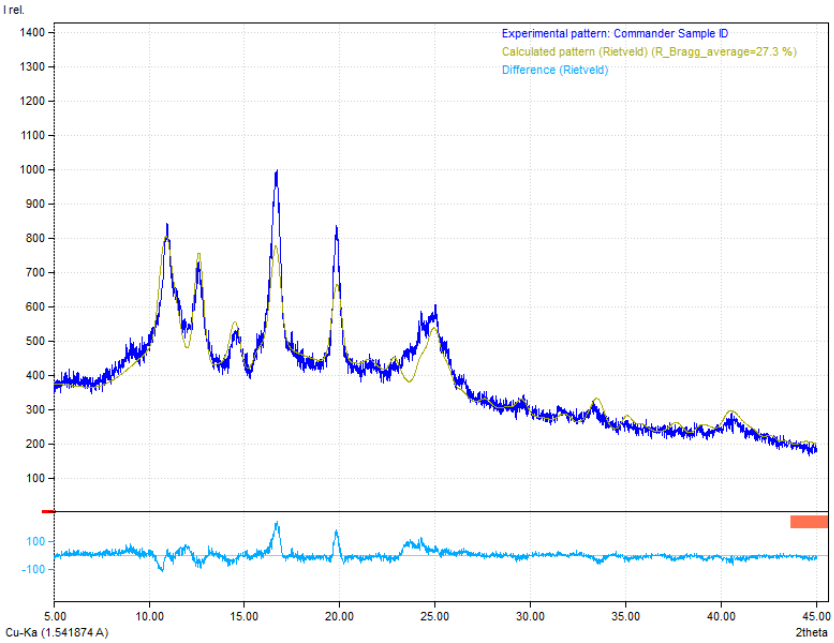

Figure 8.17 Rietveld refinement pattern of the X-ray diffraction data for Ni-MOF. Dark blue line shows the experimental profile and yellow line shows the calculated profile. The light blue line at the bottom shows the residual difference.

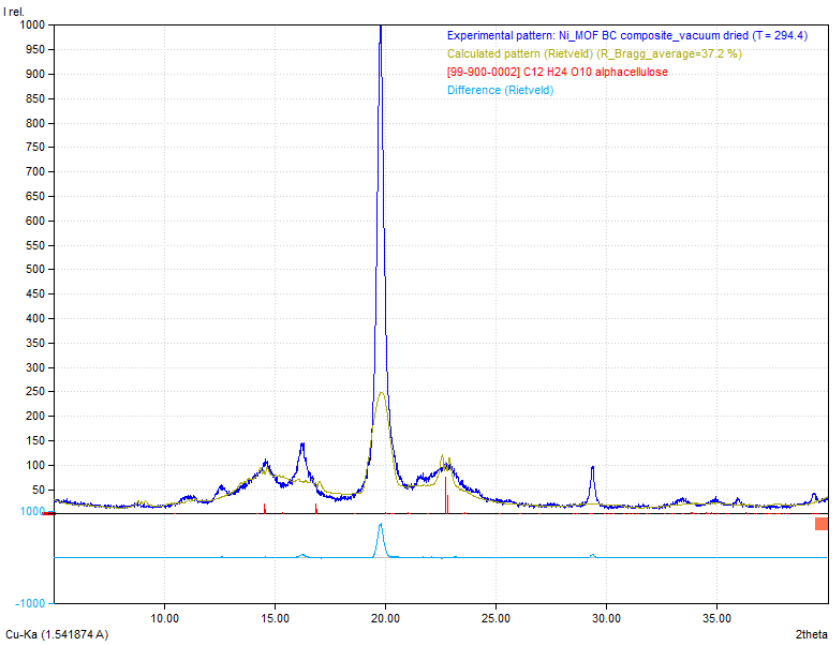

Figure 8.18 Rietveld refinement pattern of the X-ray diffraction data for Ni-MOF/BC composite. Dark blue line shows the experimental profile and yellow line shows the calculated profile. The light blue line at the bottom shows the residual difference.